AGH University of Science and Technology
Faculty of Physics and Applied Computer Science

Doctoral thesis

Inga Łakomiec

The measurement of $\phi(1020)$ meson production in proton-proton collisions at $\sqrt{s} = 13$ TeV with the ATLAS detector at the LHC

Supervisors: **Prof. dr hab. inż. Mariusz Przybycień**
Dr inż. Leszek Adamczyk

Cracow, July 2022

Declaration of the author of this dissertation:

Aware of legal responsibility for making untrue statements I hereby declare that I have written this dissertation myself and all the contents of the dissertation have been obtained by legal means.

date, author signature

Declaration of the thesis Supervisor:

This dissertation is ready to be reviewed.

date, supervisor signature

Acknowledgements

I would like to thank all people who supported me during my PhD studies, especially at the time when I was writing my PhD thesis. I am grateful to my both supervisors: Prof. Mariusz Przybycień and Dr. Leszek Adamczyk for their valuable help and scientific guidance that I really appreciate.

I would also like to thank all people who always believe in me: my husband for his big support, my parents and grandparents for their help with developing my talents and accomplishing what I planned, my parents-in-law for taking care of my child and my son for motivating me to finish my work. Thank you all!

This work was supported in part by Polish National Science Center grant no. UMO-2015/19/B/ST2/00989 and by the scholarship no. PPI/PRO/2018/1/00026/U/001 from the PROM Programme - International scholarship exchange of PhD candidates and academics of the Polish National Agency for Academic Exchange.

Streszczenie

Niniejsza rozprawa doktorska przedstawia pomiar produkcji mezonu $\phi(1020)$ w oparciu o dane zebrane w 2015 roku przez eksperyment ATLAS na LHC w zderzeniach proton-proton przy energii w układzie środka masy $\sqrt{s} = 13$ TeV. Analiza zawiera porównanie produkcji mezonu ϕ w różnych typach nieelastycznego rozpraszania proton-proton (pp):

- pojedynczej dyfrakcji (SD), $pp \to Xp$ lub $pp \to pY$,
- centralnej dyfrakcji (CD), $pp \to pXp$,
- procesach niedyfrakcyjnych (ND), $pp \to X$.

Rodzaj oddziaływań proton-proton określany jest za pomocą detektorów ARP (ATLAS Roman Pot) rejestrujących protony rozpraszane pod bardzo małymi kątami w stosunku do osi wiązki. Detektory te znajdują się blisko rury akceleratora w dużej odległości od nominalnego punktu zderzenia. Detektor centralny umożliwia natomiast śledzenie trajektorii i pomiar pędu cząstek naładowanych obecnych w stanie końcowym $X(Y)$.

Ze względu na krótki czas życia mezonu ϕ, jego produkcja mierzona jest w oparciu o rozkład masy niezmienniczej produktów jego rozpadu. Badany jest najbardziej prawdopodobny rozpad na dwa przeciwnie naładowane kaony, których wydajna identyfikacja stanowi istotny element analizy. Pomiary przeprowadzono w funkcji pędu poprzecznego i pospieszności, oraz w przypadku pojedynczej dyfrakcji, dodatkowo z podziałem na trzy zakresy względnej straty energii, ξ, protonu rozproszonego dyfrakcyjnie: $\xi < 0.035$, $0.035 < \xi < 0.08$ oraz $0.08 < \xi < 0.16$.

Praca doktorska składa się z dziewięciu rozdziałów, które poprzedza wstęp. Najważniejsze zagadnienia teoretyczne omówione zostały w rozdziale pierwszym. Przedstawienie aparatury pomiarowej znajduje się w rozdziale drugim. Rozdziały od trzeciego do siódmego zawierają szczegółowy opis analizy. Procedura identyfikacji cząstek na podstawie pomiaru ich średniej straty energii na jednostkę przebytej w detektorze drogi $\mathrm{d}E/\mathrm{d}x$ oraz pędu wyjaśniona jest w rozdziale trzecim. Rozdział czwarty zawiera procedurę selekcji przypadków i charakterystykę wykorzystanych zestawów danych oraz próbek symulacyjnych. W rozdziale piątym opisana jest selekcja kandydatów na mezony ϕ, natomiast sposób wyznaczania poprawek wprowadzanych do danych eksperymentalnych oraz analiza błędów systematycznych przedstawione są w rozdziale szóstym i siódmym. Rozdział ósmy zawiera wyniki pomiaru produkcji mezonu ϕ oraz ich dyskusję. Główną część pracy kończy rozdział dziewiąty będący podsumowaniem przeprowadzonej analizy. Dwa dodatki zawierają wykresy istotne w przeprowadzonej analizie, które nie zostały jednak umieszczone w części głównej.

Widma mezonu ϕ zostały zrekonstruowane w przedziale pędu poprzecznego $0.6 < p_{\mathrm{T},\phi} < 1.5$ GeV, scałkowanym po obszarze $|y_\phi| < 0.8$ i w zakresie pospieszności $|y_\phi| < 0.8$, scałkowanym po przedziale $0.6 < p_{\mathrm{T},\phi} < 1.5$ GeV. Biorąc pod uwagę ograniczenia wynikające z wydajności rekonstrukcji śladów oraz wydajności identyfikacji cząstek, obszar kinematyczny pomiarów został zawężony do zakresu pędu kaonu $p_K < 0.9$ GeV i pędu poprzecznego kaonu $p_{\mathrm{T},K} > 0.29$ GeV.

Otrzymane wyniki porównano z przewidywaniami fenomenologicznych modeli oddziaływań PYTHIA 8 i EPOS, które są zaimplementowane w generatorach przypadków korzystających

z metody Monte Carlo (MC). Najlepsza zgodność pomiędzy zmierzonymi wartościami a przewidywaniami została zaobserwowana w pomiarach CD i ND dla EPOS oraz w SD dla obszaru $\xi < 0.035$, również dla EPOS. W obszarze $0.035 < \xi < 0.08$ oraz $0.08 < \xi < 0.16$ przewidywania żadnego z modeli nie są zgodne z wynikami pomiarów.

Produkcję mezonu ϕ zmierzoną dla procesów niedyfrakcyjnych przy energii $\sqrt{s} = 13$ TeV porównano z wynikami pomiaru przekroju czynnego na produkcję $\phi \to K^+K^-$ w zderzeniach proton-proton przy energii $\sqrt{s} = 7$ TeV opublikowanymi wcześniej przez Współpracę ATLAS. Uzyskano zgodność pomiędzy pomiarami przedstawionymi w tej pracy a wynikami uzyskanymi przy energii $\sqrt{s} = 7$ TeV.

Porównano również produkcję mezonu ϕ w analizach SD, CD i ND. Najwyższe wartości widm mezonu ϕ zostały zmierzone dla ND, a najniższe dla CD. Największa produkcja ϕ w analizie SD obserwowana jest w obszarze $0.08 < \xi < 0.16$ a najmniejsza dla zakresu $\xi < 0.035$. Różnice w produkcji mezonu ϕ są zatem związane z krotnościami cząstek naładowanych w danej próbce. Im większa średnia liczba cząstek naładowanych, tym większa produkcja ϕ jest obserwowana. Wyniki te sugerują, że mezony ϕ pochodzą głównie z procesu fragmentacji a stany początkowe w danym procesie, Pomeron-proton w SD, Pomeron-Pomeron w CD i proton-proton w ND nie wpływają znacząco na udział kwarków dziwnych w stanach końcowych.

Wyniki przedstawionych badań są istotne dla rozwoju fenomenologicznych modeli produkcji hadronów w kierunku opisu oddziaływań charakteryzujących się małym przekazem czteropędu, gdzie Perturbacyjna Chromodynamika Kwantowa nie może być stosowana i niezbędne jest wykorzystanie danych doświadczalnych pochodzących ze zderzeń hadronów o bardzo wysokich energiach. W szczególności, zmierzone widma mezonu ϕ mogą pomóc w ograniczeniu wartości swobodnych parametrów w modelach fenomenologicznych.

Contents

Acronyms

AFP ATLAS Forward Proton
AGS Alternating Gradient Synchrotron
ALFA Absolute Luminosity For ATLAS
ALICE A Large Ion Collider Experiment
ARP ATLAS Roman Pots
ATLAS A Toroidal LHC Apparatus
BL beam line
CD Central Diffraction
CEP Central Exclusive Production
CERN European Laboratory for Particle Physics
CMS Compact Muon Solenoid
CR Colour Reconnection
CTP Central Trigger Processor
DD Double Diffraction
DIS deep inelastic scattering
DL Donnachie and Landshoff
EF Event Filter
EM Electromagnetic
EMEC electromagnetic end-caps
FCAL Forward Calorimeters
FSR Final-State Radiation
FWHM Full Width at Half Maximum
HCAL Hadronic Calorimeter
HEC Hadronic End-Cap
HLT High Level Trigger
IBL Insertable B-Layer

ID Inner Detector
IP Interaction Point
ISR Initial-State Radiation
L1 Level-1
L1A Level-1 Accept
L2 Level-2
LAr Liquid Argon
LEP Large Electron Positron Collider
LHC Large Hadron Collider
LHCb LHC *beauty*
LRG Large Rapidity Gap
MB Minimum Bias
MBTS Minimum Bias Trigger Scintillators
MC Monte Carlo
MD Main Detector
MPIs Multi Parton Interactions
MPV Most Probable Value
MSTW Martin-Stirling-Thorne-Watt
ND Non-Diffractive processes
OD Overlap Detector
PD Pixel Detector
PDF Parton Distribution Functions
PID Particle Identification
pp proton-proton
pQCD perturbative Quantum Chromodynamics
PS Proton Synchrotron
PSB Proton Synchrotron Booster
PSs Parton Showers
QCD Quantum Chromodynamics
QED Quantum Electrodynamics
QGP quark-gluon plasma
ROI Region-of-Interest
RP Roman Pot
SPS Super Proton Synchrotron
SD Single Diffraction
SCT Semiconductor Tracker
SM Standard Model

sQCD soft Quantum Chromodynamics

TDAQ Trigger and Data Acquisition

ToT Time over Threshold

TR Transition Radiation

TRT Transition Radiation Tracker

Introduction

Understanding our world is one of the essential desires of humankind. We would like to predict behaviour and know each object's structure, regardless of its size. Constituents of matter are constantly researched from both the macroscopic and the microscopic points of view. Scientists examine fundamental forces to describe phenomena surrounding us. However, there are still unsolved questions about our Universe. One of the not fully described issues regards soft Quantum Chromodynamics (QCD) processes that can be investigated using data from particle accelerators. These machines enable us to explore the world of particles including their interactions at a soft scale which this thesis is focused on.

The aim of the study is the measurement of $\phi(1020)$ meson production in different types of proton-proton (pp) inelastic scattering based on data collected by the ATLAS experiment at the Large Hadron Collider (LHC) at the centre-of-mass energy $\sqrt{s} = 13$ TeV. The results can be helpful in understanding high-energy physical processes with low momentum transfers (~ 1 GeV) and they may play a significant role in developing phenomenological soft hadroproduction models to improve the total inelastic pp cross-section predictions.

The thesis consists of nine Chapters. The first two contain the theoretical framework and the experimental apparatus description. The subsequent steps of the analysis are presented in Chapters 3 - 7. The particle identification procedure which is based on tracks' ionisation energy loss and momentum measurements is explained in Chapter 3 while Chapter 4 contains details on the event selection. The ϕ meson candidate selection and corrections applied to data are discussed in Chapters 5 and 6, respectively. Chapter 7 includes closure tests and systematic uncertainty analysis. Results and their deeper discussion are presented in Chapter 8. Comparisons of data and model predictions as well as differences in ϕ meson production rates in different types of pp inelastic scattering processes are also shown. In addition, the current measurement is compared to the results obtained earlier by the ATLAS experiment based on pp Minimum Bias data collected at $\sqrt{s} = 13$ TeV and $\sqrt{s} = 7$ TeV. Chapter 9 contains the summary of the most important results obtained in this thesis. The dissertation also includes two Appendices where some additional figures relevant for the analysis are shown.

During her doctoral studies, the author also participated in other scientific activities not directly related to the research presented in this thesis. They included work on developing software for the ATLAS experiment. The author's qualification task for becoming co-author of the ATLAS was implementation of the overlay technique of Monte Carlo (MC) signal events with zero-bias data from the ATLAS Roman Pots. In addition, the author has studied the proton reconstruction efficiency with the ALFA detector using the overlay technique and the outcomes were applied in the analysis shown in Ref. [155]. The results were also presented at the Seventh Annual Large Hadron Collider Physics Conference in Puebla, Mexico, 2019 and published [1].

The author is a member of five ATLAS analysis teams whose research is focused on the following physics topics:

- Strangeness in Single Diffractive, Central Diffractive and Non-Diffractive events with ALFA at 13 TeV,
- Exclusive pion pair production at 13 TeV,
- Low-mass Single Diffraction at 13 TeV (the charge-particle ALFA analysis),
- Diffractive jets in Single Diffractive and Central Diffractive events with ALFA at 13 TeV,
- Observation of $\gamma\gamma \to WW \to l\nu jj$ (with and without AFP detector).

The author has major contribution to the first of the above listed analyses and it is the main subject of this dissertation. Author's task in the exclusive pion pair production analysis was related to the particle identification, MC validation and ALFA overlay technique whereas the latter involves studies on proton reconstruction efficiency. The author has contributed to the other three analyses by validating MC simulation. The author also participated in the alignment optimisation process for the ALFA detectors.

The author has spent in total four months at CERN including participation in the LHC Run 2 data-taking as an ALFA detector coordinator in 2018 and attended AFP detector beam tests in 2016.

The analysis presented in this thesis has been shown and discussed on a regular basis at ATLAS Soft QCD Working Group meetings and at ARP General Meetings. The author is a co-author of 150 publications of the ATLAS Collaboration. The list of these scientific papers can be found in INSPIRE data base (ID: 1789522).

CHAPTER 1
Theoretical Framework

1.1 The Standard Model

The Standard Model (SM) [2] of particle physics formulated in the 1970s is a theory that describes elementary particles and forces between them. It takes into account three out of four known fundamental interactions in the Universe - weak, electromagnetic and strong ones. Gravity is not included in this theoretical model. There are two types of fundamental particles according to the SM:

- fermions - particles carrying half-integer spin that obey Fermi-Dirac statistics [3, 4],
- bosons - particles carrying integer spin that obey Bose-Einstein statistics [5].

The theory predicts that matter in the Universe is built from fermions - six quarks and six leptons, placed in three generations. The different interactions between them are described as the exchange of gauge boson mediators: gluons (strong interactions), photons (electromagnetic interactions), W^+, W^- and Z^0 bosons (weak interactions). There is also the introduced in 1964 [6] and discovered in 2012 [7,8] Higgs boson. This particle is produced by the scalar Higgs field quantum excitation. The process is responsible for the mass generation of fermions and W and Z bosons. Figure 1.1 shows all the SM elementary particles together with their masses, electric charges, and spins.

The strong interaction is most important for the analysis presented in this dissertation and it is described in more detail in the following Section.

1.1.1 Strong Interaction

The theory which describes the strong interaction is called QCD and is based on the SU(3) gauge group which is also called the colour group [9]. The name is connected to the quantum number - *colour charge*, carried by partons - quarks, antiquarks and gluons. The number was introduced so that the Pauli principle could be preserved [10]. Therefore, there is also a colour index - r, g, b for each flavour index of a quark (u, d, s, c, b, t). Quarks interact via strong force and there are eight massless vector gluons that enable the strong processes. The gluons carry simultaneously colour and anticolour [11] and they are mediators of the strong colour field which is described by the QCD potential:

$$V_{\mathrm{QCD}}(r) = -\frac{4}{3}\frac{\alpha_s}{r} + kr, \tag{1.1}$$

where the factor of 4/3 is related to the number of quark colours and the number of gluons, α_s is the strong coupling constant, and the constant $k > 0$ determines the energy per unit length

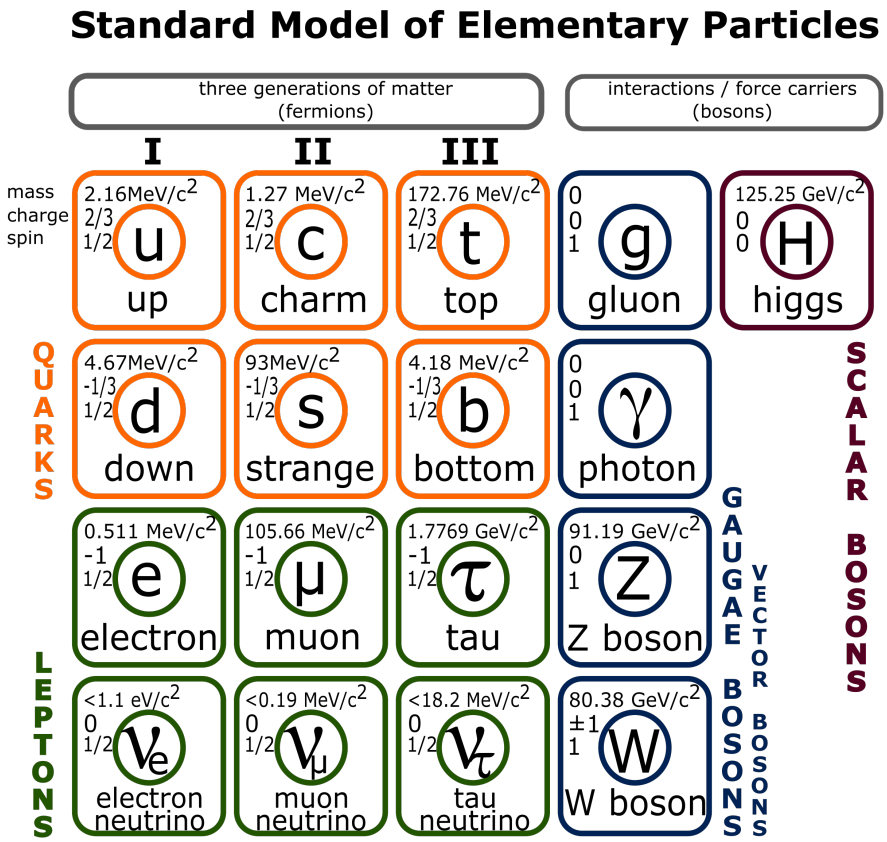

Figure 1.1: The SM elementary particles with their masses, electric charges and spins, numbers taken from [13].

in the colour field [2,11]. The QCD potential is similar to the quantum electrodynamics (QED) potential at short distances. Since quarks are confined in hadrons, there is also the second part of the QCD potential that grows linearly with the distance r. An important part of the formula (1.1) is the strong coupling constant α_s. It depends on the momentum transfer Q as follows:

$$\alpha_s(Q^2) = \frac{12\pi}{(33 - 2n_f)\ln\left(Q^2/\Lambda^2_{\mathrm{QCD}}\right)}, \tag{1.2}$$

where n_f is the number of active quark flavours, and $\Lambda_{\mathrm{QCD}} \approx 0.2$ is the QCD scale parameter at which α_s becomes large [15]. The $\alpha_s(Q)$ dependence is shown in Figure 1.2 that presents the comparison between predictions (black curves) and experimental data points. It is crucial to understand the $\alpha_s(Q)$ dependence both at long distances when the Q^2 is low and at the proton scale distances [12]. The QCD coupling decreases for larger momentum transfers and vanishes at asymptotically high energies. This property is called asymptotic freedom [14]. It is considered that quarks and gluons can be treated as approximately free at short distances and the perturbation theory can be applied for the scattering process calculations [10, 16]. Interactions at this energy scale are called hard hadronic processes and they are described by the perturbative QCD (pQCD). There is also the soft QCD (sQCD) which is focused on interactions with lower momentum transfer (soft processes) where complete theoretical calculations cannot be performed. The sQCD processes are described just by phenomenological models based on Regge theory [20] and the data analyses performed at a soft scale ($Q \sim 1$ GeV) are helpful to their development. The coupling constant increases dramatically leading to the quark confinement in hadrons at small Q scales and it is relevant to form a comprehensive description of hadronisation - the process by which coloured partons transform into colour-neutral hadrons [17]. These particles are divided into two groups:

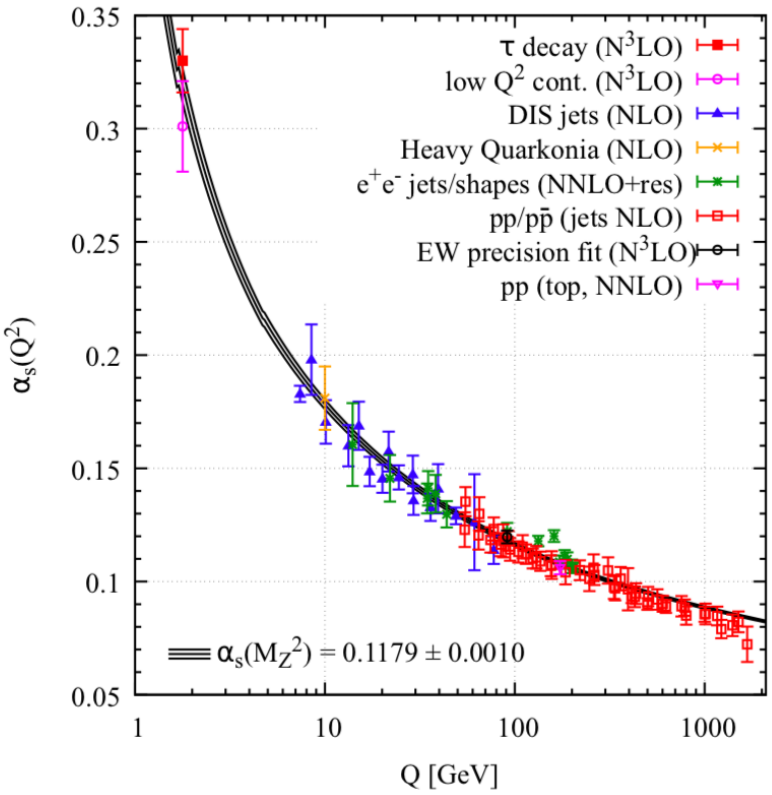

Figure 1.2: The summary of measurements of α_s as a function of Q, from [13].

- baryons - made of the odd number of valence quarks (three in the simplest cases),
- mesons - made of the even number of valence quarks - (two in the simplest cases - a quark and an antiquark) [13, 73],

where the valence quarks contribute to quantum numbers of hadrons. One of the mesons is $\phi(1020)$ meson and its cross section in different types of proton-proton inelastic scattering is calculated in this dissertation.

1.1.2 Inelastic Proton-Proton Scattering

The total cross section of proton-proton collisions is divided into elastic and inelastic processes. The latter ones are investigated in this analysis. They are split into diffractive and non-diffractive interactions as follows:

- Single Diffraction (SD), $pp \to Xp$ or $pp \to pY$,
- Double Diffraction (DD), $pp \to XY$,
- Central Diffraction (CD), $pp \to pXp$,
- Non-Diffractive processes (ND), $pp \to X$.

The diagrams of the inelastic processes are shown in Figure 1.3, where the $X(Y)$ is the representation of a dissociated proton or a centrally-produced hadronic system. The diffractive processes (SD, CD and DD) are characterised as interactions in which no quantum numbers are exchanged between the colliding particles. The diffraction is also defined as a process with at least one non-exponentially suppressed empty rapidity region - the large rapidity gap (LRG),

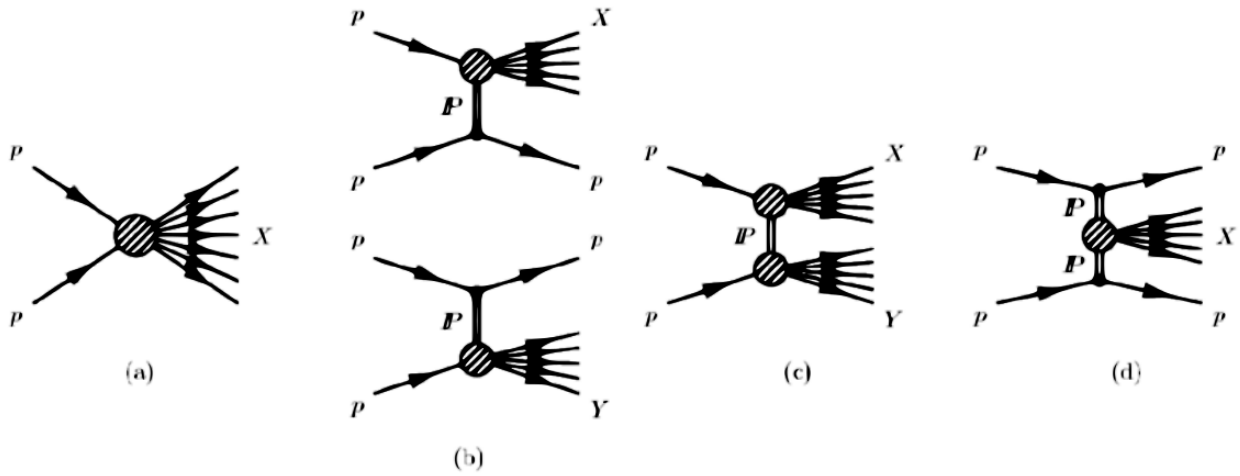

Figure 1.3: The diagrams of non- (a), single- (b), double- (c) and central-diffractive (d) processes. The X(Y) is the representation of a dissociated-proton or a centrally-produced hadronic system. Figure taken from [18].

in the final state [19,25], where rapidity is a quantity characterised in Section 1.4. The different topologies of inelastic *pp* scattering can be experimentally associated with an exchanged colour singlet - the Pomeron trajectory [21, 24]. Hadronic interactions are described in the Regge theory [22,23] by an exchange of objects, Reggeon trajectories. The soft hadronic processes are dominated by the Regge trajectory with the quantum number of the vacuum - the Pomeron trajectory [19]. It can be imagined as independent microscopic colour singlet parton cascades [21] or as a new object which is emitted from proton. Inelastic *pp* processes can be depicted using the Pomeron concept as the following fusion processes (also shown in Figure 1.3):

- proton-proton (ND),
- Pomeron-proton (SD and DD),
- Pomeron-Pomeron (CD).

1.2 Strangeness

Strangeness S is a quantum number that was postulated in 1953 by M. Gell-Mann and K. Nishijima independently [32–35]. Before the term *strangeness* was introduced to particle physics, the existence of strange behaving particles had been experimentally proved [31]. The first discovery of particles that showed unusual properties was in 1944. These particles were then observed in Cosmic Rays by L. Leprince-Ringuet and M. L'Héritier [27, 28]. G. D. Rochester and C. C. Butler detected strange particles in Cosmic Rays in 1947 [29]. The particles were named *Vparticles* because the tracks of the final decay particles in the cloud chamber were V shaped [30]. Moreover, they had a mass between a proton and a pion mass, they were unstable and they had strangely long lifetime ($\sim 3 \cdot 10^{-10}$ s), typical of weak interactions [31]. Therefore, it was assumed that the *new* particles were produced by strong interactions but they decayed by weak processes. Besides, the observed particles were always created in pairs. All the mentioned unknowns were solved when a new additive quantum number S was introduced. The strangeness was assigned to every strongly interacting particle. It is postulated that this quantum number is conserved in strong and electromagnetic interactions but the weak processes are permitted to violate S [27, 36].

Elementary particles for which $S \neq 0$ are quarks s and $\bar{s}$. The strangeness of the strange quark s equals -1 while the strangeness of the anti-strange quark $\bar{s}$ is 1. The particles that contain the s or $\bar{s}$ quarks are called strange particles and their strangeness is determined as the sum of the strangeness of their constituent quarks.

1.2.1 Strangeness in Proton-Proton Collisions

Protons consist of three valence quarks - uud and $S = 0$ for protons. The total strangeness of strongly interacting particles must be the same before and after the process according to the strangeness conservation rule. This implies that s and $\bar{s}$ quarks are always produced in pairs in pp collisions. Quarks cannot be observed directly because the existence of coloured partons as freely propagating states is not permitted by QCD [26]. Hence, the only way to measure strangeness is to detect hadrons containing strange or anti-strange quarks. Furthermore, sources of strangeness in these high-energy reactions should be investigated. The following paragraphs describe possible strangeness origins in pp collisions.

Sea Quarks

The proton structure was examined using mainly the deep inelastic scattering (DIS) - inelastic scattering with large momentum transfer - data [37,40–42] and it is described in terms of Parton Distribution Functions (PDFs), $f_p(x, Q^2)$ [45]. The inferred from measurements functions denote the probability of finding a parton carrying a fraction x of the proton momentum at an energy scale Q of the hard interaction [38]. There are a few physics groups carrying out research on PDFs [39, 43, 44]. The proton PDFs obtained by the Martin-Stirling-Thorne-Watt (MSTW) group [39] are shown in Figure 1.4. It is inferred from measurements that a proton is composed of three valence quarks contributing to the proton quantum numbers and of sea quarks - the quark-antiquark pairs which carry a low momentum fraction x. The valence quarks are more dominant at low Q^2 whereas there are more sea quarks at high Q^2. Proton constituents are also virtual gluons that can fluctuate into virtual $q\bar{q}$ pairs which are continuously created and annihilated within the proton [45].

The proton structure studies prove that there is a contribution to the pp inelastic scattering processes from strange quarks through interactions with virtual $s\bar{s}$ pairs. The intrinsic strangeness proton content is related to the strange sea quarks and the probability to get strangeness from the proton is given by the PDFs.

Fragmentation Process

Another strangeness source in pp collisions is the fragmentation process. Partons are scattered out of the bound states and new partons are formed during the process. These coloured partons are then grouped into colour singlet states and create hadrons [26]. Two fragmentation phases which depend on the momentum transfer squared Q^2 are distinguished:

- at high Q^2 - additional quarks and gluons can be produced in addition to those coming from the primary interaction (pQCD is used for the calculations) [47, 48],
- at lower Q^2 ($\lesssim 1$ GeV) - the final creation of colour-neutral hadrons (the fragmentation is modelled phenomenologically as a non-perturbative QCD process) [13, 46, 49].

There are currently two main phenomenological approaches describing the hadronisation - the cluster and the string models. The Cluster fragmentation model [52] can be divided into three successive phases:

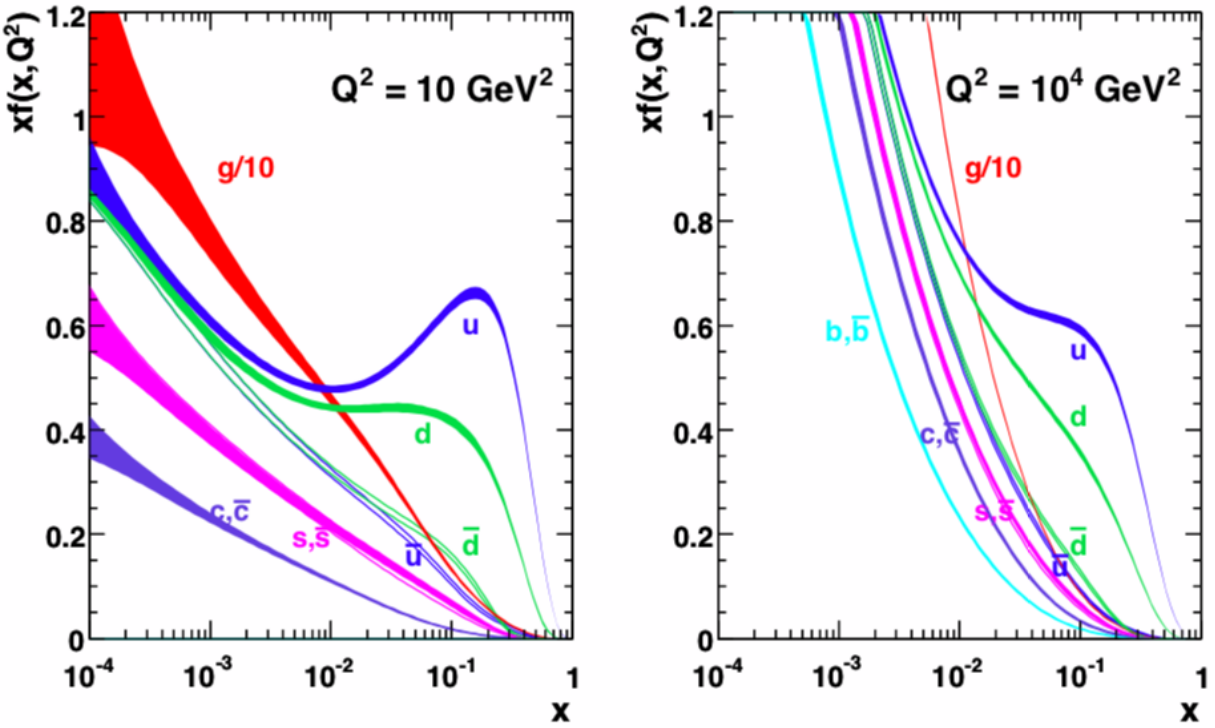

Figure 1.4: The MSTW PDFs in the proton at two energy scales (left) $Q^2 = 10\,\mathrm{GeV}^2$ and (right) $Q^2 = 10^4\,\mathrm{GeV}^2$, as a function of the parton's momentum fraction x. Figure taken from [39].

1. all gluons split into $q\bar{q}$ pairs,
2. the preconfinement phase - adjoining quarks and antiquarks form colour-neutral clusters [53],
3. an isotropic two-body decay of the clusters into hadrons.

The schematic view of the cluster hadronisation is shown in Figure 1.5.

The string model is applied in the MC generators (Section 1.5) that were tested in this analysis. One of the most successful string frameworks is The Lund string model [50]. The string is characterised there as a colour field tube formed between quarks from a $q\bar{q}$ pair [51]. The energy density of this object is called string tension κ and $\kappa \approx 0.9$ GeV/fm ≈ 0.18 GeV^2 [55] which corresponds to the assumption that when the particle separation is large ($\gtrsim 1$ fm), the confinement potential between quarks rises linearly with the distance r between them:

$$V(r) = \kappa r. \tag{1.3}$$

When r becomes greater, the energy stored in the colour field is at some point high enough to create a new $q\bar{q}$ pair. The string breaks then up and smaller colour field tubes are formed. The process continues until the energy of all the quark pairs is sufficiently low to form hadrons - that is equivalent to the case that the energy is too low to create another string. The scheme of the process is pictured in Figure 1.6.

Different flavours can be produced during the fragmentation process. The probability of the production of a flavour varies for each of them. The effect is connected to the mass of individual quarks. The higher mass of a quark leads to the lower probability of the string creation. Since the s quark is heavier than the u or d quarks, there is the strangeness suppression with respect to non-strange flavours which is described by the factor [56]:

$$P(s : u/d) \approx 0.2 - 0.3. \tag{1.4}$$

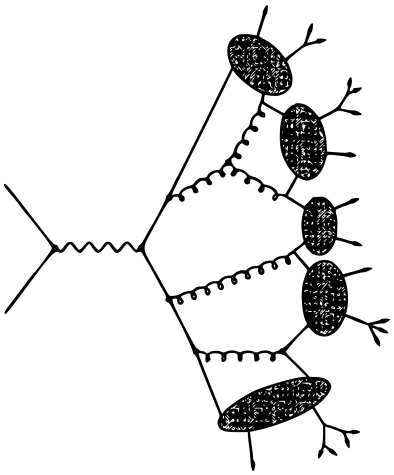

Figure 1.5: Scheme of the parton shower with the cluster hadronisation model for $e^+e^- \rightarrow$ hadrons. Figure taken from [54].

The strangeness suppression was investigated in many experiments using data coming from different hadronic interactions at various energies [57–60].

1.3 Resonances

Resonances are particles which cannot be detected directly because of their extremely small lifetime ($\sim 10^{-25}$ s) [27] which is calculated as:

$$\tau = \frac{\hbar}{\Gamma}, \tag{1.5}$$

where Γ is the resonance width (the Full Width at Half Maximum - FWHM). Registering decay products of highly unstable particles is the way to observe them. A resonance appears as a peak in the invariant mass distribution and we may extract its properties by fitting the Breit-Wigner [13, 59–61] function. The non-relativistic form of the Breit-Wigner formula, also known as the Cauchy one, can be employed to extract the yield of the resonance from its invariant mass distribution and it is expressed as follows:

$$f(M) = \frac{\Gamma}{2\pi} \frac{1}{(M - M_0)^2 + \Gamma^2/4}, \tag{1.6}$$

where M_0 is the resonance mass. The Breit-Wigner distribution shape is shown in Figure 1.7.

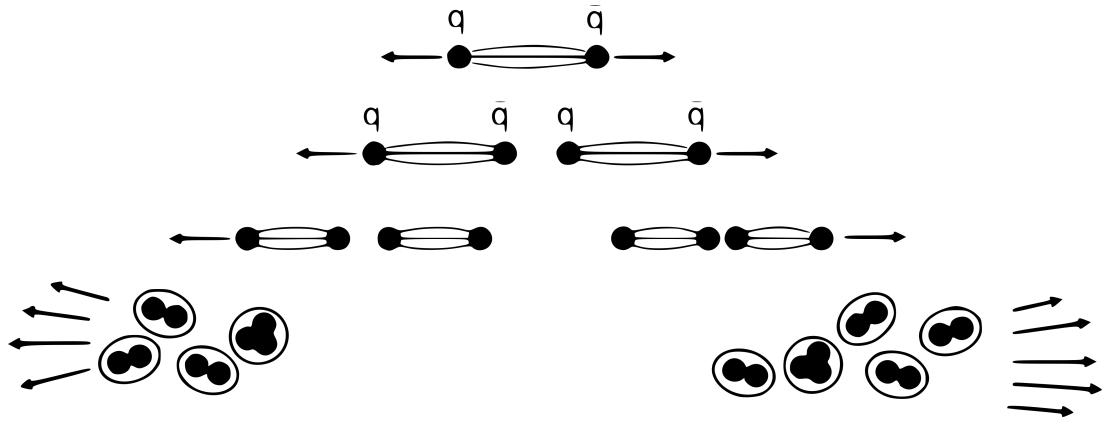

Figure 1.6: The illustration of the string hadronisation model. Figure taken from [45].

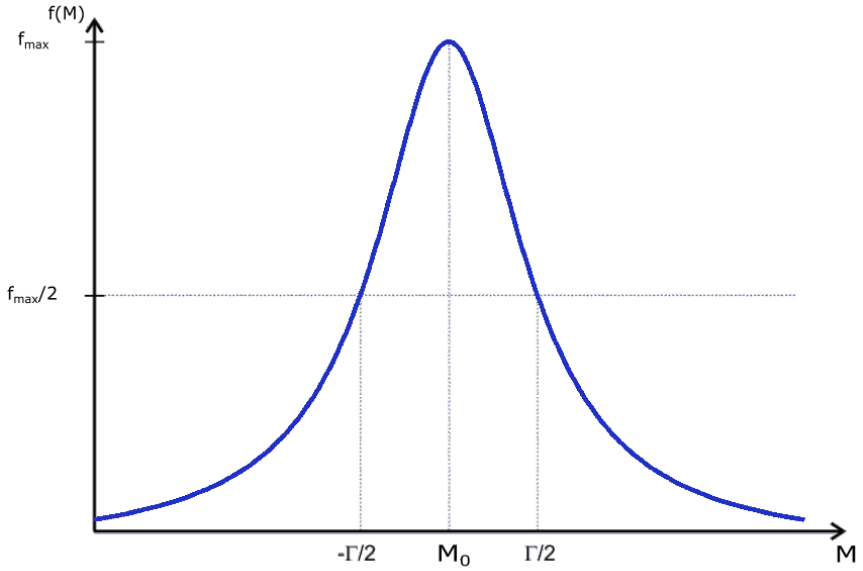

Figure 1.7: The Breit-Wigner distribution.

1.3.1 $\phi(1020)$ Meson

The $\phi(1020)$ meson was discovered in 1962 in data from a bubble chamber experiment at the Brookhaven Alternating Gradient Synchrotron (AGS) [72]. Since that time the particle was investigated using different collision data at various energies [65–71] providing precise $\phi(1020)$ meson properties' measurements [13].

$\phi(1020)$ meson is the lightest bound state of strange quarks. This hadron is a $s\bar{s}$ resonance with a lifetime $1.55 \pm 0.01 \cdot 10^{-22}$ s. Hence, this particle cannot be observed directly. The investigation of its production is possible by the decay products' identification. $\phi(1020)$ meson decays strongly and around thirty ways of its decay are known. The most probable one is the $\phi \to K^+K^-$ decay and the scheme of the process is shown in Figure 1.8. Basic properties of $\phi(1020)$ meson are collected in Table 1.1.

Table 1.1: $\phi(1020)$ meson properties [13].

mass	1019.461 ±0.0016 MeV
width	4.249 ±0.013 MeV
valence quarks	$s\bar{s}$
electric charge	0
the most probable decay mode (branching fraction)	K^+K^- (49.2±0.5 %)

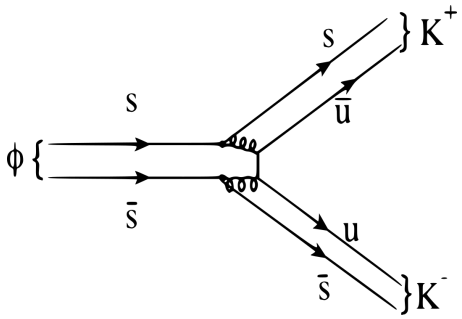

Figure 1.8: Scheme of the decay process $\phi \to K^+K^-$ at the quark level. Figure taken from [74].

1.4 Kinematic Variables

This study is focused on differences between the $\phi(1020)$ meson production mechanisms in different types of proton-proton inelastic scattering processes. Particles that take part in these processes can be characterised using kinematic variables [13]. The most important and necessary quantities to perform this analysis are described in this Chapter.

The Mandelstam variables are employed to characterise the two-body final state process shown in Figure 1.9 where p_i and m_i $(i = 1, 2, 3, 4)$ are respectively four-momenta and masses of incoming $(i = 1, 2)$ and outgoing $(i = 3, 4)$ particles. The Mandelstam quantities are Lorentz invariants and they are defined as follows:

$$s = (p_1 + p_2)^2 = (p_3 + p_4)^2 \tag{1.7a}$$
$$t = (p_1 - p_3)^2 = (p_2 - p_4)^2 \tag{1.7b}$$
$$u = (p_1 - p_4)^2 = (p_2 - p_3)^2. \tag{1.7c}$$

They are not independent, and satisfy the relation:

$$s + t + u = m_1^2 + m_2^2 + m_3^2 + m_4^2. \tag{1.8}$$

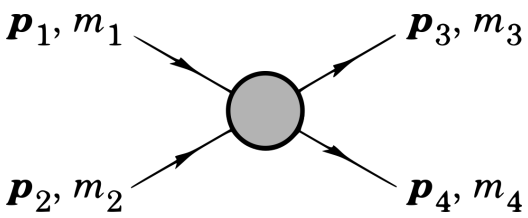

Figure 1.9: Definitions of variables for a two-body final state. Figure taken from [13].

The different types of inelastic pp scattering processes can be distinguished by the number of forward protons in the final state. One of the quantities which are used to describe the protons is the fractional energy loss ξ which is defined as:

$$\xi = \frac{E_b - E}{E_b} \tag{1.9}$$

where E is the total proton energy after the collision and E_b is the beam energy.

Another useful quantity is the rapidity y which is defined for each particle by:

$$y = \frac{1}{2} \ln \left(\frac{E + p_z}{E - p_z} \right), \tag{1.10}$$

where E and p_z are the particle's energy and its z-component of its momentum, respectively. For $p \gg m$ (p and m are the momentum and the mass of the particle respectively) the rapidity is approximated by pseudorapidity η:

$$\eta = -\ln \tan (\theta/2), \tag{1.11}$$

where θ is the particle polar angle - the angle between the particle momentum and the beam axis. According to the formula (1.11), η can be measured even when we do not know the mass and the momentum of the particle. Hence, the particle identification is not required when η is used and it is experimentally simpler to choose this quantity than y.

The $\phi(1020)$ meson production cross-section is measured in this study as a function of y and transverse momentum p_{T} which is the component of the particle momentum perpendicular to the beam axis:

$$p_{\mathrm{T}} = \sqrt{p_x^2 + p_y^2}, \tag{1.12}$$

where p_x and p_y are the particle's momentum components in the plane perpendicular to the beam axis.

1.5 Monte Carlo Generators

Phenomenological hadroproduction models are implemented in the MC event generators. Two of them, PYTHIA 8 [75, 76] and EPOS [77, 82, 86, 87], were employed in this analysis and they are briefly discussed below.

PYTHIA 8 enables to handle collisions between hadrons or between same-generation leptons and it is a complete standalone general-purpose event generator [78] which includes almost all physics phenomena of the SM expected at the LHC. This generator simulates parton interactions and parton showers [85]. It is important for this analysis that PYTHIA 8 describes the total pp cross section and depicts both hard and soft processes, i.a. Multi Parton Interactions (MPIs) [80, 81], Parton Showers (PSs) divided into Initial-State Radiation (ISR) and Final-State Radiation (FSR), beam remnants' decays, colour reconnection (CR), fragmentation and particle decays. Hadronisation is based on the Lund string fragmentation model and the diffractive processes are described using the Regge formalism. The scheme of the event generation is shown in Figure 1.10 and the description of the procedure can be found in [79]. A set of parameters (the tune) must be adjusted before the program is used in the particular analysis. The two main prepackages of parameter sets are prepared for the ATLAS detector [112] analyses - the A2 [83] and the A3 [84] tunes.

EPOS is the MC event generator which was originally used for the cosmic ray shower simulations. It applies the parton based description which is combined with the string and the Regge theory [85]. An elementary scattering is described as the exchange of the parton ladder

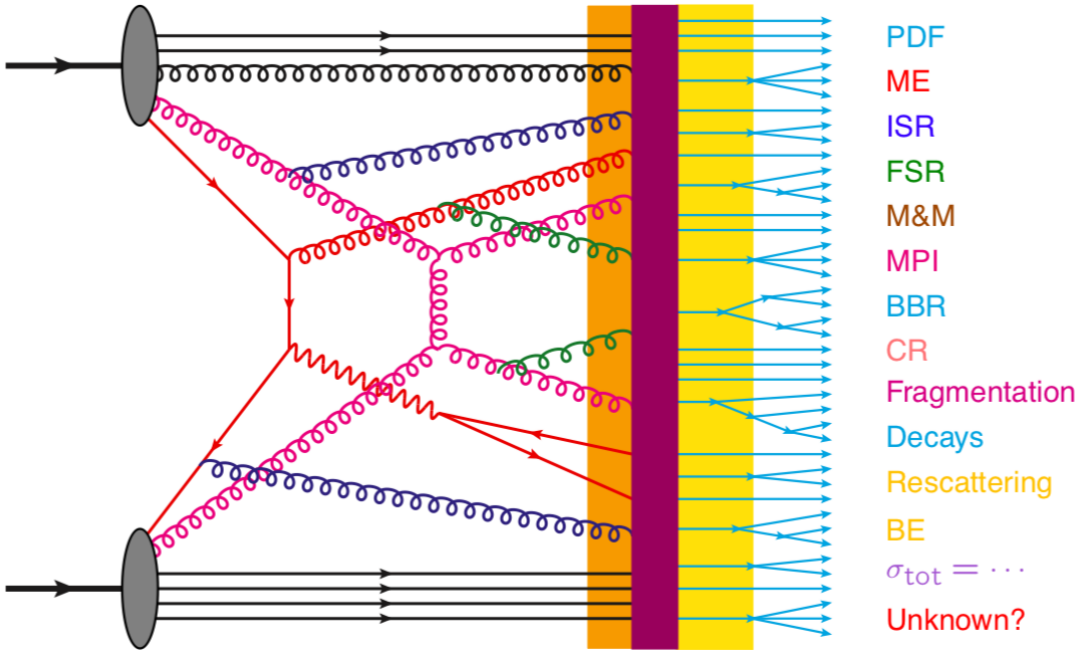

Figure 1.10: The main physics processes taken into account in the event generation. Figure taken from [79].

which denotes the parton evolutions from the projectile and the target side towards the centre (small x) (see [86,88,91]). The ladder is the first source of the particle production in this model and it can be imagined as strings which consist of two parts - the hard one (partons) and the purely phenomenological soft one (the Pomerons) [89]. The second particle production origin is the two off-shell remnants [87]. The scheme of the EPOS elementary scattering is pictured in Figure 1.11. This event generator has one parameter set which cannot be tuned by the user.

There are two classes of events generated by EPOS, SD and SD', which are considered as the single diffraction samples. They are characterised by exactly one forward proton and the large rapidity gap (LRG) in the final state. The reason to differentiate the two classes is the origin of the proton in the final state. The SD class is a diffractive sample, modelled by the Pomeron exchange. The SD' class is characterised by protons which come from non-diffractive events. The forward-scattered protons appear because of the low mass excitation of the proton remnant (< 1 GeV) which leads to the hadronisation of the beam remnant back to the proton [90]. It is considered the SD' EPOS class is as an alternative model to the PYTHIA 8 high-mass diffraction which is described by pQCD.

1.6 Motivation and Goals

It is highly important to broaden the knowledge of the fundamental physics reactions, such as phenomena associated with strongly interacting objects. The aims of the studies preformed in this thesis are:

- testing soft hadronic interactions in the non-perturbative regime which leads to the development of the soft hadroproduction models describing high-energy physical processes at the lower momentum transfer,
- serving as a baseline for a better understanding of the interactions in the quark-gluon plasma (QGP) [106].

pQCD describes successfully only processes in the high momentum transfer region but it cannot be applied to non-perturbative QCD interactions [70] where the phenomenological hadroproduction models are required. Gathering and analysing as much as possible high-energy experimental data allows for their improvement. This research contributes to the models' development by $\phi(1020)$ meson production cross-section measurements which are based on the pp collision data at the centre-of-mass energy of 13 TeV. The results of the analysis participate particularly in validating the sQCD models and in making constraints on their free parameters. The production of strange hadrons is suppressed with respect to hadrons that contain just u and d

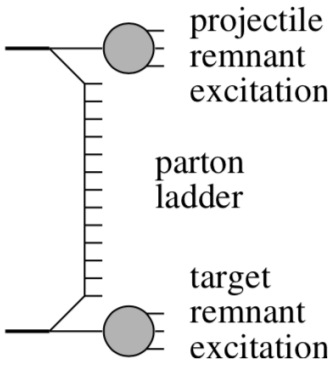

Figure 1.11: Scheme of the elementary EPOS parton-parton scattering. Figure taken from [87].

quarks. The amount of strangeness suppression in pp collisions is the MC generator parameter that must be constrained by the strange hadron production measurements [103]. Production of mesons with hidden strangeness such as ϕ or η' is also crucial for constraining hadroproduction models [104]. The formation of such mesons is described in PYTHIA 8 using the Lund string model. However, the dominant mechanism for the ϕ or η' production is not fully known and requires more experimental data.

Another significant scientific issue is related to the ϕ meson quark composition. It is critical to understand whether the meson with $s\bar{s}$ valence quarks reacts more violently compared to the single-strange particles [73]. The theoretical approaches are based either on hadronic degrees of freedom or on the basic degrees of freedom of QCD - quarks and gluons. On the one hand, the ϕ meson should not be sensitive to the effects related to strangeness when we take into consideration a purely hadronic scenario with the strangeness-neutral meson. On the other hand, the ϕ meson is expected to react more sensitively than a single-strange particle when its production is ruled by the partonic degrees of freedom [108].

Since the analysis shows the comparison between ϕ meson production among different types of pp inelastic scattering, it is valuable for the development of the diffraction theoretical description. The interactions between the ϕ meson and the proton are mediated by the Pomeron. Therefore, they are a valuable probe for the investigations concerning processes when the Pomereon is exchanged. The presented studies can also help with modelling the final state of hadronic interactions. The research is involved then in improving the total inelastic pp cross section predictions and provides an input for a better understanding of physical processes at the lower momentum transfer.

Another motivation of this research is to provide a benchmark for the studies of QGP which is expected to be formed in the ultra-relativistic heavy-ion collisions [92, 98, 99]. QGP exists at extremely high temperatures and densities and it is created when hadrons dissolve into a soup of quarks and gluons [93]. The production of strange particles is enhanced in the QGP phase (the deconfined phase) compared to the hadronic system (the confined phase) [100, 101, 105]. The effect is caused by the abundant creation of strange and anti-strange quarks through the following processes [102]:

- flavour creation ($qq \to s\bar{s}$, $gg \to s\bar{s}$),
- gluon splitting ($g \to s\bar{s}$), and
- flavour excitation ($gs \to gs$, $qs \to qs$).

The strangeness enhancement [97] is considered as the signature of the phase transition between the hadronic matter and the QGP [92, 94–96, 102, 107] and plays a special role in the studies of QGP. Hence the comparison of strange particles which are produced in heavy-ion and in proton-proton collisions is needed for a better understanding of the QGP properties [97, 102, 103].

CHAPTER 2
Experimental Apparatus

The thesis presents $\phi(1020)$ meson production measurements using the LHC [109, 110] data. They were collected in pp collisions at the centre-of-mass energy $\sqrt{s} = 13$ TeV with A Toroidal LHC Apparatus (ATLAS) [112] detector. The main features of the LHC collider and the ATLAS detectors are described below.

2.1 The Large Hadron Collider

The largest and highest-energy particle accelerator on Earth, the LHC, is situated on the France-Switzerland border near Geneva and it is part of the European Laboratory for Particle Physics (CERN). The goal of the international scientific society is to carry out high-energy physics research by constructing and developing numerous experiments.

The LHC is located around 100 m underground in the tunnel of 27 km circumference which was previously occupied by the e^+e^- Large Electron Positron Collider (LEP). In 2000, the experiments at LEP finished collecting data and the LEP accelerator was dismantled to

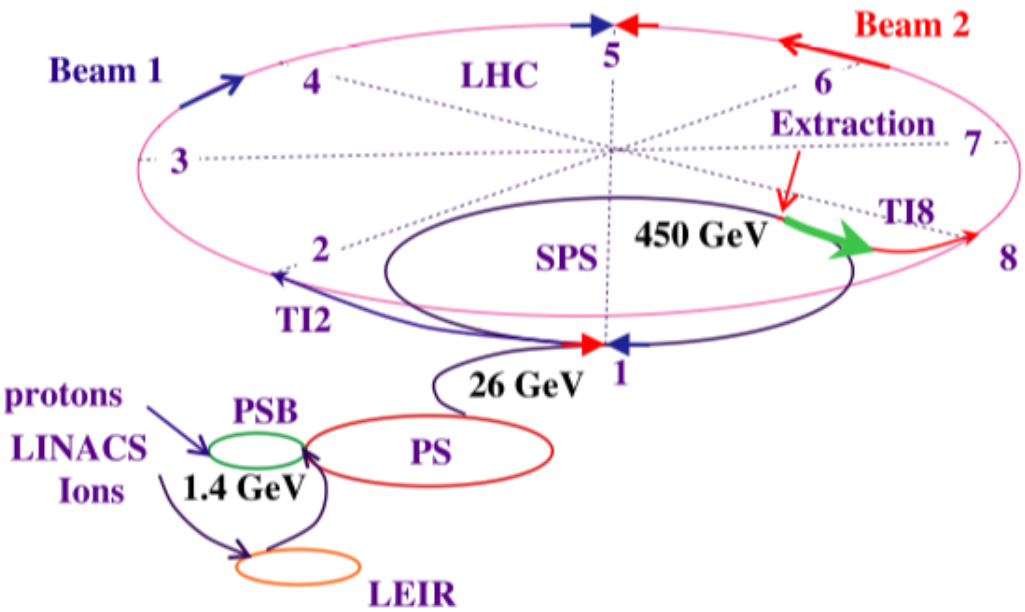

Figure 2.1: Scheme of the LHC and its injectors. Figure taken from [110].

make room for the LHC. The new collider was designed to handle *pp* and heavy-ion collisions with centre-of-mass energies of up to 14 TeV per nucleon-nucleon collision. The aim of this high-powered apparatus is to accelerate and collide hadron beams. All the operations require employment of advanced technologies and a huge number of expert engineers and scientists. The effort provides significant benefits to the investigation of the smallest building blocks of the Universe. It is valuable for the validation and for the improvement of different particle physics theories, especially for examining both the widely used Standard Model and physics beyond this theoretical concept. Therefore, the high-energy measurements are crucial for a deeper understanding of fundamental forces and matter and antimatter constituents.

The *pp* collisions at the LHC involve a sophisticated injection and acceleration complex (presented in Figure 2.1) and there are many challenging operations that enable protons to reach the extremely high energy and to collide [116]. In the beginning, protons that are provided by an ion source are accelerated in the Linac 2 to the energy of 50 MeV. Next, they are transported to the Proton Synchrotron Booster (PSB) and this machine accelerates them to 1.4 GeV. The beam enters then the Proton Synchrotron (PS) where it reaches energy of 25 GeV. The consecutive step is the proton injection into the Super Proton Synchrotron (SPS) and acceleration to 450 GeV. Each beam can consist of up to 2808 high intensity proton bunches. Eventually, the beams with 25 ns bunch spacing [117] are transferred into the two LHC rings where they are accelerated to the nominal energy. The beam-pipes cross at four interaction points (IPs) and there are four main experiments situated around the collision regions: ATLAS [112] (IP1), CMS (Compact Muon Solenoid) [113] (IP5), LHCb (LHC *beauty*) [114] (IP8) and ALICE (A Large Ion Collider Experiment) [115] (IP2). Each of them is focused on different aspects of physics and applies distinct technologies. The location of the detectors at the LHC is shown in Figure 2.2.

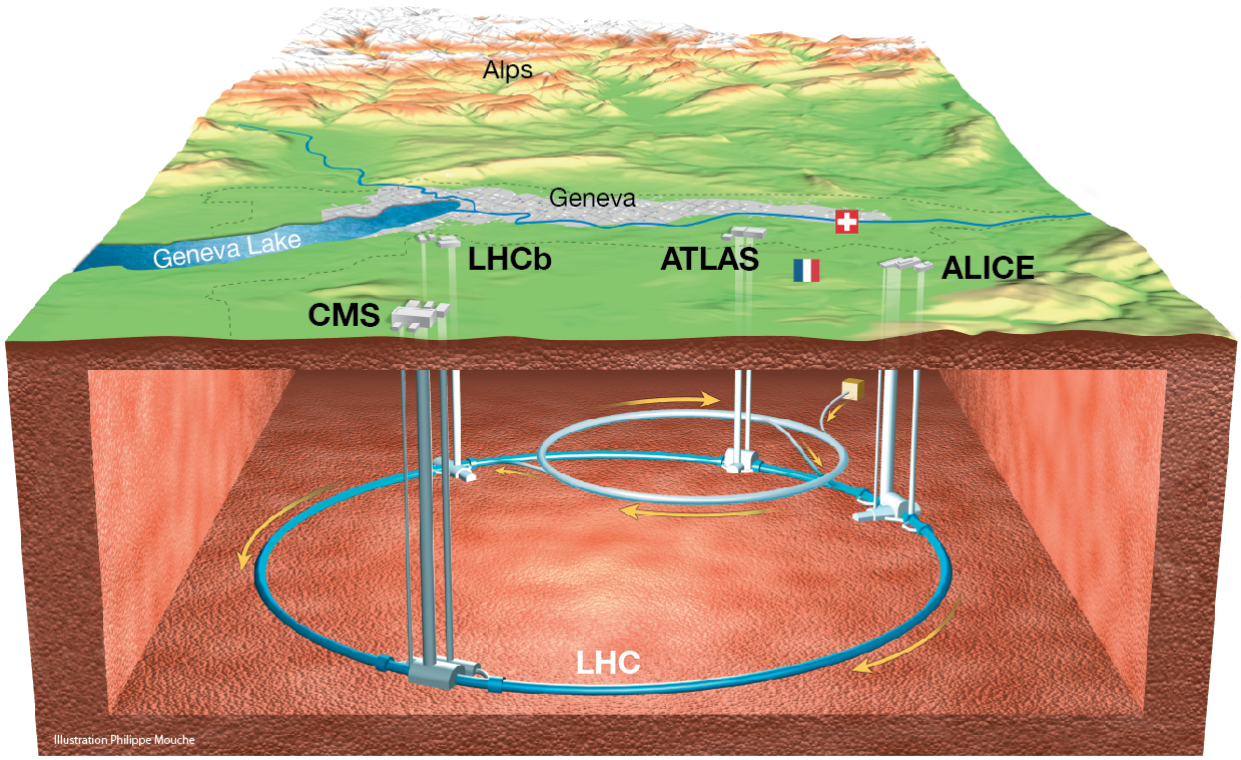

Figure 2.2: Locations of the four main LHC experiments: ATLAS, CMS, LHCb and ALICE. Figure taken from [111].

2.2 The ATLAS Experiment

The ATLAS experiment [112] is installed in the experimental cavern at Point 1. The detector allows for a comprehensive exploration of proton-proton and heavy-ion collisions. The coordinate system used by ATLAS has its origin at the nominal ATLAS interaction point and the z-axis is defined as the beam direction. The positive x-axis points from the IP to the centre of the LHC ring whereas the y-axis is defined as pointing upwards. There are two ATLAS sides - side-A with positive z and side-C with negative z.

The ATLAS detector is a general-purpose device and consists of a huge number of instruments which enable detection of extremely energetic particles. The cut-away view of the ATLAS main subdetectors is shown in Figure 2.3. The detector subsystems that were used to perform the analysis presented in this thesis are described in the following sections.

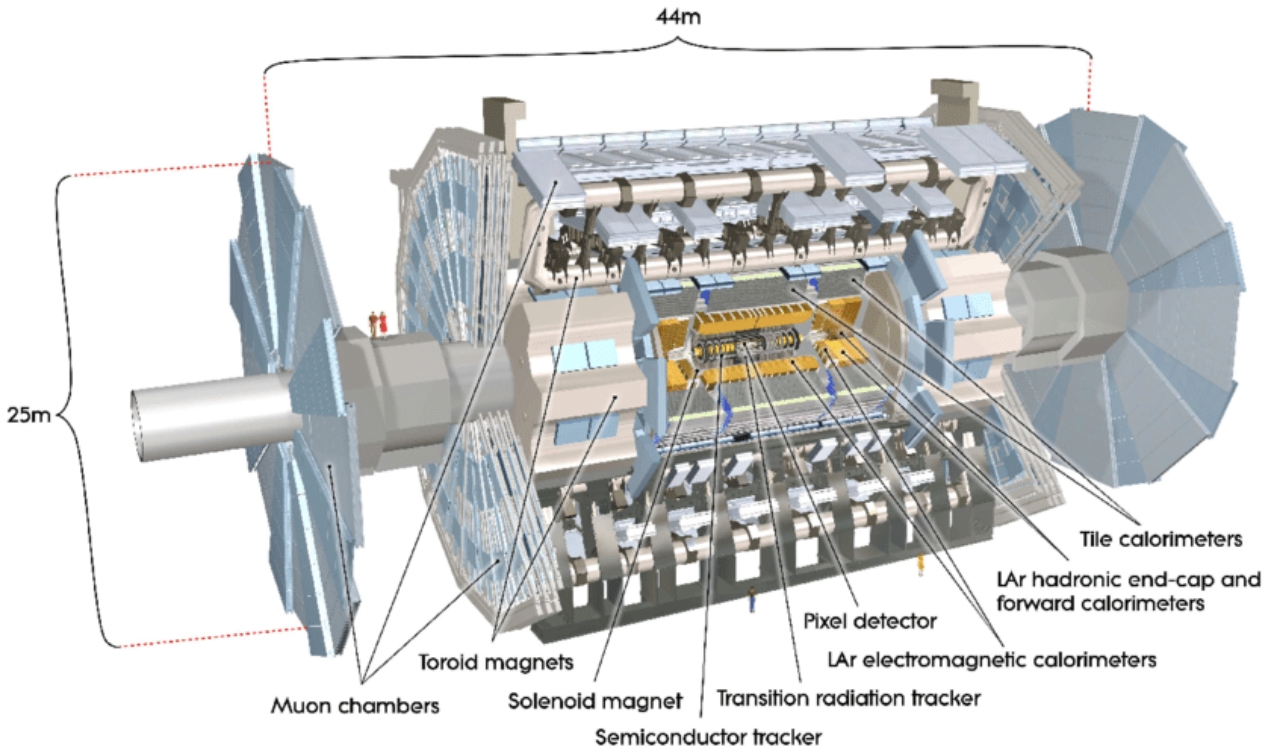

Figure 2.3: The cut-away view of the ATLAS detector. Figure taken from [112].

2.2.1 The ATLAS Inner Detector

The Inner Detector (ID) [119] is placed in the centre of the ATLAS detection system, inside a solenoid magnet which is aligned to the beam axis and provides a 2 T axial symmetric field. The ID surrounds the LHC beam pipe and measures momenta and trajectories of charged particles in the pseudorpidity range of $|\eta| < 2.5$. Three independent but complementary subdetectors whose layout is presented in Figure 2.4 make up the ID and there are:

- Pixel Detector (PD) [120],
- Semiconductor Tracker (SCT) [124] and
- Transition Radiation Tracker (TRT) [131, 132].

The PD [120] is a silicon pixel system and the critical innermost ID part which provides charged-particle tracking and vertexing. Approximately 92 million channels [123] of the device guarantee

the track reconstruction with high-efficiency and the proper resolution to distinguish between the primary and the secondary vertices [121]. This ID subsystem is formed of four barrel layers and of two end-cap regions where each contains three disk layers. A fourth barrel element - the Insertable B-Layer (IBL) [122] was added to the PD between the beam-pipe and the existing inner Pixel layer (B-layer) in 2015. The distances of the layers to the IP are shown in Figure 2.5. The reason to add the IBL was the improvement of the track and vertex reconstruction performance at the higher luminosities which were expected during the next LHC Run - Run 2 [123]. The another motivation of the new barrel layer was the mitigation of the detector radiation damage.

Silicon sensors are the basic building blocks of the PD. Their nominal size is 50×400 μm^2 and 50×250 μm^2 for the outer layers and for the IBL respectively. Pixels are located in the modules and function as solid-state ionisation chambers. Charge particles deposit their energy there and a hit position together with the time over threshold (ToT) information is read [126–128].

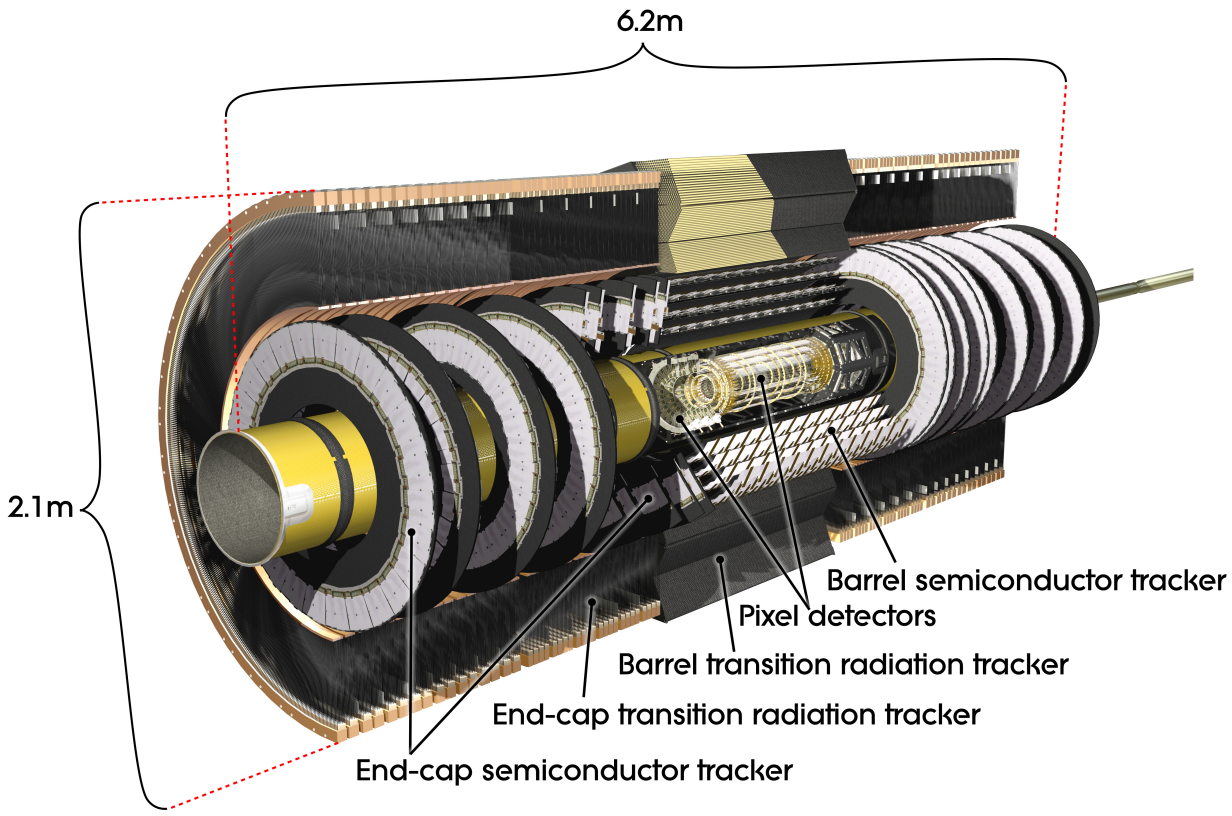

Figure 2.4: The cut-away view of the ATLAS Inner Detector. Figure taken from [112].

The SCT [124] is a silicon strip detector and it comprises four concentric barrels [129] and two end-cap components [130] where each end-cap consists of nine disks surrounding the beam axis. The position of the barrel layers with respect to the beam is presented in Figure 2.5. Such construction provides measurements of at least four space points along each charged particle track that occurred as a result of a hadron collision. The silicon strip modules are the basic building blocks of the SCT. This detector employs silicon semiconductor technology which is used by the PD as well and each SCT layer is capable of reading a hit position in two dimensions [129].

The TRT [131,132] is the outermost system of the ID. It is a gaseous straw apparatus which consists of a central TRT barrel detector, shown in Figure 2.5 and a forward and backward

TRT end-cap detector. This ID part operates with a 70 % Xe, 27 % $CO_2$2 and 3 % O_2 gas mixture. In contrast to the Pixel detector and the SCT, the TRT provides a continuous tracking system which is formed from almost 300k drift (straw) tubes of 4 mm diameter [125]. The construction enables detection of up to 36 coordinates of a charged particle crossing the straws and ionizing the gas. Moreover, this outer ID detector contributes to electron identification via transition radiation (TR) which is generated by highly-relativistic charged particles passing through polypropylene radiator material between the drift tubes. TR X-ray photons and signals from ionisation losses are registered then by the tubes and the separation of hadron from electron tracks is carried out [133].

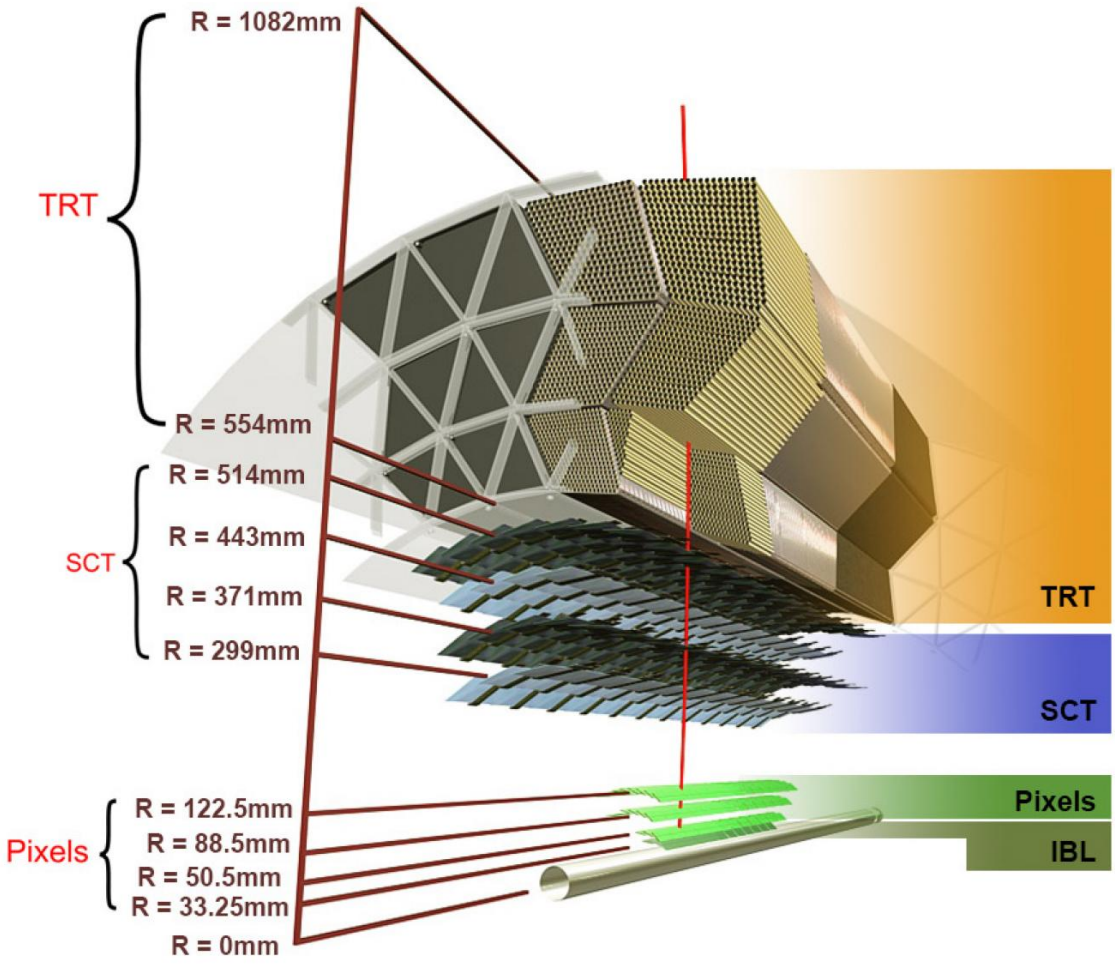

Figure 2.5: The detailed layout of the ATLAS Inner Detector. Figure taken from [118].

2.2.2 Calorimeters

The ATLAS calorimetry system [112, 136, 137] is built around the ID and it is designed to measure the individual particles' and jets' energies. The role of calorimeters is to absorb all the particles coming from a collision apart from muons which are detected by the Muon Spectrometer [112,138] and neutrinos. The calorimeters also provide information about missing transverse energy E_T. Therefore, they are a relevant part of new physics research. The cut-away view of the ATLAS calorimeters is shown in Figure 2.6.

The ATLAS detector is equipped with the Electromagnetic (EM) and the Hadronic calori-

meters. They consist of layers of an absorbing material that are interleaved with layers of an active medium. The former stops incoming particles while the latter measures their energy.

The EM calorimeters use Liquid Argon (LAr) as the active medium and lead absorber plates as the passive material. They consist of a barrel part and two EM end-caps (EMEC) which cover pseudorapidity regions $|\eta| < 1.475$ and $1.375 < |\eta| < 3.2$ respectively. Each element is situated in its own cryostat. These calorimeters are responsible for measuring the energy and the direction of electrons, positrons and photons.

The LAr technology together with the scintillator-tile one is used for the ATLAS Hadronic Calorimeters (HCAL) to measure the energy of hadrons and jets. This system is divided into two parts: the LAr Hadronic End-Cap (HEC) which is situated behind the EMEC and shares the same cryostats and the Tile Calorimeter. The first one employs cooper plate absorbers and covers the range $1.5 < |\eta| < 3.2$. The Tile calorimeter uses plastic scintillator tiles as the sampling medium and steel as the absorber material. Three parts which are located in the pseudorapidity region $|\eta| < 1.7$ are its components - one central barrel and two extended barrels.

The region closest to the beam, $3.1 < |\eta| < 4.9$ is covered by the LAr forward calorimeters (FCal) [139]. They are placed in the same cryostats as the end-cap calorimeters and they comprise one EM module (FCal1) and two hadronic modules (FCal2 and FCal3). All of them use LAr as the sensitive medium while the EM absorber compartment is made of copper and the hadronic calorimeters apply mainly tungsten to provide containment of hadronic showers.

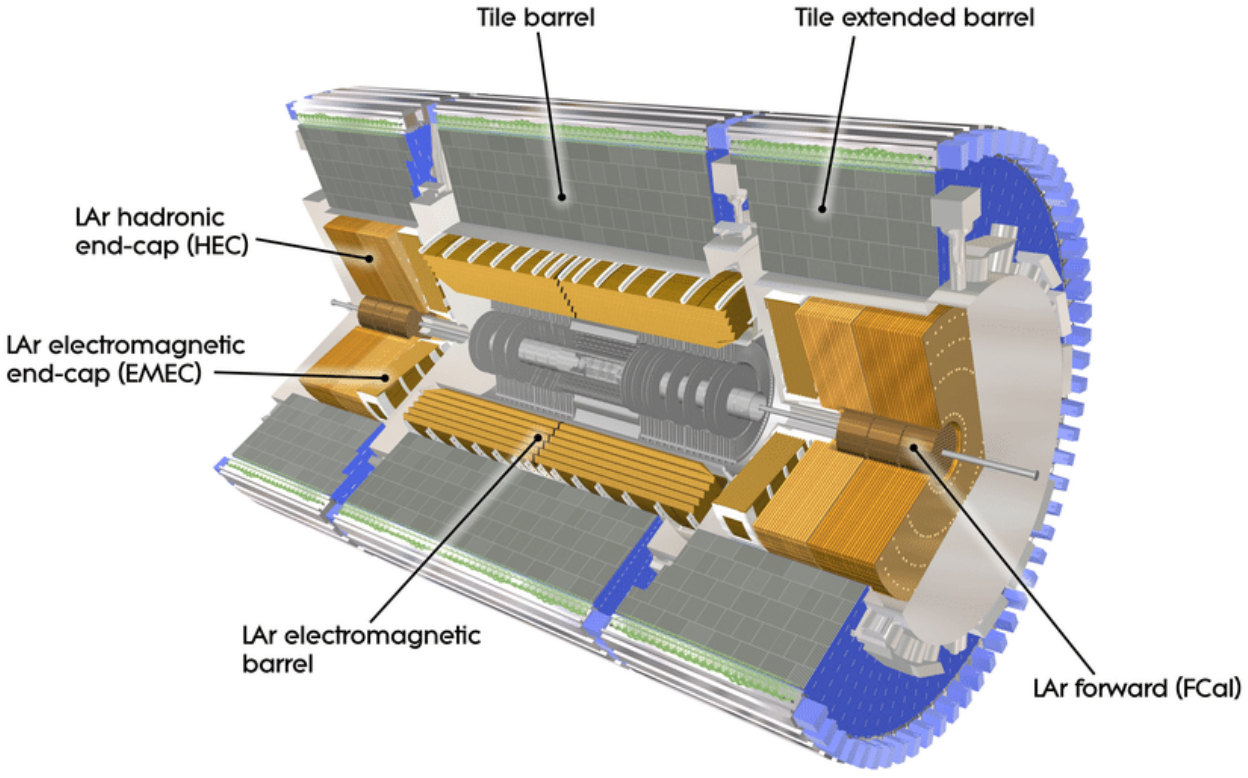

Figure 2.6: The layout of the ATLAS calorimeter system. Figure taken from [112].

2.2.3 The Minimum Bias Trigger Scintillators

The Minimum Bias Trigger Scintillators (MBTS) [134] are installed at $|z| = 3.56$ m between the ID and the Liquid Argon (LAr) EM calorimeter. The MBTS system is segmented into two disks, each for one ATLAS side and covers the pseudorapidity range $2.07 < |\eta| < 3.86$ [135]. The disk comprises eight inner and four outer azimuthally arranged sectors (counters) of 2 cm thick polystyrene scintillators. The MBTS detector system is sensitive to a minimum of the detector activity and acts as a Minimum Bias (MB) event trigger.

2.2.4 The ATLAS Roman Pots

The ATLAS Roman Pot (ARP) Forward Detector System consists of the ATLAS Forward Proton (AFP) [142] and the ALFA (Absolute Luminosity for ATLAS) detectors [140] that are designed to detect protons scattered at very small angles. The detectors are used to examine processes where at least one of two incoming protons stays intact after the collision. Elastic and diffractive events, exclusive production and photon-induced interactions can be studied in particular.

The data that were analysed in this dissertation come from the ALFA detectors and their description is presented below.

The ALFA Detectors

The ALFA detector system [140, 141] comprises eight devices that are located inside Roman Pot (RP) cylindrical movable vessels on both ATLAS sides. The pots can approach as close as 1 mm to the beam. There are four RPs on side-A and four on side-C. Moreover, they are grouped into four branches. The detectors which are situated at $z = \pm 237$ m are called close (near) RPs and those ones placed at $z = \pm 245$ m - far RPs. The ALFA detector layout with the names of the subsystems is presented in Figure 2.7.

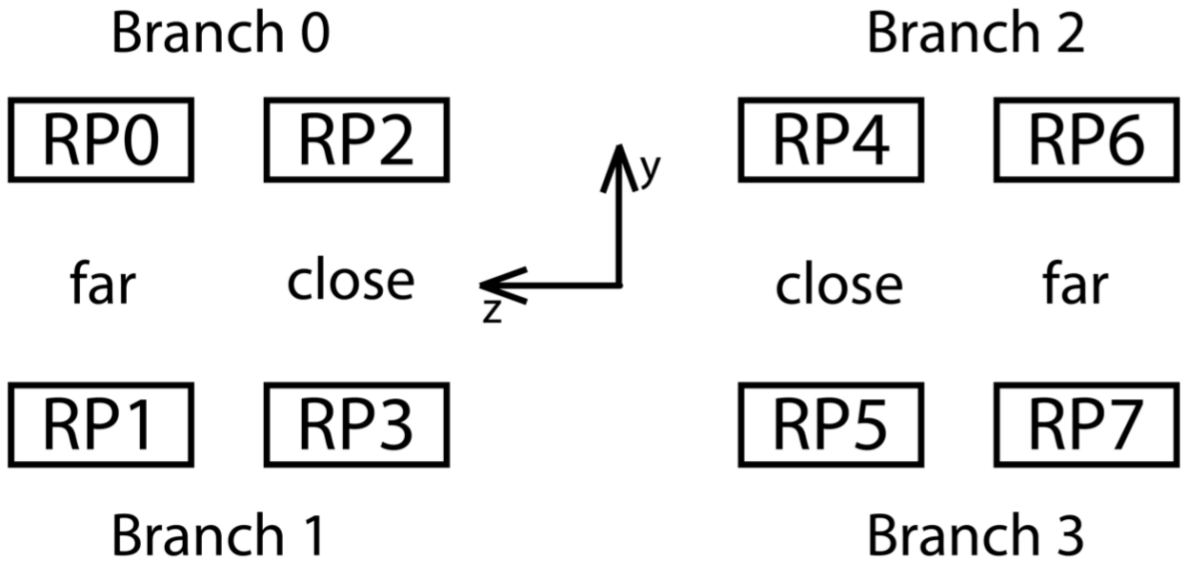

Figure 2.7: The ALFA detector layout. Arm 0 consists of Branch 0 and Branch 3, Arm 1 - of Branch 1 and 2.

Each of the eight RP vessels contains the Main Detector (MD) which serves as a tracker and an Overlap Detector (OD) which is used to align two detectors placed at the same z distance

from the IP. The OD is composed of three layers with thirty horizontally oriented scintillating fibres in each layer. The MD is made of ten scintillating fibre modules with two interleaved layers (U and V) of 64 orthogonally arranged fibres per layer. The fibre has a width of 0.5 mm. Such construction allows for measurements of forward proton transverse positions which are determined by a superposition of active fibres attributed to the track. Figure 2.8 shows a hit pattern of a proton trajectory in the U layer of fibre orientation while a schematic view of a pair of ALFA detectors in the upper and lower RPs is shown in Figure 2.9.

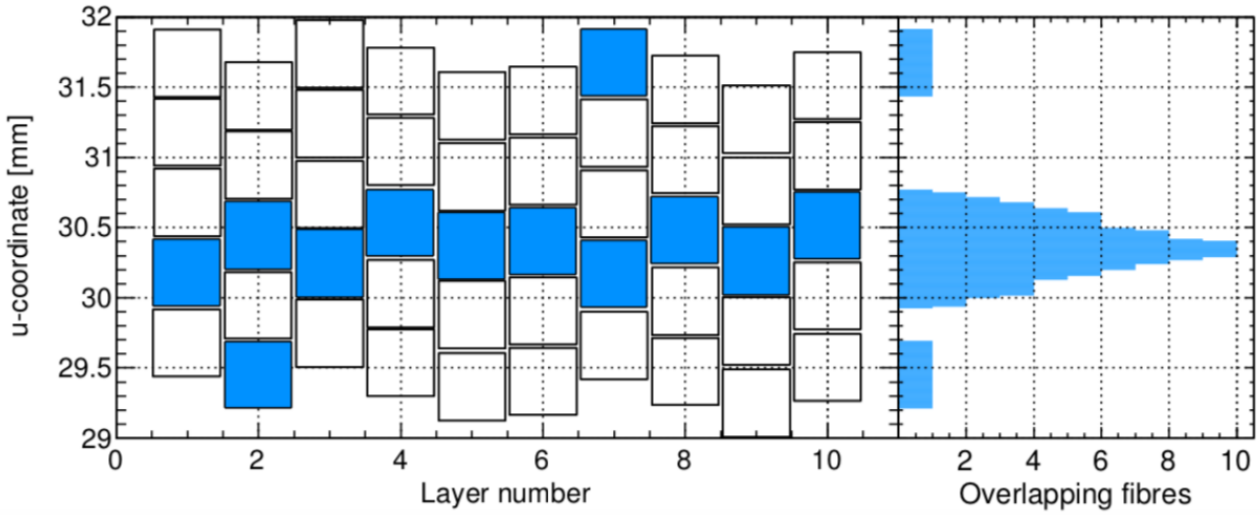

Figure 2.8: The hit pattern of a proton trajectory in ten fibre layers comprising the u coordinate. The superposition of active fibres attributed to a track is shown in the histogram. The position of maximum overlap is used to determine the track position. Figure taken from [143].

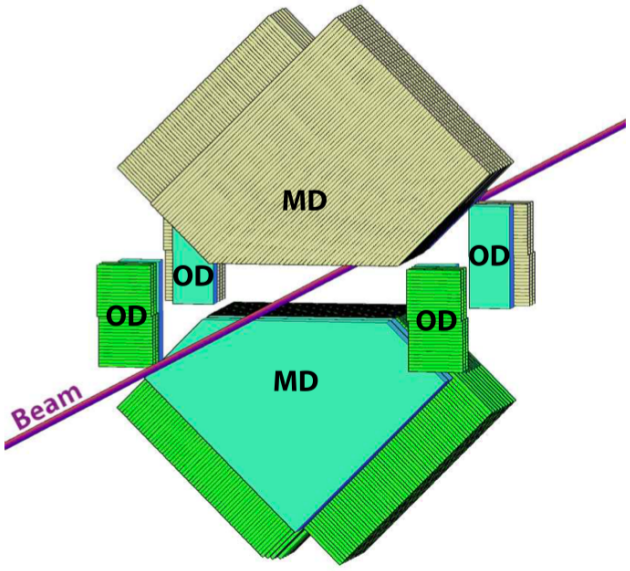

Figure 2.9: The schematic view of a pair of ALFA detectors in the upper and lower RPs. Figure taken from [143].

Each RP is equipped with four trigger tiles. They are made of a 3 mm thick plastic scintillator and generate the signal which is transmitted to the CTP (see Section 2.2.5). Two scintillating

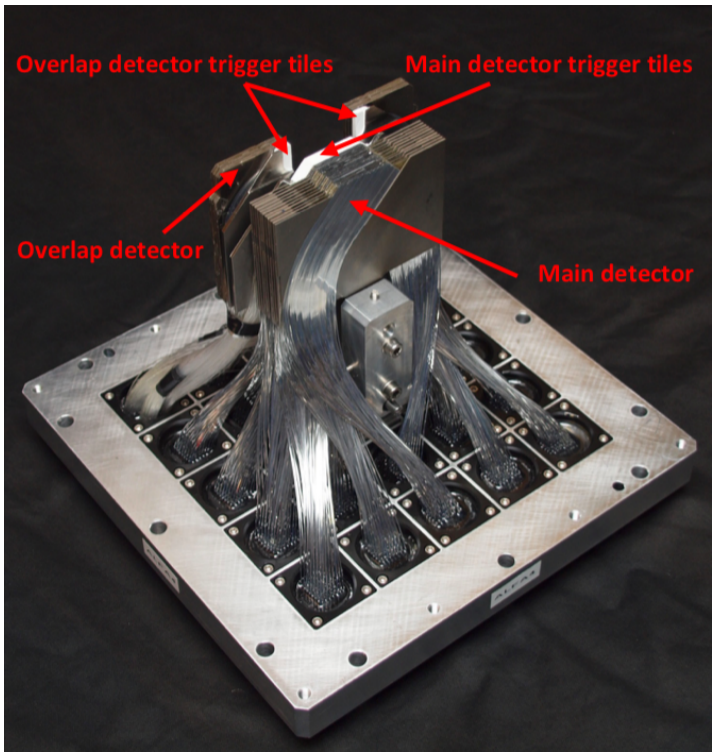

Figure 2.10: The ALFA detector. Figure taken from [154].

tiles are attached to the MD and the trigger signal is created when there is a coincidence between both tiles. Each OD has one trigger tile. Figure 2.10 presents the ALFA detector photograph with the location of the above elements.

The forward proton measurements involve extremely low scattering angles in the range of a few μrad which are smaller than the nominal beam divergence [112]. Therefore, the ALFA studies require the special beam conditions which are set during the dedicated LHC runs. The beam emittance for the ALFA measurements has to be reduced and the high-beta (β^*) optics is needed. The β^* is the betatron function at the IP which indicates the distance from the IP where the beam dimensions in the transverse to the motion plane are twice bigger [13, 144].

2.2.5 The ATLAS Trigger and Data Acquisition System

A significant component of the ATLAS experiment is the ATLAS Trigger and Data Acquisition System (TDAQ) [149]. It is responsible for making a decision whether to save a given collision event or to exclude it [147]. Since the nominal LHC bunch crossing interval is very short (25 ns), it is challenging to introduce the special trigger system which is able to select interesting events for physics analyses.

The ATLAS TDAQ is composed of the hardware-based first level trigger - Level-1 (L1) [150] and of the software-based High Level Trigger (HLT) [148] which consists of the Level-2 (L2) trigger and the Event Filter (EF). The L1 reduces the event rate from approximately 40MHz to 100kHz, while the HLT decreases the value to around 1kHz. The ATLAS trigger decision chain is presented in Figure 2.11.

The selection of the L1 trigger is based on information from the Calorimeters, Muon Spectrometer and other detectors which support a fast readout [152]. The condition is needed due to the upper L1 latency limit of 2.5 μs. ALFA [151] and MBTS are one of the detectors which fulfil this requirement and provide trigger inputs to the Central Trigger Processor (CTP) [150]. This L1 trigger component combines all trigger information which was sent from detector processors

and makes the final Level-1 Accept (L1A) decision [153]. The scheme of the procedure is shown in Figure 2.12. The L1 trigger also determines the Region-of-Interest (ROI) in the detector and passes it on to the HLT. Next, the event data are reconstructed and the sophisticated trigger algorithms are executed to provide the final level of the online selection and to form the HLT decision. Such filtered data are stored for offline analyses.

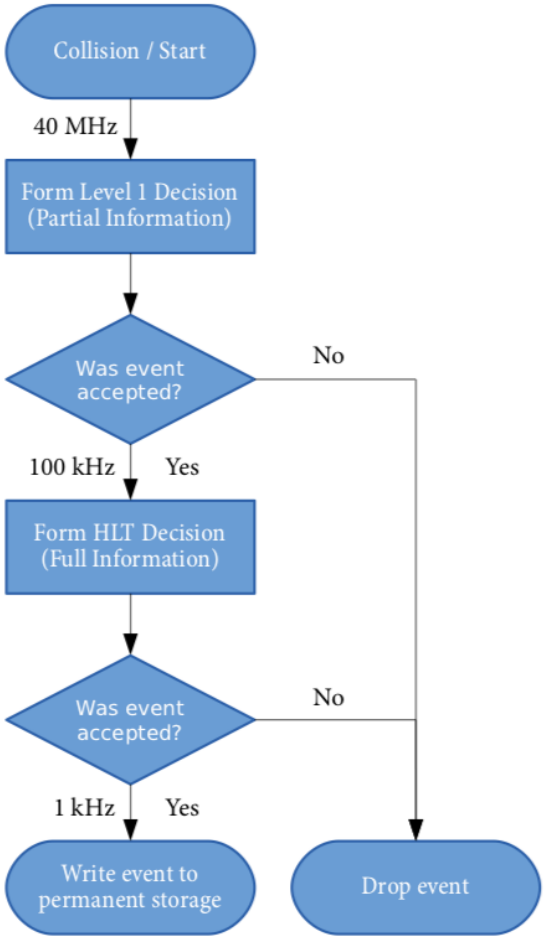

Figure 2.11: The ATLAS trigger decision chain. Figure taken from [152].

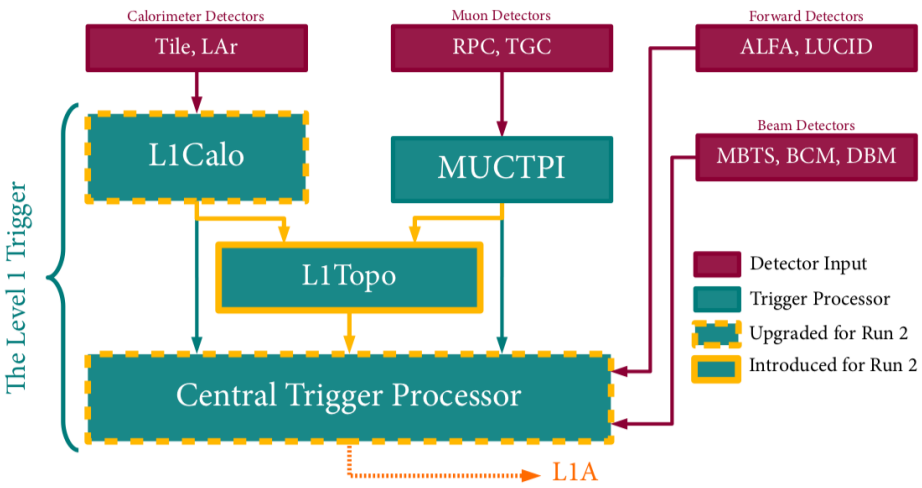

Figure 2.12: Scheme of the ATLAS L1 trigger processors. Figure taken from [152].

CHAPTER 3
Particle Identification

The measurement of the $\phi(1020)$ meson production is based on its reconstruction in the $\phi \to K^+K^-$ decay channel. A method of particle identification is needed to select kaon candidates and to suppress background of oppositely charged particle pairs that are not kaons.

The particle identification is performed by using the specific energy loss $\mathrm{d}E/\mathrm{d}x$ measurements that are provided by the PD. The ToT technique is employed to measure the charge collected in each pixel and to provide information about the ionisation energy losses of charged particles that cross pixel modules. The detector hits are grouped into clusters (space-points) and the $\mathrm{d}E/\mathrm{d}x$ is derived for each of them by the use of the cluster charge Q measurements as:

$$\frac{\mathrm{d}E}{\mathrm{d}x} = \frac{Q}{e}\frac{W\cos\alpha}{\rho d}, \tag{3.1}$$

where W denotes the average energy needed to create an electron-hole pair, $W = 3.68 \pm 0.02$ eV/pair, $x = d/\cos\alpha$ is the path in silicon, α represents a spatial incident angle, d is the silicon layer thickness and ρ symbolises the silicon density [165].

The $\mathrm{d}E/\mathrm{d}x$ of a track is calculated based on the $\mathrm{d}E/\mathrm{d}x$ measurements of clusters that are associated with the track. Since the individual cluster dE/dx measurements follow the Landau distribution, the mean $\mathrm{d}E/\mathrm{d}x$ can be biased by a hit with a very high dE/dx which lays in the Landau tail. Therefore, the cluster with the highest dE/dx is excluded for tracks with two, three or four clusters and two clusters with the highest $\mathrm{d}E/\mathrm{d}x$ are eliminated in the rare case of more than four clusters on a track. Then, a truncated mean is calculated for the clusters that remain [165, 166].

The mean rate of energy loss for charged particles, heavier than the electron, that have relativistic velocities is described by the Bethe-Bloch formula [13, 167]:

$$\left\langle -\frac{\mathrm{d}E}{\mathrm{d}x} \right\rangle = Kz^2\frac{Z}{A}\frac{1}{\beta^2}\left[\frac{1}{2}\ln\frac{2m_ec^2\beta^2\gamma^2W_{\max}}{I^2} - \beta^2 - \frac{\delta(\beta\gamma)}{2}\right], \tag{3.2}$$

where $K = 4\pi N_A r_e^2 m_e c^2 \approx 0.307\,\mathrm{MeV\,mol^{-1}\,cm^2}$, with N_A being the Avogadro's number and m_e the electron mass. The classical electron radius equals $r_e = e^2/4\pi\epsilon_0 m_e c^2 \approx 2.818$ fm. z is the charge of the incident particle (in units of e), Z and A are respectively the atomic and the mass number of the absorber, $\beta = v/c$, v is the particle's velocity, $\gamma = 1/\sqrt{1-\beta^2}$ represents the Lorentz factor. $W_{\max} = 2m_ec^2\beta^2\gamma^2/(1+2\gamma m_e/M+(m_e/M)^2)$ is the maximum energy transfer to an electron in a single collision, M is the incident particle mass, I denotes the mean excitation energy and $\delta(\beta\gamma)$ is the density effect correction to the ionisation energy loss. The Bethe-Bloch formula is a function of $\beta\gamma = p/m$, where p and m denote the momentum magnitude and the mass of the particle, respectively. Thus, the charged particle identification is possible based

on dE/dx and p measurements. The dependence of the dE/dx Most Probable Value (MPV) $\mathrm{MPV}_{dE/dx}$ on $\beta\gamma$ can be described by the following parametric function [165, 166]:

$$\mathrm{MPV}_{dE/dx}(\beta\gamma) = \frac{p_1}{f(\beta\gamma)^{p_3}} \ln\left(1 + (p_2 \cdot \beta\gamma)^{p_5}\right) - p_4, \tag{3.3}$$

where $f(\beta\gamma) = (\beta\gamma)^2/(1+(\beta\gamma)^2)$ and $p_1, ..., p_5$ are free parameters whose values do not rely on any prior knowledge concerning particle species. Figure 3.1 shows the two-dimensional distribution of dE/dx versus the charge signed momentum (qp) for tracks with three PD hits, for SD data and for PYTHIA 8 (the data and MC samples' details are presented in Section 4.1 and 4.2, respectively). The fitted $MPV_{\mathrm{d}E/\mathrm{d}x}$ functions for pions, kaons and protons are shown as well. The description of the fitting procedure is provided in Section 3.2.

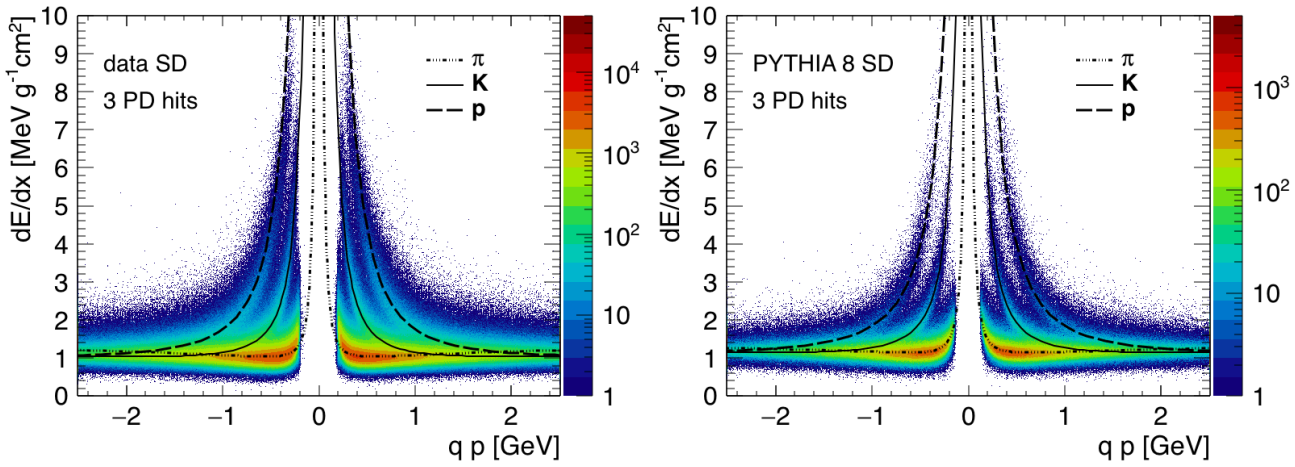

Figure 3.1: The two-dimensional distribution of dE/dx versus the charge signed momentum (qp) for tracks with three PD hits, for data (left) and PYTHIA 8 (right). The fitted $MPV_{\mathrm{d}E/\mathrm{d}x}$ functions for pions, kaons and protons are indicated as well.

3.1 Bias in Momentum Reconstruction

The particle identification is only possible when simultaneous measurements of both dE/dx and p are provided. Any systematic bias in the momentum reconstruction degrades power of particle species separation. The track reconstruction requires applying corrections for energy losses in the detector material. No particle identification is performed and all particles are assumed to be pions in the standard momentum reconstruction procedure. The bias between the true and the reconstructed momentum is observed for other particle species due to this pion assumption. This effect is taken into account in the analysis because there is an underestimation of the dead material correction for low-momentum kaons and protons in the reconstruction [165].

The corrections that are applied in the analysis were calculated as a function of particle's reconstructed transverse momentum $p_{\mathrm{T,rec}}$ in four η ranges: $|\eta| < 0.5$, $0.5 < |\eta| < 1.0$, $1.0 < |\eta| < 1.5$ and $1.5 < |\eta| < 2.0$. Figure 3.2 shows the energy loss corrections that are calculated based on PYTHIA 8 for pions, kaons and protons and for negative and positive charges separately. The EPOS MC model shows similar corrections. The bias in momentum reconstruction increases with lower $|\eta|$ and it decreases with higher $p_{\mathrm{T,rec}}$ tending to zero. The biggest momentum bias is observed for protons. The biases in the momentum reconstruction are derived from MC models but they were checked for data. The $\phi(1020)$ meson mass was calculated as a function of $p_{\mathrm{T},\phi}$. The mass was extracted from the fits to the invariant mass distributions

of $\phi(1020)$ meson candidates with and without applying the corrections for the bias in the momentum reconstruction. The results are shown in Figure 3.3. A correct $\phi(1020)$ meson's mass is obtained when the corrections are applied. This effect is significant for $p_{\mathrm{T},\phi} < 1$ GeV.

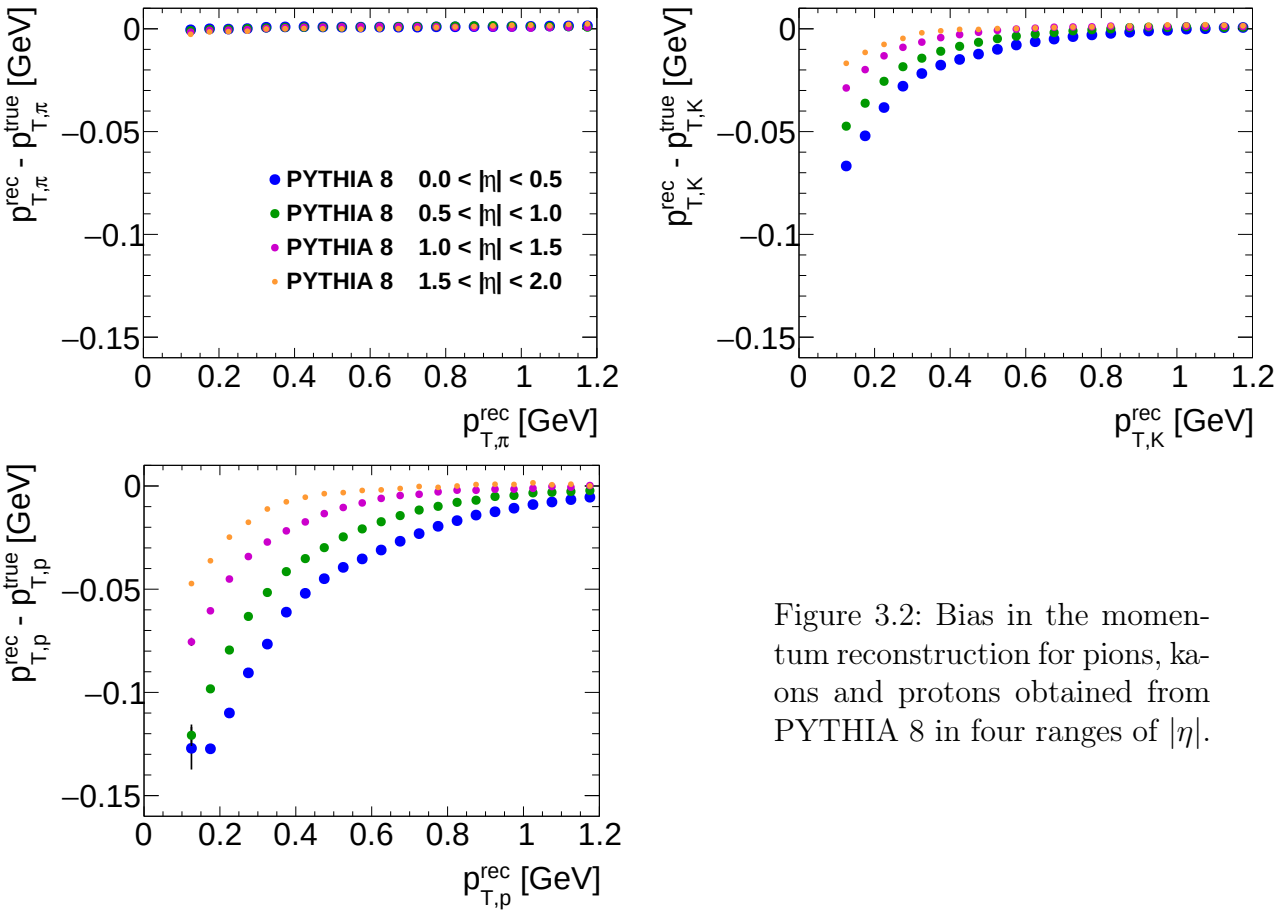

Figure 3.2: Bias in the momentum reconstruction for pions, kaons and protons obtained from PYTHIA 8 in four ranges of $|\eta|$.

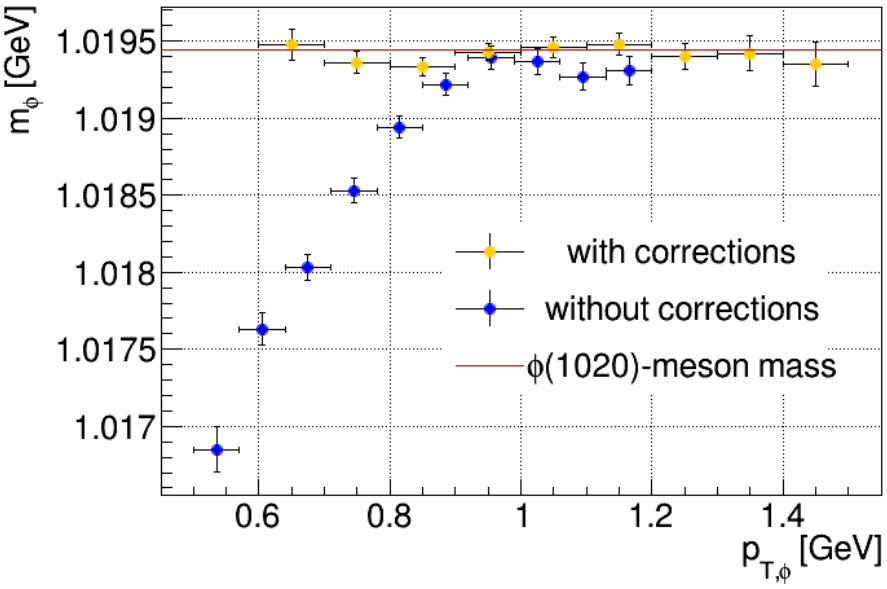

Figure 3.3: $\phi(1020)$ meson mass extracted from fits to invariant mass distributions with and without applying the corrections for biases in the momentum reconstruction specific to kaons. Figure taken from [169].

3.2 dE/dx Fits

The particle identification procedure follows the approach which is presented in [165,166]. Since $\mathrm{d}E/\mathrm{d}x$ is a function of p, the fits to the $\ln(\mathrm{d}E/\mathrm{d}x)$ distributions were done in a few ranges of the reconstructed momentum. The correction for the bias in the momentum reconstruction was applied in the case of simulation where the particle species are known. Furthermore, because of the dependence of the fit results on the particle charge and on the number of hits that were used for the track $\mathrm{d}E/\mathrm{d}x$ calculations (so-called good hits), the $\mathrm{d}E/\mathrm{d}x$ calibration was performed separately for particles and anti-particles and for the tracks that have two, three or more than three good PD hits (called later PD hits). There are separate fits for data and simulation.

dE/dx Fits - Monte Carlo Simulation

The $\mathrm{d}E/\mathrm{d}x$ MC calibration was performed based on the PYTHIA 8 SD sample and the ExpGaussExp function defined in (3.4) [168] was chosen to describe fluctuations around the $\mathrm{MPV}_{\mathrm{d}E/\mathrm{d}x}$ at fixed $\beta\gamma$:

$$f(x;\overline{x},\sigma,k_{\mathrm{L}},k_{\mathrm{H}}) = \begin{cases} \exp\left[\frac{k_{\mathrm{L}}^2}{2} + k_{\mathrm{L}}\left(\frac{x-\overline{x}}{\sigma}\right)\right], & \text{for } \frac{x-\overline{x}}{\sigma} \leq -k_{\mathrm{L}} \\ \exp\left[-\frac{1}{2}\left(\frac{x-\overline{x}}{\sigma}\right)^2\right], & \text{for } -k_{\mathrm{L}} < \frac{x-\overline{x}}{\sigma} \leq k_{\mathrm{H}} \\ \exp\left[\frac{k_{\mathrm{H}}^2}{2} - k_{\mathrm{H}}\left(\frac{x-\overline{x}}{\sigma}\right)\right], & \text{for } k_{\mathrm{H}} < \frac{x-\overline{x}}{\sigma} \end{cases} \tag{3.4}$$

where $x = \ln(\mathrm{d}E/\mathrm{d}x)$, $\bar{x} = \ln(\mathrm{MPV}_{\mathrm{d}E/\mathrm{d}x}(\beta\gamma))$, σ denotes the standard deviation of the Gaussian core, k_L and k_H are decay constants of the low and high exponential tails. The $\ln(\mathrm{d}E/\mathrm{d}x)$ distributions in six ranges of the reconstructed momentum, corrected for the bias in the momentum reconstruction: 0.29 - 0.4 - 0.5 - 0.7 - 0.9 - 1.1 - 1.2 GeV for pions, kaons and protons were fitted separately. The fit was not done for antiprotons with $0.29 < p < 0.4$ GeV because of too low statistics in this momentum range. We also checked the fit results by using the Crystal Ball function [168] but the fit quality and stability were lower in comparison to the ExpGaussExp fit outcomes. ExpGaussExp fits for negative kaons and three PD hits are shown in Figure 3.4 while ExpGaussExp fits for other cases are presented in Appendix A.1.

σ, k_{L} and k_{H} parameters were fitted independently for each momentum bin, each number of PD hits and each particle and antiparticle species. Fits of linear, second order polynomial and exponential functions were used to describe the dependencies of ExpGaussExp fit parameters (σ, k_{L} and k_{H}) on the momentum. All results are shown in Appendix A.1 while the fits for kaons with three PD hits are presented in Figure 3.5. The figures contain also results for data where we assumed that the parameters' values are the same in each momentum bin. This assumption was introduced to limit the number of free parameters in a common fit, done for all particle species simultaneously.

The differences between $\mathrm{d}E/\mathrm{d}x$ distributions for negatively and positively charged particles are not significant. Furthermore, σ, k_{L} and k_{H} show the same dependencies on the momentum for positive and negative particles of the same species with the same number of PD hits. The fits to the dependencies of mean values $\overline{x}$ on the momentum are not shown in Figures A.1.19 - A.1.27 because a common fit was done to the $\mathrm{MPV}_{\mathrm{d}E/\mathrm{d}x}(\beta\gamma)$ distribution for pions, kaons and protons. The fitting was performed for the different number of hits and particles and antiparticles separately. The function (3.3) was used to make the fits and the results are shown in Figure 3.6.

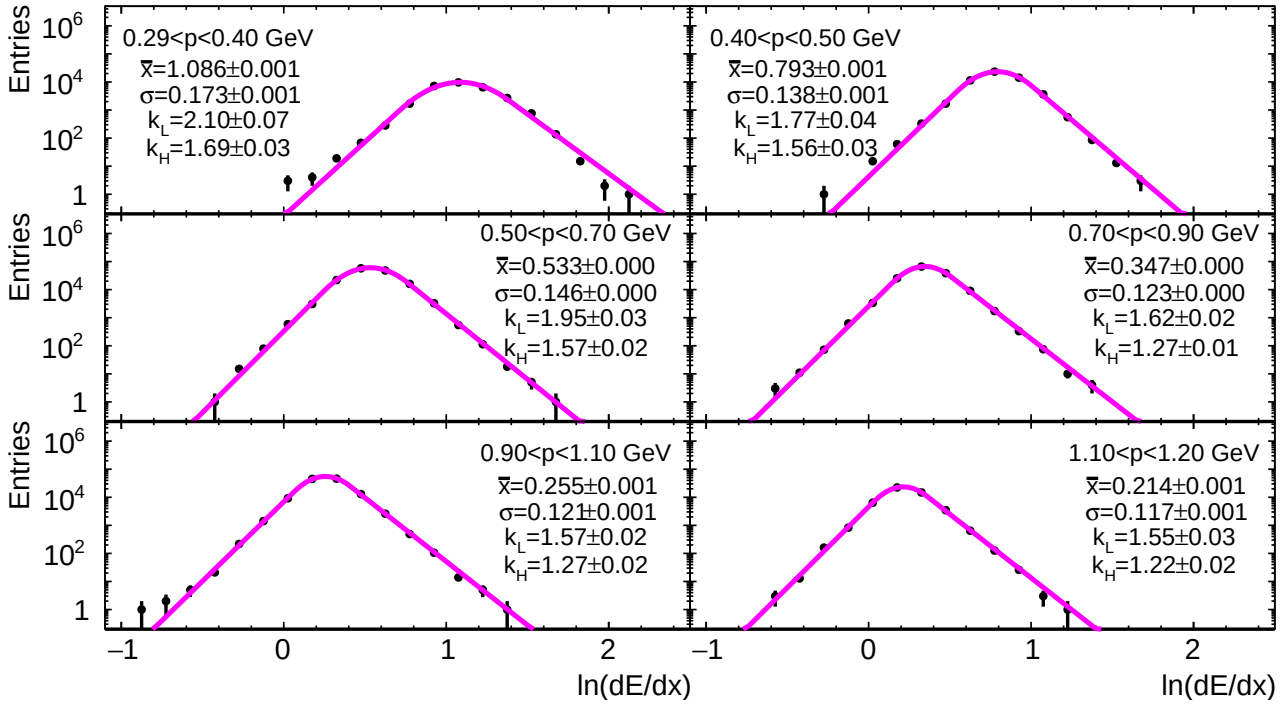

Figure 3.4: $\mathrm{d}E/\mathrm{d}x$ distributions for PYTHIA 8 in six momentum ranges for negative kaons and three PD hits. The parameters of the fitted function (3.4) are shown in the plots.

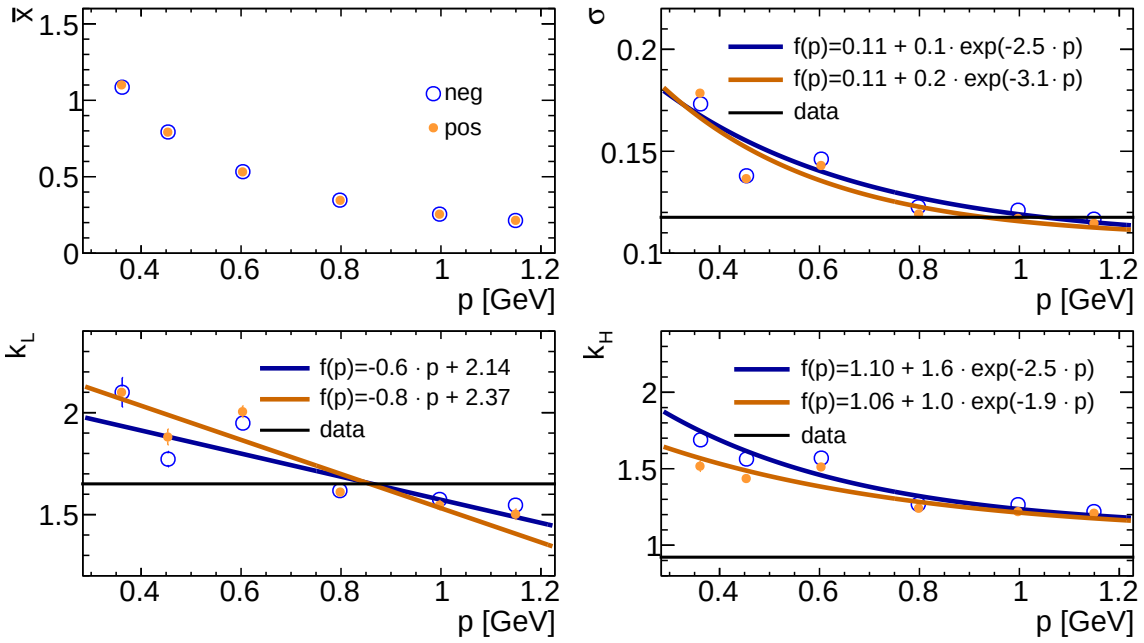

Figure 3.5: The fitted dependencies of $\ln(\mathrm{d}E/\mathrm{d}x)$ fit parameters (σ, k_L and k_H) on the momentum (fits shown in Figures 3.4 and A.1.10) for PYTHIA 8 for positive (pos) and negative (neg) kaons and three PD hits. Black solid lines indicate $\ln(\mathrm{d}E/\mathrm{d}x)$ fit parameters (σ, k_L and k_H) obtained for data distributions, shown in Figure A.2.4 for positively charged particles and in Figure 3.7 for negatively charged particles.

dE/dx Fits - Data

The $\mathrm{d}E/\mathrm{d}x$ calibration for data is based on the approach which is presented in [90, 165]. The track momentum range 0.3 -1.0 GeV was divided into 10 slices of equal width in $\ln(p)$. No particle identification was done yet at this stage of the analysis, so p was not corrected for any bias specific to kaons or protons. It was hypothesised that three charged particle species: π, K and p are present in the samples. Thus, the sum of three ExpGaussExp (3.4) functions with a hypothesis of pion, kaon and proton masses was used to describe the $\ln(\mathrm{d}E/\mathrm{d}x)$ distribution in each logarithmic bin of the reconstructed momentum but the $\ln(p)$ slices were fitted simultaneously. This fitting procedure was performed for particles and anti-particles and for the different number of the PD hits (2, 3 or greater than 3) separately. Fits for negatively charged tracks and three PD hits are presented in Figure 3.7 while fits for all six cases are shown in Appendix A.2.

σ, k_{L} and k_{H} are assumed to be the same for pions, kaons and protons with the same charge and the same number of the PD hits, which is supported by MC results. Their values are indicated in Figures A.1.19-A.1.27 to compare them with the MC fit results. Figure 3.8 presents the $\mathrm{MPV}_{\mathrm{d}E/\mathrm{d}x}(\beta\gamma)$ dependencies (Equation (3.3)) for data, where the momentum is

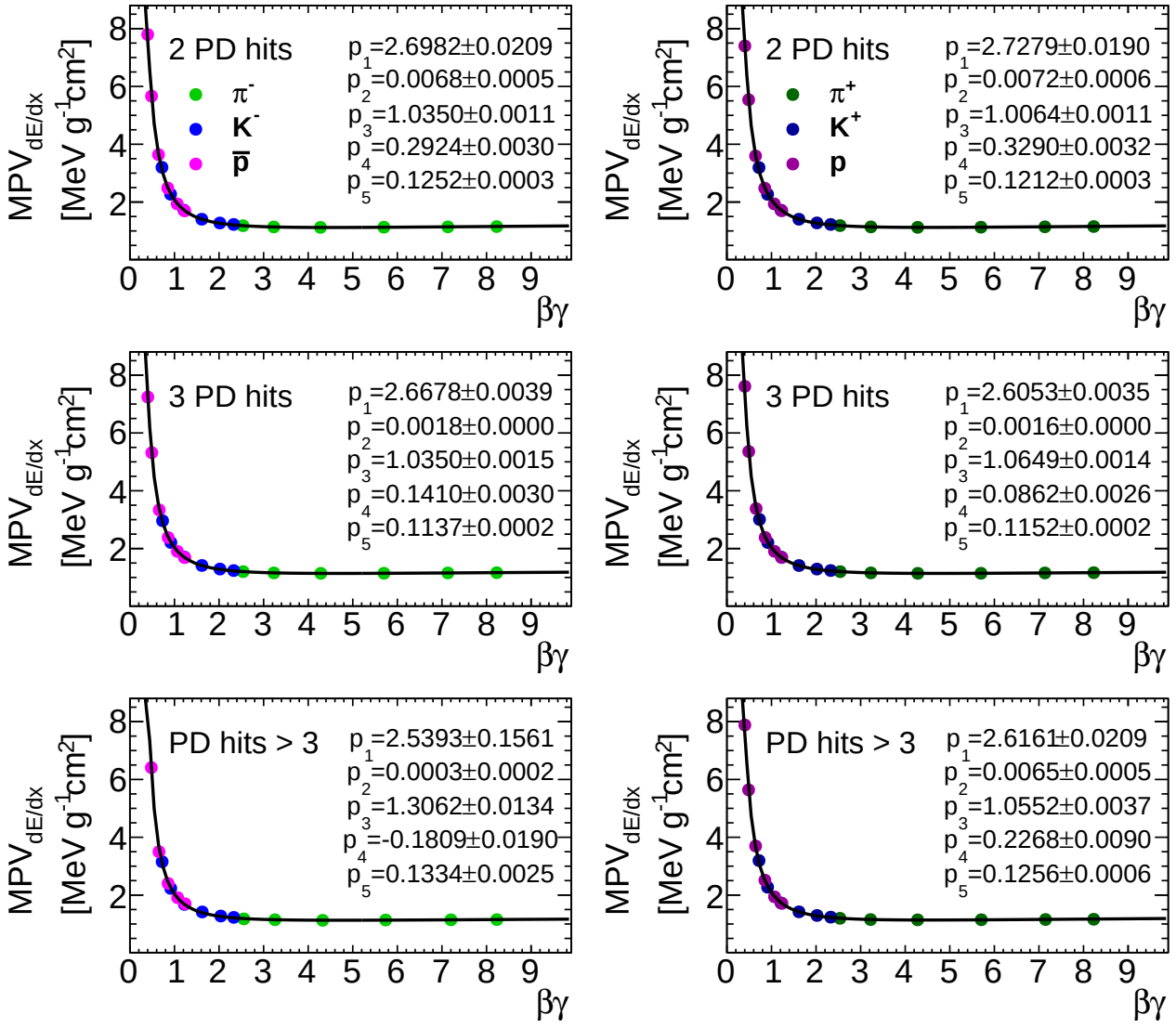

Figure 3.6: The dependencies of $\mathrm{MPV}_{\mathrm{d}E/\mathrm{d}x}$, coming from fits to $\ln(\mathrm{d}E/\mathrm{d}x)$ distributions (Figures A.1.1-A.1.18), on $\beta\gamma$ with a fitting function (3.3) and its parameters, separately for the different number of PD hits (two, three and more than three) and the charge of a particle.

corrected for the bias in the momentum reconstruction for kaons and protons. $\mathrm{MPV}_{\mathrm{d}E/\mathrm{d}x}(\beta\gamma)$ fit parameters for data and MC are listed in Table 3.1.

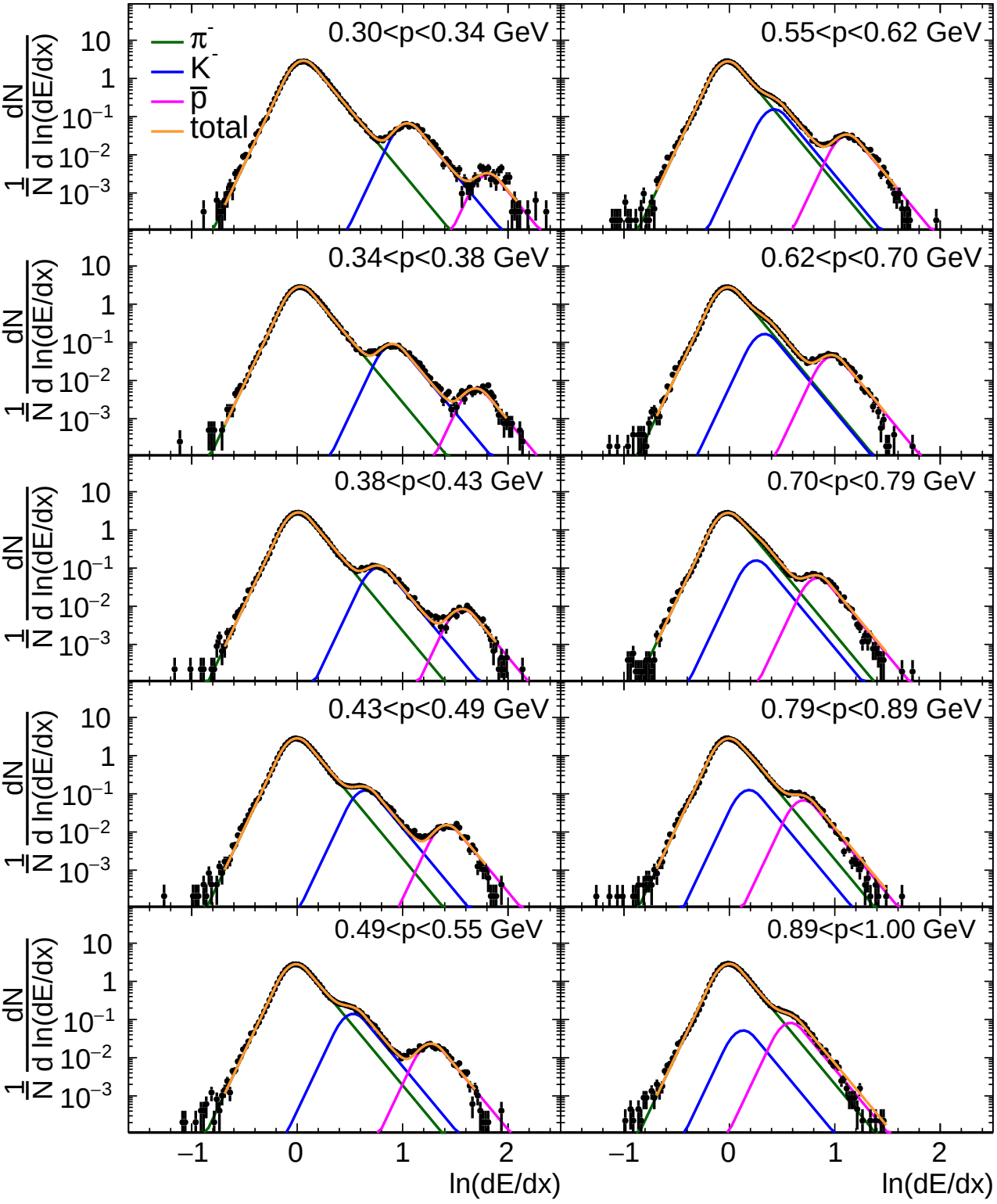

Figure 3.7: $\mathrm{d}E/\mathrm{d}x$ distributions for data in ten momentum ranges for negative particles and three PD hits. The sum of three ExpGaussExp functions (3.4) with a hypothesis of π, K and p masses was fitted in each p slice.

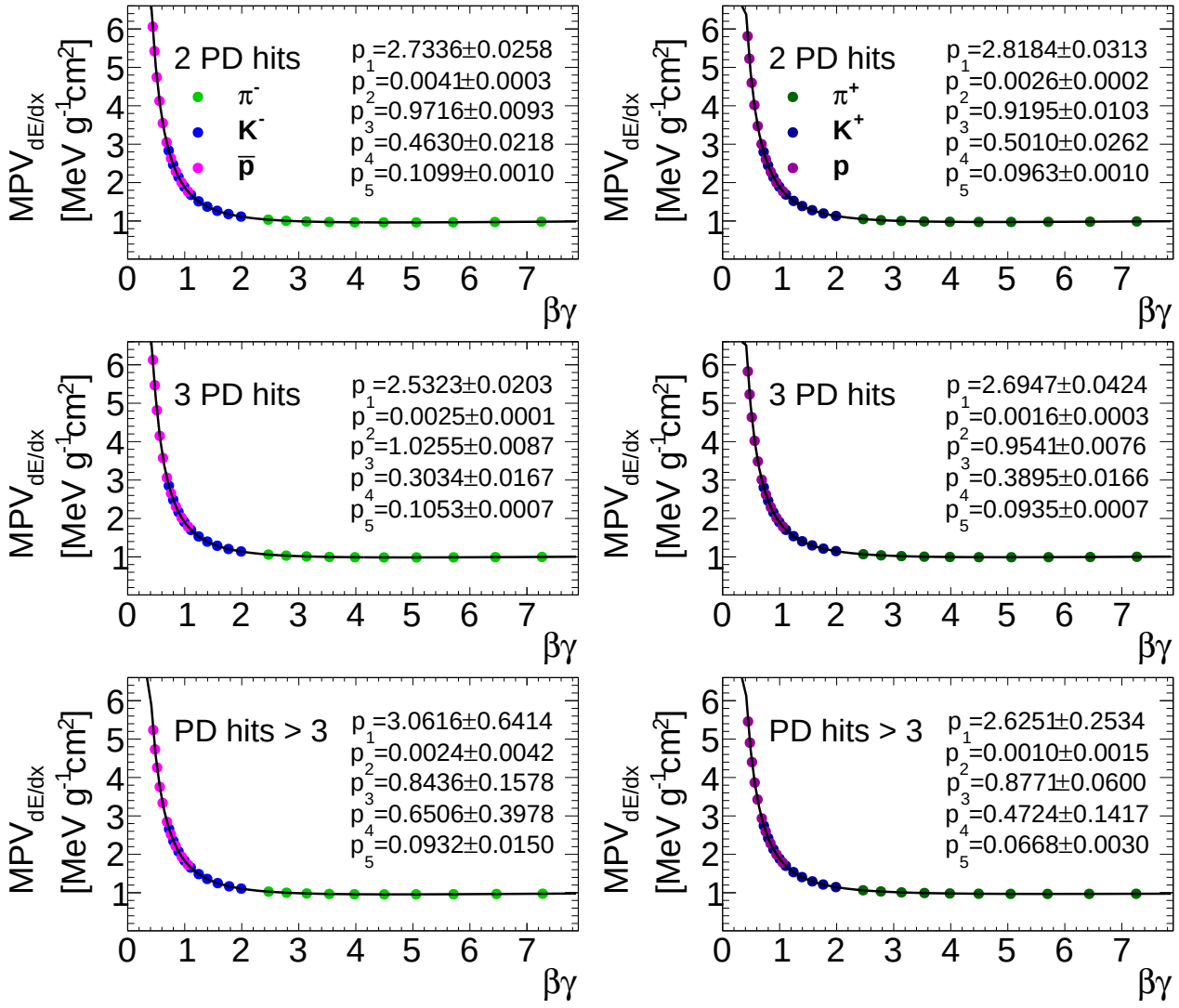

Figure 3.8: The dependencies of $\mathrm{MPV}_{\mathrm{d}E/\mathrm{d}x}$, coming from fits to $\ln(\mathrm{d}E/\mathrm{d}x)$ distributions (Figures A.2.1-A.2.6), on $\beta\gamma$ with a fitting function (3.3) and its parameters, separately for the different number of PD hits (two, three and more than three) and the charge of a particle.

Table 3.1: $\mathrm{MPV}_{\mathrm{d}E/\mathrm{d}x}(\beta\gamma)$ fit parameters for data and MC, separately for negatively (neg) and positively (pos) charged particles. The fits are shown in Figure 3.8 for data and in Figure 3.6 for PYTHIA 8.

		$\boldsymbol{p_1}$	$\boldsymbol{p_2}$	$\boldsymbol{p_3}$	$\boldsymbol{p_4}$	$\boldsymbol{p_5}$
data, neg	2 PD hits	2.73 ±0.03	0.0041 ±0.0003	0.972 ±0.009	0.46 ±0.03	0.1099 ±0.0002
	3 PD hits	2.53 ±0.03	0.0025 ±0.0001	1.025 ±0.009	0.30 ±0.02	0.1053 ±0.0007
	PD hits > 3	3.06 ±0.65	0.0024 ±0.0042	0.844 ±0.158	0.65 ±0.40	0.09324 ±0.0151
data, pos	2 PD hits	2.82 ±0.04	0.0026 ±0.0002	0.920 ±0.011	0.50 ±0.03	0.0963 ±0.0010
	3 PD hits	2.69 ±0.05	0.0016 ±0.0003	0.954 ±0.008	0.39 ±0.02	0.0935 ±0.0007
	PD hits > 3	2.63 ±0.26	0.0010 ±0.0015	0.877 ±0.061	0.47 ±0.15	0.0668 ±0.0030
PYTHIA 8, neg	2 PD hits	2.70 ±0.03	0.0068 ±0.0005	1.035 ±0.002	0.29 ±0.01	0.1252 ±0.0003
	3 PD hits	2.67 ±0.01	0.0018 ±0.0001	1.035 ±0.002	0.14 ±0.01	0.1137 ±0.0002
	PD hits > 3	2.54 ±0.16	0.0003 ±0.0002	1.306 ±0.014	0.18 ±0.02	0.1334 ±0.0025
PYTHIA 8, pos	2 PD hits	2.73 ±0.02	0.0072 ±0.0006	1.006 ±0.002	0.33 ±0.01	0.1212 ±0.0003
	3 PD hits	2.61 ±0.01	0.0016 ±0.0001	1.065 ±0.002	0.09 ±0.01	0.1152 ±0.0002
	PD hits > 3	2.62 ±0.03	0.0065 ±0.0005	1.055 ±0.004	0.23 ±0.01	0.1256 ±0.0006

CHAPTER 4
Event Samples and Selection

4.1 Data Samples

The data which are analysed in this thesis were collected by the ATLAS experiment during the LHC special *pp* runs in October 2015. In these special runs ALFA detector was inserted 6 mm from the beam centre. The centre-of-mass energy of the collisions was $\sqrt{s} = 13$ TeV and the crossing angle at the IP equalled $\theta_c = 2 \times 50\,\mu\text{rad}$. The data were taken at special beam conditions, namely the beam intensity was lower in comparison to the standard LHC runs and the value of the nominal LHC betatron function at the IP was changed to β^*=90 m. Moreover, the time space between bunches was 100 ns. Consequently, the instantaneous luminosity $\mathcal{L}$ and pile-up μ were lower compared to nominal values. Luminosity is defined as the proportionality factor between the rate of events of a given process and the cross section σ for this process [13]:

$$\frac{dN}{dt} = \mathcal{L} \cdot \sigma. \tag{4.1}$$

Pile-up μ denotes the average number of simultaneous *pp* interactions per bunch crossing and for these special ALFA runs $\mu = 0.1$.

This analysis utilises SD, CD and MB-triggered data. The triggers below were chosen to select the samples of interest:

- SD: HLT_noalg_L1ALFA_Diff_Phys which requires that events are accepted by the L1ALFA diffractive triggers and passed through HLT without further requirements.

  The L1ALFA diffractive trigger is formed by:
  L1_MBTS_1_A_ALFA_C .OR. L1_MBTS_1_C_ALFA_A that are fired when there is a coincidence of:

  - at least one MBTS counter with a signal above threshold on side-A (-C),
  - a hit in the ALFA trigger tiles on side-C (-A).

- CD: HLT_mb_sptrk_vetombts2in_L1ALFA_CEP which requires that events are accepted by the L1ALFA_CEP (Central Exclusive Production) triggers and following requirements at HLT :

  - no more than one inner MBTS counter with a signal above threshold,
  - at least three space points in the PD, at least four space points in the SCT and at least one L2 ID track with $p_{\text{T}} > 0.2$ GeV.

The L1ALFA_CEP trigger is formed by a hit in the ALFA trigger tiles on two opposite ATLAS sides at L1.

- MB: logical .OR. between the two triggers:
  - the HLT_noalg_mb_L1MBTS_1 trigger with the requirement of at least one MBTS counter with a signal above threshold on L1 and no additional requirements at HLT,
  - the HLT_mb_sptrk trigger which is a highly prescaled random trigger at the L1 level and it requires space points in the PD and SCT detectors at the HLT level.

Around 20 M SD and 8 M MB events corresponding to the integrated luminosity of 729.96 nb^{-1} were used in the analysis. The SD triggers were prescaled by ~ 200, while the MB ones by ~ 1200. The integrated luminosity in the CD sample with approximately 21 M events was 660 nb^{-1} and the L1 triggers formed by the elastic pp configurations of ALFA branches were prescaled by about a factor of two.

4.2 Monte Carlo Samples

Monte Carlo samples were used to compare data with models and to perform corrections for detector effects. The format of the output from MC simulation is the same as that of the real data. Standard steps in the production of MC samples involve:

(a) event generation,

(b) simulation of interactions with detector material,

(c) simulation of detector response and its digitisation,

(d) reconstruction (this step is identical for both data and MC samples).

The second step is executed using the simulation toolkit GEANT4 [156]. It provides the set of software components which are employed to model the interaction of particles with environment. The GEANT4 package was specifically used for the particles which are generated in the central detector acceptance and for protons in the ALFA acceptance. Besides, the FPTracker package [157, 158] was applied to transport protons through the LHC apertures. This tool has information about all components of the LHC magnetic lattice and it is responsible for the propagation of protons from the IP to the ALFA stations. Another package which was used is ALFAReco, also known as the Copenhagen Reconstruction package [157, 159, 160]. It is applied to reconstruct proton kinematics in ALFA.

All the phases of the MC production chain were performed within the ATLAS simulation infrastructure [145] which is part of the ATLAS software framework Athena [146].

Two MC event generators - PYTHIA 8 and EPOS were used to produce the following MC samples for this analysis:

- PYTHIA 8:
  - SD with the filter: $0.03 < \xi < 0.2$ - 1M events,
  - SD without the filter - 8M events,
  - CD with the filter: $0.03 < \xi < 0.2$ - 0.5M events,
  - CD without the filter - 0.5M events,
  - ND without the filter - 0.5M events,
  - DD without the filter - 0.5M events,

- EPOS (inelastic: SD, SD′, CD, DD and ND):
  - with the filter: $\xi < 0.2$ - 3M events,
  - without the filter - 10M events.

All PYTHIA 8 samples were generated with nominal ATLAS geometry using the A3 tune with the Donnachie and Landshoff (DL) parametrisation of the Pomeron flux [84] and the NNPDF23LO PDFs [161]. The LHC setting was applied in the generation of the EPOS samples [82].

PYTHIA 8 SD (CD) samples with and without the filter $0.03 < \xi < 0.2$ were added with proper weights to obtain the final SD (CD) sample. The sample with filter was prepared to increase the number of events with protons generated within the ALFA acceptance and to decrease statistical fluctuations, especially for higher ξ.

4.3 Event Selection

Several selection cuts were applied in the analysis. The requirements concerning the MBTS and ALFA measurements are different for SD, CD and MB analysis whereas the particles measured in the ID should satisfy the same conditions.

4.3.1 The ID Track Selection

The requirements related to tracks that are measured in the ID follow the ATLAS low-p_{T} charge-particle analysis at $\sqrt{s} = 13$ TeV [162]. The following selection criteria were introduced to keep high track reconstruction efficiency and to exclude low quality tracks:

- accepted tracks have $p_{\mathrm{T}} > 100$ MeV and $|\eta| < 2.5$,
- there is at least one hit in the PD and additionally an IBL hit if it is expected (if the extrapolated track crosses an active pixel module region),
- tracks have at least two, four or six SCT hits for $p_{\mathrm{T}} < 300$ MeV, $300 < p_{\mathrm{T}} < 400$ MeV and $p_{\mathrm{T}} > 400$ MeV, respectively.

The following two cuts were used to reject tracks that do not originate from the primary interaction vertex:

- $|d_0| < 1.5$ mm, where d_0 is the transverse impact parameter with respect to the primary vertex,
- $|z_0 \sin\theta| < 1.5$ mm, where z_0 is the longitudinal impact parameter with respect to the primary vertex and θ is the polar angle of the track.

The accepted events are required to have exactly one primary vertex which is reconstructed from at least two primary tracks that meet the criteria above, $n_{\mathrm{sel}} \geq 2$. Events with a pile-up vertex with the number of associated particles greater than three are rejected to suppress the background coming from more than one interaction per beam crossing.

4.3.2 The ALFA Track Selection

Selection of tracks in the ALFA detectors follows the previous diffractive analysis described in Ref. [90]. The following cuts are used:

- a track is created from at least six overlapping fibre layers in each orientation (U and V),
- events with more than one track reconstructed in a single station are rejected,
- a track has to be reconstructed in all stations (close and far ones) of the given branch,
- a reconstructed proton track is required in exactly one ALFA branch in the SD analysis and in exactly two branches on opposite sides of the IP in the CD analysis.

The criteria above were applied to reduce the amount of background which may be accidental or may come from other physics processes. Then, the restrictions on x and y track coordinates were set to measure tracks that are reconstructed away from the beam line (BL) apertures. The cuts are slightly different for each ALFA station. Their approximate values are:

- $|x_{\text{close}}| \lesssim 10$ mm,
- $|x_{\text{far}}| \lesssim 15$ mm,
- $6 \lesssim |y| \lesssim 19$ mm.

The next selection cuts (formula (4.2)) were introduced to reduce the number of events that come from beam-halo protons or showers in the ALFA stations. A measured proton track has to fulfil the cut on the average x-position in the close and far ALFA stations, $\bar{x} = (x_{\text{close}} + x_{\text{far}})/2$ and the cut on θ_x versus $\bar{x}$:

$$\begin{aligned} \bar{x} &> -2.5 \text{ mm}, \\ \theta_x &> \left(\bar{x} \cdot 4.8 \, \frac{\text{rad}}{\text{mm}} - 4.9 \text{ rad} \right) \cdot 10^{-5} , \end{aligned} \tag{4.2}$$

where $\theta_x = (x_{\text{far}} - x_{\text{close}})/|z_{\text{far}} - z_{\text{close}}|$ is the track's local angle in the (x, z) plane. The correlation between $\bar{x}$ and θ_x for data and PYTHIA 8 is shown in Figure 4.1. The region which is removed from the analysis by the requirements (4.2) is indicated in the plots.

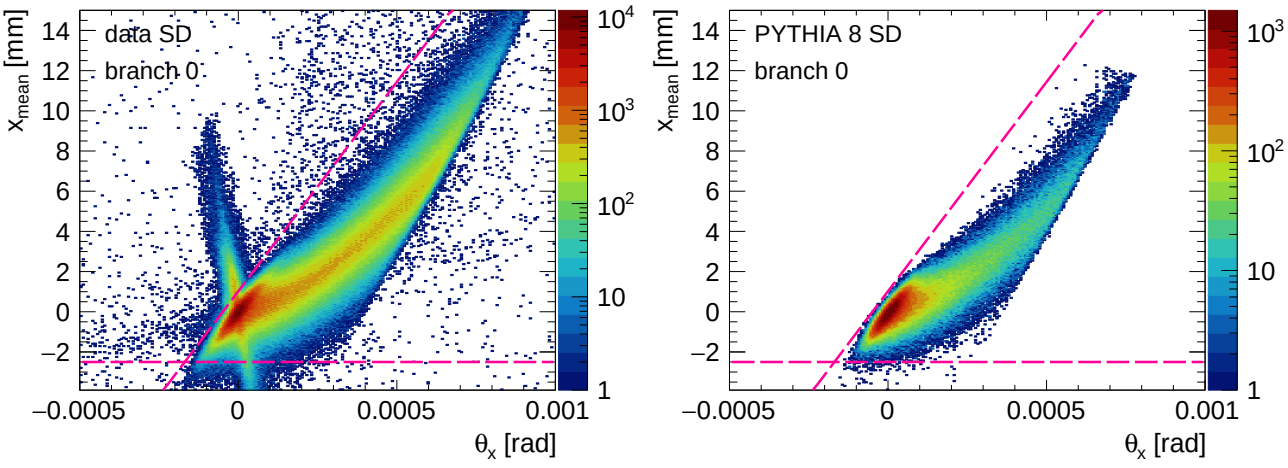

Figure 4.1: The correlation between $\bar{x}$ and θ_x for data (left) and PYTHIA 8 (right) for the ALFA branch 0 (RPs 0-2). Dashed lines indicate the cuts used in the analysis.

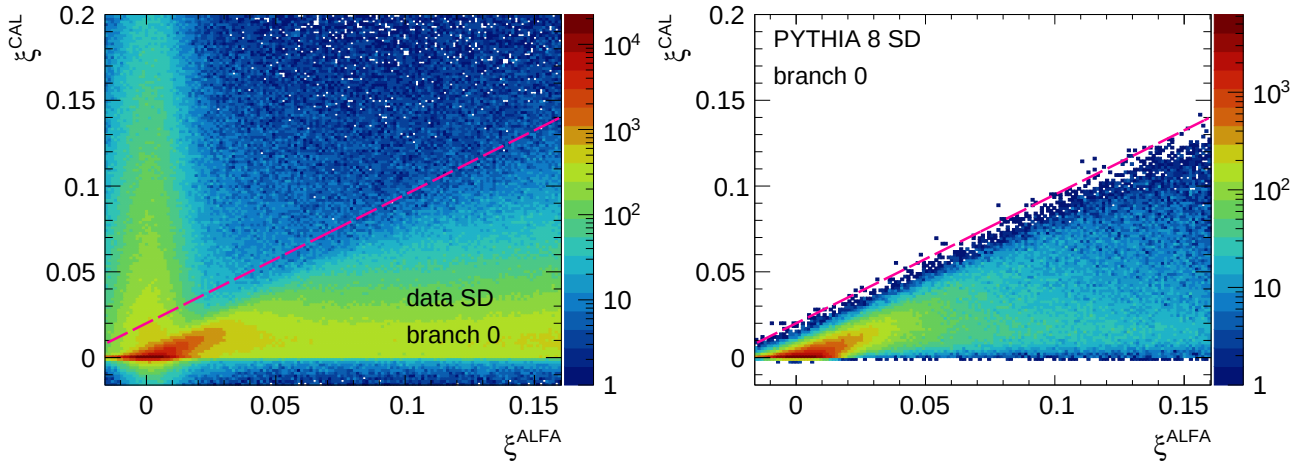

Figure 4.2: The ξ^{CAL} versus ξ^{ALFA} distribution for data (left) and PYTHIA 8 (right). Dashed lines indicate the cuts on ξ that were applied in the analysis.

In the SD analysis, the fractional energy loss ξ is measured based on the proton kinematics in the ALFA detectors (ξ^{ALFA}) or from the variables that characterise the hadronic system X [163]:

$$\xi^X = \frac{1}{\sqrt{s}} \sum_{i \in X} p_{\mathrm{T}}^i e^{\pm y^i}, \tag{4.3}$$

where $\sqrt{s}$ is the pp centre-of-mass energy and the sum runs over all particles in the hadronic system X. y values are calculated with an assumption of a pion mass. A sign of y in Eq. (4.3) corresponds to the $\pm$ z direction of the forward proton. ξ^X can be obtained from calorimeter measurements and it is denoted then as ξ^{CAL}. The ξ resolution depends on the ALFA spatial resolution and LHC optics in the case of ξ^{ALFA} and on the energy resolution of calorimeter clusters when the ξ^{CAL} is measured. Figure 4.2 shows the ξ^{CAL} versus ξ^{ALFA} distribution for data and PYTHIA 8. The accepted region in the SD analysis is restricted by:

$$\xi^{\mathrm{CAL}} < 0.02 + 0.75 \cdot \xi^{\mathrm{ALFA}}. \tag{4.4}$$

The cut above suppresses background which is accidental or which comes from other processes except the selected one but it keeps high efficiency of the signal selection. The ξ region which is accepted in the SD analysis was divided into three ranges: $10^{-5} < \xi < 0.035$, $0.035 < \xi < 0.08$, and $0.08 < \xi < 0.16$. The lowest ξ limit follows the requirement of $n_{\mathrm{sel}} \geq 2$ whereas the cut on the upper ξ value is imposed by the ALFA acceptance. The ξ ranges are the same as in the charge-particle ALFA analysis [90] which is intended to be comparable with the charge-particle AFP analysis [164] where the ξ region is limited by $0.035 < \xi < 0.08$. Migrations between the three selected ξ regions are smaller for ξ^{ALFA} than for ξ^{CAL} and ξ^{ALFA} is used in this analysis.

The CD analysis was restricted to the region where $\xi_{\mathrm{A}} < 0.02$ and $\xi_{\mathrm{C}} < 0.02$, where ξ_{A} and ξ_{C} are ξ of a proton detected on the ATLAS side A and C, respectively. The requirements are related to the the veto on the MBTS in the CD analysis (see Section 4.3.4). We checked that the efficiency of the veto is lower than 10% for $\xi_{\mathrm{A}} > 0.02$ and $\xi_{\mathrm{C}} > 0.02$.

The $|t|$ range used in this analysis is based on the acceptance of the ALFA detector, which is defined by means of the probability of a scattered proton reaching the z-coordinate of the ALFA detectors and being within its geometrical acceptance. In addition the cut in (4.2) must be satisfied. Figure 4.3 shows the ALFA acceptance as a function of $|t|$ in three ξ ranges whereas the acceptance as a function of ξ is presented in Figure 4.4. The acceptance for protons that have small $|t|$ and large ξ is higher in the upper branches which is caused by the crossing angle at the IP. The acceptance in t is required to be greater than 10%. This condition is satisfied in

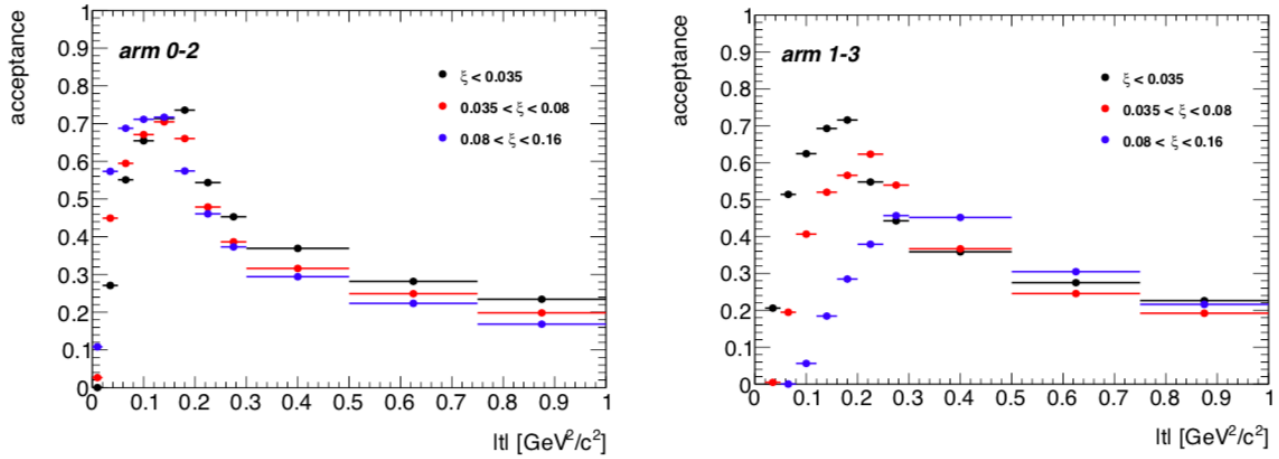

Figure 4.3: The ALFA acceptance as a function of $|t|$ in three ξ ranges, separately for the ALFA branch 0 (left), indicated as arm 0-2 in the plot, and for the branch 1 (right), indicated as arm 1-3 in the plot. Figure taken from [90].

the range of $0.02 < |t| < 1\,\mathrm{GeV}^2/\mathrm{c}^2$ for the upper branches and it depends on ξ for the lower branches:

- $0.02 < |t| < 1\,\mathrm{GeV}^2/\mathrm{c}^2$ for $10^{-5} < \xi < 0.035$,
- $0.03 < |t| < 1\,\mathrm{GeV}^2/\mathrm{c}^2$ for $0.035 < \xi < 0.08$,
- $0.08 < |t| < 1\,\mathrm{GeV}^2/\mathrm{c}^2$ for $0.08 < \xi < 0.16$.

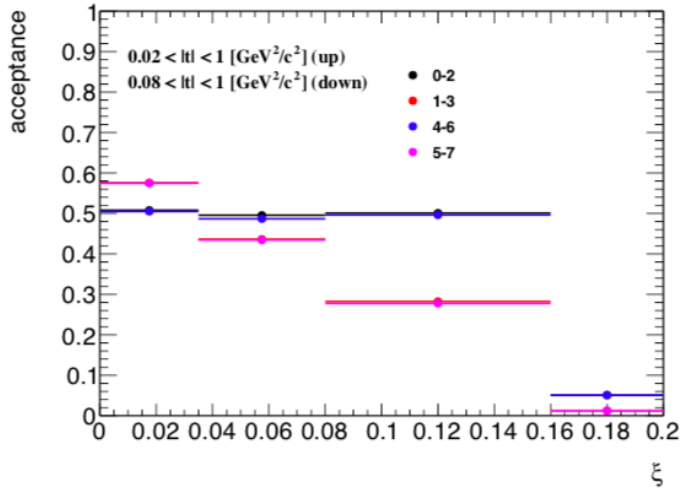

Figure 4.4: The ALFA acceptance as a function of ξ, separately for each ALFA branch. The numbers of RPs from a given branch are shown in the legend. Figure taken from [90].

4.3.3 The Anti-elastic Cut in CD

The CD triggered data contain accidental background. Its potential sources are coincidences of:

- a beam-halo proton and a proton that comes from the SD process with mid-rapidity charged particles observed in the central part of the ATLAS detector,
- two protons from the elastic interaction and the non-diffractive process with mid-rapidity charged particles observed in the central part of the ATLAS detector.

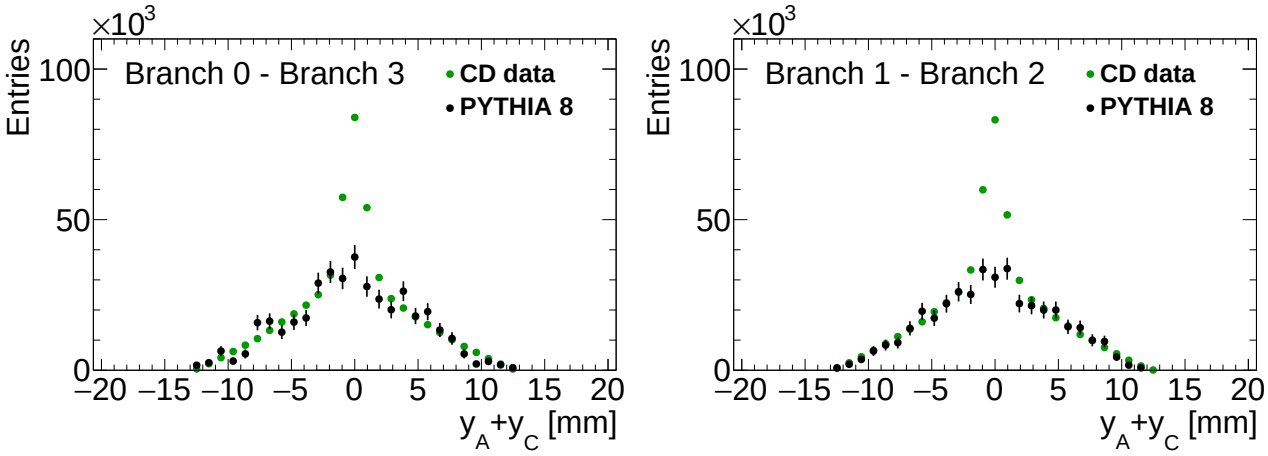

Figure 4.5: $y_{\mathrm{A}} + y_{\mathrm{C}}$ distributions for the elastic pp configurations of ALFA branches - (left) Branch 0 - Branch 3 and (right) Branch 1 - Branch 2. The data (green dots) are compared to PYTHIA 8 predictions (black dots). The MC distributions are normalised to the number of events in the data in the range $|y_{\mathrm{A}} + y_{\mathrm{C}}| > 3$ mm.

The first source was estimated to be negligible based on the rates of individual sources while the second one was suppressed using a cut on protons' collinearity in the elastic pp configuration of ALFA branches (Branch 0 + Branch 3 or Branch 1 + Branch 2):

$$|y_{\mathrm{A}} + y_{\mathrm{C}}| > 3 \text{ mm}, \tag{4.5}$$

where y_{A} and y_{C} are proton y-positions in the close ALFA stations at side A(C). Figure 4.5 shows $y_{\mathrm{A}} + y_{\mathrm{C}}$ distributions for data and PYTHIA 8 for the elastic pp configuration of ALFA branches. The MC distributions are normalised to the number of events in the data in the range $|y_{\mathrm{A}} + y_{\mathrm{C}}| > 3$ mm. The anti-elastic cut (4.5) suppresses elastic background which is present for $|y_{\mathrm{A}} + y_{\mathrm{C}}| < 3$ mm.

4.3.4 The MBTS Requirements

MBTS requirements are applied in the triggers that are used in the analysis. The same cuts are also set on the reconstructed energy in the offline procedure. The offline threshold on the measured charge for a signal in the inner MBTS tiles is set to be $e > 0.5$ pC and $e > 0.75$ pC for a signal in the outer MBTS tiles. A signal in at least one MBTS counter on the opposite ATLAS side to the outgoing proton which was tagged in the ALFA detector is required in the SD analysis. There is a veto on more than one inner MBTS counter with a signal in the CD analysis.

CHAPTER 5
ϕ Meson Yield Extraction

5.1 Kaon Candidate Selection

The tracks' kinematic requirements (5.1) were applied to select kaon candidates with keeping the high efficiency of the kaon identification (the efficiencies are shown in Section 6):

$$p < 0.9 \text{ GeV}, \tag{5.1a}$$

$$p_{\mathrm{T}} > 0.29 \text{ GeV}. \tag{5.1b}$$

The requirement (5.1a) determines the momentum region where the relativistic effects are small enough to identify kaons with the high efficiency (proper efficiency plots are presented in Section 6.3). The cut (5.1b) is applied to select the region of high ID efficiency for kaons.

The Particle Identification (PID) cuts were introduced to suppress background of particles that are not kaons. This background comes mainly from pions. The probabilities that a track originates from a pion, a kaon or a proton were derived according to the $\ln(\mathrm{d}E/\mathrm{d}x)$ fit outcomes that are shown in Section 3. The fits were done in a few ranges of the reconstructed momentum. The momentum was corrected for the bias in the momentum reconstruction in the case of MC where particle species were known. The procedure was performed separately for data and simulation, for particles and anti-particles and for tracks that have two, three or more than three PD hits.

In the beginning, we calculated likelihood for each track with a pion, kaon or proton hypothesis. The parametrisation of $\ln(\mathrm{d}E/\mathrm{d}x)$ fit parameters as a function of momentum was used to calculate N_σ of a normal distribution for each track, based on its $\mathrm{d}E/\mathrm{d}x$ value and using pion, kaon and proton mass hypothesis. N_σ denotes a deviation, in units of standard deviations of the normal distribution, of a measured $\mathrm{d}E/\mathrm{d}x$ value from the mean $\mathrm{d}E/\mathrm{d}x$ value expected for a given particle. The N_σ distributions for PYTHIA 8, for true kaons are shown in Figure 5.1. One can see that the N_σ values are distributed around zero when the kaon hypothesis is applied. Likelihood was than calculated based on the N_σ for each track and a fraction of pions, kaons or protons (depending on the particle type assumption), obtained separately for:

- each momentum range where the $\ln(\mathrm{d}E/\mathrm{d}x)$ fits were done,
- data and simulation,
- particles and anti-particles,
- two, three or more than three PD hits of a track,
- SD, CD and MB analyses.

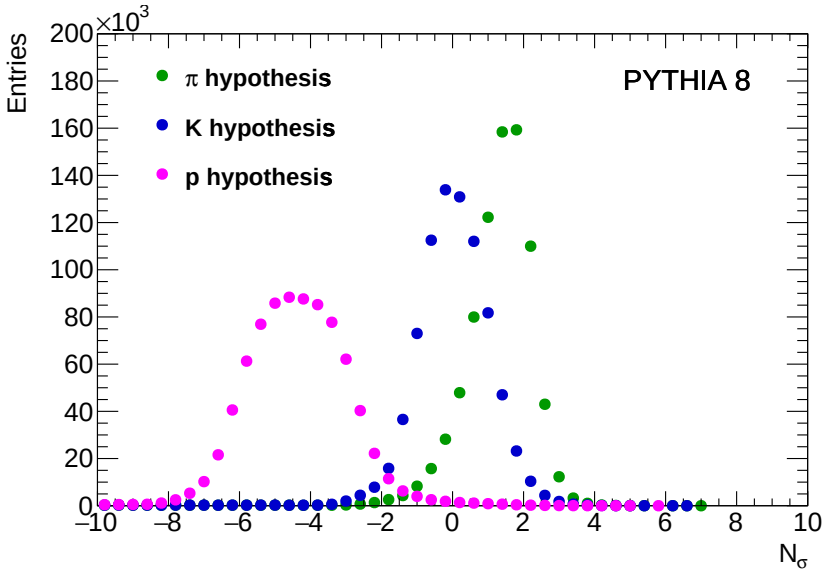

Figure 5.1: Distribution of N_σ of a normal distribution for true kaons' $\mathrm{d}E/\mathrm{d}x$, based on parametrisation of $\ln(\mathrm{d}E/\mathrm{d}x)$ fit parameters on momentum; with pion (magenta), kaon (blue) and proton (green) mass hypothesis for PYTHIA 8.

Then, the proper probabilities were obtained based on the following formula:

$$P_i = \frac{L_i}{L_\pi + L_K + L_p}, \quad (i = \pi, K, p) \tag{5.2}$$

where L indicates likelihood with a pion, kaon or proton hypothesis and P denotes the probability that a track originates from a given particle - a pion, a kaon or a proton. The probability distributions for tracks that are in the measurement region which is restricted by (5.1) are presented in Figure 5.2 for data and PYTHIA 8. There are a lot of events with high P_π and low P_K both for data and MC. These events are dominated by pions. Furthermore, there are differences between data and MC. Possible sources of these differences can be:

- different $\mathrm{d}E/\mathrm{d}x$ distributions for data and MC (the simulation is not perfect); in general the widths of the core Gaussian peak are smaller in data but transition to exponential behaviour appears earlier,
- different fractions of pions, kaons and protons in data and MC; excess of events with high P_π in data over PYTHIA 8 suggests that the relative fraction of pions modelled in PYTHIA 8 is underestimated,
- fractions of particles in MC are expected to be model-dependent and therefore they can differ for different MC generators.

Therefore, we expect different PID efficiencies for data and MC. No attempt was made to tune the relative fraction of different particle types in PYTHIA 8 or to improve $\mathrm{d}E/\mathrm{d}x$ simulation. Instead, the PID efficiency was determined from data by applying a tag-and-probe method. Firstly, to measure the PID efficiency for data (see Section 6.3). Secondly, to validate the method by comparing its results with the direct PID efficiency calculations for MC. This efficiency is defined as the probability that a true kaon which is reconstructed in the fiducial region (the cuts (5.1)) fulfils the given PID cuts. The comparison between the tag-and-probe efficiency and the directly derived one is shown in Section 6.3.

Simulation is not used to determine the PID efficiency but it is applied to optimise selection

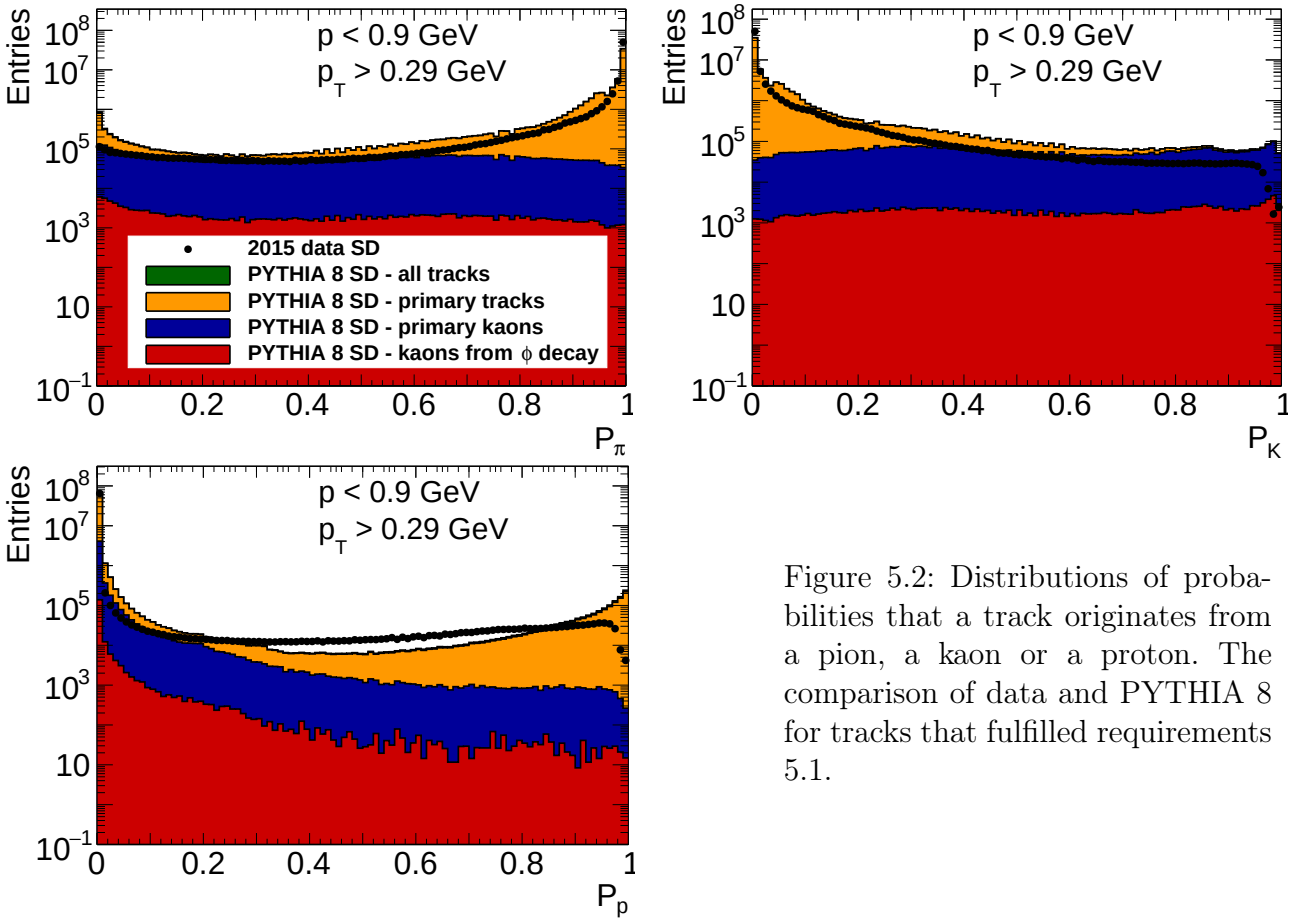

Figure 5.2: Distributions of probabilities that a track originates from a pion, a kaon or a proton. The comparison of data and PYTHIA 8 for tracks that fulfilled requirements 5.1.

cuts, for which the PID efficiency is determined from the tag-and-probe method. The optimisation is performed by studies of efficiency and purity. The purity is defined as the probability that a particle which satisfies the kinematic requirements (5.1) and the given PID cuts is a true kaon. The purity and the efficiency of three different sets of PID cuts were tested in order to find the optimal ones. Three cases below were examined:

$$P_K > 0.1 \text{ and } P_\pi < 0.9, \tag{5.3a}$$
$$P_K > 0.2 \text{ and } P_\pi < 0.7, \tag{5.3b}$$
$$P_K > 0.3 \text{ and } P_\pi < 0.6. \tag{5.3c}$$

Efficiencies and purities corresponding to the sets of cuts are shown for PYTHIA 8 in Figures 5.3 and 5.4 for negatively and positively charged kaons, respectively. The quantities were measured in four $|\eta|$ ranges: $0.0 < |\eta| < 0.5$, $0.5 < |\eta| < 1.0$, $1.0 < |\eta| < 1.5$ and $1.5 < |\eta| < 2.0$, independently. We observe higher efficiency and lower purity with the increasing $|\eta|$ values. The set of cuts (5.3a) was chosen as the nominal one due to the highest kaon identification efficiency compared to other requirement sets: (5.3b) and (5.3c). Bigger efficiency values are associated with lower purity. Hence, the last cuts (5.3c) that provide better purity compared to the nominal cuts (5.3a) were used in the tag-and-probe method (introduced in Section 6.3) to select tags.

Criteria (5.1) together with the PID cuts (5.3a) were imposed in order to select kaon candidates with high efficiency and to suppress background tracks. Figure 5.5 shows $p_{\mathrm{T},K}$ and η_K distributions for data and PYTHIA 8 for tracks that passed the above cuts except the one which is put on the plotted quantity. The MC distributions are normalised to the number of events in the data. Solid points indicate data with error bars corresponding to the statistical uncertainties. The MC predictions are presented as coloured histograms. The green histogram

shows all tracks - primary that are assigned to the primary vertex, secondary that originate from the secondary interaction vertex and fake that are not attached to a true level primary particle. The orange histogram corresponds to all primary tracks, the blue one represents true kaons and the red one shows a signal - true kaons from ϕ decay. The $p_{\mathrm{T},K}$ and η_K distributions are not well described by predictions.

5.2 ϕ Meson Candidate Selection

ϕ meson candidates were selected as pairs of oppositely charged kaon candidates. The pairs had to be in the kinematic region of a high acceptance defined as:

$$0.6 < p_{\mathrm{T},K^+K^-} < 1.5 \text{ GeV}, \tag{5.4a}$$

$$|y_{K^+K^-}| < 0.8. \tag{5.4b}$$

The track kinematic requirements (5.1) together with the criteria (5.4) form the fiducial region of the measurement. Figure 5.6 shows p_{T,K^+K^-} and $y_{K^+K^-}$ distributions for data and PYTHIA 8 for ϕ candidates that satisfy the requirements (5.1), (5.4) and (5.3a) apart from the one which is put on the plotted quantity. Figure 5.7 presents the invariant mass distribution of ϕ candidates. The MC is normalised to the number of events in data. The histograms for data and MC are indicated in the same way as in Figure 5.5. PYTHIA 8 predicts the lower number of phi mesons than is shown by data.

5.2.1 Signal Extraction

The yield of $\phi(1020)$ mesons was extracted from fits to the invariant mass distribution of two oppositely charged kaon candidates that are considered to come from the $\phi(1020)$ decay. The signal in data and PYTHIA 8 samples is described as a convolution of the non-relativistic Breit-Wigner function (5.6) with the Gaussian distribution:

$$f_{\mathrm{SIG}}(m) = f_{\mathrm{BW}}(m^*; m_0, \Gamma_0) \otimes Gauss(m; \mu = m^*, \sigma_{\mathrm{exp}}), \tag{5.5}$$

where m is the reconstructed invariant mass of the pair of oppositely charged kaon candidates, μ is the mean of the normal distribution which is equal to the true mass of the pair of oppositely charged kaon candidates m^*, σ_{exp} is the standard deviation interpreted as an experimental resolution and a non-relativistic Breit-Wigner function is defined as [13]:

$$f_{\mathrm{BW}}(m^*; m_0, \Gamma_0) = \frac{\Gamma_0}{2\pi} \frac{1}{(m^* - m_0)^2 + (\Gamma_0/2)^2}, \tag{5.6}$$

where m_0 denotes the $\phi(1020)$ meson mass and Γ_0 is the $\phi(1020)$ meson full width. The signal shape in the EPOS sample is characterised just by a Gaussian because the natural width of the ϕ meson is not implemented in this generator.

The background distribution is described as the following empirical formula [70]:

$$f_{\mathrm{BKG}}(m) = \left(1 - e^{(2m_K - m)/C}\right) \cdot \left(\frac{m}{2m_K}\right)^A + B\left(\frac{m}{2m_K} - 1\right), \tag{5.7}$$

where m_K is the charged kaon mass, and A, B and C determine the background shape.

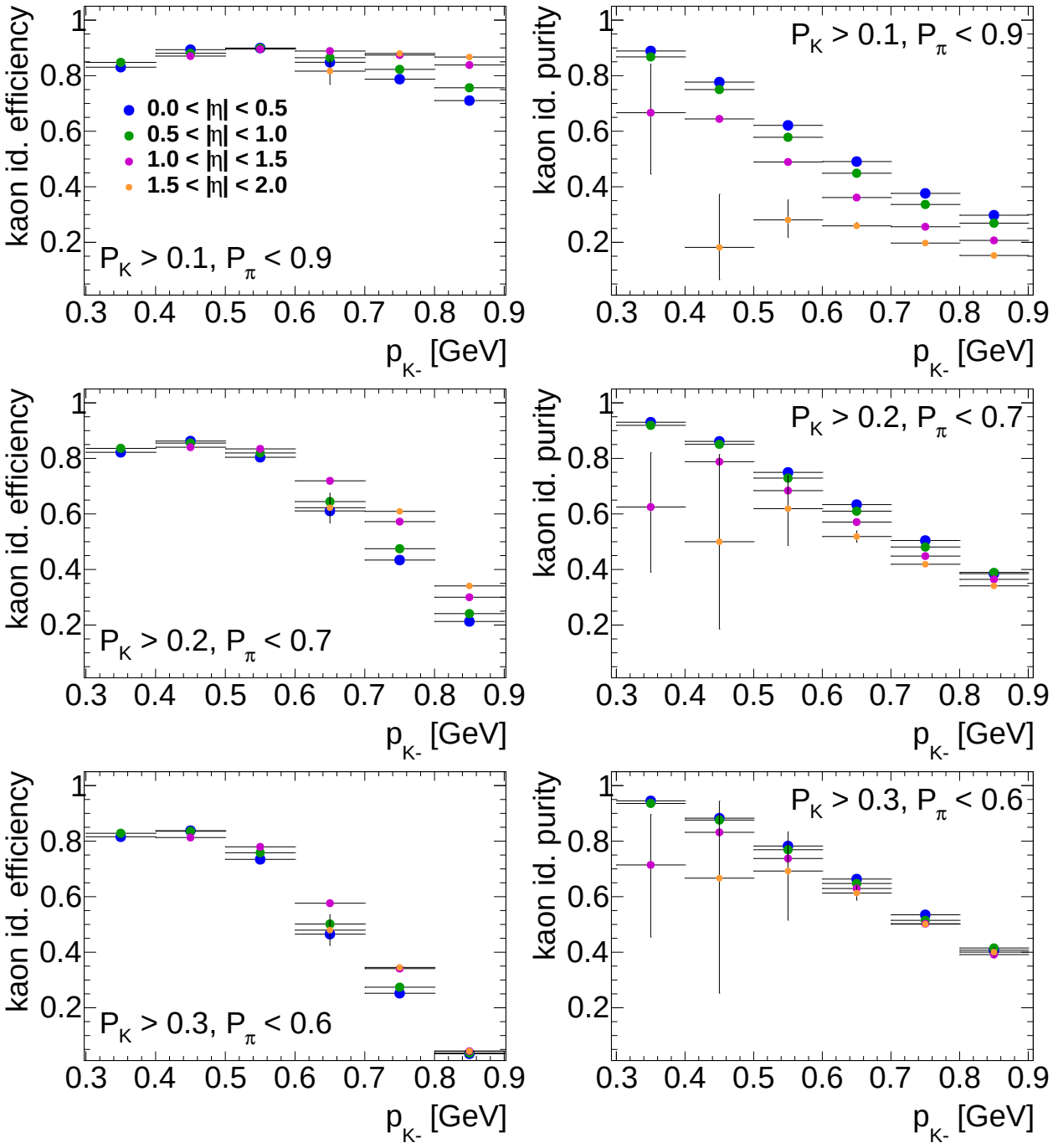

Figure 5.3: Kaon identification efficiencies and purities as a function of p_{K^-} for three sets of PID cuts (5.3) for PYTHIA 8.

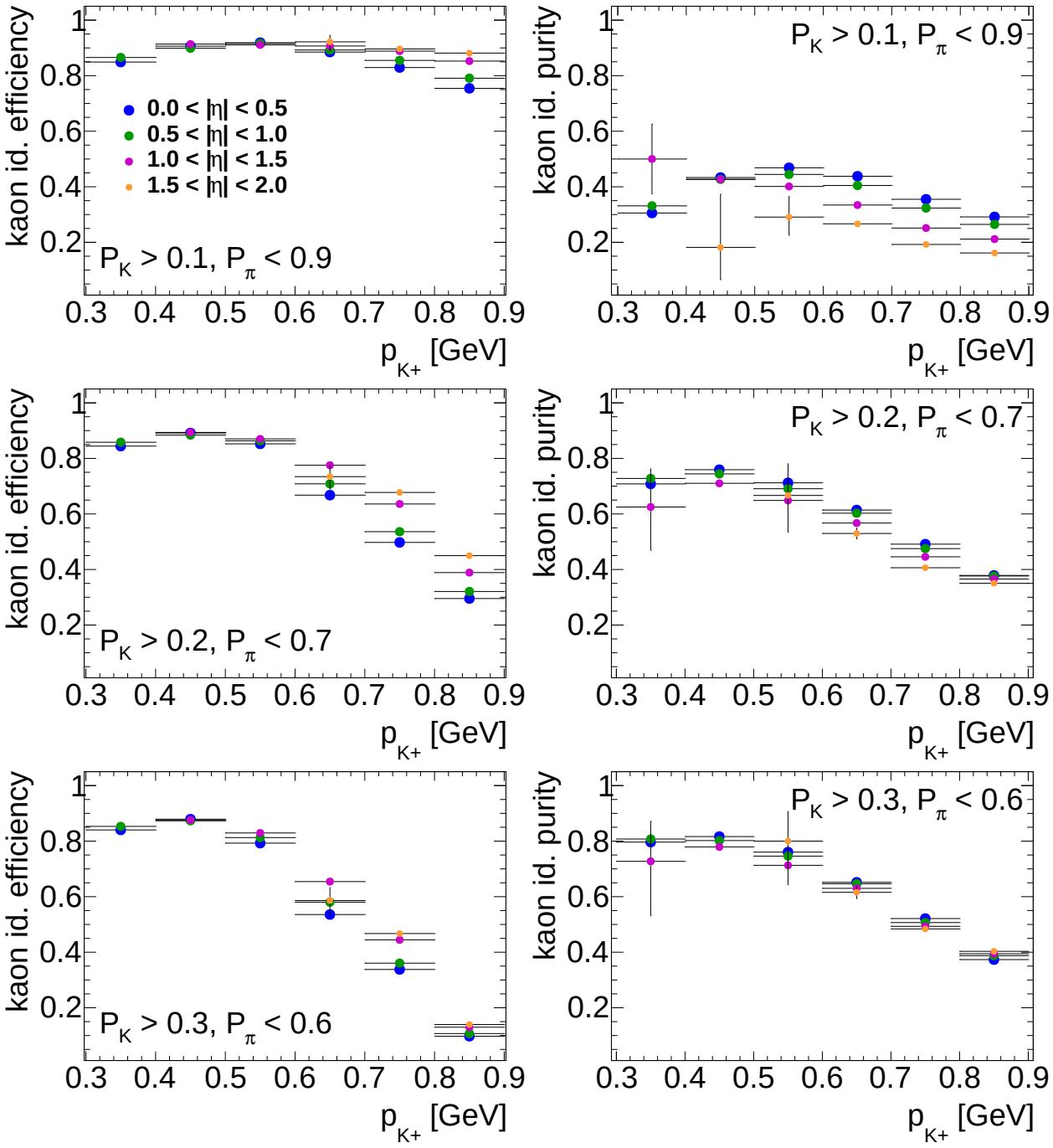

Figure 5.4: Kaon identification efficiencies and purities as a function of p_{K^+} for three sets of PID cuts (5.3) for PYTHIA 8.

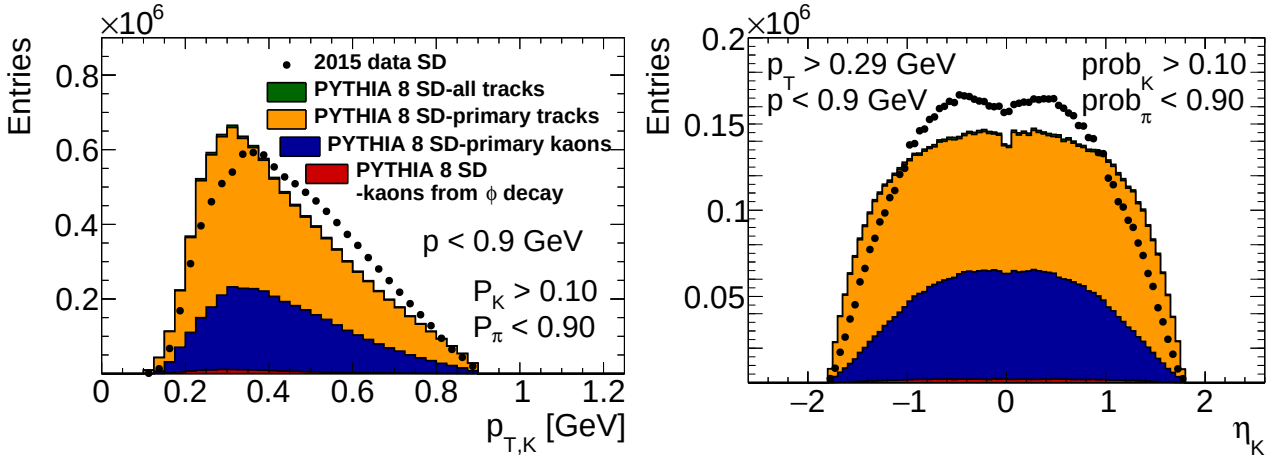

Figure 5.5: Distributions of kaon candidates' (left) $p_{\mathrm{T},K}$, and (right) η_K. The data are compared to PYTHIA 8 predictions.

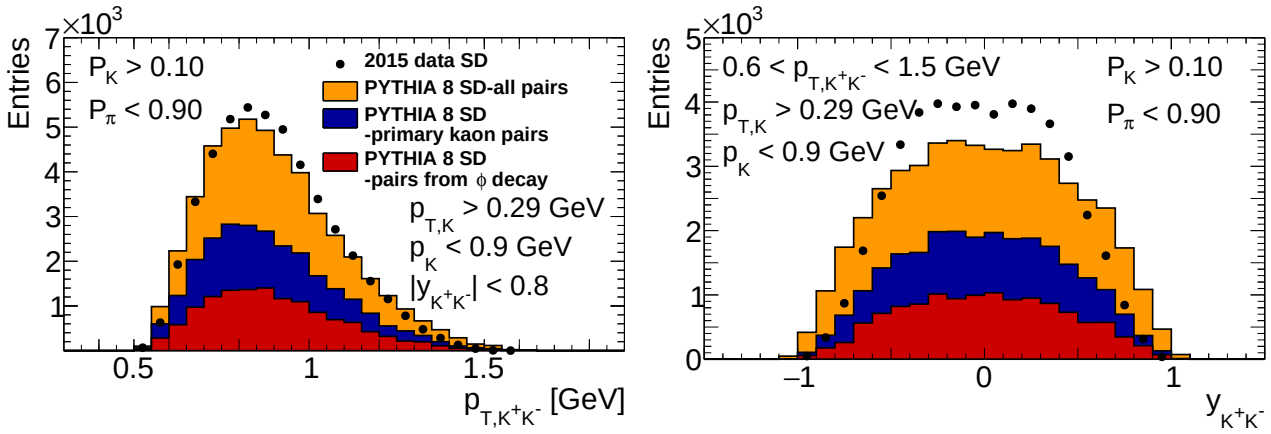

Figure 5.6: Distributions of $\phi(1020)$ meson candidates' (left) p_{T,K^+K^-}, and (right) $y_{K^+K^-}$. The data are compared to PYTHIA 8 predictions.

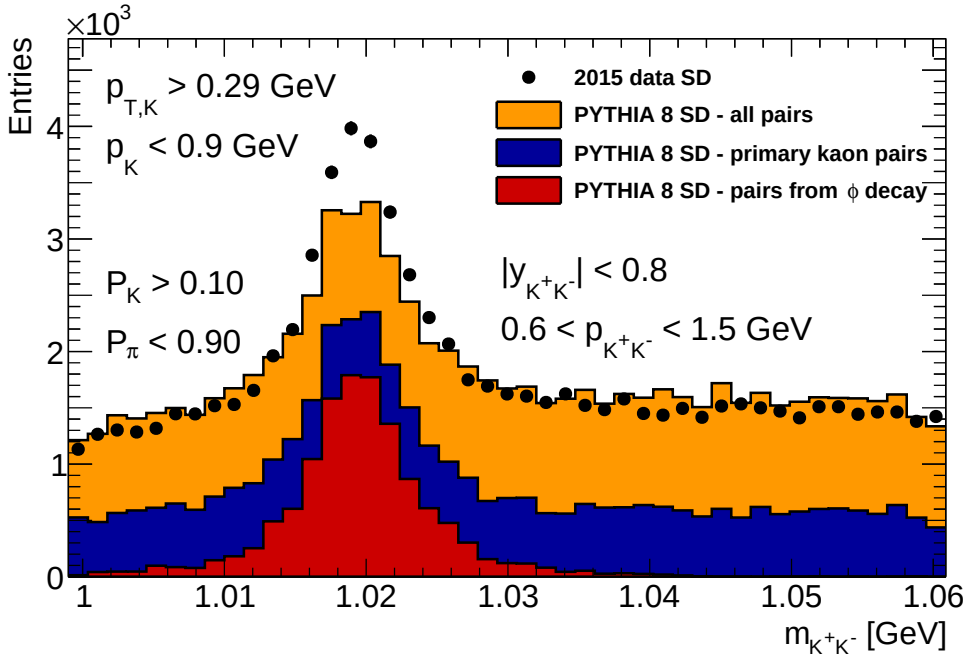

Figure 5.7: An invariant mass distribution for $\phi(1020)$ meson candidates. The data and PYTHIA 8 SD comparison.

CHAPTER 6
Corrections to ϕ Meson Spectra

Sections 6.1 - 6.4 describe corrections that were applied to data to correct for different kinds of observed inefficiencies.

6.1 Vertex Reconstruction Efficiency

The vertex reconstruction efficiency, ϵ_{vrt}, is defined as the ratio of the number of good reconstructed events to the number of all processed events, where the good reconstructed events indicate these with a reconstructed primary vertex with $n_{\mathrm{sel}} \geq 2$ and without a secondary vertex with four or more matched tracks; see Section 4.3. The efficiency, as a function of the number of selected tracks n_{sel} was calculated for data and two MC samples: PYTHIA 8 and EPOS. The calculations were also done for MC just for events where a true $\phi(1020)$ meson appeared. Such efficiency is defined then as the ratio of the number of good reconstructed events with a $\phi(1020)$ meson to all events where a $\phi(1020)$ meson was present. The results for data and PYTHIA 8 are shown in Figure 6.1. The ϵ_{vrt} predicted by EPOS is not presented in the figure because the results are not model dependent and they are similar to those calculated for PYTHIA 8. The $\epsilon_{\mathrm{vrt}} \approx 88\%$ for events with $n_{\mathrm{sel}} = 2$, $\epsilon_{\mathrm{vrt}} \approx 98\%$ for $n_{\mathrm{sel}} = 3$ and $\epsilon_{\mathrm{vrt}} \approx 100\%$ at higher multiplicities, according to data. The efficiency which is obtained for events with a true $\phi(1020)$ meson is $\epsilon_{\mathrm{vrt}} \approx 84\%$ for events with $n_{\mathrm{sel}} = 2$ and it is approximately at the same level as for events without the true $\phi(1020)$ meson requirement at higher multiplicities. The large statistical uncertainty for $n_{\mathrm{sel}} = 2$, observed for the sample with a true $\phi(1020)$ meson, indicates only that the contribution of $\phi(1020)$ mesons in the $n_{\mathrm{sel}} = 2$ sample is very small.
Each event is corrected for the vertex reconstruction inefficiency by applying the weight:

$$w_{\mathrm{vrt}} = 1/\epsilon_{\mathrm{vrt}}. \tag{6.1}$$

6.2 Track Reconstruction Efficiency

The track reconstruction efficiency, ϵ_{trk}, is defined as the probability that a primary true-level particle is reconstructed according to the selection criteria introduced in Section 4.3. We determined the efficiency for positively and negatively charged particles separately, in the same η ranges that were applied for the calculations of the correction for the bias in the momentum reconstruction (Section 3.1). Figure 6.2 shows the kaon reconstruction efficiency as a function of true p_{T,K^-} and p_{T,K^+} for PYTHIA 8 (upper plots) and ratios of the efficiencies predicted by PYTHIA 8 and EPOS (bottom plots). The predictions of both generators are similar. The efficiency is higher for lower $|\eta|$ values and it decreases with lower p_{T}. The selection cut (5.1b) was applied to provide the track reconstruction efficiency bigger than 40%.

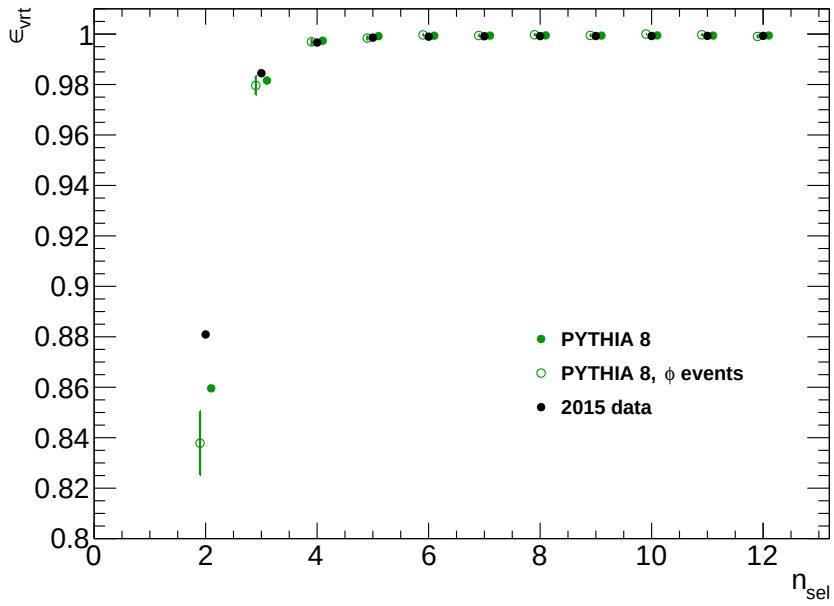

Figure 6.1: Vertex reconstruction efficiency as a function of the number of selected tracks for data and PYTHIA 8 MC (with and without the requirement of a presence of a true ϕ meson). The points are shifted in each bin horizontally by small distance for a better visibility.

The invariant mass distributions of two oppositely charged kaon candidates are corrected for the track reconstruction inefficiency using the following weight w_{trk}:

$$w_{\text{trk}} = 1/(\epsilon_{\text{trk},K^-} \cdot \epsilon_{\text{trk},K^+}). \tag{6.2}$$

The correction for the inefficiency of the ID is applied not only to N_ϕ but also to the number of all selected events, N. The latter is denoted as ϵ_{ID} and it was calculated as a probability that an event with $n_{\text{ch}} \geq 2$ at the particle level has $n_{\text{sel}} < 2$ at the reconstructed level. The correction was obtained as the mean of PYTHIA 8 and EPOS predictions for SD, CD and MB analysis, separately. The difference between the two expectations was taken as the systematic uncertainty and presented in Section 7.4. ϵ_{ID} is around 5% in SD, 7% in CD and 1% in MB. Moreover, it was obtained in three ξ ranges in the SD analysis, separately and it is 7.5% for $\xi < 0.035$, 2.1% for $0.035 < \xi < 0.08$, and 1.8% for $0.08 < \xi < 0.16$. The following weight w_{ID} was used to scale N in the final distributions:

$$w_{\text{ID}} = 1/(1 - \epsilon_{\text{ID}}). \tag{6.3}$$

6.3 Kaon Identification Efficiency

The kaon identification efficiency, ϵ_{PID}, is defined as the probability, that a kaon which is reconstructed in the fiducial region of this analysis, fulfils the nominal PID cuts (5.3a). The efficiency was calculated as a function of the kaon's momentum corrected for the bias in the momentum reconstruction. It was performed for positively and negatively charged kaons separately, in the same η ranges that were applied for the calculations of the correction for the bias in the momentum reconstruction (Section 3.1). The efficiency obtained from PYTHIA 8 and the ratio of efficiencies predicted by PYTHIA 8 and EPOS are shown in Figure 6.3. The two MC models predict similar kaon identification efficiency. Slightly lower efficiency values are obtained for negatively charged kaons than for positively charged ones.

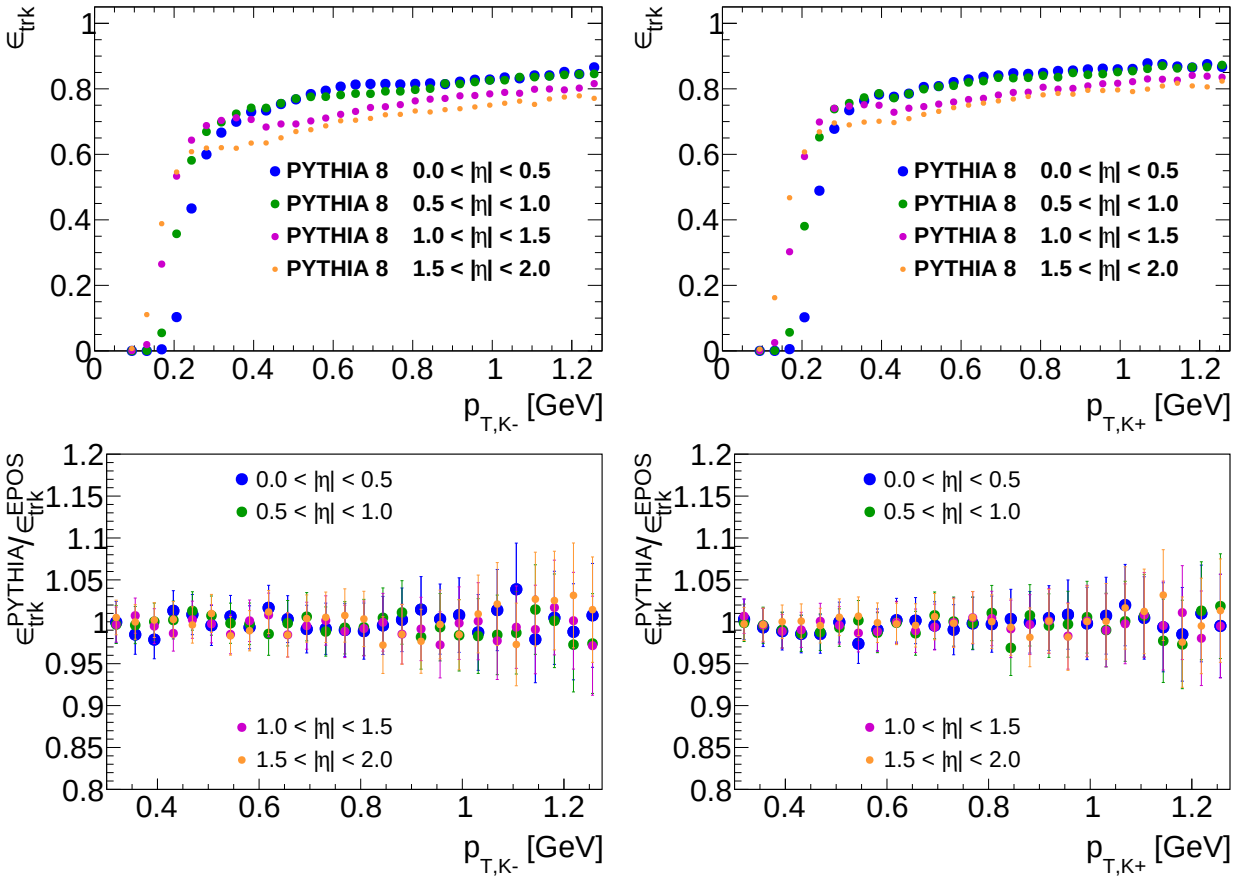

Figure 6.2: The kaon reconstruction efficiency as a function of true p_{T,K^-} and p_{T,K^+}. Upper plots show the efficiency in four ranges of η for PYTHIA 8. Bottom plots present ratios of the efficiencies predicted by PYTHIA 8 and EPOS.

The Tag-and-Probe Method

The tag-and-probe method was used to calculate the PID efficiency for data and it consists of the following steps:

1. Oppositely charged tag-and-probe pairs' selection, where:
   (a) the tag is a track reconstructed in the fiducial region of the measurement with a high probability that it originates from a kaon; it satisfies the PID cuts (5.3c),
   (b) the probe is selected as an oppositely charged track to the tag, reconstructed in the fiducial region of the measurement,
   (c) there are two possible cases of the probe:
      (A) the probe which satisfies the nominal PID cuts (5.3a),
      (B) the probe which does not satisfy the nominal PID cuts (5.3a).
2. The extraction of the number of $\phi(1020)$ mesons, denoted as $N_{\phi,\mathrm{A}}$ and $N_{\phi,\mathrm{B}}$ according to the description in the item (c), by fitting the signal and background functions (presented in Section 5.2.1) to the invariant mass distribution of the tag-and-probe pairs in six ranges of the probe's momentum: 0.3 - 0.4 - 0.5 - 0.6 - 0.7 - 0.8 - 1.0 GeV. The last range is wider due to low statistics.
3. The calculation of the probability that the probe was a kaon as:

$$\epsilon_{\mathrm{TP}} = \frac{N_{\phi,\mathrm{A}}}{N_{\phi,\mathrm{A}} + N_{\phi,\mathrm{B}}}. \tag{6.4}$$

The tag-and-probe efficiency, ϵ_{TP}, for data is shown in Figure 6.5. Example fits that were done to extract the number of ϕ mesons for the probe's momentum range $0.7 < p_{K,\mathrm{probe}} < 0.8$ GeV are shown in Figure 6.4. They clearly demonstrate that there is higher signal contribution for K^+K^- pairs where the probe meets the nominal PID cuts (5.3a).

There are significant differences between efficiency values in the six momentum ranges and the $\epsilon_{\mathrm{TP}}(p)$ was parametrised to suppress the fluctuations. The following formula is used to

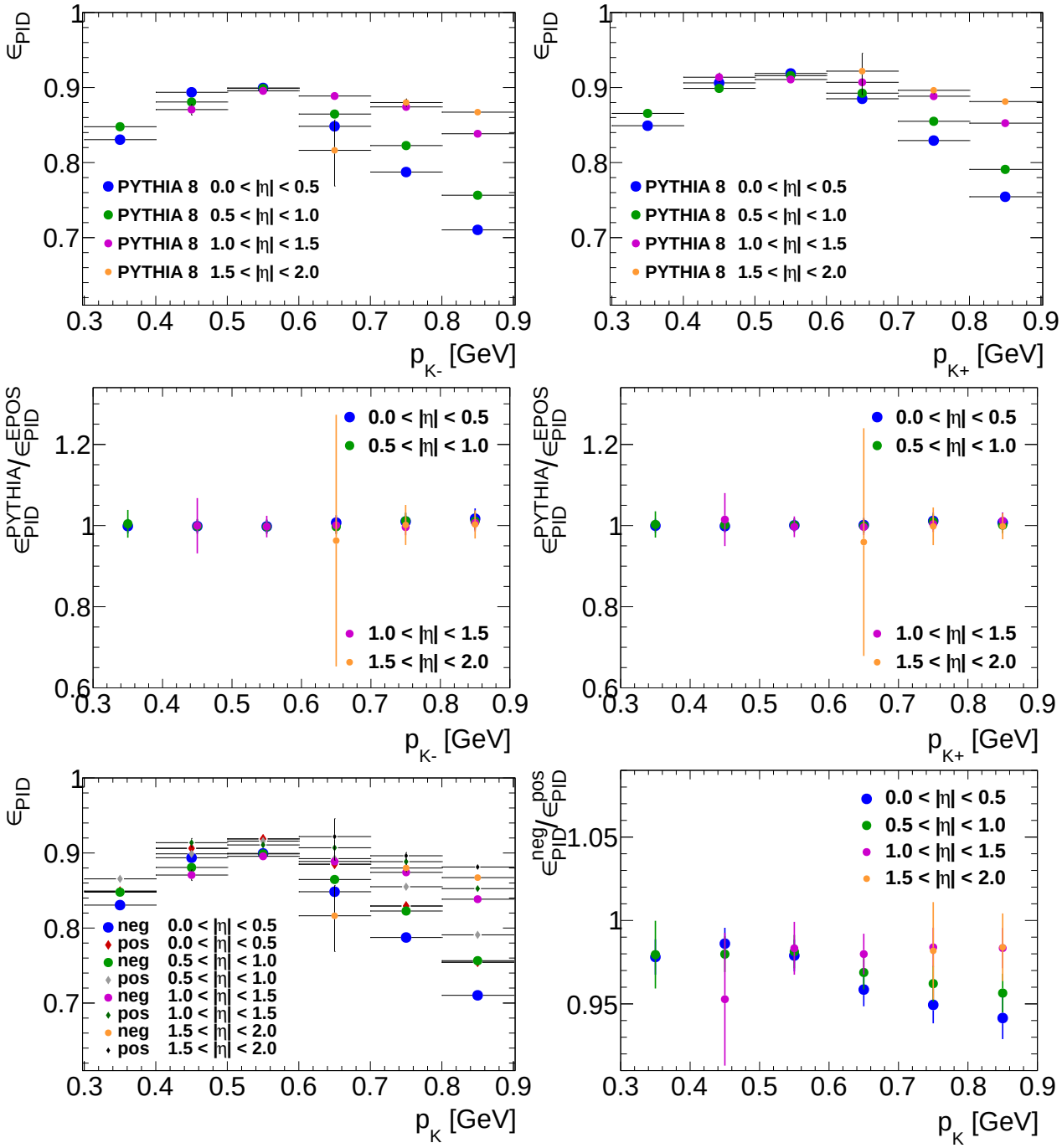

Figure 6.3: The kaon identification efficiency as a function of kaon's momentum corrected for the bias in the momentum reconstruction. Upper plots show the efficiency in four ranges of $|\eta|$ for PYTHIA 8. Plots in the middle present ratios of the efficiencies for PYTHIA 8 and EPOS. The comparison between positively (pos) and negatively (neg) charged kaons for PYTHIA 8 is shown in bottom plots.

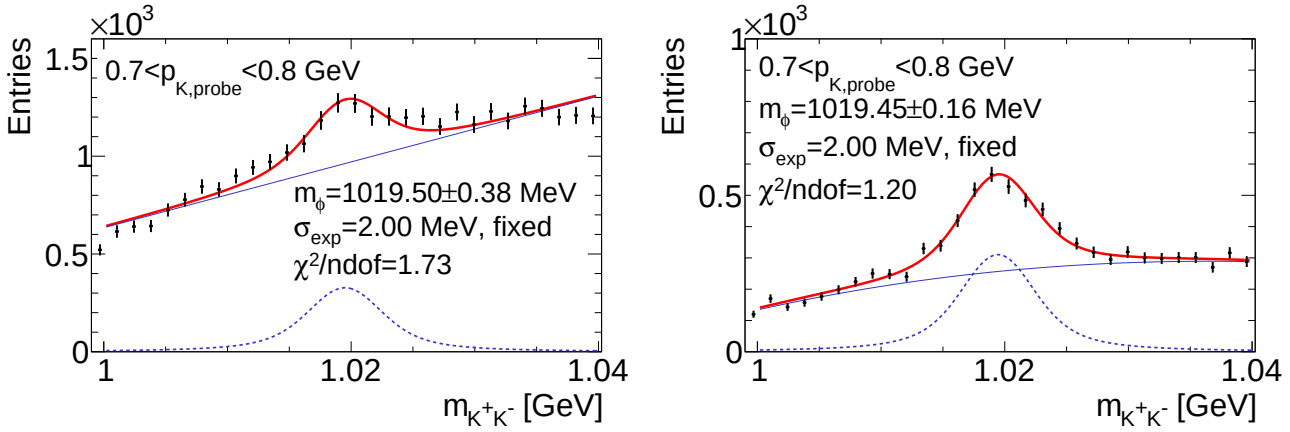

Figure 6.4: Fits to invariant mass distributions of: (left) pairs of negatively charged tags and positively charged probes that did not fulfil nominal PID cuts (5.3a), (right) pairs of negatively charged tags and positively charged probes that fulfilled nominal PID cuts (5.3a). The distributions are for data in the range of probe's momentum corrected for the bias in the momentum reconstruction, $0.7 < p_{K,\text{probe}} < 0.8$ GeV. Red curves represent a convolution of the non-relativistic Breit-Wigner function with the Gaussian distribution as a signal function (5.5) plus a background described by (5.7). Blue solid lines represent the background shape and dashed blue curves - the signal contribution. The fit parameters are displayed in the plots.

describe the $\epsilon_{\text{TP}}(p)$:

$$\epsilon_{\text{TP}}(p) = 0.5 \cdot P_0 \cdot (1 + \text{erf}((p - P_1)/P_2)), \tag{6.5}$$

where P_0, P_1 and P_2 are free parameters, and erf is the error function. The fitted function is shown in Figure 6.5. Data are corrected according to this parametrisation which was obtained for negatively and positively charged kaons separately and denoted as $\epsilon_{\text{PID,data},K^-}$ and $\epsilon_{\text{PID,data},K^+}$, respectively. The invariant mass distributions of two oppositely charged kaon candidates are re-weighted by $w_{\text{PID,data}}$:

$$w_{\text{PID,data}} = 1/(\epsilon_{\text{PID,data},K^-} \cdot \epsilon_{\text{PID,data},K^+}). \tag{6.6}$$

The tag-and-probe method was validated by measuring the tag-and-probe kaon identification efficiency for PYTHIA 8 and comparing it with the directly derived efficiency, described in the above Section. The ϵ_{TP} for data and MC is shown in Figure 6.6 together with the directly measured efficiency based on PYTHIA 8. The tag-and-probe efficiency is higher for MC compared to data because of better separation of kaons from pions in PYTHIA 8. The results obtained for PYTHIA 8 show that the tag-and-probe efficiency and the efficiency measured directly are identical within the statistical uncertainties. Thus, the data-driven tag-and-probe efficiency can be applied to correct data for the inefficiencies induced by the kaon identification procedure.

6.4 MBTS Correction

The MBTS correction was obtained based on PYTHIA 8 and EPOS simulations. We calculated a difference between the nominal true-level $p_{\text{T},\phi}$ and $|y_\phi|$ spectra (see Section 8) and the spectra obtained with the MBTS requirements that are described in Section 4.1. The requirements were introduced to both the number of ϕ mesons, N_ϕ, and to the number of all selected events, N.

At least one MBTS counter with a signal was required in the MB analysis. There is no difference in the number of ϕ mesons from the true-level with and without the MBTS requirement. Since the difference is at the level of 0.04% for the number of all selected events, no correction

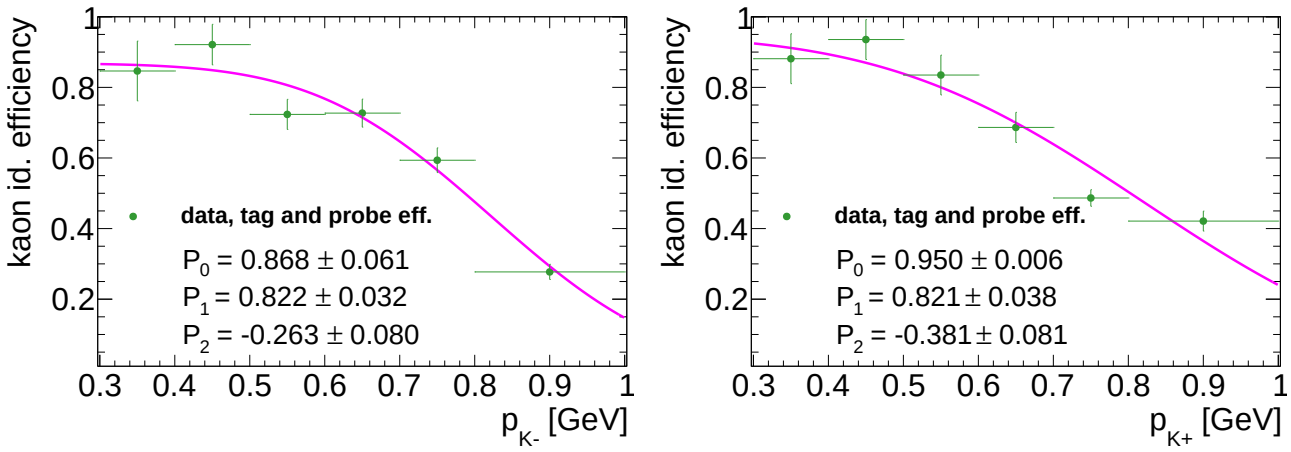

Figure 6.5: The data-driven tag-and-probe efficiency as a function of the reconstructed momentum, corrected for the bias in the momentum reconstruction, for negatively (left) and positively (right) charged kaons. The magenta line represents the function (6.5) fitted to the $\epsilon_{\mathrm{TP}}(p)$ distributions. The fit parameters are displayed in the figure.

to the MBTS was applied in the MB analysis.

A signal in at least one MBTS counter on the opposite ATLAS side to the proton tagged in the ALFA detector was required in the SD analysis. The difference between the nominal spectra and these ones with the MBTS cut is significant for the SD analysis. The nominal and changed results for PYTHIA 8 SD and EPOS SD+SD' are shown as a function of $p_{\mathrm{T},\phi}$ and y_ϕ in Figure 6.7. Larger differences are observed for PYTHIA 8 than for EPOS in both $p_{\mathrm{T},\phi}$ and $|y_\phi|$ spectra. The spectra with the MBTS cut increase of about 35% with respect to the nominal ones for PYTHIA 8 and of around 15% for EPOS. The differences are approximately the same in each $p_{\mathrm{T},\phi}$ and $|y_\phi|$ ranges and they are mostly related to the change of N after the MBTS cut. The correction was applied only for $\xi < 0.0.035$ in the SD analysis because it is negligible for higher ξ values, as in the MB analysis.

The mean of the PYTHIA 8 and EPOS ratios was used to scale data in order to correct for the MBTS inefficiency. The difference between the mean and the specific prediction was used

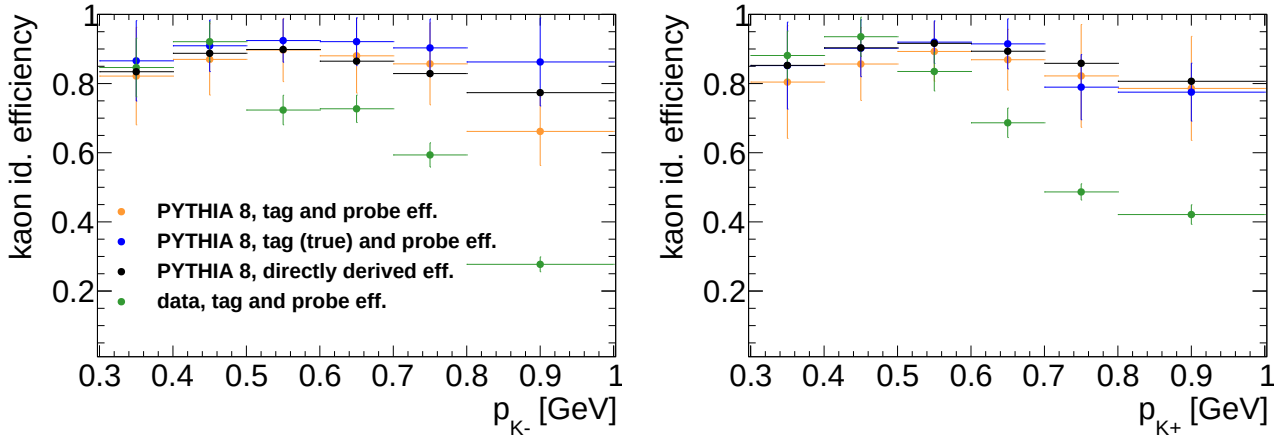

Figure 6.6: The tag-and-probe efficiency for data (green dots) and PYTHIA 8 (orange and blue dots) compared with the kaon identification efficiency calculated directly using PYTHIA 8 (black dots). The efficiencies are presented as a function of the reconstructed momentum, corrected for the bias in the momentum reconstruction, for negatively (left) and positively (right) charged kaons.

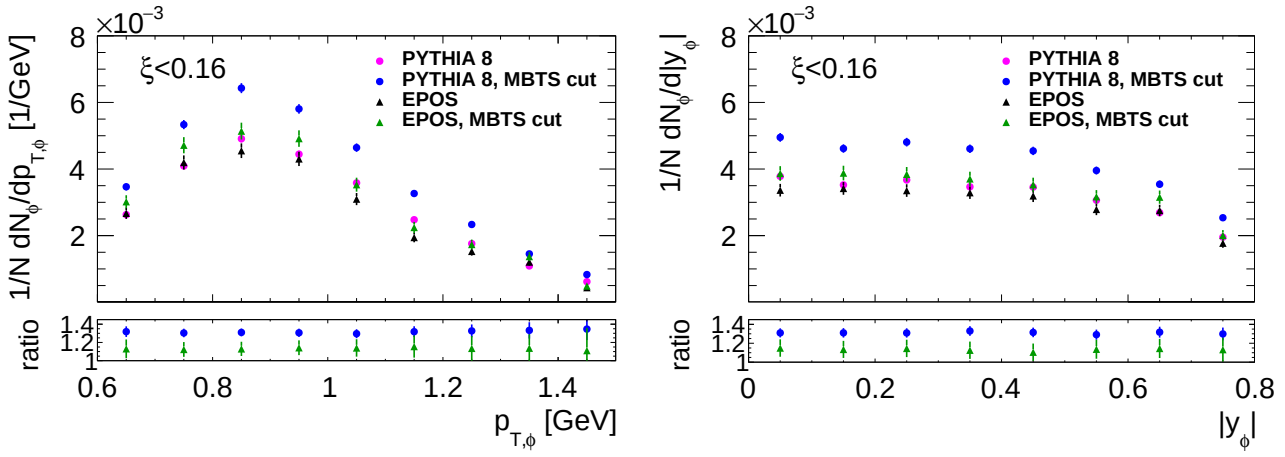

Figure 6.7: (left) $p_{\mathrm{T},\phi}$ spectrum integrated over $|y_\phi| < 0.8$, and (right) $|y_\phi|$ spectrum integrated over $0.6 < p_{\mathrm{T},\phi} < 1.5$ GeV in the SD analysis. Comparison between nominal predictions and predictions with the cut on the MBTS. The predictions are shown in the full $\xi < 0.16$ range. Ratios of the modified to the nominal distributions are shown for PYTHIA 8 (blue) and EPOS (green) in the bottom panels.

to get the systematic uncertainty on the correction which is described in Section 7.4.

The MBTS correction should be also calculated in the CD analysis where the MBTS requirement is different. Thus, we repeated the same procedure as in the case of SD but the statistics in CD MC samples was too low to estimate the correction.

6.5 Migration Correction

The $p_{\mathrm{T},\phi}$ and $|y_\phi|$ spectra were also corrected for migrations inside and outside the fiducial region of the measurement. The migrations are discussed in Section 7. The correction factors where ϕ mesons' and their decay products' migrations are considered are expressed as (7.3) and (7.4) for migrations outside and inside the fiducial region, respectively. Formulas (7.5) and (7.6) show the correction factors for migrations concerning ξ and t of forward protons that was obtained for each of three ξ ranges separately. They are not applied in the analysis because the final correction equals 1 within uncertainties that was shown in Section 7.3.

6.6 Accidental Background Correction

SD data were corrected for accidental background contribution which was estimated from appropriate data samples to be $10\% \pm 2\%$ in the first $\xi < 0.035$ range and negligible at $\xi > 0.035$ [90]. Accidental background in SD analysis consists mainly of a random overlap of elastic or beam-halo protons in ALFA with minimum bias processes in central ATLAS detectors. Therefore, we used $p_{\mathrm{T},\phi}$ and $|y_\phi|$ spectra obtained for MB analysis (see Fig. 8.11) to estimate the final corrections. Since the MB spectra are around 50% higher than the ones measured for SD, the accidental background correction for the number of ϕ mesons was estimated as:

$$N_{\phi,\mathrm{corr}} = N_\phi - 0.1 \cdot 1.5 N_\phi = 0.85 N_\phi, \tag{6.7}$$

and the correction for the number of all selected events was set as:

$$N_{\mathrm{corr}} = 0.9N. \tag{6.8}$$

Finally, the spectra are corrected by:

$$\frac{N_{\phi,\mathrm{corr}}}{N_{\mathrm{corr}}} = 0.94 \frac{N_\phi}{N}. \tag{6.9}$$

Thus, the $p_{\mathrm{T},\phi}$ and $|y_\phi|$ spectra in the SD analysis are expected to be $6\% \pm 1\%$ smaller due to the accidental background contribution. This correction will be applied only for $\xi < 0.035$.

The accidental background in the CD analysis was discussed in Section 4.3.3. The background is suppressed using the anti-elastic cut on protons' collinearity in the elastic pp configuration of ALFA branches, Eq. (4.5). The anti-elastic cut affects in the same way both N_ϕ and N measurements according to MC predictions. Therefore, no correction for accidental background was introduced to spectra in the CD analysis.

CHAPTER 7
Closure Tests and Systematics

Closure tests were made to validate corrections that are applied to data. The tests are based on MC samples and they rely on comparing distributions at the true-level and the detector-level. The latter are shown with and without corrections. The distributions in the closure tests are presented as a function of $p_{\mathrm{T},\phi}$ and y_ϕ at a few stages of the analysis.

7.1 Closure Tests I: ϵ_{vrt} and ϵ_{trk} Corrections

The true-level distributions show the number of ϕ mesons from the true-level kinematic region (5.4) that decay into two oppositely charged kaons with p and η restricted by (5.1). These distributions are compared with the number of ϕ mesons from the same kinematic region but at the detector-level. The corrections for the bias in the momentum reconstruction are taken into account in the case of the reconstructed momentum. The detector-level distributions are also corrected for the vertex reconstruction and track reconstruction inefficiencies by applaying for each ϕ meson candidate a weight given by $w_{\mathrm{vrt}} \cdot w_{\mathrm{trk}}$, while w_{vrt} and w_{trk} are described by Eq. (6.1) and (6.2), respectively.

Migrations outside the fiducial region of the measurement, f_{I}^{-}, were calculated as the fraction of true ϕ mesons that, together with their decay products, are generated in the fiducial region but are reconstructed outside this region. The detector-level distributions are corrected for the migrations by weighting them by:

$$f_{\mathrm{I}}^{\mathrm{o}} = 1/(1 - f_{\mathrm{I}}^{-}). \tag{7.1}$$

The migrations are shown in Figure 7.1 for PYTHIA 8 and EPOS. The two generators predict similar migration. The biggest effect is observed at the edges of the fiducial region.

Closure tests I for PYTHIA 8 and EPOS are shown in Figures 7.2 and 7.3, respectively. The true-level distributions and the corrected detector-level ones agree well, which verifies the validity of the calculated efficiencies and migrations.

7.2 Closure Tests II and III: ϵ_{PID} Corrections

All criteria that were applied for closure tests I are also valid for closure tests II but there is an additional requirement that the ϕ meson's decay products have to satisfy the nominal PID cuts (5.3a). The detector-level distributions are corrected then by $w_{\mathrm{vrt}} \cdot w_{\mathrm{trk}} \cdot w_{\mathrm{PID}}$, where:

$$w_{\mathrm{PID}} = 1/(\epsilon_{\mathrm{PID},K^-} \cdot \epsilon_{\mathrm{PID},K^+}). \tag{7.2}$$

$\epsilon_{\mathrm{PID},K^-}$ and $\epsilon_{\mathrm{PID},K^+}$ indicate respectively the K^- and K^+ particle identification efficiencies that were derived directly based on PYTHIA 8 true level (see Section 6.3). The efficiencies

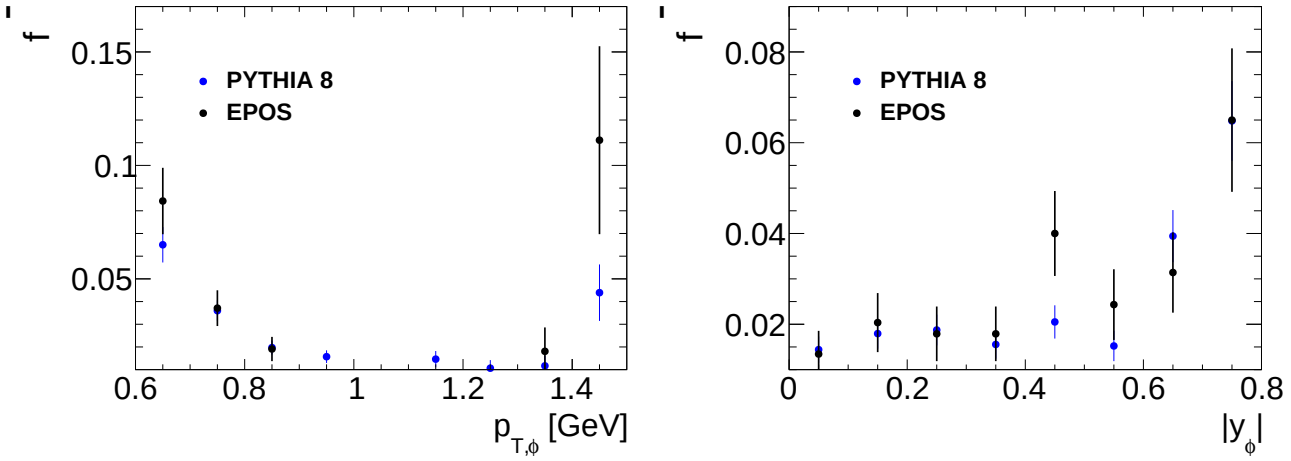

Figure 7.1: Migrations outside the fiducial region as a function of $p_{T,\phi}$ (left) and y_ϕ (right) for PYTHIA 8 and EPOS.

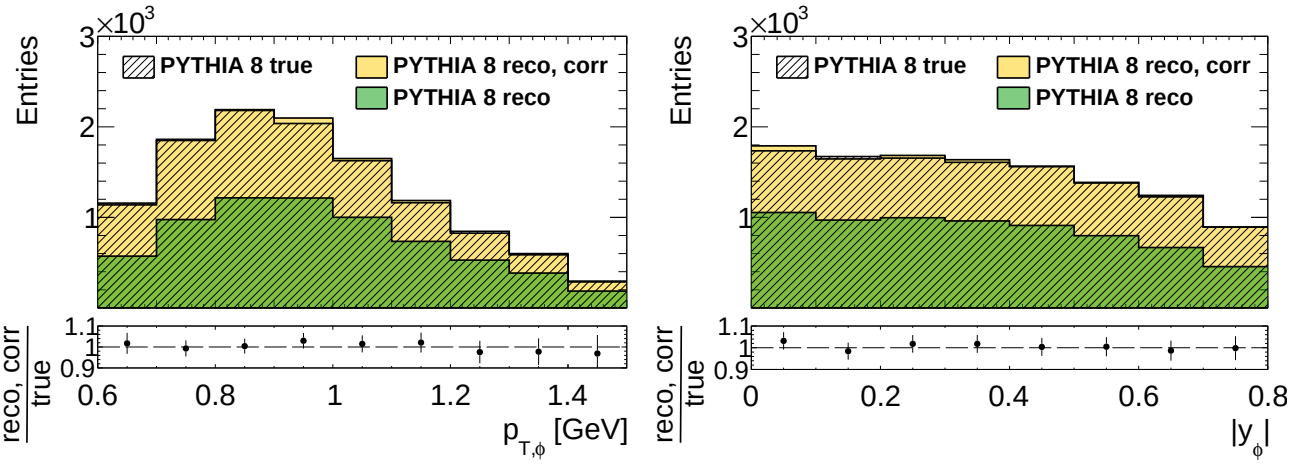

Figure 7.2: Closure tests I for PYTHIA 8. The striped transparent histogram represents the number of ϕ mesons at the true level, the green one - from the uncorrected reconstructed level and the yellow one from the reconstructed level after applying corrections (6.1−7.1).

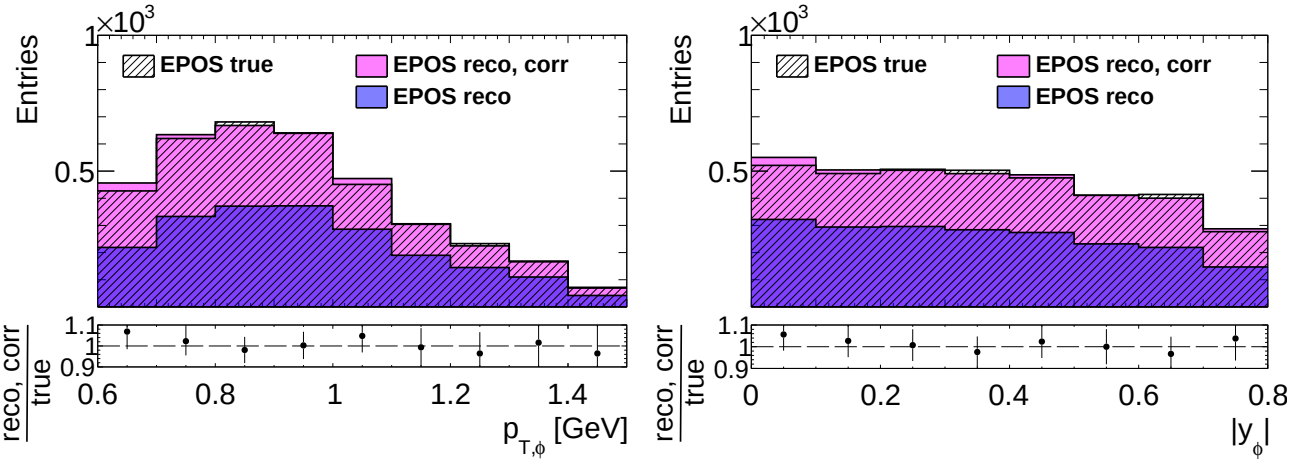

Figure 7.3: Closure tests I for EPOS. The striped transparent histogram represents the number of ϕ mesons at the true level, the blue one - from the uncorrected reconstructed level and the magenta one from the reconstructed level after applying corrections (6.1−7.1).

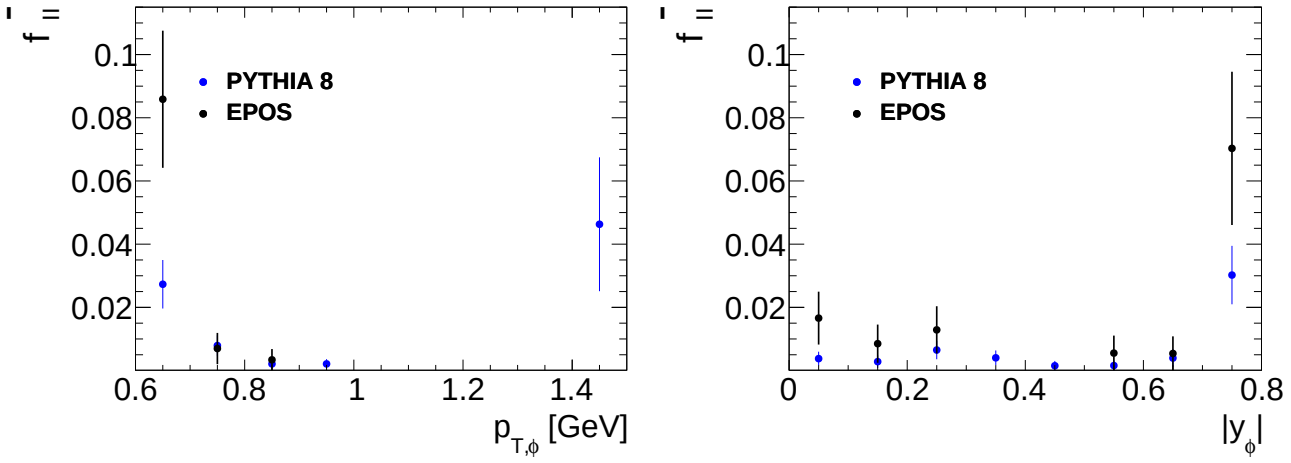

Figure 7.4: Migrations outside the fiducial region (with kaon identification based on the nominal PID cuts (5.3a)) as a function of $p_{T,\phi}$ (left) and y_ϕ (right) for PYTHIA 8 and EPOS.

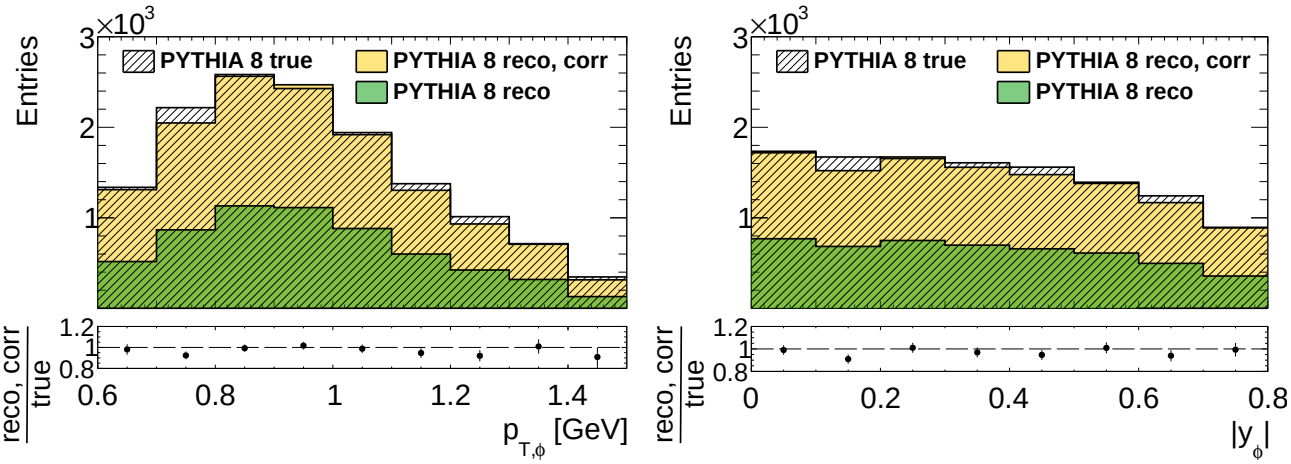

Figure 7.5: Closure tests II for PYTHIA 8. The striped transparent histogram represents the number of ϕ mesons from the true level, the green one - from the uncorrected reconstructed level and the yellow one from the reconstructed level after applying corrections (6.1), (6.2), (7.2) and (7.3).

were calculated as a function of the kaon's momentum corrected for the bias in the momentum reconstruction, in nine p_T bins between 0.6 and 1.5 GeV with widths of 0.1 GeV.

Migrations outside the fiducial region of the measurement, f_{II}^{-}, were calculated as the fraction of the number of true ϕ mesons that, together with their decay products, are generated in the fiducial region but are reconstructed outside this region, while the ϕ meson's decay products fulfil the nominal PID cuts (5.3a). The detector-level distributions are corrected for the migrations by weighting them by:

$$f_{II}^{o} = 1/(1 - f_{II}^{-}). \tag{7.3}$$

The migrations are presented in Figure 7.4 for PYTHIA 8 and EPOS. The results from the two generators are similar and they predict the biggest migrations at the edges of the fiducial region of the measurement.

Closure tests II for PYTHIA 8 and EPOS are shown in Figures 7.5 and 7.6, respectively. The good agreement between the true-level and the corrected detector-level distributions is demonstrated which validates the calculated efficiencies and migrations.

All criteria that were applied for closure tests II are also used in closure tests III. The difference between the two tests is that in tests III the number of detector-level ϕ mesons is

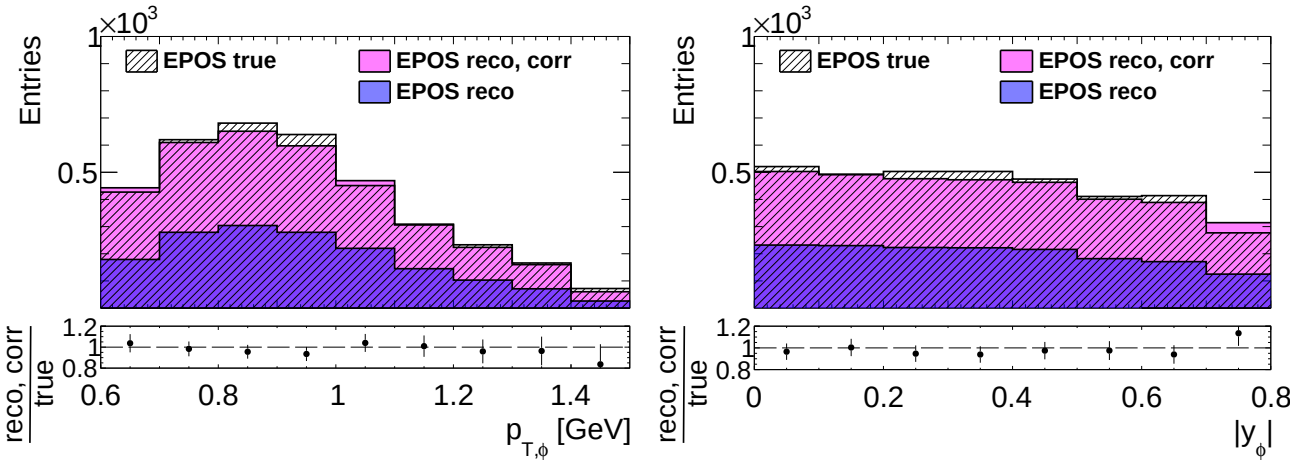

Figure 7.6: Closure tests II for EPOS. The striped transparent histogram represents the number of ϕ mesons from the true level, the blue one - from the uncorrected reconstructed level and the magenta one from the reconstructed level after applying corrections (6.1), (6.2), (7.2) and (7.3).

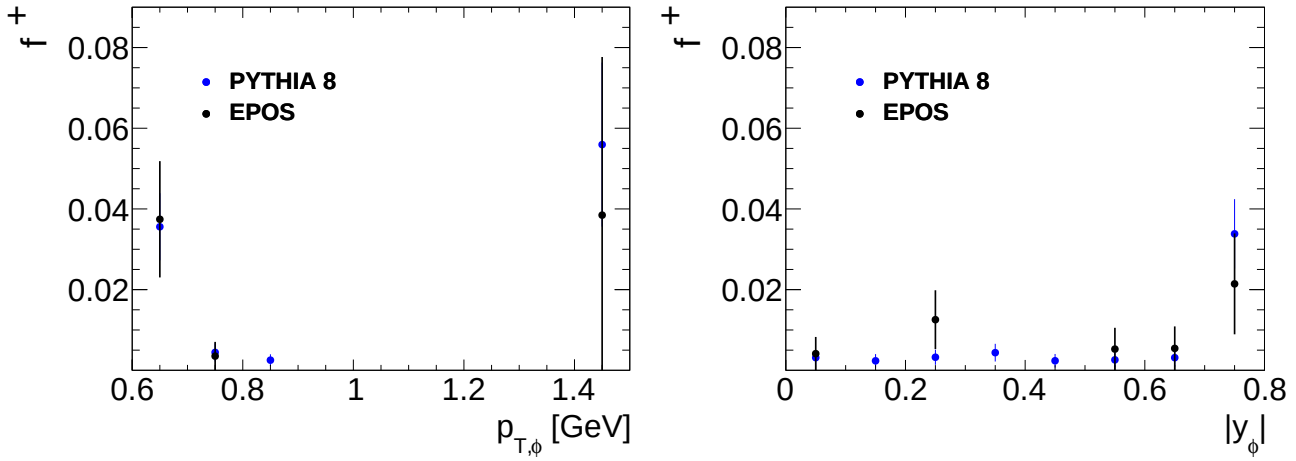

Figure 7.7: Migrations inside the fiducial region (with kaon identification based on the nominal PID cuts (5.3a)) as a function of $p_{\mathrm{T},\phi}$ (left) and y_ϕ (right) for PYTHIA 8 and EPOS.

extracted from the fits to the invariant mass distributions of ϕ meson candidates. Therefore, the measured sample may also contain ϕ mesons that are outside the fiducial region of the measurement at the true level.

Migrations inside the fiducial region of the measurement, f^+, are defined as the fraction of the true ϕ mesons and their decay products that are not in the true-level fiducial region but are reconstructed in the fiducial region of the measurement. The detector-level distributions in closure tests III are corrected for these migrations by weighting them by:

$$f^{\mathrm{i}} = 1 - f^{+}. \tag{7.4}$$

The migrations are presented in Figure 7.7 for PYTHIA 8 and EPOS. Both models predict bigger migrations at the edges of the fiducial region. The final migration correction that was applied to data, $f^{\mathrm{o}}_{\mathrm{II}} \cdot f^{\mathrm{i}}$, is shown in Figure 7.8 as a function of $p_{\mathrm{T},\phi}$ and y_ϕ and is lower than 1% in each $p_{\mathrm{T},\phi}$ and $|y_\phi|$ bin.

Closure tests III for PYTHIA 8 and EPOS are shown in Figures 7.9 and 7.10, respectively. The true-level distributions are quite well reproduced by the corrected detector-level distributions what validates the correction procedure.

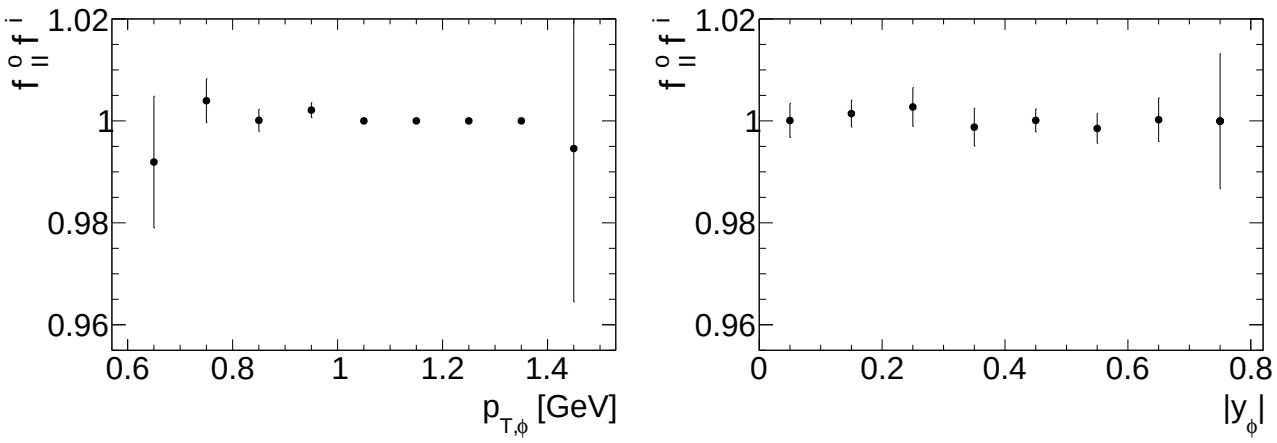

Figure 7.8: The final correction for migrations outside and inside the fiducial region as a function of $p_{\mathrm{T},\phi}$ (left) and y_ϕ (right) for PYTHIA 8.

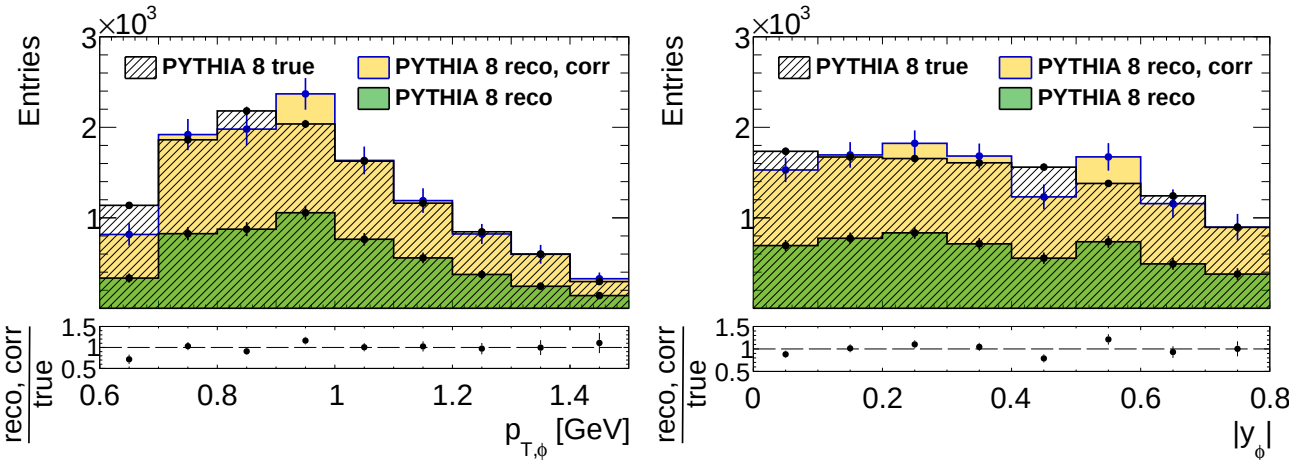

Figure 7.9: Closure tests III for PYTHIA 8. The striped transparent histogram represents the number of ϕ mesons from the true level, the green one - from the uncorrected reconstructed level and the yellow one from the reconstructed level after applying corrections (6.1), (6.2) and (7.2−7.4). Statistical errors are shown in the plots.

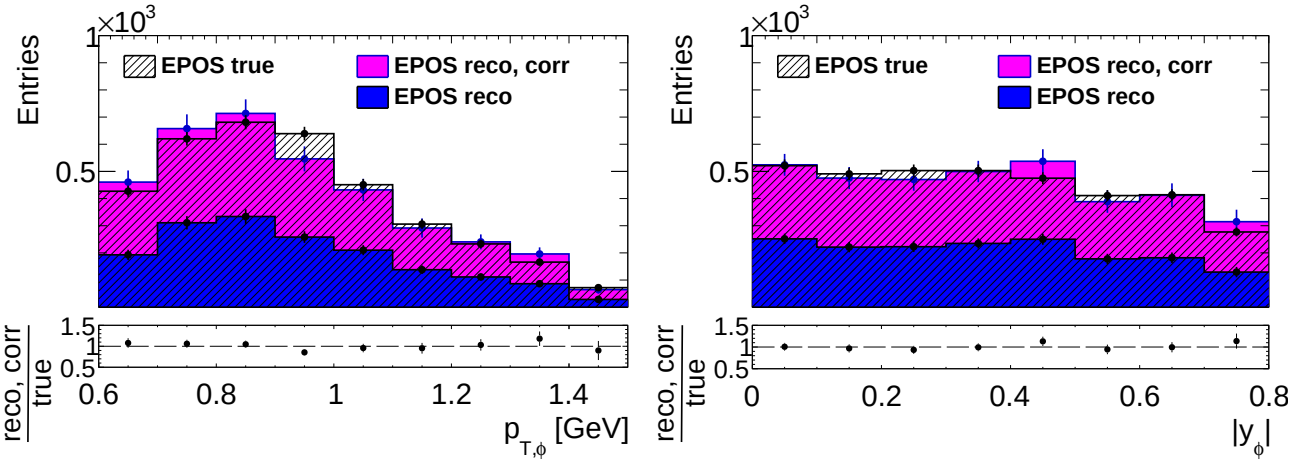

Figure 7.10: Closure tests III for EPOS. The striped transparent histogram represents the number of ϕ mesons from the true level, the blue one - from the uncorrected reconstructed level and the magenta one from the reconstructed level after applying corrections (6.1), (6.2) and (7.2−7.4). Statistical errors are shown in the plots.

7.3 Closure Tests IV: ξ and t Migrations

Migrations in ξ and t were not taken into account in closure tests I, II and III. These migrations are related to both the number of all selected events, N, and to the number of ϕ mesons, N_ϕ. The latter were calculated as a function of $p_{\mathrm{T},\phi}$ and y_ϕ. The migrations in ξ and t were validated in closure tests IV in three ξ ranges. The PYTHIA 8 SD sample was used.

The fiducial region of the forward proton measurement was restricted by ξ and t ranges presented in Section 4.3.2. Migrations outside the fiducial region of the measurement, f_p^-, are calculated as the fraction of events with a true ϕ meson for which ξ and t are in the true-level fiducial region but they are not in the corresponding detector-level fiducial region. The migrations related to the number of ϕ mesons, f_{p,N_ϕ}^- are shown in Figure 7.11. The biggest values are predicted for $0.035 < \xi < 0.08$.

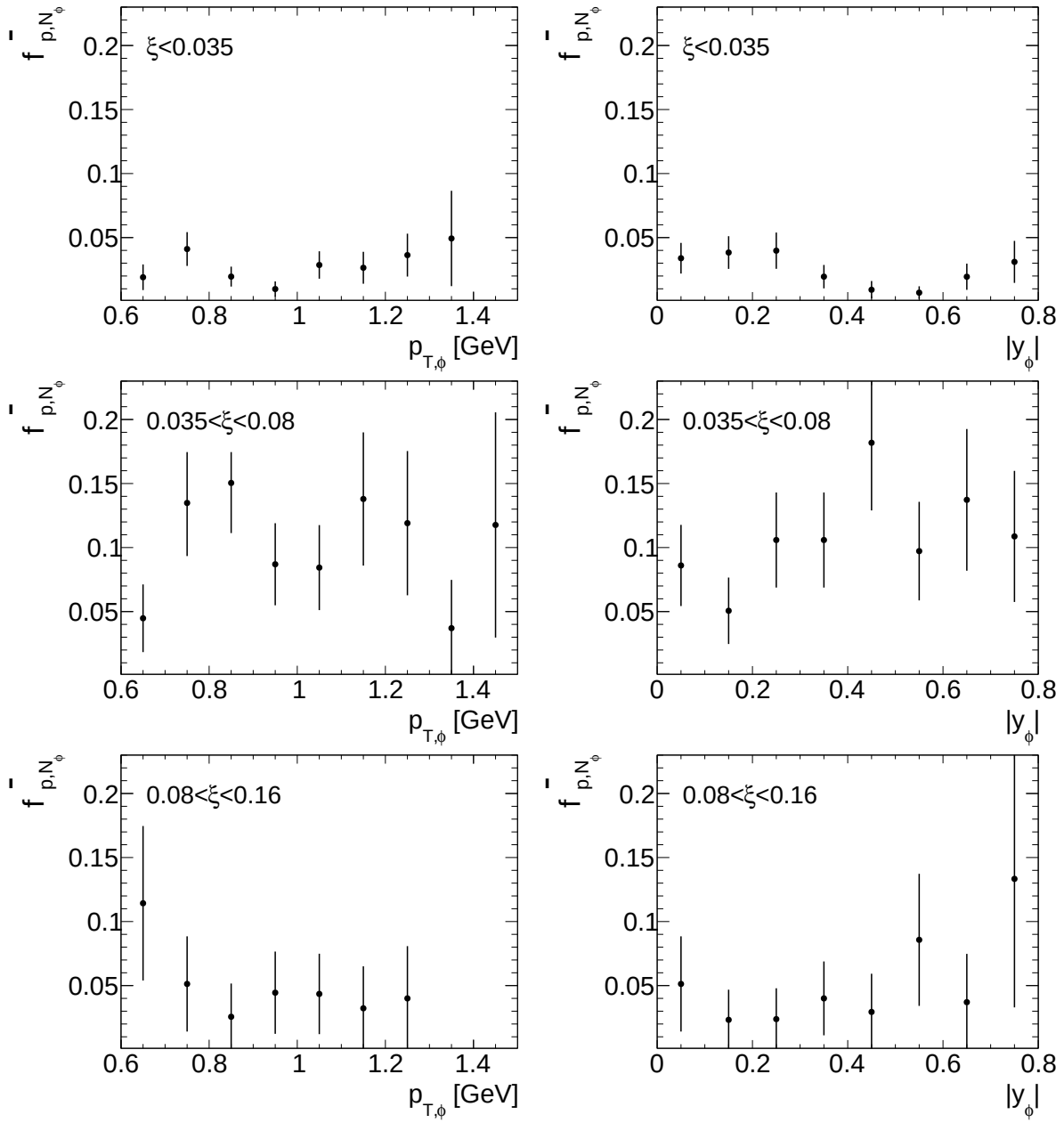

Figure 7.11: Migrations outside the fiducial region of the ξ and t measurement as a function of $p_{\mathrm{T},\phi}$ (left plots) and y_ϕ (right plots) for PYTHIA 8 SD in three ξ ranges.

Migrations outside the fiducial region related to N, $f^{-}_{p,N}$, were obtained for three ξ ranges and they are 12%, 9% and 4% for $\xi < 0.035$, $0.035 < \xi < 0.08$ and $0.08 < \xi < 0.16$, respectively. Migrations inside the fiducial region of the measurement, f^{+}_{p}, are calculated as the fraction of true ϕ mesons for which ξ and t are in the detector-level fiducial region but are not in the corresponding true-level fiducial region. The migrations related to the number of ϕ mesons, f^{+}_{p,N_ϕ}, are shown in Figure 7.12. The biggest ones are observed for $0.08 < \xi < 0.16$. Bigger migrations inside than outside the fiducial region of the measurement are observed.

The migrations inside the fiducial region related to N, $f^{+}_{p,N}$, were calculated in three ξ ranges separately and they are 10%, 21% and 23% for $\xi < 0.035$, $0.035 < \xi < 0.08$ and for $0.08 < \xi < 0.16$, respectively.

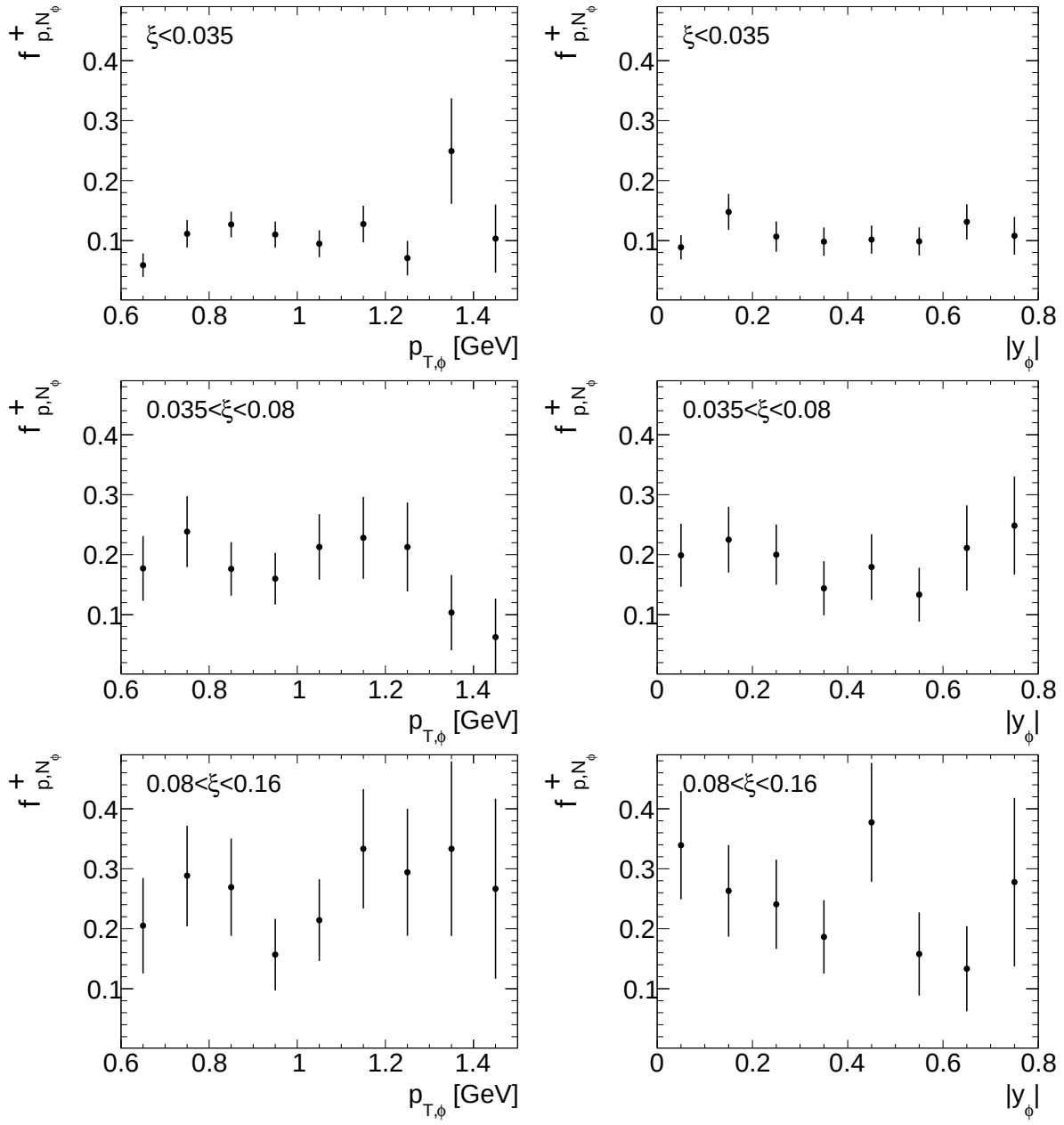

Figure 7.12: Migrations inside the fiducial region of the ξ and t measurement as a function of $p_{\mathrm{T},\phi}$ (left plots) and y_ϕ (right plots) for PYTHIA 8 SD in three ξ ranges.

Closure tests IV involve comparison between the number of events with a true ϕ meson for which ξ and t are in the true-level fiducial region with the number of the events with a true ϕ meson for which ξ and t are in the detector-level fiducial region. The detector-level distributions

are then corrected for the ξ and t migrations by re-weighting N_ϕ by:

$$f_{p,N_\phi} = (1 - f^+_{p,N_\phi})/(1 - f^-_{p,N_\phi}), \tag{7.5}$$

while N was corrected using the following weight:

$$f_{p,N} = (1 - f^+_{p,N})/(1 - f^-_{p,N}). \tag{7.6}$$

Plots on the left in Figures 7.13 and 7.14 show the true-level and detector-level distributions

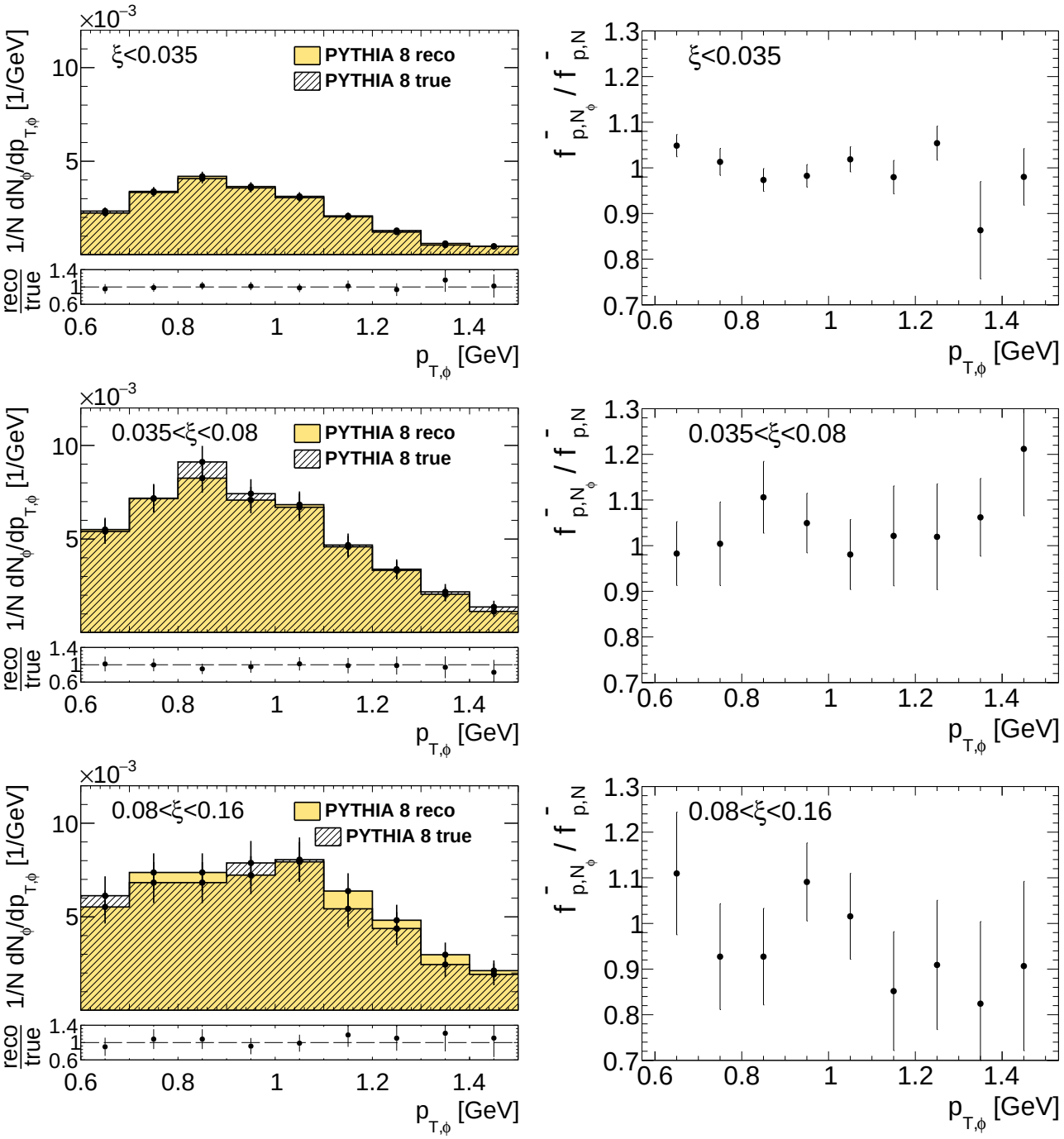

Figure 7.13: Closure tests IV for PYTHIA 8 SD shown as a function of $p_{\mathrm{T},\phi}$ in three ξ ranges. The striped transparent histograms represent distributions of ϕ mesons at the true level, the yellow histograms show the reconstructed level distributions without corrections (7.5), (7.6) (left plots). The corrections are shown in the plots on the right. All errors are statistical.

without applying the corrections for migrations (7.5) and (7.6). Migration correction which has to be applied to the detector-level distributions is presented in right plots. One can see a good agreement even between the true-level and the uncorrected detector-level distributions. The ratio of the corrected detector-level distributions to the true-level ones equals approximately one after applying the migration correction. This proves the hypothesis that ξ and t migrations cancel out in the ratio of N_ϕ/N. Hence, the correction is not applied to data.

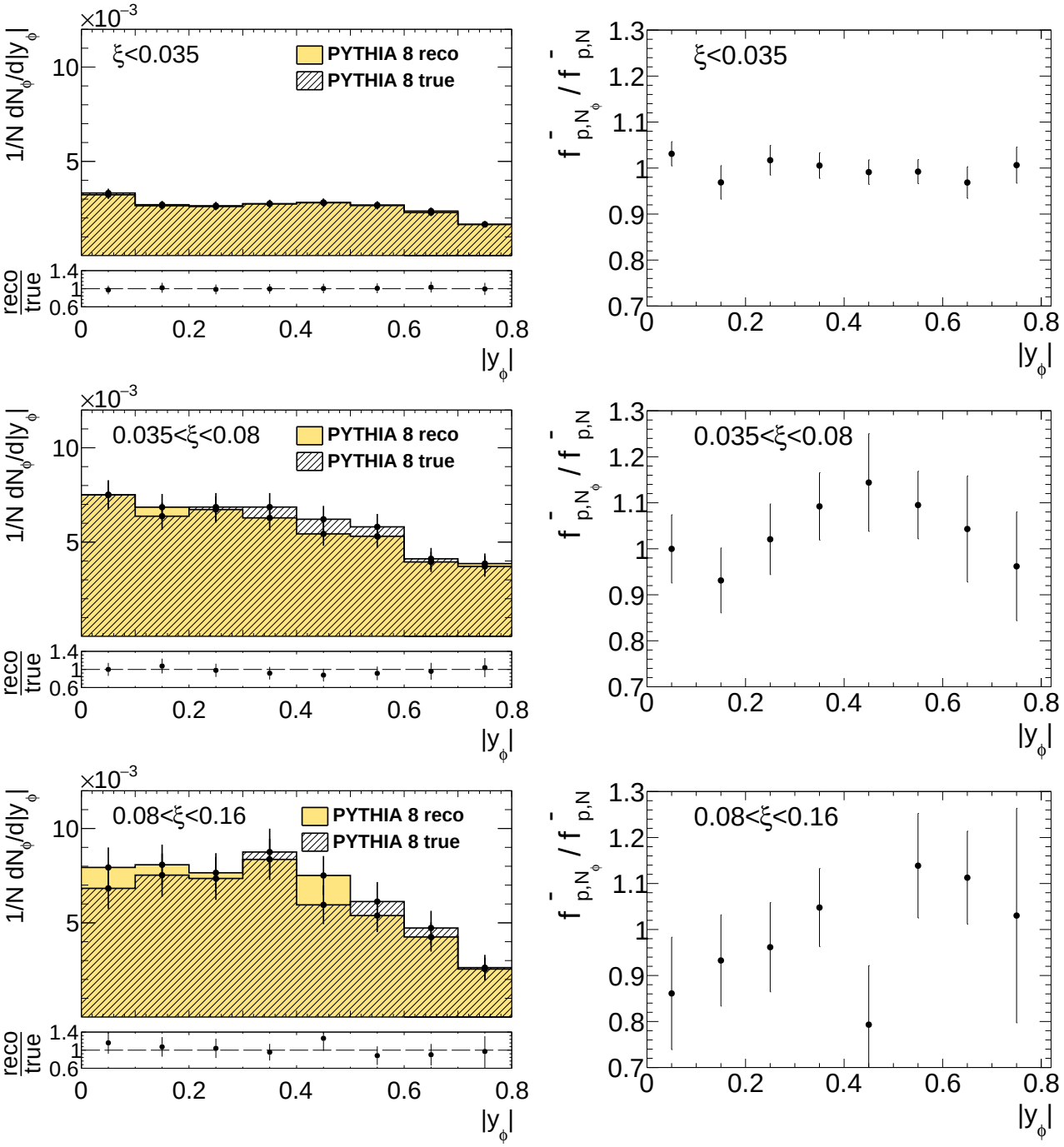

Figure 7.14: Closure tests IV for PYTHIA 8 SD shown as a function of $|y_\phi|$ in three ξ ranges. The striped transparent histograms represent distributions of ϕ mesons at the true level, the yellow histograms show the reconstructed level distributions without corrections for migrations (7.5), (7.6) (left plots). The correction are shown in the plots on the right. All errors are statistical.

7.4 Systematic Uncertainties

Corrections applied to all events, N, and to events involving ϕ meson candidates, N_ϕ, are mostly the same. Thus, systematic uncertainties related to them cancel out in $1/N\ \mathrm{d}N/\mathrm{d}p_{\mathrm{T},\phi}$ and $1/N\ \mathrm{d}N/\mathrm{d}|y_\phi|$ distributions. One of such systematic uncertainty in SD and CD analyses is related to the proton reconstruction efficiency in ALFA and was studied in Ref. [170]. Since cuts on protons in ALFA are applied to both N and N_ϕ, systematic uncertainties related to them cancel out. Three sources of systematic uncertainties that do not cancel out are also considered:

- the simulation-based track reconstruction efficiency correction,
- the simulation-based correction for the different modelling of charged-particle multiplicity in MC models: PYTHIA 8 and EPOS,
- the data-driven PID efficiency correction,
- the simulation-based MBTS correction.

The studies performed to calculate these uncertainties are presented in this Section.

7.4.1 Uncertainty on Track Reconstruction Efficiency

The systematic uncertainty on track reconstruction efficiency is associated with the imprecise modelling of the ID dead material and is calculated as a function of p_{T} and η, as the sum of the contributions of:

- 5% additional material in the entire ID,
- 10% additional material in the IBL,
- and 50% additional material located in the PD services region at $|\eta| > 1.5$.

The differences in the amount of the passive material in the real data and in the simulation [171] lead to the systematic uncertainty of 1% at low η and high p_{T} and up to 10% for higher η or lower p_{T} [162, 172].

Standard track reconstruction efficiency was varied within these uncertainties for each K^+ and K^- candidates and the modified $1/N\ \mathrm{d}N/\mathrm{d}p_{\mathrm{T},\phi}$ and $1/N\ \mathrm{d}N/\mathrm{d}|y_\phi|$ distributions were compared to the nominal ones. The final systematic uncertainty on tracking efficiency related to N_ϕ, but not to N, was estimated as the difference between the changed and the nominal results in each $p_{\mathrm{T},\phi}$ and $|y_\phi|$ bin. The outcomes are shown in Figure 7.15. The relative systematic uncertainty on ID tracking efficiency is at the level of $1 - 8\%$.

7.4.2 Uncertainty on Modelling of Charged-particle Multiplicity

The correction for the different modelling of charged-particle multiplicity in PYTHIA 8 and EPOS, was also taken into account in the systematic uncertainty analysis. The correction was obtained as the mean of PYTHIA 8 and EPOS predictions for SD, CD and MB analysis, separately. Figure 7.16 shows comparison between the correction predicted by PYTHIA 8 and EPOS in the SD analysis. The difference between the two expectations was taken as the systematic uncertainty which is at the level of 5%.

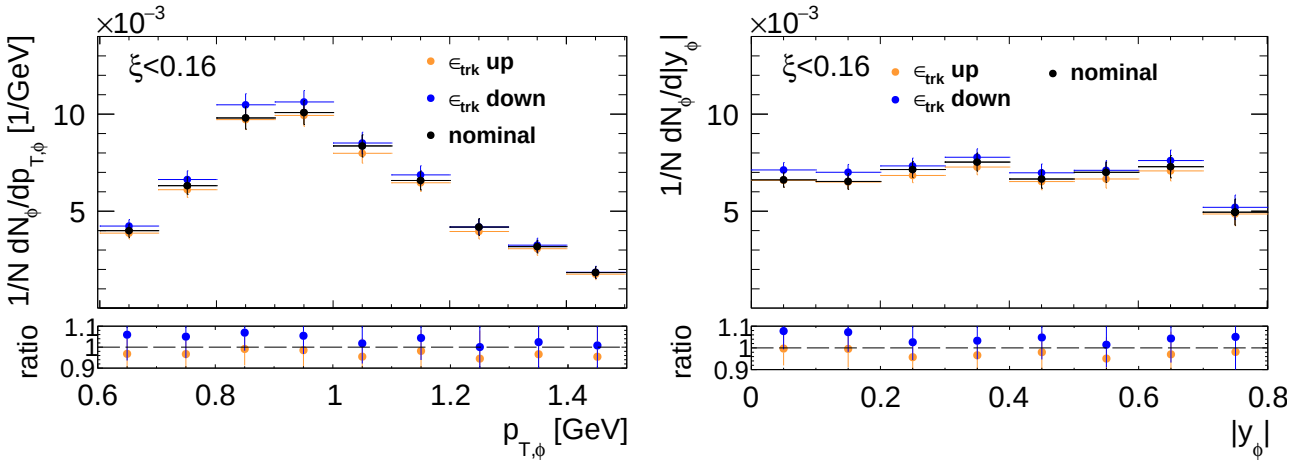

Figure 7.15: Systematic uncertainties on tracking efficiency as a function of $p_{\mathrm{T}}(\phi)$ (left) and $y(\phi)$ (right). Black dots represent the nominal distributions while the blue and the orange ones show modified results. Their ratios to the nominal distributions are shown in the bottom panels.

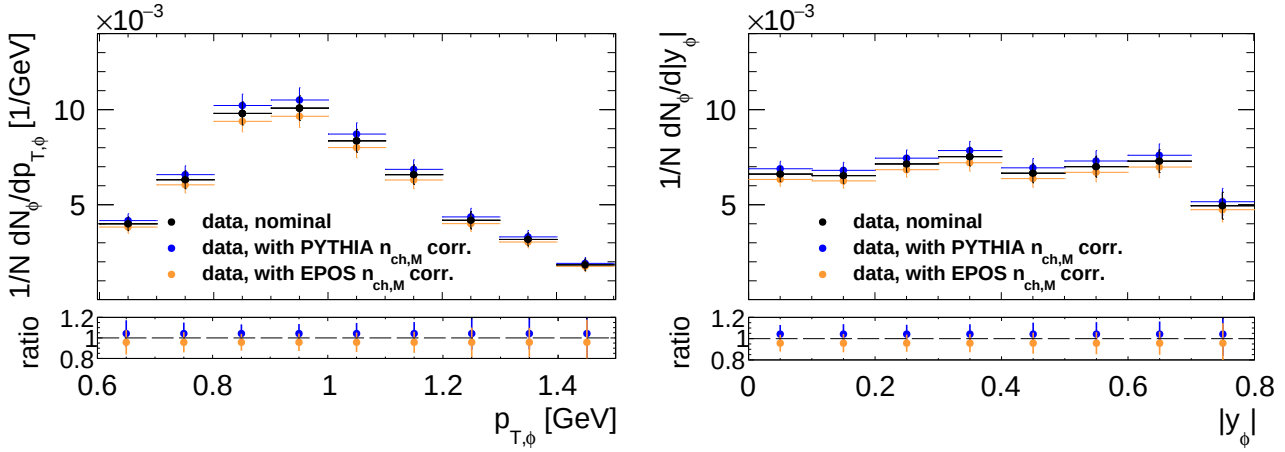

Figure 7.16: Systematic uncertainties on different modelling of charged-particle multiplicity in PYTHIA 8 and EPOS, as a function of $p_{\mathrm{T}}(\phi)$ (left) and $y(\phi)$ (right). Black dots represent the nominal distributions while the blue and the orange ones show modified results. Their ratios to the nominal distributions are shown in the bottom panels.

7.4.3 Uncertainty on Particle Identification Efficiency

Systematic uncertainty on kaon identification efficiency is related to the $\epsilon_{\mathrm{TP}}(p)$ parametrisation procedure for data, described in Section 6.3. This uncertainty was assessed by varying parameters P_0, P_1 and P_2 (see Equation (6.5)) within their statistical uncertainties obtained from the fit. Since the parametrisation is different for positively and negatively charged kaons, six checks were done for K^+ and six for K^-. Separate systematic uncertainties on parametrisation for K^+ and for K^- were estimated taking the biggest difference between the nominal and changed $1/N\ \mathrm{d}N/\mathrm{d}p_{\mathrm{T},\phi}$ and $1/N\ \mathrm{d}N/\mathrm{d}|y_\phi|$ distributions. The systematic uncertainties on K^+ and on K^- parametrisation are presented in Figures 7.17 and 7.18, respectively. The relative uncertainties are $4-16\%$ on K^+ parametrisation and $5-15\%$ on K^- parametrisation, depending on a p_{T} and y bin.

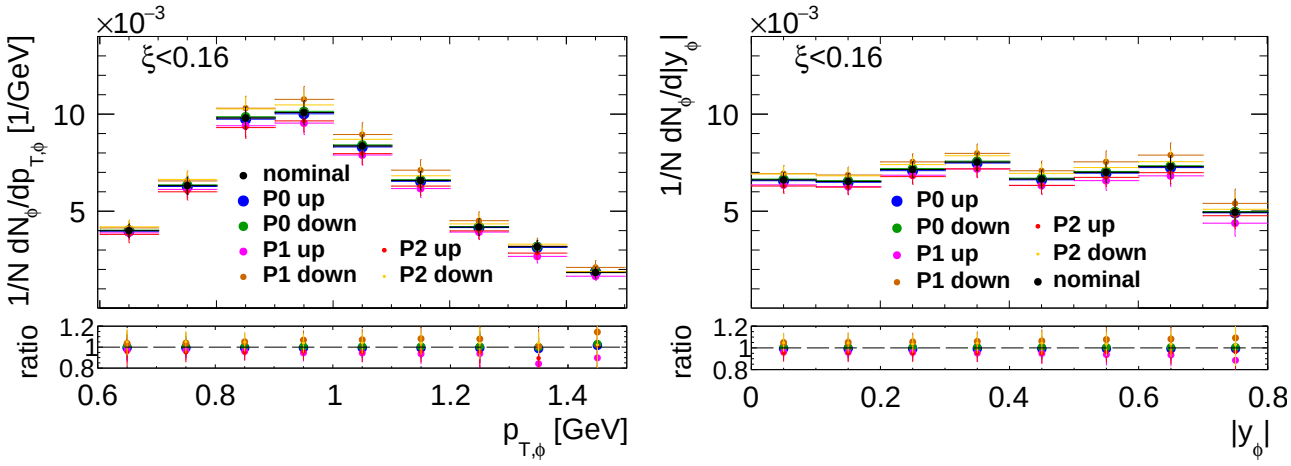

Figure 7.17: Systematic uncertainties on $\epsilon_{\mathrm{TP}}(p)$ parametrisation for K^+ as a function of $p_{\mathrm{T}}(\phi)$ (left) and $y(\phi)$ (right). Black dots represent the nominal distributions while the other colours show modified results. Ratios of the modified to the nominal distributions are shown in the bottom panels.

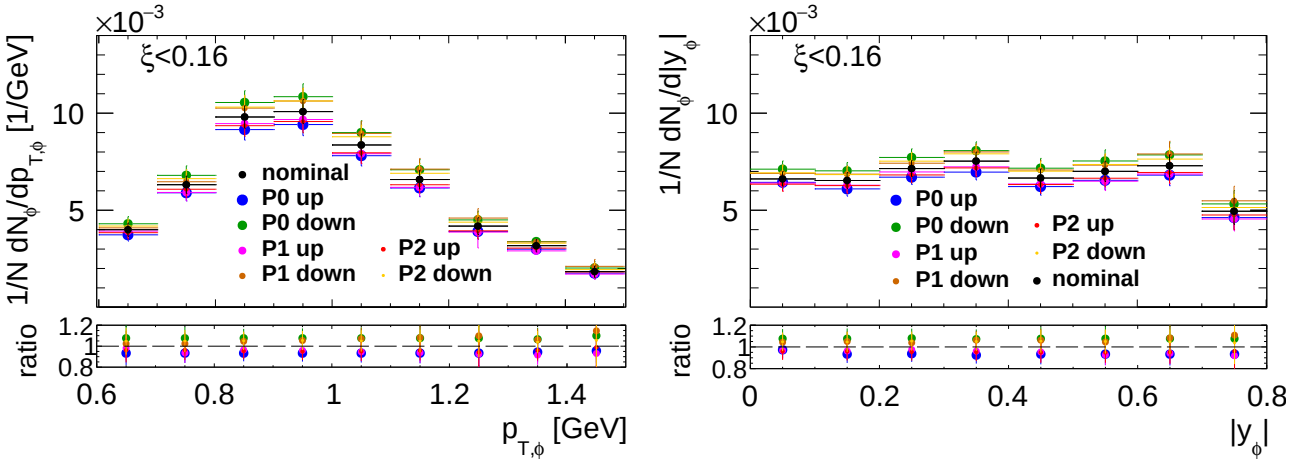

Figure 7.18: Systematic uncertainties on $\epsilon_{\mathrm{TP}}(p)$ parametrisation for K^- as a function of $p_{\mathrm{T}}(\phi)$ (left) and $y(\phi)$ (right). Black dots represent the nominal distributions while the other colours show modified results. Ratios of the modified to the nominal distributions are shown in the bottom panels.

7.4.4 Uncertainty on the MBTS Correction

The MBTS correction for SD data was introduced in Section 7.4.4. This correction comes from simulation and it was calculated as a difference between the nominal true-level $p_{\mathrm{T},\phi}$ and $|y_\phi|$ spectra and the spectra obtained with the MBTS requirements, described in Section 4.1. The final correction is determined as the mean of PYTHIA 8 and EPOS while the systematic uncertainty on the effect is assessed as the difference between the mean and the specific prediction. Figure 7.19 shows $p_{\mathrm{T},\phi}$ and $|y_\phi|$ spectra corrected for the MBTS correction inefficiency with the corresponding systematic uncertainty which was calculated for each $p_{\mathrm{T},\phi}$ and y_ϕ bin. The uncertainty is at the level of $7-10\%$.

Comparison of contributions from tracking efficiency, particle identification efficiency and MBTS correction to systematic uncertainties is shown in Figure 7.20. The largest systematic uncertainty is mainly connected with the MBTS correction.

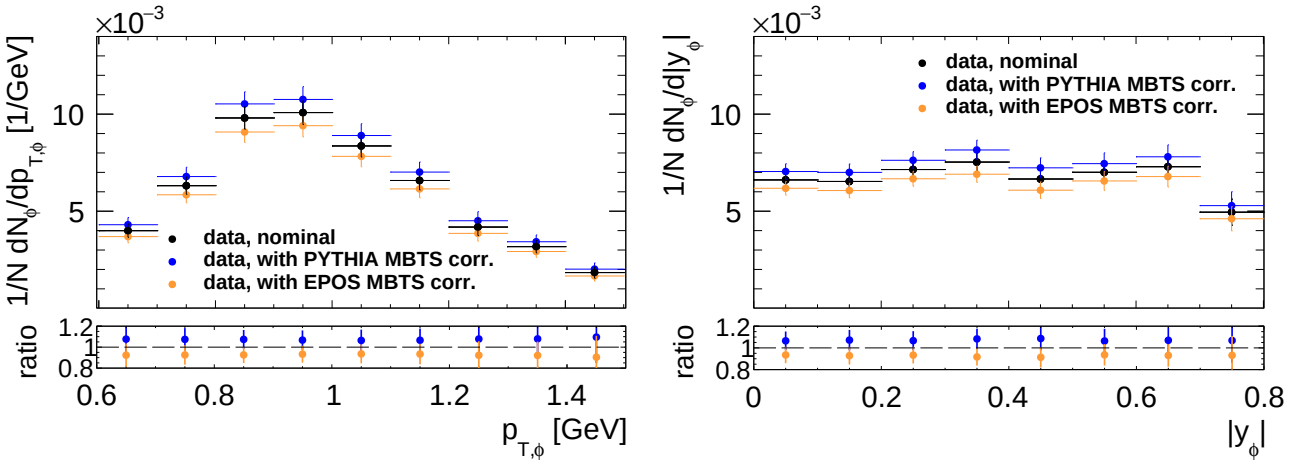

Figure 7.19: Systematic uncertainties on the MBTS correction as a function of $p_{\mathrm{T}}(\phi)$ (left) and $y(\phi)$ (right). Black dots represent the nominal distributions while the blue and orange dots indicate the corrected results based on the PYTHIA 8 and EPOS predictions, respectively. Bottom panels show ratios of the distributions corrected according to the PYTHIA 8/EPOS predictions to the distributions corrected using the mean of these expectations.

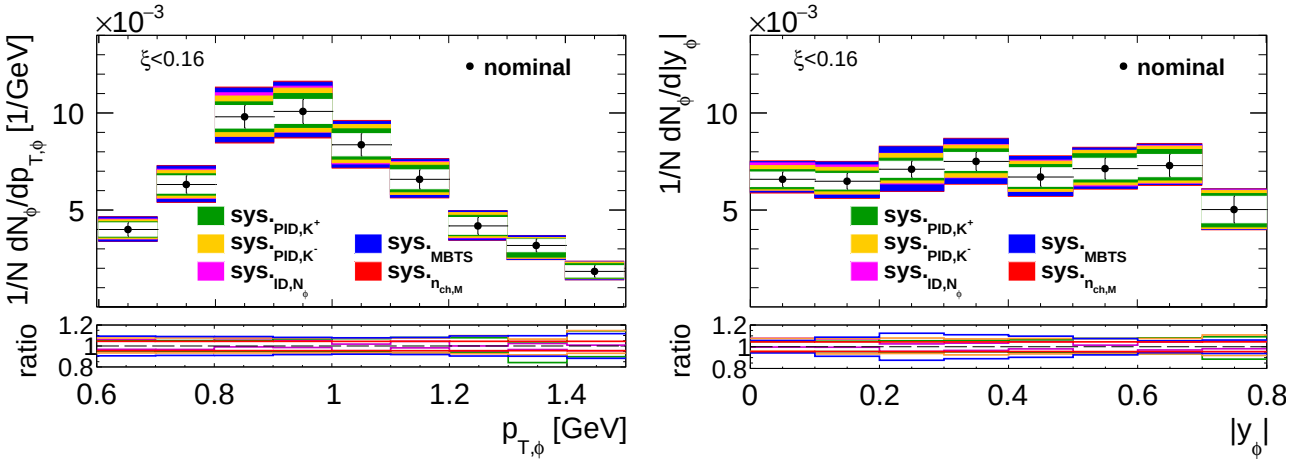

Figure 7.20: Contributions from tracking efficiency, particle identification efficiency and MBTS correction to systematic uncertainties as a function of $p_{\mathrm{T}}(\phi)$ (left) and $y(\phi)$ (right). Ratios of the modified to the nominal distributions are shown in the bottom panels.

CHAPTER 8
Results and Discussion

The $\phi(1020)$ meson production in pp collisions at $\sqrt{s} = 13$ TeV was measured using $\phi \to K^+K^-$ decay channel in Single Diffraction, Central Diffraction and Minimum Bias data.

The ϕ meson transverse momentum spectra at midrapidity $|y_\phi| < 0.8$ in the range $0.6 < p_{\mathrm{T},\phi} < 1.5$ GeV and the ϕ rapidity spectra integrated over $0.6 < p_{\mathrm{T},\phi} < 1.5$ GeV in the range $|y_\phi| < 0.8$ were extracted from data and compared to model predictions of PYTHIA 8 and EPOS. The fiducial region is also restricted to $p_K < 0.9$ GeV and $p_{\mathrm{T},K} > 0.29$ GeV due to track reconstruction and particle identification efficiency constraints. The fiducial region of the kaon kinematics restricts kaon rapidity coverage which is thinner than the geometrical acceptance of the ID and therefore it is not stated here explicitly.

The ϕ meson yield was extracted from the K^+K^- invariant mass distributions in nine $p_{\mathrm{T},\phi}$ bins of the width of 0.1 GeV and in eight $|y_\phi|$ bins of the width of 0.1. The $p_{\mathrm{T},\phi}$ and $|y_\phi|$ spectra were constructed from the measured yields. The invariant mass distributions were corrected for vertex reconstruction efficiency (6.1), track reconstruction efficiency (6.2), particle identification efficiency (6.6) and the bias in the momentum reconstruction (see Section 3.1). The signal yield extraction was performed by fitting the corrected invariant mass distributions with a function which describes the signal and background contributions, while the former is determined by a convolution of the non-relativistic Breit-Wigner function with the Gaussian distribution (5.5) and the latter is described by Eq. (5.7). The global fit without dividing the $p_{\mathrm{T},\phi}$ and $|y_\phi|$ ranges into bins was performed at first. In order to reduce the number of free parameters in the fits, the σ_{exp} in Eq. (5.5) was set to 2 MeV according to the global fit results. An example fit in the $1.0 < p_{\mathrm{T},\phi} < 1.1$ GeV range for SD data is shown in Figure 8.1.

The number of ϕ mesons, N_ϕ, extracted from the fits was scaled by the number of all events selected in the given process: SD, CD and MB, N, applying the corrections for vertex reconstruction efficiency, track reconstruction efficiency, MBTS efficiency and accidental background. Effectively N was corrected for the number of events with at least two charged particles with $p_{\mathrm{T}} > 0.2$ GeV and $|\eta| < 2.5$.

8.1 Single Diffraction Measurements

The $p_{\mathrm{T},\phi}$ spectrum at midrapidity $|y_\phi| < 0.8$ and the rapidity spectrum integrated over $0.6 < p_{\mathrm{T},\phi} < 1.5$ GeV were measured using SD triggered data and compared to PYTHIA 8 and EPOS expectations. Figure 8.2 shows the spectra for data and for inelastic MC samples containing SD, CD, DD and ND components. The statistical and systematic uncertainties were evaluated per each $p_{\mathrm{T},\phi}$ and $|y_\phi|$ bin. They are added in quadrature and shown as boxes in the figures.

The signal yields for data were extracted from the fits to the corrected invariant mass distributions of oppositely charged kaon candidates. The fits are presented in Appendix B.1,

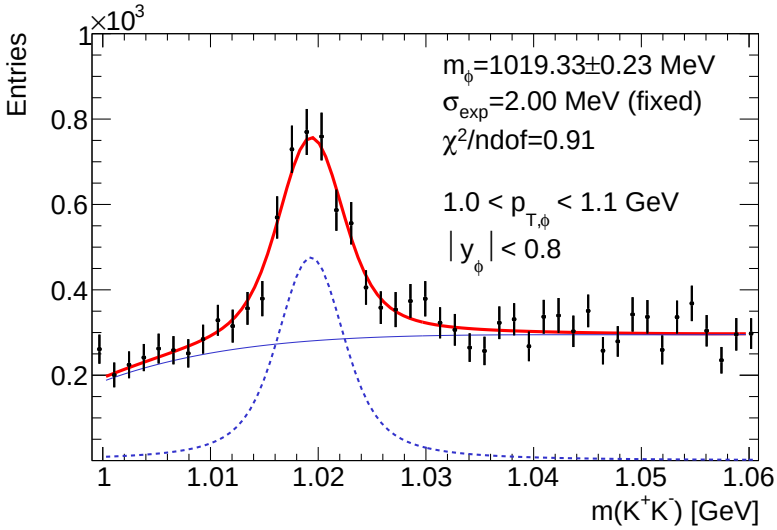

Figure 8.1: An example fit to the K^+K^- invariant mass distribution in the $1.0 < p_{\mathrm{T},\phi} < 1.1$ GeV range for SD data. Red curve represents a convolution of the non-relativistic Breit-Wigner function with the Gaussian distribution as the signal function (5.5) plus a background fitting function described by Eq. (5.7). Blue solid line represents the background shape and dashed blue curve is the signal contribution. The fit parameters are shown in the plot.

in Figure B.1.2 for $p_{\mathrm{T},\phi}$ bins and in Figure B.1.1 for y_ϕ ranges. The resulting χ^2/ndof values range from 0.85 to 2.05 which demonstrates good quality of the fits. The $1/N\ \mathrm{d}N_\phi/\mathrm{d}p_{\mathrm{T},\phi}$ and $1/N\ \mathrm{d}N_\phi/\mathrm{d}|y_\phi|$ yields including the corresponding statistical and systematic uncertainties are listed in Tables 8.1 and 8.2, respectively.

The number of measured $\phi \to K^+K^-$ decays increases as a function of $p_{\mathrm{T},\phi}$ in the range $0.6 < p_{\mathrm{T},\phi} < 0.95$ GeV. The increase is caused by the $p_{\mathrm{T},K} > 0.29$ GeV requirement for efficient ID track reconstruction. $p_{\mathrm{T},\phi}$ spectrum integrated over $|y_\phi| < 0.8$ reaches a maximum at $p_{\mathrm{T},\phi} \sim 0.95$ GeV and decreases for $p_{\mathrm{T},\phi} \gtrsim 0.95$ GeV.

The $|y_\phi|$ spectrum is flat within the uncertainties in the range $|y_\phi| < 0.7$ and decreases in the last rapidity bin due to the cut on $p_K < 0.9$ GeV that limits the number of kaons in this rapidity region but provides high PID efficiency.

The transverse momentum and rapidity spectra are compared to PYTHIA 8 and EPOS predictions. Both generators show similar yields. The predicted $|y_\phi|$ spectrum and $p_{\mathrm{T},\phi}$ spectrum for $p_{\mathrm{T},\phi} > 0.8$ GeV are on average a factor two below the data. The differences between the models and data are smaller at $p_{\mathrm{T},\phi} < 0.8$ GeV.

The forward proton's ξ range was divided into three regions in this analysis: $10^{-5} < \xi < 0.035$, $0.035 < \xi < 0.08$, and $0.08 < \xi < 0.16$. Therefore, the $p_{\mathrm{T},\phi}$ and $|y_\phi|$ spectra were also measured independently in each ξ range and compared to model predictions. Figure 8.3 shows the ϕ spectra in three ξ ranges for data and PYTHIA 8 and EPOS inelastic samples.

Fits of the invariant mass of K^+K^- pairs that were used to extract signal yields are shown in Appendix B.1, in Figures B.1.6, B.1.7 and B.1.8 for $p_{\mathrm{T},\phi}$ bins and in Figures B.1.3, B.1.4 and B.1.5 for y_ϕ ranges, for $10^{-5} < \xi < 0.035$, $0.035 < \xi < 0.08$, and $0.08 < \xi < 0.16$, respectively. Quality of the fits is good that is confirmed by χ^2/ndof values that are mostly lower than 2.

The highest ϕ production rate is measured for $0.08 < \xi < 0.16$ and the lowest one for $10^{-5} < \xi < 0.035$. PYTHIA 8 and EPOS samples that include all inelastic processes predict similar ϕ production rate for $\xi < 0.035$. The spectra are there about a factor of two too small. PYTHIA 8 describes data better than EPOS for $0.035 < \xi < 0.08$ and $0.08 < \xi < 0.16$. The best agreement between PYTHIA 8 and data is observed for $0.08 < \xi < 0.16$.

Table 8.1: The $1/N\ \mathrm{d}N_\phi/\mathrm{d}p_{\mathrm{T},\phi}$ yields at midrapidity $|y_\phi| < 0.8$ in the range $0.6 < p_{\mathrm{T},\phi} < 1.5$ GeV for the SD analysis. Statistical and systematic uncertainties are listed in the table.

Bin [GeV]	$\mathbf{1/N\ dN_\phi/dp_{T,\phi}}$ $\mathbf{[GeV^{-1}]}$	$\mathbf{sys._{ID,N_\phi}}$ $\mathbf{[GeV^{-1}]}$	$\mathbf{sys._{PID,K-}}$ $\mathbf{[GeV^{-1}]}$	$\mathbf{sys._{PID,K+}}$ $\mathbf{[GeV^{-1}]}$	$\mathbf{sys._{MBTS}}$ $\mathbf{[GeV^{-1}]}$
$0.6 < p_{\mathrm{T},\phi} \leq 0.7$	$(3.97 \pm 0.35)\cdot10^{-3}$	$^{+0.22\cdot10^{-3}}_{-0.12\cdot10^{-3}}$	$^{+0.28\cdot10^{-3}}_{-0.25\cdot10^{-3}}$	$^{+0.18\cdot10^{-3}}_{-0.18\cdot10^{-3}}$	$\pm\ 0.35\cdot10^{-3}$
$0.7 < p_{\mathrm{T},\phi} \leq 0.8$	$(6.34 \pm 0.45)\cdot10^{-3}$	$^{+0.30\cdot10^{-3}}_{-0.20\cdot10^{-3}}$	$^{+0.45\cdot10^{-3}}_{-0.39\cdot10^{-3}}$	$^{+0.30\cdot10^{-3}}_{-0.30\cdot10^{-3}}$	$\pm\ 0.53\cdot10^{-3}$
$0.8 < p_{\mathrm{T},\phi} \leq 0.9$	$(9.80 \pm 0.58)\cdot10^{-3}$	$^{+0.63\cdot10^{-3}}_{-0.08\cdot10^{-3}}$	$^{+0.69\cdot10^{-3}}_{-0.60\cdot10^{-3}}$	$^{+0.46\cdot10^{-3}}_{-0.46\cdot10^{-3}}$	$\pm\ 0.81\cdot10^{-3}$
$0.9 < p_{\mathrm{T},\phi} \leq 1.0$	$(10.10 \pm 0.62)\cdot10^{-3}$	$^{+0.50\cdot10^{-3}}_{-0.14\cdot10^{-3}}$	$^{+0.71\cdot10^{-3}}_{-0.61\cdot10^{-3}}$	$^{+0.63\cdot10^{-3}}_{-0.50\cdot10^{-3}}$	$\pm\ 0.76\cdot10^{-3}$
$1.0 < p_{\mathrm{T},\phi} \leq 1.1$	$(8.36 \pm 0.58)\cdot10^{-3}$	$^{+0.14\cdot10^{-3}}_{-0.35\cdot10^{-3}}$	$^{+0.59\cdot10^{-3}}_{-0.51\cdot10^{-3}}$	$^{+0.54\cdot10^{-3}}_{-0.43\cdot10^{-3}}$	$\pm\ 0.60\cdot10^{-3}$
$1.1 < p_{\mathrm{T},\phi} \leq 1.2$	$(6.58 \pm 0.49)\cdot10^{-3}$	$^{+0.27\cdot10^{-3}}_{-0.11\cdot10^{-3}}$	$^{+0.49\cdot10^{-3}}_{-0.40\cdot10^{-3}}$	$^{+0.49\cdot10^{-3}}_{-0.38\cdot10^{-3}}$	$\pm\ 0.49\cdot10^{-3}$
$1.2 < p_{\mathrm{T},\phi} \leq 1.3$	$(4.18 \pm 0.44)\cdot10^{-3}$	$^{+0.01\cdot10^{-3}}_{-0.21\cdot10^{-3}}$	$^{+0.38\cdot10^{-3}}_{-0.28\cdot10^{-3}}$	$^{+0.30\cdot10^{-3}}_{-0.24\cdot10^{-3}}$	$\pm\ 0.37\cdot10^{-3}$
$1.3 < p_{\mathrm{T},\phi} \leq 1.4$	$(3.18 \pm 0.33)\cdot10^{-3}$	$^{+0.07\cdot10^{-3}}_{-0.10\cdot10^{-3}}$	$^{+0.19\cdot10^{-3}}_{-0.25\cdot10^{-3}}$	$^{+0.12\cdot10^{-3}}_{-0.46\cdot10^{-3}}$	$\pm\ 0.29\cdot10^{-3}$
$1.4 < p_{\mathrm{T},\phi} \leq 1.5$	$(1.83 \pm 0.30)\cdot10^{-3}$	$^{+0.02\cdot10^{-3}}_{-0.08\cdot10^{-3}}$	$^{+0.25\cdot10^{-3}}_{-0.12\cdot10^{-3}}$	$^{+0.25\cdot10^{-3}}_{-0.18\cdot10^{-3}}$	$\pm\ 0.20\cdot10^{-3}$

Table 8.2: The $1/N\ \mathrm{d}N_\phi/\mathrm{d}|y_\phi|$ yields integrated over $0.6 < p_{\mathrm{T},\phi} < 1.5$ GeV in the range $|y_\phi| < 0.8$ for the SD analysis. Statistical and systematic uncertainties are listed in the table.

Bin	$\mathbf{1/N\ dN_\phi/d|y_\phi|}$	$\mathbf{sys._{ID,N_\phi}}$	$\mathbf{sys._{PID,K-}}$	$\mathbf{sys._{PID,K+}}$	$\mathbf{sys._{MBTS}}$
$0.0 < |y_\phi| \leq 0.1$	$(6.61 \pm 0.38)\cdot10^{-3}$	$^{+0.47\cdot10^{-3}}_{-0.02\cdot10^{-3}}$	$^{+0.46\cdot10^{-3}}_{-0.25\cdot10^{-3}}$	$^{+0.30\cdot10^{-3}}_{-0.29\cdot10^{-3}}$	$\pm\ 0.49\cdot10^{-3}$
$0.1 < |y_\phi| \leq 0.2$	$(6.54 \pm 0.41)\cdot10^{-3}$	$^{+0.44\cdot10^{-3}}_{-0.03\cdot10^{-3}}$	$^{+0.46\cdot10^{-3}}_{-0.40\cdot10^{-3}}$	$^{+0.31\cdot10^{-3}}_{-0.27\cdot10^{-3}}$	$\pm\ 0.53\cdot10^{-3}$
$0.2 < |y_\phi| \leq 0.3$	$(7.17 \pm 0.42)\cdot10^{-3}$	$^{+0.17\cdot10^{-3}}_{-0.28\cdot10^{-3}}$	$^{+0.53\cdot10^{-3}}_{-0.41\cdot10^{-3}}$	$^{+0.36\cdot10^{-3}}_{-0.34\cdot10^{-3}}$	$\pm\ 0.54\cdot10^{-3}$
$0.3 < |y_\phi| \leq 0.4$	$(7.52 \pm 0.47)\cdot10^{-3}$	$^{+0.23\cdot10^{-3}}_{-0.24\cdot10^{-3}}$	$^{+0.50\cdot10^{-3}}_{-0.52\cdot10^{-3}}$	$^{+0.41\cdot10^{-3}}_{-0.33\cdot10^{-3}}$	$\pm\ 0.70\cdot10^{-3}$
$0.4 < |y_\phi| \leq 0.5$	$(6.66 \pm 0.48)\cdot10^{-3}$	$^{+0.30\cdot10^{-3}}_{-0.13\cdot10^{-3}}$	$^{+0.47\cdot10^{-3}}_{-0.41\cdot10^{-3}}$	$^{+0.40\cdot10^{-3}}_{-0.32\cdot10^{-3}}$	$\pm\ 0.65\cdot10^{-3}$
$0.5 < |y_\phi| \leq 0.6$	$(6.99 \pm 0.53)\cdot10^{-3}$	$^{+0.10\cdot10^{-3}}_{-0.32\cdot10^{-3}}$	$^{+0.50\cdot10^{-3}}_{-0.47\cdot10^{-3}}$	$^{+0.50\cdot10^{-3}}_{-0.40\cdot10^{-3}}$	$\pm\ 0.50\cdot10^{-3}$
$0.6 < |y_\phi| \leq 0.7$	$(7.30 \pm 0.58)\cdot10^{-3}$	$^{+0.29\cdot10^{-3}}_{-0.20\cdot10^{-3}}$	$^{+0.55\cdot10^{-3}}_{-0.44\cdot10^{-3}}$	$^{+0.55\cdot10^{-3}}_{-0.43\cdot10^{-3}}$	$\pm\ 0.57\cdot10^{-3}$
$0.7 < |y_\phi| \leq 0.8$	$(4.95 \pm 0.68)\cdot10^{-3}$	$^{+0.24\cdot10^{-3}}_{-0.09\cdot10^{-3}}$	$^{+0.50\cdot10^{-3}}_{-0.18\cdot10^{-3}}$	$^{+0.42\cdot10^{-3}}_{-0.52\cdot10^{-3}}$	$\pm\ 0.38\cdot10^{-3}$

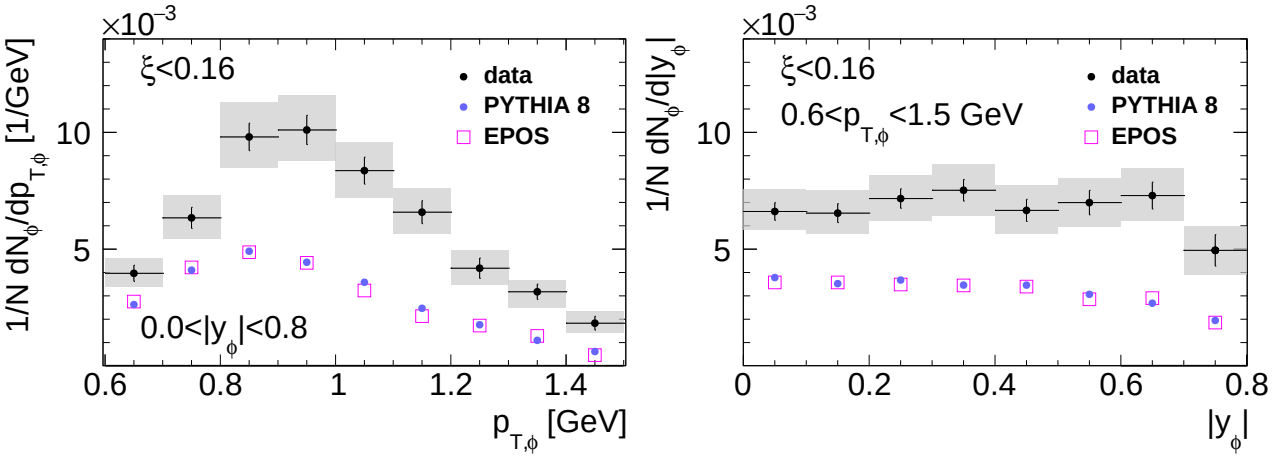

Figure 8.2: Comparison between SD data and two MC models - PYTHIA 8 and EPOS. Data and MC predictions are shown in the full $\xi < 0.16$ range. (left) $p_{\mathrm{T},\phi}$ spectrum integrated over $|y_\phi| < 0.8$, and (right) $|y_\phi|$ spectrum integrated over $0.6 < p_{\mathrm{T},\phi} < 1.5$ GeV.

8.1.1 Subtraction of contributions from CD, DD and ND Processes

SD triggered data includes contributions from CD, DD and ND processes that should be subtracted in order to compare the measurement with pure SD predictions. The expected amount of CD, DD and ND in SD triggered sample was calculated based on PYTHIA 8 and EPOS simulations as:

$$C_i = \frac{N_i}{N_{\mathrm{T}}}, \tag{8.1}$$

where $i = \mathrm{SD}, \mathrm{CD}, \mathrm{DD}, \mathrm{ND}$ indicates the given subprocess, N_i represents the number of events in the i-th sample that satisfy all SD selection cuts at the detector-level and $N_{\mathrm{T}} = N_{\mathrm{SD}} + N_{\mathrm{CD}} + N_{\mathrm{DD}} + N_{\mathrm{ND}}$. Figure 8.5 presents the CD, DD and ND contributions predicted by PYTHIA 8 and EPOS.

One can see that the ND process does not constitute a significant background to the SD sample. It is also observed that the amounts of ND and DD contributions increase with increasing ξ and both DD and ND contributions predicted by EPOS are larger than those predicted by PYTHIA 8. The ND subtraction, even with the large normalisation uncertainty, does not change the results and does not contribute to the systematic uncertainty. The DD contribution is much larger (up to 10%). However, the N_ϕ/N prediction for DD process is very similar to the measured N_ϕ/N and its subtraction also does not change the results and does not contribute to the systematic uncertainty. Only the subtraction of CD contribution influences the measurement in the case of the SD sample.

There are significant differences between CD contributions predicted by PYTHIA 8 and EPOS. EPOS shows generally bigger values than PYTHIA 8. PYTHIA 8 predicts $C_{\mathrm{CD}} \approx 0.12$ while the values for EPOS are around $0.3 - 0.5$ depending on the ξ range. Normalisations of the CD sample predicted by PYTHIA 8 CD and EPOS CD were compared to the normalisation measured using CD triggered data. PYTHIA 8 shows around 1.8 times smaller and EPOS around 2.6 times greater normalisation than data. These differences (1/1.8 for PYTHIA CD and 2.6 for EPOS CD) describe differences in the normalisations in the PYTHIA/EPOS SD samples. Furthermore, it is observed that the ϕ production rate for CD data is reproduced by EPOS CD reasonably well (see Figure 8.9) whereas the results presented by PYTHIA 8 CD are around twice lower compared to data. We assume that the relations between data and MC CD concerning the ϕ production rate are also the same in the case of SD samples. Thus, proper corrections that are applied to SD data to subtract the CD contribution are based on

the comparison between CD data and CD MC. Normalisation predicted by EPOS is scaled by 0.38, normalisation predicted by PYTHIA 8 is scaled by 1.8 and N_ϕ/N for PYTHIA 8 is scaled by 2. The DD and ND contributions to SD triggered data were subtracted based on pure MC predictions, while CD subtraction is partially data-driven and only the shape of ξ is taken from MC models. The identical procedure was applied in three ξ ranges taking into account the same scale factors for PYTHIA 8 and EPOS as for $\xi < 0.16$.

The CD, DD and ND contributions which are subtracted from SD data are defined as a mean of PYTHIA 8 and EPOS while the difference between the specific prediction and the mean is used to estimate the systematic uncertainty on the subtraction. Figure 8.4 shows comparison

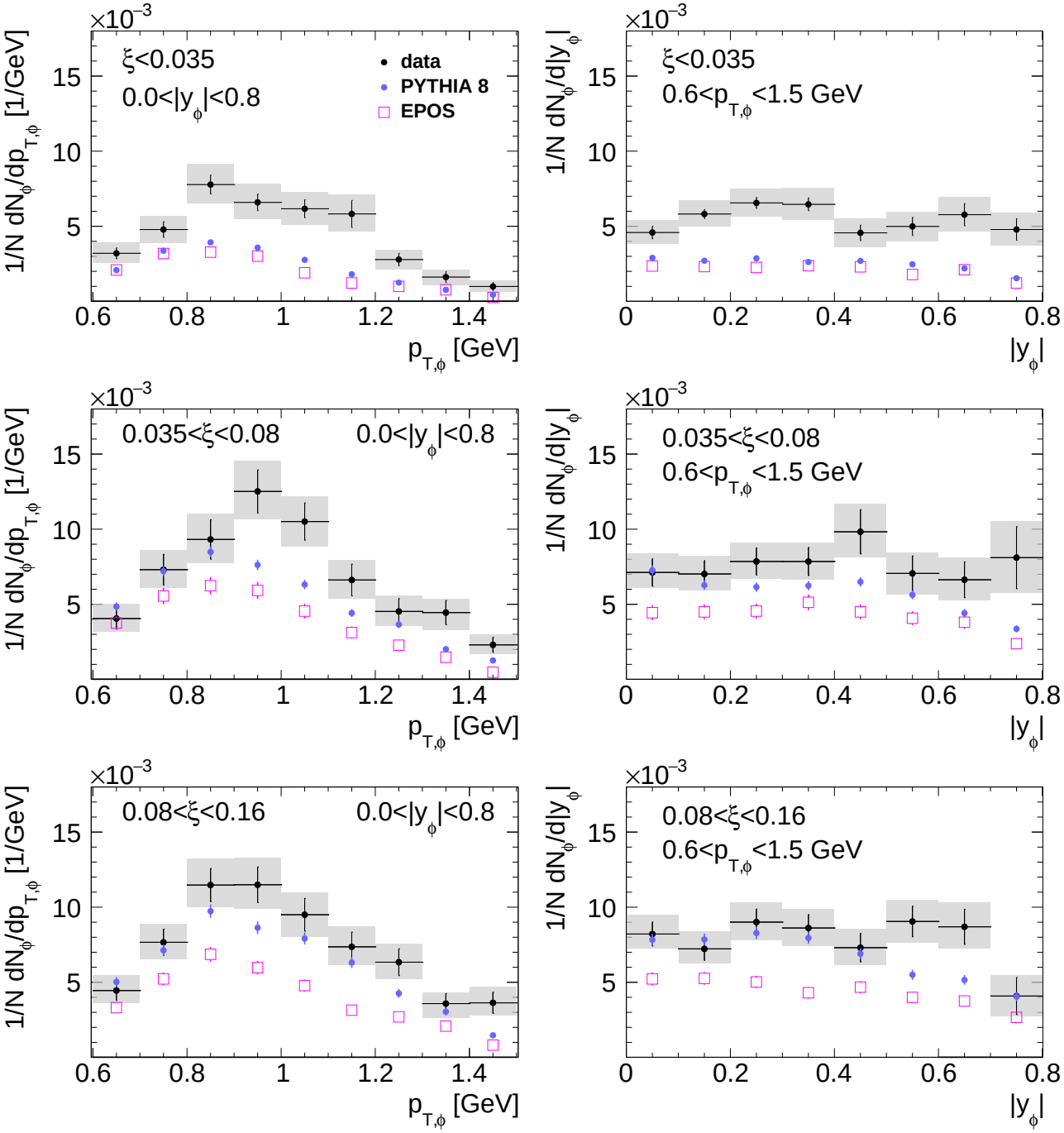

Figure 8.3: Comparison between SD data and two MC models - PYTHIA 8 and EPOS. Data and MC predictions are shown in three ξ ranges, separately. (left) $p_{\mathrm{T},\phi}$ spectra integrated over $|y_\phi| < 0.8$, and (right) $|y_\phi|$ spectra integrated over $0.6 < p_{\mathrm{T},\phi} < 1.5$ GeV.

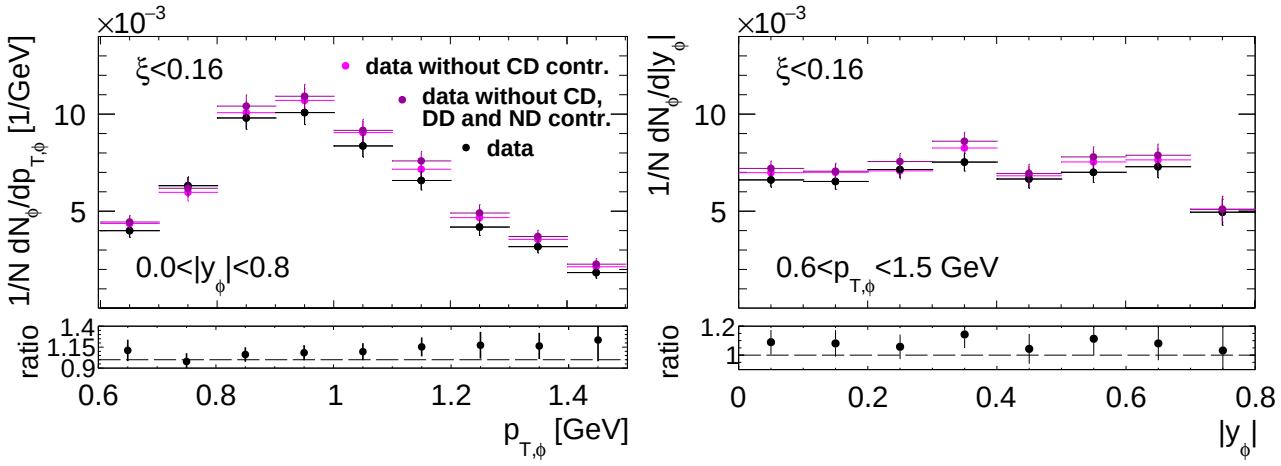

Figure 8.4: Comparison of SD triggered data before and after subtraction of CD, DD and ND contributions. (left) $p_{\mathrm{T},\phi}$ spectrum integrated over $|y_\phi| < 0.8$. (right) $|y_\phi|$ spectrum integrated over $0.6 < p_{\mathrm{T},\phi} < 1.5$ GeV. Data are shown in the full $\xi < 0.16$ range. Ratios of the distributions after CD, DD and ND subtraction to the nominal distributions are shown in the bottom panels.

between SD triggered data before and after the subtraction of CD, ND and DD contribution. The subtraction changes the nominal $p_{\mathrm{T},\phi}$ spectrum by approximately 10-15%, depending on the $p_{\mathrm{T},\phi}$ bin. The difference is larger at the right edge of the distribution but is not greater than 25 %. The CD, DD and ND subtraction changes the $|y_\phi|$ spectrum by around 10%. Since the CD contribution influences the SD measurement the most and there is lower ϕ production rate in CD than in SD, there is mainly higher ϕ production rate after the CD, DD and ND contribution subtraction. Consequently, the CD contribution decreases N_ϕ/N values in the SD sample. The DD and ND contribution practically does not influence the measured $p_{\mathrm{T},\phi}$ and $|y_\phi|$ spectra and their subtraction does not increase systematic uncertainties.

The $p_{\mathrm{T},\phi}$ and $|y_\phi|$ spectra after CD, DD and ND subtraction are shown in Figure 8.6 in the full ξ range and they are compared with predictions of PYTHIA 8 SD, EPOS SD' and EPOS SD'+SD, while the differences between EPOS SD and SD' samples are described in Section 1.5. PYTHIA 8 SD predictions do not agree with data and there are similar differences between

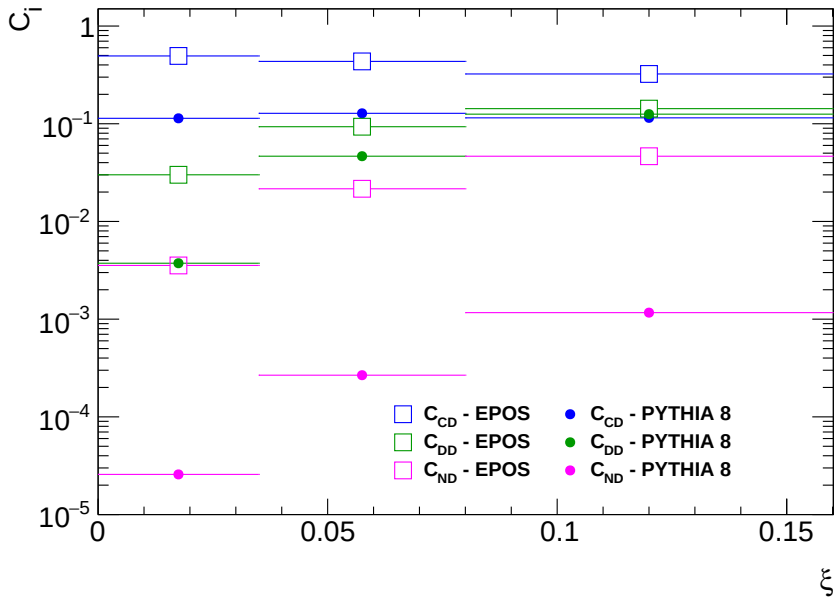

Figure 8.5: CD, DD and ND contributions to SD calculated based on PYTHIA 8 and EPOS.

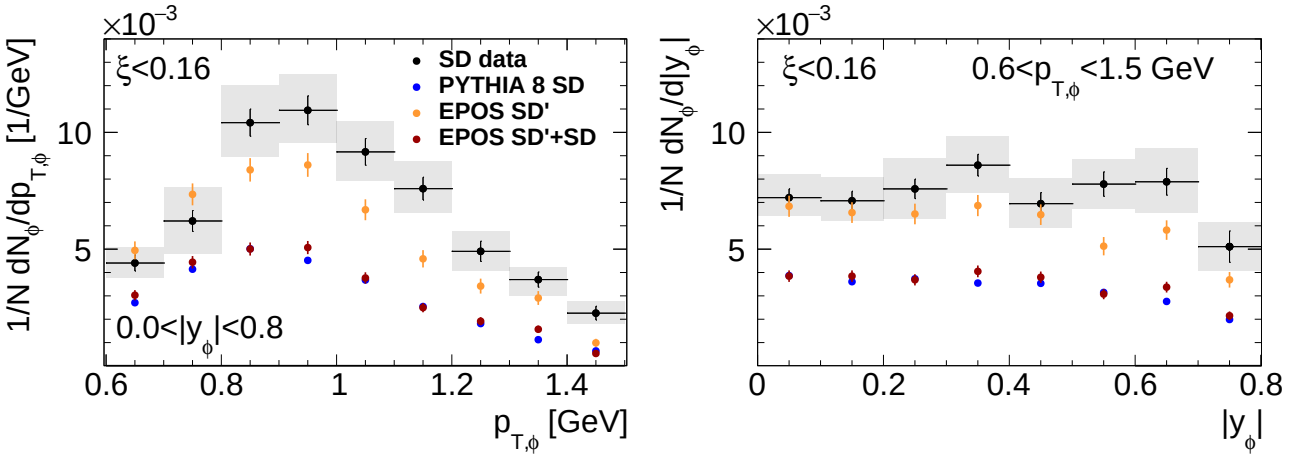

Figure 8.6: Comparison of SD data after the CD, DD and ND subtraction with PYTHIA 8 and EPOS. (left) $p_{\mathrm{T},\phi}$ spectrum integrated over $|y_\phi| < 0.8$, and (right) $|y_\phi|$ spectrum integrated over $0.6 < p_{\mathrm{T},\phi} < 1.5$ GeV. Data and MC predictions are shown in the full $\xi < 0.16$ range.

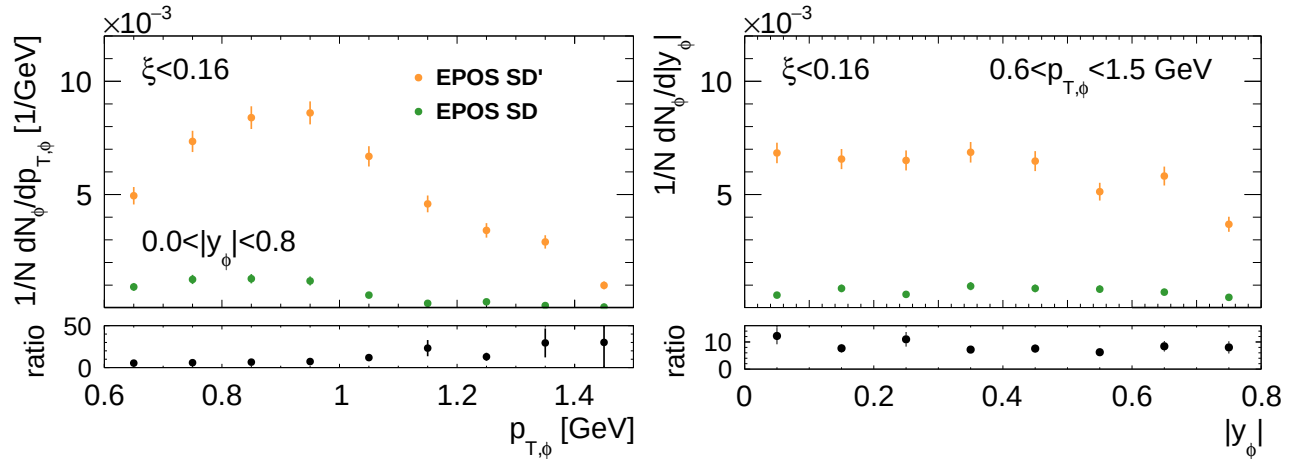

Figure 8.7: Comparison between EPOS SD' and SD samples. (left) $p_{\mathrm{T},\phi}$ spectrum integrated over $|y_\phi| < 0.8$. (right) $|y_\phi|$ spectrum integrated over $0.6 < p_{\mathrm{T},\phi} < 1.5$ GeV. The results are shown in the full $\xi < 0.16$ range. Ratios of SD' to SD prediction are shown in the bottom panels.

the model and data distributions as in the case of the full inelastic PYTHIA 8 sample. The best agreement is found for EPOS SD'. Combined EPOS SD and EPOS SD' expectations are similar to those presented by PYTHIA 8 SD.

Comparison between EPOS SD and EPOS SD' predicted spectra is presented in Figure 8.7. The ratio of EPOS SD' to EPOS SD increases as a function of $p_{\mathrm{T},\phi}$ and, for $p_{\mathrm{T},\phi} \gtrsim 1.3$ GeV, the N_ϕ/N predicted by EPOS SD' is almost 30 times greater than in the EPOS SD sample. The EPOS SD' to EPOS SD ratio is fairly constant as a function of rapidity and equals about 8.

Figure 8.8 presents $p_{\mathrm{T},\phi}$ and $|y_\phi|$ spectra after CD, DD and ND contribution subtraction for $10^{-5} < \xi < 0.035$, $0.035 < \xi < 0.08$, and $0.08 < \xi < 0.16$, separately. Larger differences between CD, DD and ND contributions predicted by PYTHIA 8 and EPOS are for $0.035 < \xi < 0.08$ and $0.08 < \xi < 0.16$ than for the range where $\xi < 0.035$. PYTHIA 8 SD predictions are similar to those of combined EPOS SD and EPOS SD' models for $0.035 < \xi < 0.08$ and $0.08 < \xi < 0.16$. EPOS SD expectations were not shown in the figure because they are negligible in the case of $\xi > 0.035$ (predictions of both EPOS SD' and EPOS SD' + EPOS SD are similar). The contribution of EPOS SD is larger for $\xi < 0.035$. N_ϕ/N for EPOS SD' + EPOS SD does not describe data in this ξ region, whereas EPOS SD' reproduces data well.

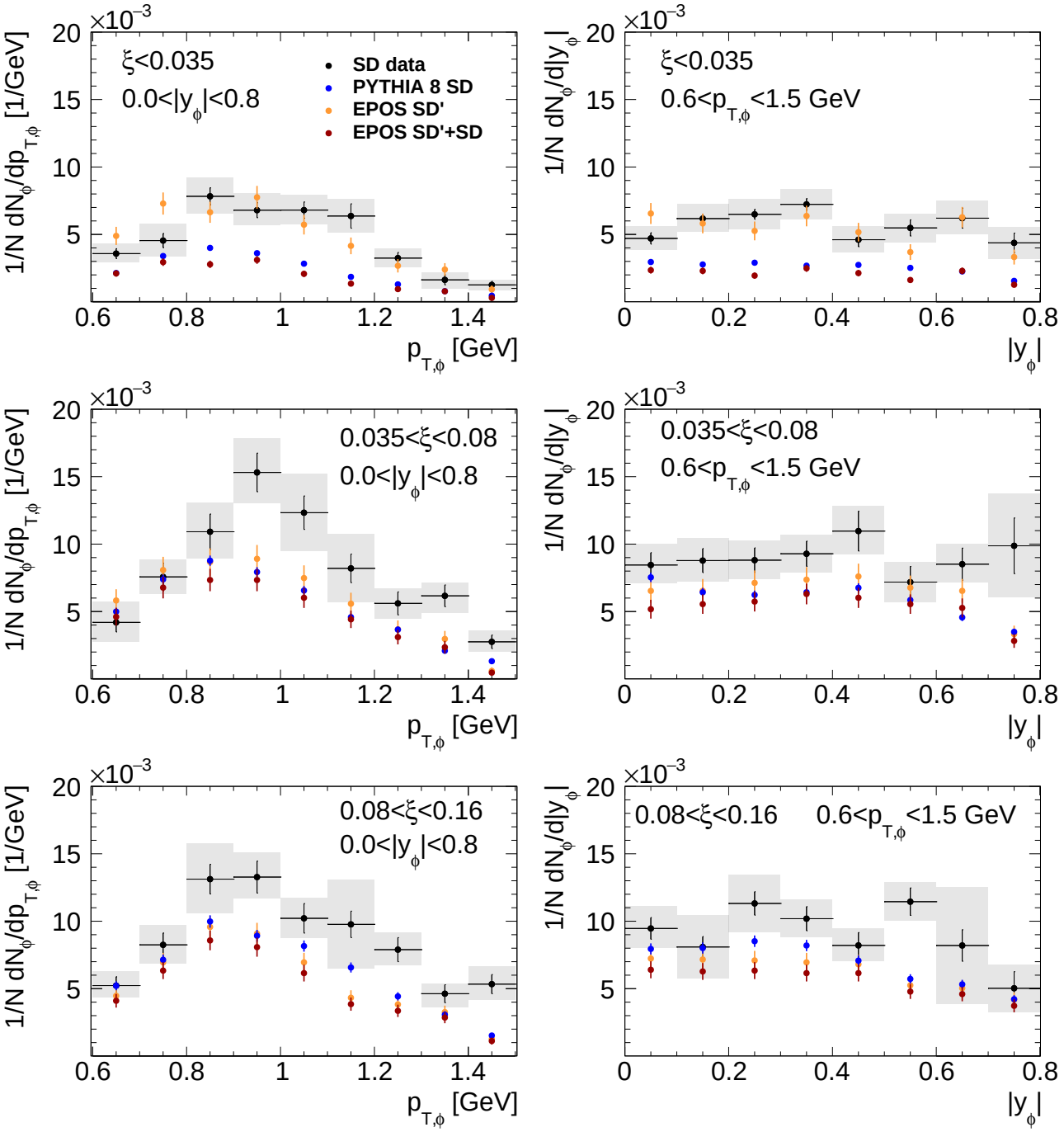

Figure 8.8: Comparison between SD data after the CD, DD and ND subtraction and two MC models - PYTHIA 8 and EPOS. Data and MC predictions are shown in three ξ ranges. (left) $p_{\mathrm{T},\phi}$ spectra integrated over $|y_\phi| < 0.8$, and (right) $|y_\phi|$ spectra integrated over $0.6 < p_{\mathrm{T},\phi} < 1.5$ GeV.

8.2 Central Diffraction Measurements

The $p_{\mathrm{T},\phi}$ and $|y_\phi|$ spectra were measured for CD data and compared to PYTHIA 8 CD and EPOS CD expectations in Figure 8.9. The statistical and systematic uncertainties added in quadrature are presented in the figure as boxes. The background contributions from DD and ND processes predicted by PYTHIA 8 and EPOS are negligible. The analysis was performed in the range $\xi_{\mathrm{A}} < 0.02$, $\xi_{\mathrm{C}} < 0.02$, where ξ_{A} and ξ_{C} denote ξ of a proton detected on the ATLAS side A and C, respectively. The ξ range was restricted because the efficiency of the veto on the MBTS is lower than 10% for bigger ξ_{A} and ξ_{C} values.

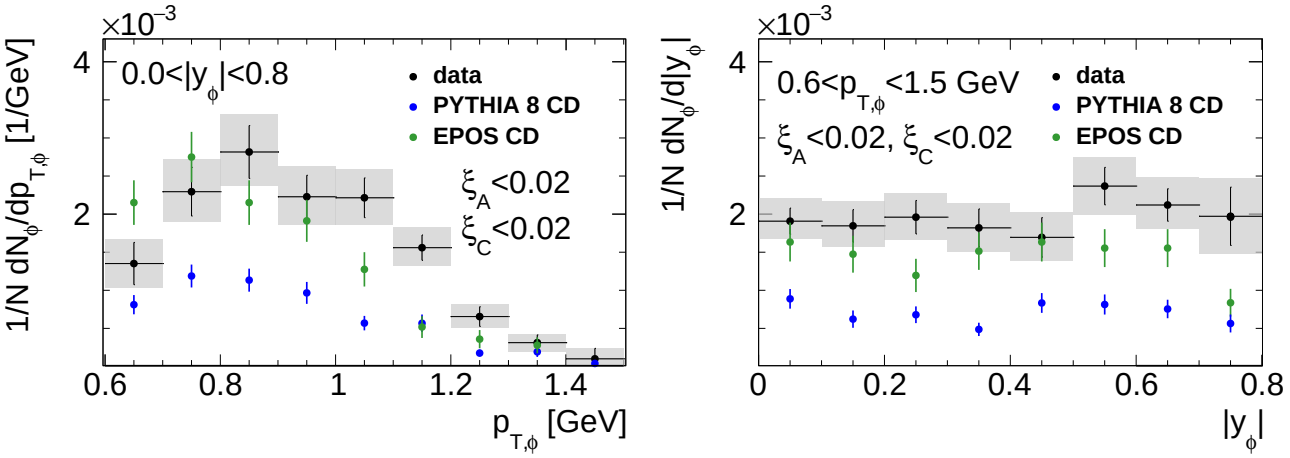

Figure 8.9: Comparison between CD data and two MC models - PYTHIA 8 and EPOS. (left) $p_{\mathrm{T},\phi}$ spectrum integrated over $|y_\phi| < 0.8$, and (right) $|y_\phi|$ spectrum integrated over $0.6 < p_{\mathrm{T},\phi} < 1.5$ GeV.

The signal yields for data were extracted from the fits of the invariant mass of K^+K^- pairs after applying (6.1), (6.2), (6.6) and corrections for the bias in the momentum reconstruction. The fits are shown in Appendix B.2, in Figure B.2.2 for $p_{\mathrm{T},\phi}$ ranges and in Figure B.2.1 for y_ϕ ranges. The values of χ^2/ndof are lower than 2 in most of the $p_{\mathrm{T},\phi}$ and $|y_\phi|$ bins that demonstrates good quality of the fits. The $1/N\ \mathrm{d}N_\phi/\mathrm{d}p_{\mathrm{T},\phi}$ and $1/N\ \mathrm{d}N_\phi/\mathrm{d}|y_\phi|$ yields are reported with corresponding uncertainties in Table 8.3 and 8.4, respectively.

The $p_{\mathrm{T},\phi}$ and y_ϕ yields are lower than the ones measured for SD, but shapes of the distributions are similar. The number of measured $\phi \to K^+K^-$ decays increases as a function of $p_{\mathrm{T},\phi}$ in the range $0.6 < p_{\mathrm{T},\phi} < 0.85$ GeV, reaches a maximum at $p_{\mathrm{T},\phi} \sim 0.85$ and decreases for $p_{\mathrm{T},\phi} \gtrsim 0.85$ GeV. The $|y_\phi|$ spectrum is constant within the uncertainties.

Predictions from PYTHIA 8 CD and EPOS CD are different. PYTHIA 8 underestimates $\phi(1020)$ meson production by around a factor of two compared to data, whereas EPOS reproduces data quite well.

8.3 Minimum Bias Measurements

The $p_{\mathrm{T},\phi}$ and $|y_\phi|$ spectra were also measured in MB data. Comparison between ϕ production rate for data, PYTHIA 8 and EPOS is shown in Figure 8.10. The signal yields were extracted from the fits to the corrected invariant mass distributions of oppositely charged kaon candidates. The fits are shown in Appendix B.3, in Figure B.3.2 for $p_{\mathrm{T},\phi}$ and in Figure B.3.1 for $|y_\phi|$ ranges. The resulting χ^2/ndof values range from 0.87 to 1.95 which proves good quality of the fits. Tables 8.5 and 8.6 contain the $1/N\ \mathrm{d}N_\phi/\mathrm{d}p_{\mathrm{T},\phi}$ and $1/N\ \mathrm{d}N_\phi/\mathrm{d}|y_\phi|$ yields for MB analysis.

The $p_{\mathrm{T},\phi}$ and y_ϕ yields in the MB analysis are greater than those measured for SD. The ϕ spectrum increases as a function of $p_{\mathrm{T},\phi}$ in the range $0.6 < p_{\mathrm{T},\phi} < 0.95$ GeV reaching a maximum at $p_{\mathrm{T},\phi} \approx 0.95$ GeV and decreases for $p_{\mathrm{T},\phi} \gtrsim 0.95$ GeV. The $|y_\phi|$ spectrum is constant within the uncertainties in the range $0.0 < |y_\phi| < 0.7$ and decreases for $|y_\phi| \gtrsim 0.7$. EPOS reproduces data better than PYTHIA 8 but it overestimates ϕ spectrum for $|y_\phi| < 0.5$. EPOS provides a good description in the full $p_{\mathrm{T},\phi}$ range and for $|y_\phi| \gtrsim 0.5$. PYTHIA 8 predicts around 30% lower ϕ production than data.

Table 8.3: The $1/N\ \mathrm{d}N_\phi/\mathrm{d}p_{\mathrm{T},\phi}$ yields at midrapidity $|y_\phi| < 0.8$ in the range $0.6 < p_{\mathrm{T},\phi} < 1.5$ GeV for CD analysis. Statistical and systematic uncertainties are listed in the table.

Bin [GeV]	$\mathbf{1/N\ \mathrm{d}N_\phi/\mathrm{d}p_{T,\phi}}$ $\mathbf{[GeV^{-1}]}$	$\mathbf{sys._{ID,N_\phi}}$ $\mathbf{[GeV^{-1}]}$	$\mathbf{sys._{n_{ch},M}}$ $\mathbf{[GeV^{-1}]}$	$\mathbf{sys._{PID,K-}}$ $\mathbf{[GeV^{-1}]}$	$\mathbf{sys._{PID,K+}}$ $\mathbf{[GeV^{-1}]}$
$0.6 < p_{\mathrm{T},\phi} \leq 0.7$	$(1.35 \pm 0.28)\cdot10^{-3}$	$^{+0.09}_{-0.05}\cdot10^{-3}$	$\pm\ 0.06\cdot10^{-3}$	$^{+0.11}_{-0.10}\cdot10^{-3}$	$^{+0.07}_{-0.07}\cdot10^{-3}$
$0.7 < p_{\mathrm{T},\phi} \leq 0.8$	$(2.29 \pm 0.32)\cdot10^{-3}$	$^{+0.14}_{-0.10}\cdot10^{-3}$	$\pm\ 0.09\cdot10^{-3}$	$^{+0.22}_{-0.19}\cdot10^{-3}$	$^{+0.15}_{-0.14}\cdot10^{-3}$
$0.8 < p_{\mathrm{T},\phi} \leq 0.9$	$(2.82 \pm 0.35)\cdot10^{-3}$	$^{+0.22}_{-0.03}\cdot10^{-3}$	$\pm\ 0.11\cdot10^{-3}$	$^{+0.25}_{-0.21}\cdot10^{-3}$	$^{+0.17}_{-0.17}\cdot10^{-3}$
$0.9 < p_{\mathrm{T},\phi} \leq 1.0$	$(2.23 \pm 0.29)\cdot10^{-3}$	$^{+0.14}_{-0.04}\cdot10^{-3}$	$\pm\ 0.09\cdot10^{-3}$	$^{+0.19}_{-0.17}\cdot10^{-3}$	$^{+0.17}_{-0.14}\cdot10^{-3}$
$1.0 < p_{\mathrm{T},\phi} \leq 1.1$	$(2.21 \pm 0.27)\cdot10^{-3}$	$^{+0.05}_{-0.11}\cdot10^{-3}$	$\pm\ 0.09\cdot10^{-3}$	$^{+0.18}_{-0.16}\cdot10^{-3}$	$^{+0.17}_{-0.14}\cdot10^{-3}$
$1.1 < p_{\mathrm{T},\phi} \leq 1.2$	$(1.56 \pm 0.17)\cdot10^{-3}$	$^{+0.07}_{-0.03}\cdot10^{-3}$	$\pm\ 0.06\cdot10^{-3}$	$^{+0.12}_{-0.10}\cdot10^{-3}$	$^{+0.12}_{-0.09}\cdot10^{-3}$
$1.2 < p_{\mathrm{T},\phi} \leq 1.3$	$(0.65 \pm 0.13)\cdot10^{-3}$	$^{+0.01}_{-0.05}\cdot10^{-3}$	$\pm\ 0.03\cdot10^{-3}$	$^{+0.09}_{-0.07}\cdot10^{-3}$	$^{+0.07}_{-0.06}\cdot10^{-3}$
$1.3 < p_{\mathrm{T},\phi} \leq 1.4$	$(0.31 \pm 0.11)\cdot10^{-3}$	$^{+0.01}_{-0.02}\cdot10^{-3}$	$\pm\ 0.02\cdot10^{-3}$	$^{+0.03}_{-0.03}\cdot10^{-3}$	$^{+0.02}_{-0.05}\cdot10^{-3}$
$1.4 < p_{\mathrm{T},\phi} \leq 1.5$	$(0.10 \pm 0.14)\cdot10^{-3}$	$^{+0.01}_{-0.01}\cdot10^{-3}$	$\pm\ 0.01\cdot10^{-3}$	$^{+0.03}_{-0.02}\cdot10^{-3}$	$^{+0.02}_{-0.02}\cdot10^{-3}$

Table 8.4: The $1/N\ \mathrm{d}N_\phi/\mathrm{d}|y_\phi|$ yields integrated over $0.6 < p_{\mathrm{T},\phi} < 1.5$ GeV in the range $|y_\phi| < 0.8$ for CD analysis. Statistical and systematic uncertainties are listed in the table.

Bin	$\mathbf{1/N\ \mathrm{d}N_\phi/\mathrm{d}\lvert y_\phi\rvert}$	$\mathbf{sys._{ID,N_\phi}}$	$\mathbf{sys._{n_{ch},M}}$	$\mathbf{sys._{PID,K-}}$	$\mathbf{sys._{PID,K+}}$
$0.0 < \lvert y_\phi\rvert \leq 0.1$	$(1.91 \pm 0.18)\cdot10^{-3}$	$^{+0.18}_{-0.01}\cdot10^{-3}$	$\pm\ 0.08\cdot10^{-3}$	$^{+0.18}_{-0.10}\cdot10^{-3}$	$^{+0.12}_{-0.11}\cdot10^{-3}$
$0.1 < \lvert y_\phi\rvert \leq 0.2$	$(1.85 \pm 0.22)\cdot10^{-3}$	$^{+0.14}_{-0.01}\cdot10^{-3}$	$\pm\ 0.07\cdot10^{-3}$	$^{+0.15}_{-0.13}\cdot10^{-3}$	$^{+0.10}_{-0.09}\cdot10^{-3}$
$0.2 < \lvert y_\phi\rvert \leq 0.3$	$(1.96 \pm 0.22)\cdot10^{-3}$	$^{+0.06}_{-0.09}\cdot10^{-3}$	$\pm\ 0.08\cdot10^{-3}$	$^{+0.17}_{-0.13}\cdot10^{-3}$	$^{+0.12}_{-0.11}\cdot10^{-3}$
$0.3 < \lvert y_\phi\rvert \leq 0.4$	$(1.82 \pm 0.25)\cdot10^{-3}$	$^{+0.07}_{-0.07}\cdot10^{-3}$	$\pm\ 0.07\cdot10^{-3}$	$^{+0.15}_{-0.15}\cdot10^{-3}$	$^{+0.12}_{-0.10}\cdot10^{-3}$
$0.4 < \lvert y_\phi\rvert \leq 0.5$	$(1.70 \pm 0.26)\cdot10^{-3}$	$^{+0.09}_{-0.04}\cdot10^{-3}$	$\pm\ 0.07\cdot10^{-3}$	$^{+0.14}_{-0.13}\cdot10^{-3}$	$^{+0.12}_{-0.10}\cdot10^{-3}$
$0.5 < \lvert y_\phi\rvert \leq 0.6$	$(2.37 \pm 0.25)\cdot10^{-3}$	$^{+0.03}_{-0.10}\cdot10^{-3}$	$\pm\ 0.09\cdot10^{-3}$	$^{+0.15}_{-0.15}\cdot10^{-3}$	$^{+0.15}_{-0.12}\cdot10^{-3}$
$0.6 < \lvert y_\phi\rvert \leq 0.7$	$(2.12 \pm 0.22)\cdot10^{-3}$	$^{+0.09}_{-0.06}\cdot10^{-3}$	$\pm\ 0.08\cdot10^{-3}$	$^{+0.16}_{-0.13}\cdot10^{-3}$	$^{+0.16}_{-0.13}\cdot10^{-3}$
$0.7 < \lvert y_\phi\rvert \leq 0.8$	$(1.97 \pm 0.39)\cdot10^{-3}$	$^{+0.10}_{-0.04}\cdot10^{-3}$	$\pm\ 0.08\cdot10^{-3}$	$^{+0.20}_{-0.15}\cdot10^{-3}$	$^{+0.17}_{-0.21}\cdot10^{-3}$

Table 8.5: The $1/N\ \mathrm{d}N_\phi/\mathrm{d}p_{\mathrm{T},\phi}$ yields at midrapidity $|y_\phi| < 0.8$ in the range $0.6 < p_{\mathrm{T},\phi} < 1.5$ GeV for MB analysis. Statistical and systematic uncertainties are listed in the table.

Bin [GeV]	$\mathbf{1/\mathit{N}\ \mathrm{d}\mathit{N}_\phi/\mathrm{d}\mathit{p}_{\mathrm{T},\phi}}$ $\mathbf{[GeV^{-1}]}$	$\mathbf{sys._{ID,N_\phi}}$ $\mathbf{[GeV^{-1}]}$	$\mathbf{sys._{n_{ch},M}}$ $\mathbf{[GeV^{-1}]}$	$\mathbf{sys._{PID,K^-}}$ $\mathbf{[GeV^{-1}]}$	$\mathbf{sys._{PID,K^+}}$ $\mathbf{[GeV^{-1}]}$
$0.6 < p_{\mathrm{T},\phi} \leq 0.7$	$(5.38 \pm 0.45)\cdot10^{-3}$	$^{+0.33\cdot10^{-3}}_{-0.18\cdot10^{-3}}$	$\pm\ 0.04\cdot10^{-3}$	$^{+0.42\cdot10^{-3}}_{-0.37\cdot10^{-3}}$	$^{+0.28\cdot10^{-3}}_{-0.27\cdot10^{-3}}$
$0.7 < p_{\mathrm{T},\phi} \leq 0.8$	$(12.90 \pm 0.67)\cdot10^{-3}$	$^{+0.66\cdot10^{-3}}_{-0.43\cdot10^{-3}}$	$\pm\ 0.08\cdot10^{-3}$	$^{+0.99\cdot10^{-3}}_{-0.86\cdot10^{-3}}$	$^{+0.67\cdot10^{-3}}_{-0.65\cdot10^{-3}}$
$0.8 < p_{\mathrm{T},\phi} \leq 0.9$	$(16.99 \pm 0.80)\cdot10^{-3}$	$^{+1.19\cdot10^{-3}}_{-0.15\cdot10^{-3}}$	$\pm\ 0.10\cdot10^{-3}$	$^{+1.31\cdot10^{-3}}_{-1.14\cdot10^{-3}}$	$^{+0.88\cdot10^{-3}}_{-0.87\cdot10^{-3}}$
$0.9 < p_{\mathrm{T},\phi} \leq 1.0$	$(19.58 \pm 0.87)\cdot10^{-3}$	$^{+1.08\cdot10^{-3}}_{-0.29\cdot10^{-3}}$	$\pm\ 0.12\cdot10^{-3}$	$^{+1.51\cdot10^{-3}}_{-1.31\cdot10^{-3}}$	$^{+1.14\cdot10^{-3}}_{-1.07\cdot10^{-3}}$
$1.0 < p_{\mathrm{T},\phi} \leq 1.1$	$(15.38 \pm 0.85)\cdot10^{-3}$	$^{+0.28\cdot10^{-3}}_{-0.71\cdot10^{-3}}$	$\pm\ 0.10\cdot10^{-3}$	$^{+1.19\cdot10^{-3}}_{-1.03\cdot10^{-3}}$	$^{+1.10\cdot10^{-3}}_{-0.87\cdot10^{-3}}$
$1.1 < p_{\mathrm{T},\phi} \leq 1.2$	$(14.06 \pm 0.79)\cdot10^{-3}$	$^{+0.63\cdot10^{-3}}_{-0.26\cdot10^{-3}}$	$\pm\ 0.09\cdot10^{-3}$	$^{+1.16\cdot10^{-3}}_{-0.94\cdot10^{-3}}$	$^{+1.15\cdot10^{-3}}_{-0.90\cdot10^{-3}}$
$1.2 < p_{\mathrm{T},\phi} \leq 1.3$	$(9.60 \pm 0.73)\cdot10^{-3}$	$^{+0.01\cdot10^{-3}}_{-0.54\cdot10^{-3}}$	$\pm\ 0.06\cdot10^{-3}$	$^{+0.96\cdot10^{-3}}_{-0.72\cdot10^{-3}}$	$^{+0.77\cdot10^{-3}}_{-0.60\cdot10^{-3}}$
$1.3 < p_{\mathrm{T},\phi} \leq 1.4$	$(5.90 \pm 0.57)\cdot10^{-3}$	$^{+0.15\cdot10^{-3}}_{-0.21\cdot10^{-3}}$	$\pm\ 0.04\cdot10^{-3}$	$^{+0.40\cdot10^{-3}}_{-0.51\cdot10^{-3}}$	$^{+0.24\cdot10^{-3}}_{-0.95\cdot10^{-3}}$
$1.4 < p_{\mathrm{T},\phi} \leq 1.5$	$(4.31 \pm 0.51)\cdot10^{-3}$	$^{+0.04\cdot10^{-3}}_{-0.20\cdot10^{-3}}$	$\pm\ 0.03\cdot10^{-3}$	$^{+0.65\cdot10^{-3}}_{-0.31\cdot10^{-3}}$	$^{+0.63\cdot10^{-3}}_{-0.45\cdot10^{-3}}$

Table 8.6: The $1/N\ \mathrm{d}N_\phi/\mathrm{d}|y_\phi|$ yields integrated over $0.6 < p_{\mathrm{T},\phi} < 1.5$ GeV in the range $|y_\phi| < 0.8$ for MB analysis. Statistical and systematic uncertainties are listed in the table.

Bin	$\mathbf{1/\mathit{N}\ \mathrm{d}\mathit{N}_\phi/\mathrm{d}|\mathit{y}_\phi|}$	$\mathbf{sys._{ID,N_\phi}}$	$\mathbf{sys._{n_{ch},M}}$	$\mathbf{sys._{PID,K^-}}$	$\mathbf{sys._{PID,K^+}}$
$0.0 < \lvert y_\phi\rvert \leq 0.1$	$(12.97 \pm 0.57)\cdot10^{-3}$	$^{+1.02\cdot10^{-3}}_{-0.04\cdot10^{-3}}$	$\pm\ 0.08\cdot10^{-3}$	$^{+1.00\cdot10^{-3}}_{-0.54\cdot10^{-3}}$	$^{+0.64\cdot10^{-3}}_{-0.63\cdot10^{-3}}$
$0.1 < \lvert y_\phi\rvert \leq 0.2$	$(13.50 \pm 0.58)\cdot10^{-3}$	$^{+0.99\cdot10^{-3}}_{-0.07\cdot10^{-3}}$	$\pm\ 0.08\cdot10^{-3}$	$^{+1.04\cdot10^{-3}}_{-0.91\cdot10^{-3}}$	$^{+0.70\cdot10^{-3}}_{-0.61\cdot10^{-3}}$
$0.2 < \lvert y_\phi\rvert \leq 0.3$	$(14.46 \pm 0.62)\cdot10^{-3}$	$^{+0.39\cdot10^{-3}}_{-0.63\cdot10^{-3}}$	$\pm\ 0.09\cdot10^{-3}$	$^{+1.17\cdot10^{-3}}_{-0.91\cdot10^{-3}}$	$^{+0.81\cdot10^{-3}}_{-0.75\cdot10^{-3}}$
$0.3 < \lvert y_\phi\rvert \leq 0.4$	$(14.35 \pm 0.65)\cdot10^{-3}$	$^{+0.49\cdot10^{-3}}_{-0.50\cdot10^{-3}}$	$\pm\ 0.09\cdot10^{-3}$	$^{+1.05\cdot10^{-3}}_{-1.09\cdot10^{-3}}$	$^{+0.87\cdot10^{-3}}_{-0.68\cdot10^{-3}}$
$0.4 < \lvert y_\phi\rvert \leq 0.5$	$(13.60 \pm 0.71)\cdot10^{-3}$	$^{+0.66\cdot10^{-3}}_{-0.28\cdot10^{-3}}$	$\pm\ 0.08\cdot10^{-3}$	$^{+1.05\cdot10^{-3}}_{-0.91\cdot10^{-3}}$	$^{+0.88\cdot10^{-3}}_{-0.70\cdot10^{-3}}$
$0.5 < \lvert y_\phi\rvert \leq 0.6$	$(13.44 \pm 0.81)\cdot10^{-3}$	$^{+0.20\cdot10^{-3}}_{-0.67\cdot10^{-3}}$	$\pm\ 0.08\cdot10^{-3}$	$^{+1.04\cdot10^{-3}}_{-0.99\cdot10^{-3}}$	$^{+1.05\cdot10^{-3}}_{-0.84\cdot10^{-3}}$
$0.6 < \lvert y_\phi\rvert \leq 0.7$	$(13.08 \pm 0.67)\cdot10^{-3}$	$^{+0.58\cdot10^{-3}}_{-0.40\cdot10^{-3}}$	$\pm\ 0.08\cdot10^{-3}$	$^{+1.10\cdot10^{-3}}_{-0.88\cdot10^{-3}}$	$^{+1.09\cdot10^{-3}}_{-0.86\cdot10^{-3}}$
$0.7 < \lvert y_\phi\rvert \leq 0.8$	$(9.21 \pm 1.01)\cdot10^{-3}$	$^{+0.48\cdot10^{-3}}_{-0.18\cdot10^{-3}}$	$\pm\ 0.06\cdot10^{-3}$	$^{+1.01\cdot10^{-3}}_{-0.76\cdot10^{-3}}$	$^{+0.86\cdot10^{-3}}_{-1.07\cdot10^{-3}}$

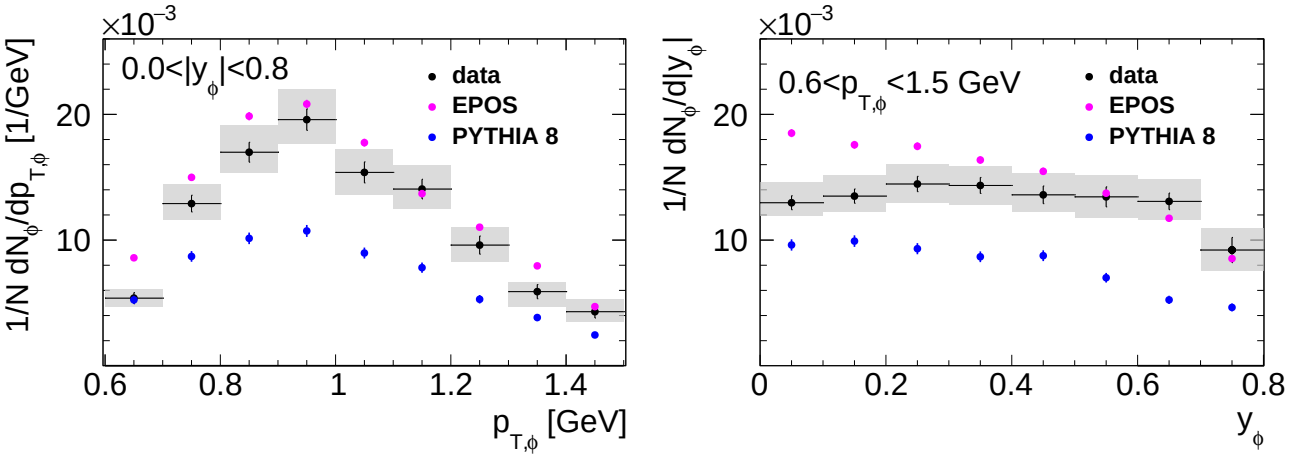

Figure 8.10: Comparison between MB data and two MC models - PYTHIA 8 and EPOS. (left) $p_{\mathrm{T},\phi}$ spectrum integrated over $|y_\phi| < 0.8$, and (right) $|y_\phi|$ spectrum integrated over $0.6 < p_{\mathrm{T},\phi} < 1.5$ GeV.

8.4 Discussion

8.4.1 ϕ Meson Production in SD, CD and MB Analyses

ϕ meson production in $p_{\mathrm{T},\phi}$ and $|y_\phi|$ bins was measured based on SD, CD and MB triggered data, where the latter are dominated by ND processes. Comparison between the transverse momentum and rapidity spectra in the three types of inelastic pp scattering is shown in Figure 8.11, where error bars represent statistical uncertainties and boxes indicate the quadratic sum of statistical and systematic uncertainties.

The highest ϕ production rates were measured for MB in each $p_{\mathrm{T},\phi}$ and $|y_\phi|$ bin, while the lowest ϕ production, also in each $p_{\mathrm{T},\phi}$ and $|y_\phi|$ bin, is observed for CD. Therefore, the $p_{\mathrm{T},\phi}$ and $|y_\phi|$ spectra are different in different types of pp inelastic scattering and their values might be related to the mean numbers of selected particles, $\langle n_{\mathrm{sel}} \rangle$, in the given process. Obtained values of $\langle n_{\mathrm{sel}} \rangle$ are 4.00 ± 0.02, 16.78 ± 0.01 and 38.12 ± 0.02 for CD, SD and MB data, respectively. Thus, the higher the mean number of selected particles is, the bigger ϕ meson production rate is observed.

We checked how $1/N\ \mathrm{d}N_\phi/\mathrm{d}p_{\mathrm{T},\phi}$ and $1/N\ \mathrm{d}N_\phi/\mathrm{d}|y_\phi|$ scale with the mean number of selected particles. The n_{sel} distribution was not unfolded in the CD analysis because of too low statistics in the CD MC samples with the full simulation of ATLAS detector. Thus, the mean number of selected particles was used consistently instead of the mean number of charged particles also in the SD and MB analyses. This weakness does not affect comparison between measured CD, SD and MB spectra. However, direct comparison to predictions is not possible.

The distributions scaled by $\langle n_{\mathrm{sel}} \rangle$ for SD, CD and MB samples are shown in Figure 8.12. A good agreement between the scaled $p_{\mathrm{T},\phi}$ spectra for SD and MB samples is visible, while the shape of the spectrum for CD is significantly different. The scaled $|y_\phi|$ spectra are similar for SD and MB samples within uncertainties. However, the spectrum for CD shows systematic excess over spectra for SD and MB processes in the full $|y_\phi|$ range. Hence, the different ϕ production rates in the studied processes are connected mostly with different multiplicities of selected particles. We conclude that ϕ mesons originate predominantly from the fragmentation process. The small difference between CD and SD(MB) might originate from the specific, rather narrow, phase-space region of the CD measurement. We checked PYTHIA 8 predictions to verify this possibility and to find out whether there is some evidence for a different $p_{\mathrm{T},\phi}$ spectrum in Pomeron-Pomeron fusion compared to Pomeron(proton)-proton interactions in the fiducial

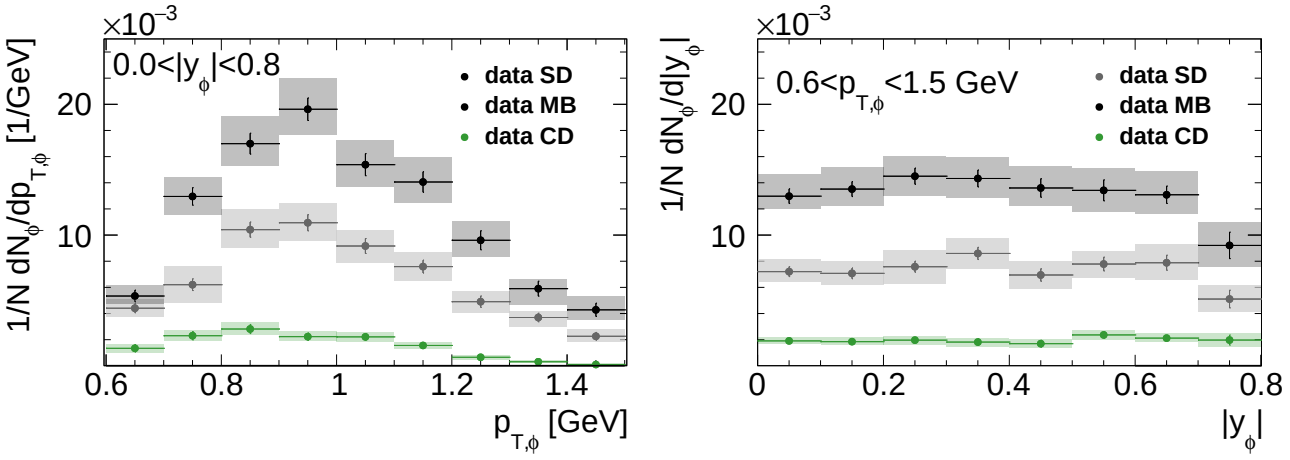

Figure 8.11: $p_{\mathrm{T},\phi}$ (left) and y_ϕ (right) spectra. Comparison between MB, SD and CD data.

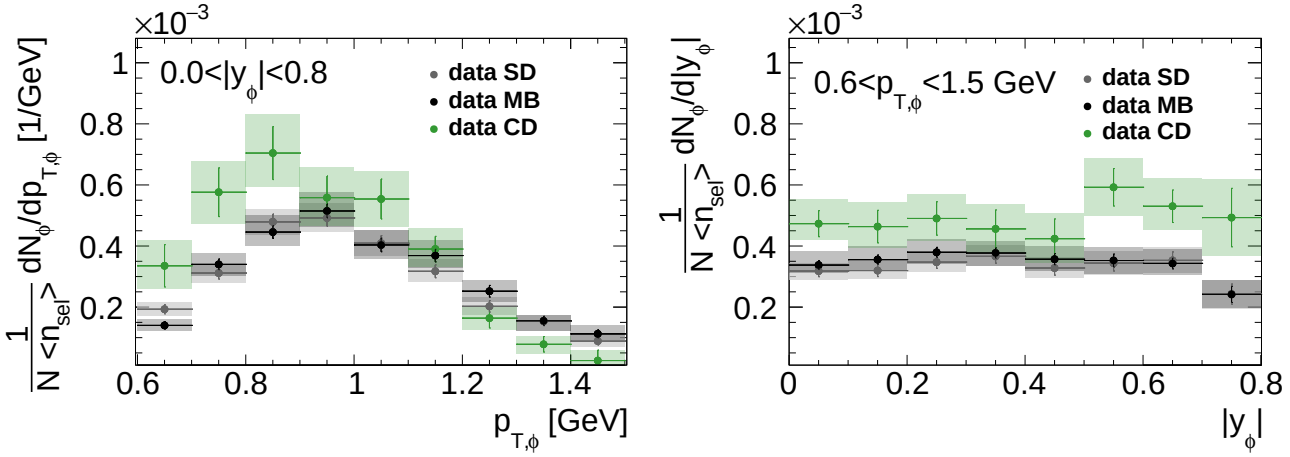

Figure 8.12: $p_{\mathrm{T},\phi}$ (left) and y_ϕ (right) spectra divided by $\langle n_{\mathrm{sel}} \rangle$. Comparison between MB, SD and CD data.

regions of this analysis. The $p_{\mathrm{T},\phi}$ and $|y_\phi|$ spectra scaled by $\langle N_{\mathrm{ch}} \rangle$ for PYTHIA 8 SD, CD and MB are shown in Figure 8.13. The ratios are similar for the SD and ND samples but they are lower for CD in almost all $p_{\mathrm{T},\phi}$ and $|y_\phi|$ bins. Since there is no MBTS correction in the CD data, the systematic differences between data and predictions concerning spectra scaled by $\langle N_{\mathrm{ch}} \rangle$ might be related to this effect. However, the shape of the distributions as a function of $p_{\mathrm{T},\phi}$ for data and PYTHIA 8 expectations shows similar differences compared to SD and MB results. We can conclude that there is no strong evidence for sensitivity of ϕ production to the initial states in the given processes, Pomeron-proton in SD, Pomeron-Pomeron in CD, and proton-proton in ND.

The ϕ meson production in SD analysis was measured in three ranges of ξ: $10^{-5} < \xi < 0.035$, $0.035 < \xi < 0.08$, and $0.08 < \xi < 0.16$. The $p_{\mathrm{T},\phi}$ and $|y_\phi|$ spectra are compared in Figure 8.14. The lowest $1/N\ \mathrm{d}N_\phi/\mathrm{d}p_{\mathrm{T},\phi}$ and $1/N\ \mathrm{d}N_\phi/\mathrm{d}|y_\phi|$ values are observed in the region where $\xi < 0.035$, whereas the highest ϕ production is shown for $0.08 < \xi < 0.16$ in most transverse momentum and rapidity bins. The measured average numbers of selected particles $\langle n_{\mathrm{sel}} \rangle$ for each ξ region are 11.62 ± 0.07, 18.39 ± 0.19 and 22.04 ± 0.19 for $10^{-5} < \xi < 0.035$, $0.035 < \xi < 0.08$, and $0.08 < \xi < 0.16$, respectively. The results demonstrate the trend shown in comparison between MB, SD and CD measurements that the higher number of produced charged particles involves the higher fraction of ϕ mesons in the final state.

Then, $p_{\mathrm{T},\phi}$ and $|y_\phi|$ spectra divided by $\langle n_{\mathrm{sel}} \rangle$ in the three ξ ranges were compared (Figu-

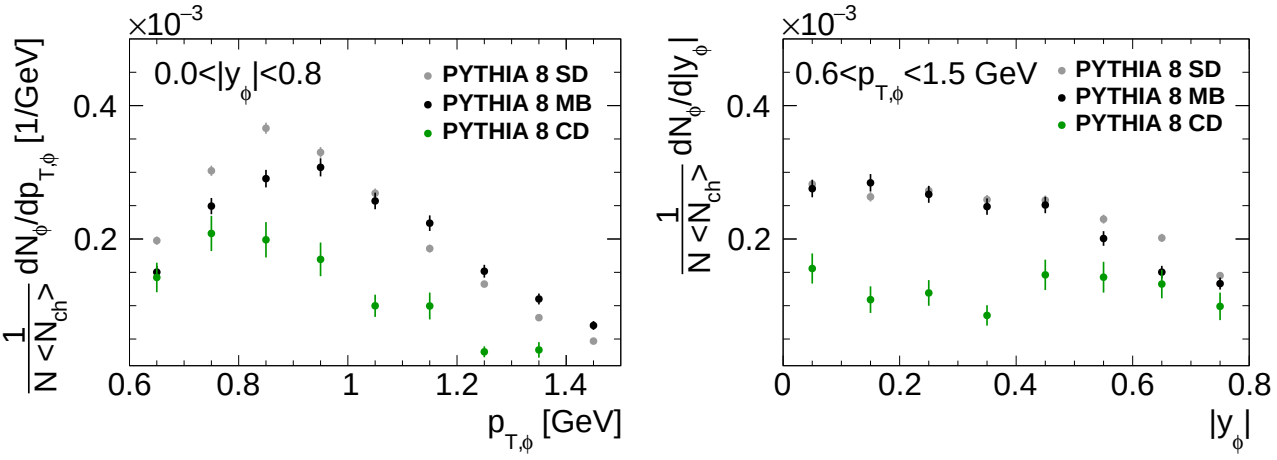

Figure 8.13: $p_{\mathrm{T},\phi}$ (left) and y_ϕ (right) spectra divided by $\langle N_{\mathrm{ch}} \rangle$. Comparison between SD, CD and ND PYTHIA 8 predictions.

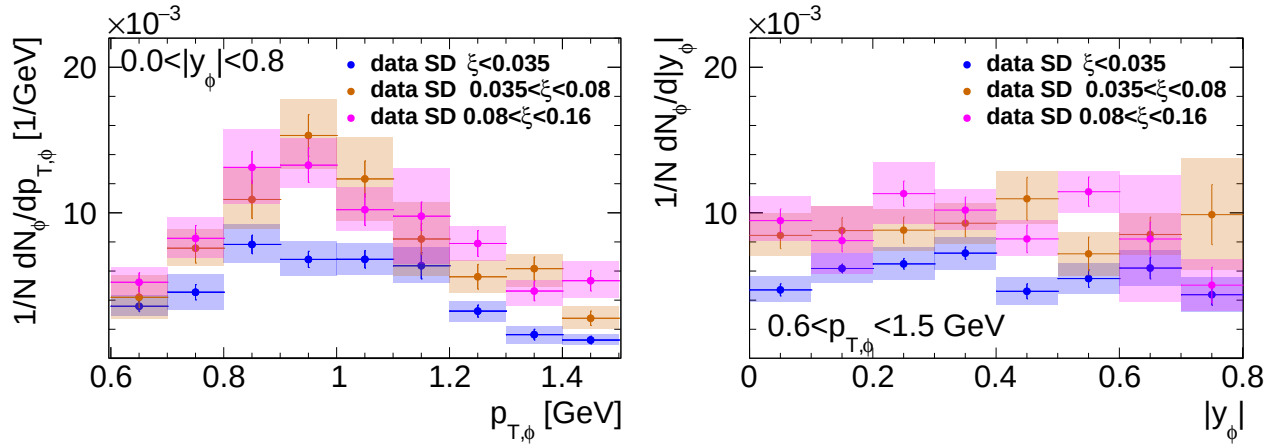

Figure 8.14: $p_{\mathrm{T},\phi}$ (left) and y_ϕ (right) spectra. Comparison between SD measurements for $\xi < 0.035$, $0.035 < \xi < 0.08$ and $0.08 < \xi < 0.16$.

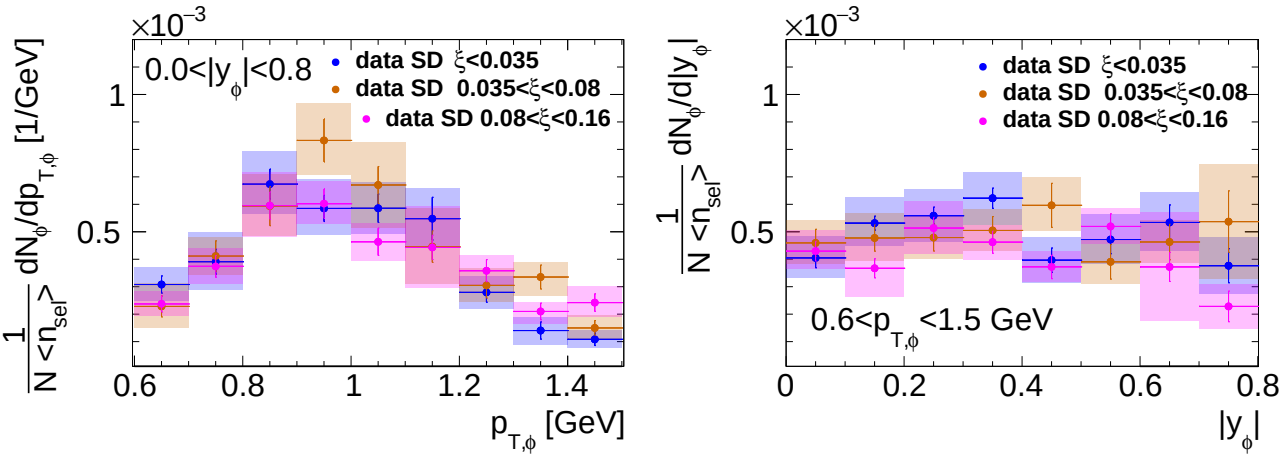

Figure 8.15: $p_{\mathrm{T},\phi}$ (left) and $|y_\phi|$ (right) spectra divided by $\langle n_{\mathrm{sel}} \rangle$. Comparison between SD measurements for $\xi < 0.035$, $0.035 < \xi < 0.08$ and $0.08 < \xi < 0.16$.

re 8.15). The results are similar within the uncertainties in most of the $p_{\mathrm{T},\phi}$ and $|y_\phi|$ bins. This confirms that the fraction of ϕ mesons in the final state increases because of higher charged-particle multiplicity.

8.4.2 Comparison to the Measurement at $\sqrt{s} = 7$ TeV

The $\phi(1020)$ production measurement which is presented in this dissertation was compared to the measurement of $\phi \to K^+K^-$ production cross section in pp collisions at $\sqrt{s} = 7$ TeV by the ATLAS Collaboration, described in Ref. [70]. The comparison involves ϕ meson production as a function of $p_{\mathrm{T},\phi}$ measured in pp collisions using Minimum Bias triggered data at different centre-of-mass energies $\sqrt{s} = 13$ TeV and $\sqrt{s} = 7$ TeV.

Kinematic regions of the two measurements are different. This analysis requires $p_{\mathrm{T},K} > 0.29$ GeV and $p_K < 0.9$ GeV, while kaons in the ATLAS measurement at $\sqrt{s} = 7$ TeV satisfy $p_{\mathrm{T},K} > 0.23$ GeV and $p_K < 0.8$ GeV. Therefore, particle level information from PYTHIA 8 (13 TeV) was used to scale the $p_{\mathrm{T},\phi}$ spectrum obtained for pp collisions at $\sqrt{s} = 13$ TeV to the kinematic region of the measurement at $\sqrt{s} = 7$ TeV. Comparison between the number of events in the two regions is shown in Figure 8.16 as a function of $p_{\mathrm{T},\phi}$. The scaling factor, which is defined as the ratio of the number of events in the kinematic region in the analysis at $\sqrt{s} = 13$ TeV to the number of events in the kinematic region in the analysis at $\sqrt{s} = 7$ TeV, is 0.44 for $0.6 < p_{\mathrm{T},\phi} < 0.7$ GeV. Then, it increases being still lower than one for $0.7 < p_{\mathrm{T},\phi} \lesssim 0.9$ GeV. In the range $0.9 \lesssim p_{\mathrm{T},\phi} < 1.5$ GeV, the number of events in the kinematic region in the analysis at $\sqrt{s} = 13$ TeV is greater compared to the number of events in the kinematic region in the analysis at $\sqrt{s} = 7$ TeV. The scaling factor increases for $0.9 \lesssim p_{\mathrm{T},\phi} < 1.5$ GeV becoming 2.9 in highest $p_{\mathrm{T},\phi}$ bin. The $p_{\mathrm{T},\phi}$ spectrum in the fiducial region was extrapolated according to the ratio.

Furthermore, to allow comparison with the measurement at $\sqrt{s} = 7$ TeV, the differential cross section $\mathrm{d}\sigma/\mathrm{d}p_{\mathrm{T}}$ of $\phi \to K^+K^-$, measured in pp collisions at $\sqrt{s} = 7$ TeV, was divided by the total inelastic cross section in pp collisions at $\sqrt{s} = 7$ TeV, $\sigma_{\mathrm{inel}} = 71.34 \pm 0.36$ mb [143].

Since the number of selected events, N, in the ϕ production measurement at $\sqrt{s} = 13$ TeV involves just events with $n_{\mathrm{ch}} \geq 2$, we extracted, based on PYTHIA 8 particle level information, the ratio of events with $n_{\mathrm{ch}} < 2$ to the number of all events. The ratio is determined to be

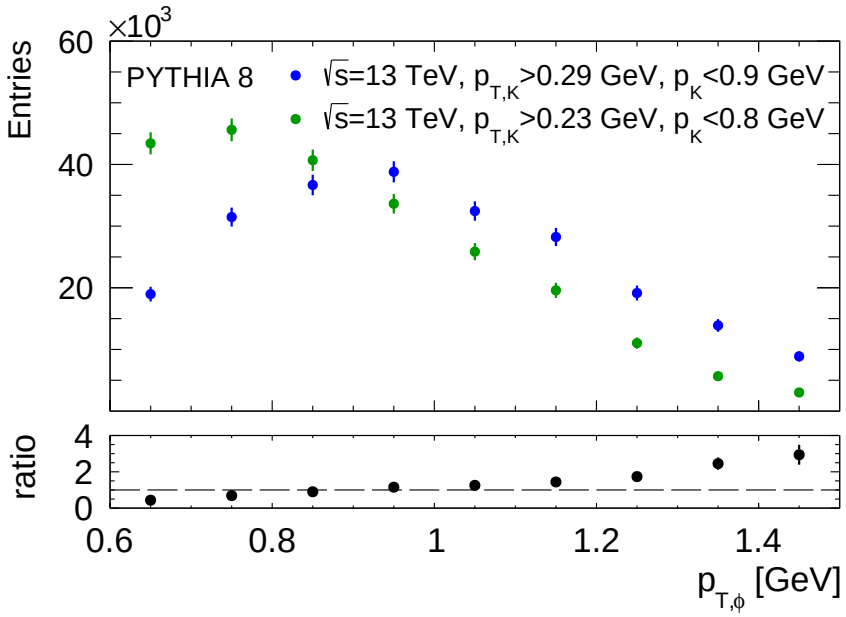

Figure 8.16: Comparison between the numbers of accepted events with $p_{\mathrm{T},K} > 0.29$ GeV and $p_K < 0.9$ GeV in the analysis at $\sqrt{s} = 13$ TeV (blue dots) and with $p_{\mathrm{T},K} > 0.23$ GeV and $p_K < 0.8$ GeV required in the analysis at $\sqrt{s} = 7$ TeV (green dots). The comparison is made as a function of $p_{\mathrm{T},\phi}$ with PYTHIA 8. Bottom panel shows ratio of the number of events in the 13 TeV analysis to the number of events in the kinematic region of 7 TeV analysis.

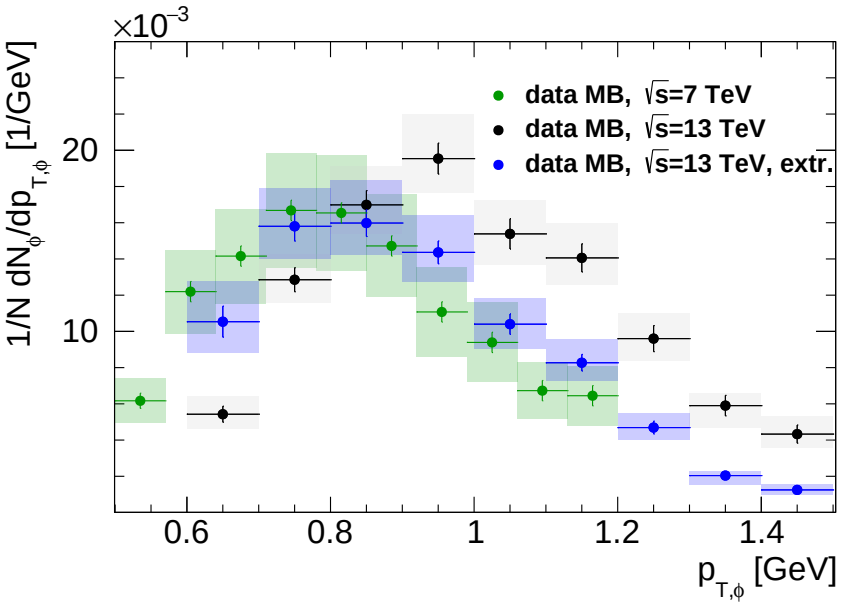

Figure 8.17: $p_{\mathrm{T},\phi}$ spectra. Black and green dots indicate ϕ production measurements in pp collisions at $\sqrt{s} = 13$ TeV and $\sqrt{s} = 7$ TeV, respectively. The spectra measured at $\sqrt{s} = 13$ TeV is extrapolated to the kinematic region from the analysis at $\sqrt{s} = 7$ TeV (blue dots). The quadratic sum of the statistical and systematic uncertainties is shown as boxes.

16%. N in the 13 TeV analysis was scaled by this value before the final comparison with the ϕ production measurement at $\sqrt{s} = 7$ TeV, shown in Figure 8.17.

There is a good agreement between ϕ production measurements at $\sqrt{s} = 7$ TeV and $\sqrt{s} = 13$ TeV. The scaled $p_{\mathrm{T},\phi}$ spectrum is greater compared to the ATLAS $\phi(1020)$ production measurement in the range $0.9 < p_{\mathrm{T},\phi} < 1.2$ GeV but the differences are still within uncertainties. The mean charged-particle multiplicity per unit of pseudorapidity was measured to be 6.422 ± 0.096 [162] and 5.630 ± 0.003 [173] in pp collisions with a centre-of-mass energy of 13 TeV and 7 TeV, respectively. Hence, the slightly larger spectrum at $\sqrt{s} = 13$ TeV can be related to the small increase of the average charged-particle multiplicity for higher collision energy.

CHAPTER 9
Summary

The measurement of $\phi(1020)$ meson production in different types of proton-proton inelastic scattering, Single Diffraction, Central Diffraction, and Non-Diffractive processes, was presented in this thesis. pp collision data collected by the ATLAS Experiment at the LHC at $\sqrt{s} = 13$ TeV were analysed to obtain $p_{\mathrm{T},\phi}$ spectrum at midrapidity $|y_\phi| < 0.8$ and $|y_\phi|$ spectrum integrated over $0.6 < p_{\mathrm{T},\phi} < 1.5$ GeV. The processes in which at least one of two incoming protons stays intact after the interaction were selected based on data gathered by the ARP detectors that enable forward-scattered protons' detection. Appropriate corrections that come from simulation or are data-driven were applied to data.

The decay channel $\phi \to K^+K^-$ was used in these measurements. Charged particles whose tracks are reconstructed in the ATLAS ID were identified to select kaons and to suppress background coming from pairs of oppositely charged particles that are not kaons. The particle identification procedure was based on ionisation energy loss and momentum measurements.

The $p_{\mathrm{T},\phi}$ and $|y_\phi|$ spectra were compared to predictions of two phenomenological models implemented in MC generators PYTHIA 8 and EPOS. The comparison between ϕ production in SD triggered data and expectations from the PYTHIA 8 and EPOS samples including all inelastic processes was made. Both generators predict similar transverse momentum and rapidity spectra and they are approximately a factor two below the data. The ϕ production rates in SD were also measured in three ξ ranges: $10^{-5} < \xi < 0.035$, $0.035 < \xi < 0.08$, and $0.08 < \xi < 0.16$ separately and they were compared to the PYTHIA 8 and EPOS inelastic samples. The predicted $p_{\mathrm{T},\phi}$ and $|y_\phi|$ spectra are about a factor of two too small compared to data for $\xi < 0.035$. PYTHIA 8 describes data better than EPOS for $0.035 < \xi < 0.08$ and $0.08 < \xi < 0.16$ but both predictions underestimate data. The best agreement between PYTHIA 8 and data is observed for $0.08 < \xi < 0.16$.

SD triggered data contain contributions from CD, DD, and ND processes that were subtracted to compare the measurement with SD expectations from PYTHIA 8 SD, EPOS SD' and EPOS SD'+SD. There is a disagreement between PYTHIA 8 SD and data and the differences are similar as in the case of the full inelastic PYTHIA 8 sample. The best agreement is observed for EPOS SD' whereas combined EPOS SD and EPOS SD' predictions are similar to those shown by PYTHIA 8 SD. The $p_{\mathrm{T},\phi}$ and $|y_\phi|$ spectra after CD, DD, and ND contributions' subtraction were compared to PYTHIA 8, EPOS SD' and EPOS SD'+SD in three ξ ranges separately. Predictions of PYTHIA 8 SD, EPOS SD' and combined EPOS SD and EPOS SD' models are similar for $0.035 < \xi < 0.08$ and $0.08 < \xi < 0.16$ and they underestimate data. EPOS SD' describes data well for $\xi > 0.035$ while the spectra shown by PYTHIA 8 SD and EPOS SD'+SD are lower than the measured ones.

The $p_{\mathrm{T},\phi}$ and $|y_\phi|$ spectra were measured in CD and compared to PYTHIA 8 CD and EPOS CD. There is quite good agreement between EPOS and data while PYTHIA 8 underestimates

the data by approximately a factor of two.

MB triggered data were used to measure ϕ production in ND processes. The results were compared to MC models. EPOS predicts higher spectrum as a function of $|y_\phi|$ than observed in data for $|y_\phi| < 0.5$ but it reproduces data well in the full $p_{\mathrm{T},\phi}$ range. The PYTHIA 8 predictions are generally too small compared to MB measurements.

The ϕ production measured using the MB data was compared to the measurement of $\phi \to K^+K^-$ production cross section in pp collisions at $\sqrt{s} = 7$ TeV obtained earlier by the ATLAS Collaboration. There is a good agreement between the $p_{\mathrm{T},\phi}$ spectra measured at $\sqrt{s} = 13$ TeV and $\sqrt{s} = 7$ TeV. The values obtained at $\sqrt{s} = 13$ TeV are higher in the range of $0.9 < p_{\mathrm{T},\phi} < 1.2$ GeV compared to the measurement at $\sqrt{s} = 7$ TeV but the differences between them remain still within uncertainties. The slightly larger spectrum at $\sqrt{s} = 13$ TeV might be related to the increasing average charged particle multiplicity for higher collision energy.

The results obtained for the ϕ meson production in SD, CD and MB triggered data were compared. The highest production rates were measured for MB while the lowest ones for CD. The ϕ production in the SD analysis was measured both in the full $\xi < 0.16$ range and in three following ranges of ξ: $10^{-5} < \xi < 0.035$, $0.035 < \xi < 0.08$, and $0.08 < \xi < 0.16$, separately. The highest $p_{\mathrm{T},\phi}$ and $|y_\phi|$ spectra were obtained for the range $0.08 < \xi < 0.16$ while the lowest ones for $10^{-5} < \xi < 0.035$. Thus, one can conclude that the different ϕ production rates in MB, CD and SD, and in SD among different ξ ranges are related to the mean number of selected particles, $\langle n_{\mathrm{sel}} \rangle$, in the given sample. It suggests that ϕ mesons originate predominantly from the fragmentation and the sensitivity of ϕ production to the initial states in the given processes, Pomeron-proton in SD, Pomeron-Pomeron in CD, and proton-proton in ND, is not observed.

The $p_{\mathrm{T},\phi}$ and $|y_\phi|$ spectra measurement presented in this thesis can provide valuable input to the development of the phenomenological hadroproduction models. In particular, the results may help with making constraints on the models' free parameters what can lead to a better theoretical description of high-energy physical processes at low momentum transfer.

Bibliography

[1] I. Łakomiec, *Study of the proton reconstruction efficiency with the ALFA detector using an overlay technique of Monte Carlo signal events with zero-bias collider data,* PoS LHCP2019 (2019) 002.

[2] D. H. Perkins, *Introduction to high energy physics.* Cambridge University Press, Cambridge, UK, 1982.

[3] E. Fermi, *On the quantization of the monoatomic ideal gas,* Rend. Lincei **3** (1926) 145.

[4] P. A. M. Dirac, *On the theory of quantum mechanics,* Proc. Roy. Soc. Lond. A **112** (1926) 661.

[5] S. N. Bose, *Plancks Gesetz und Lichtquantenhypothese,* Z. Phys. **26** (1924) 178.

[6] P. W. Higgs, *Broken Symmetries and the Masses of Gauge Bosons,* Phys. Rev. Lett. **13** (1964) 508.

[7] ATLAS Collaboration, G. Aad et al., *Observation of a new particle in the search for the Standard Model Higgs boson with the ATLAS detector at the LHC,* Phys. Lett. **B716** (2012) 1.

[8] CMS Collaboration, S. Chatrchyan et al., *Observation of a New Boson at a Mass of 125 GeV with the CMS Experiment at the LHC,* Phys. Lett. **B716** (2012) 30.

[9] P. Aurenche, *The Standard model of particle physics,* ENSLAPP-A-659-97 (1997), arXiv:hep-ph/9712342.

[10] W. Cottingham and D. Greenwood, *An Introduction to the Standard Model of Particle Physics.* Cambridge University Press, Cambridge, UK, 2007.

[11] B. Povh et al., *Particles and Nuclei: an introduction to the physical concepts;* 6th ed., Springer, Berlin, 2008.

[12] A. Deur, S. J. Brodsky and G. F. de Téramond, *The QCD running coupling,* Prog. Part. Nuc. Phys. **90** (2016) 1.

[13] Particle Data Group Collaboration, P. A. Zyla et al., *Review of Particle Physics,* Prog. Theor. Exp. Phys. **083C01** (2020).

[14] D. J. Gross and F. Wilczek, *Asymptotically Free Gauge Theories. I,* Phys. Rev. D **8** (1973) 3633.

[15] R. K. Ellis, *The Standard Theory of Particle Physics,* Chapter 3: *Quantum Chromodynamics and Deep Inelastic Scattering*, pp. 61-78 (2016).

[16] G. Dissertori, *The Standard Theory of Particle Physics,* Chapter 6: *The Determination of the Strong Coupling Constant*, pp. 113-128 (2016).

[17] P. Skands, *QCD for Collider Physics,* Lectures from the 2010 European School of High Energy Physics (ESHEP 2010), Raseborg, Finland. arXiv:1104.2863 [hep-ph]

[18] CMS Collaboration, V. Khachatryan et al., *Measurement of diffraction dissociation cross sections in pp collisions at* $\sqrt{s} = 7$ *TeV,* Phys. Rev. D **92** (2015) 012003.

[19] R. Schicker, *Diffractive production of mesons,* EPJ Web of Conferences **81** (2014) 01005.

[20] P. D. B. Collins, *An Introduction To Regge Theory And High-Energy Physics.* Cambridge University Press, Cambridge, UK, 1977.

[21] E. Levin, *An Introduction to Pomerons;* (1998), arXiv:hep-ph/9808486.

[22] T. Regge, *Introduction to complex orbital momenta,* Nuovo Cim. 14 (1959) 951.

[23] G. F. Chew and S. C. Frautschi, *Regge Trajectories and the Principle of Maximum Strength for Strong Interactions,* Phys. Rev. Lett. 8 (1962) 41.

[24] V. A. Khoze, F. Krauss, A. D. Martin, M. G. Ryskin and K. C. Zapp, *Diffraction and correlations at the LHC: definitions and observables,* Eur. Phys. J. C **69** (2010) 85.

[25] P. Z. Skands, *QCD,* in Proceedings of the 2014 Asia–Europe–Pacific School of High-Energy Physics, Puri, India, 4 – 17 November 2014, edited by M. Mulders and R. Godbole, CERN Yellow Reports: School Proceedings, Vol. 2/2017, CERN-2017-005-SP (CERN, Geneva, 2017).

[26] R. J. Fries, *Hadron Correlations from Recombination and Fragmentation,* J. Phys. **G31** (2005) S379.

[27] R. N. Cahn and G. Goldhaber, *The Experimental Foundations of Particle Physics,* Cambridge University Press, Cambridge, UK, 2009.

[28] L. Leprince-Ringuet and M. L'Héritier, *The probable existence of a particle of 900 m mass in cosmic rays,* C. R. Hebd. Acad. Sci. Paris **219** (1944) 618.

[29] G. D. Rochester and C. C. Butler, *Evidence for the Existence of New Unstable Elementary Particles,* Nature **160** (1947) 855.

[30] B. Saghai, *Associated strangeness production at intermediate energies,* Talk given at the 7. Journées d'Etudes Saturne, Ramatuelle, (France); 29 Jan - 2 Feb 1996.

[31] A. K. Wróblewski, *Hypernuclei (and Strange Particles) - How It All Began?,* Acta Phys. Pol. **B35** (2004) 3, 901.

[32] M. Gell-Mann, *Isotopic Spin and New Unstable Particles,* Phys. Rev. **92** (1953) 833.

[33] T.Nakano and K. Nishijima, *Charge Independence for V-particles,* Prog. Theor. Phys. **10** (1953) 581.

[34] K. Nishijima, *Some Remarks on the Even-odd Rule,* Prog. Theor. Phys. **12** (1954) 107.

[35] K. Nishijima, *Charge Independence Theory of V Particles,* Prog. Theor. Phys. **13** (1955) 285.

[36] J. L. Rosner and B. D. Winstein, *Kaon Physics,* University of Chicago Press, Chicago, USA, 2001.

[37] W. C. Chang and J. C. Peng, *Flavor Structure of the Nucleon Sea,* Prog. Part. Nucl. Phys. **79** (2014) 95.

[38] R. Placakyte (for the H1 Collaboration and for the ZEUS Collaboration), *Parton Distribution Functions,* Part of Proceedings, 31st International Conference on Physics in collisions (PIC 2011) : Vancouver, Canada, August 28-September 1, 2011, arXiv:1111.5452 [hep-ph]

[39] A. D. Martin, W. J. Stirling, R. S. Thorne and G. Watt, *Parton distributions for the LHC,* Eur. Phys. J. **C63** (2009) 189.

[40] A. De Roeck and R. S. Thorne, *Structure Functions,* Prog. Part. Nucl. Phys. **66** (2011) 727.

[41] E. Perez and E. Rizvi, *The Quark and Gluon Structure of the Proton,* Rep. Prog. Phys. **76** (2013) 046201.

[42] S. Forte and G. Watt, *Progress in the Determination of the Partonic Structure of the Proton,* Ann. Rev. Nucl. Part. Sci. **63** (2013) 291.

[43] P. M. Nadolsky et al., *Implications of CTEQ global analysis for collider observables,* Phys. Rev. D **78** (2008) 013004.

[44] NNPDF Collaboration, R. D. Ball et al., *A determination of parton distributions with faithful uncertainty estimation,* Nucl. Phys. B **809** (2009) 1.

[45] M. Thomson, *Modern Particle Physics,* Cambridge University Press, Cambridge, UK, 2013.

[46] K. Johannsen, *Measurement of Strangeness Production in γp Interactions at HERA with the H1 Detector,* PhD thesis, Hamburg University, Hamburg, 1996.

[47] J. Alwall et al., *Comparative study of various algorithms for the merging of parton showers and matrix elements in hadronic collisions,* Eur. Phys. J. C **53** (2009) 473.

[48] S. Mrenna and P. Richardson, *Matching Matrix Elements and Parton Showers with HERWIG and PYTHIA,* JHEP **05** (2004) 040.

[49] A. Metz and A. Vossen, *Parton Fragmentation Functions,* Prog. Part. Nucl. Phys. **91** (2016) 136.

[50] B. Andersson, G. Gustafson, G. Ingelman and T. Sjöstrand, *Parton Fragmentation and String Dynamics,* Phys. Rept. **97** (1983) 31.

[51] M. Lüscher, *Symmetry-breaking aspects of the roughening transition in gauge theories,* Nucl. Phys. **B180** (1981) 317.

[52] B. R. Webber, *A QCD model for jet fragmentation including soft gluon interference,* Nucl. Phys. **B238** (1984) 492.

[53] D. Amati, A. Bassetto, M. Ciafaloni, G. Marchesini and G. Veneziano *A treatment of hard processes sensitive to the infrared structure of QCD,* Nucl. Phys. B **173** (1980) 429.

[54] B. R. Webber, *Fragmentation and hadronization,* eConf **C990809** (2000) 577, arXiv:hep-ph/9912292.

[55] N. Hunt-Smith and P. Skands, *String fragmentation with a time-dependent tension,* Eur. Phys. J. C **80** (2020) 1073.

[56] CLAS Collaboration, M. D. Mestayer et al., *Strangeness suppression of $q\bar{q}$ creation observed in exclusive reactions,* Phys. Rev. Lett. **113** (2014) 152004.

[57] H. Satz, *Strangeness Suppression and Color Deconfinement,* EPJ Web Conf. **171** (2018) 02005.

[58] G. Bocquet et al., *A study of particle ratios and strangeness suppression in pp collisions at $\sqrt{s} = 630$ GeV with UA1,* Phys. Lett. B **366** (1996) 447.

[59] OPAL Collaboration, G. Alexander et al., *A study of K^0_S production in Z^0 decays,* Phys. Lett. B **264** (1991) 467.

[60] H1 Collaboration, F. D. Aaron et al., *Strangeness production at low Q^2 in deep-inelastic ep scattering at HERA,* Eur. Phys. J. C **61** (2009) 185.

[61] A. Beiser, *Concepts of Modern Physics,* McGraw-Hill, New York, 1973.

[62] V. Weisskopf and E. Wigner, *Calculation of the natural brightness of spectral lines on the basis of Dirac's theory,* Z. Physik **63** (1930) 54.

[63] V. Weisskopf and E. Wigner, *Over the natural line width in the radiation of the harmonic oscillator,* Z. Physik **65** (1930) 18.

[64] M. K. Hull Jr. and G. Breit, *Coulomb Wave Functions,* in Nuclear Reactions II: Theory, G. Breit, M. H. Hull, J. S. McIntosh, R. L. Gluckstern, Springer, 1959.

[65] ACCMOR Collaboration, C. Daum et al., *Inclusive ϕ-meson production in 93 and 63 GeV hadron interactions,* Nucl. Phys. B **186** (1981) 205.

[66] NA49 Collaboration, S. Afanasiev et al., *Production of ϕ-mesons in p+p, p+Pb and central Pb+Pb collisions at E_{beam} = 158 A GeV,* Phys. Lett. B **491** (2000) 59.

[67] STAR Collaboration, B. I. Abelev et al., *Measurements of ϕ meson production in relativistic heavy-ion collisions at the BNL Relativistic Heavy Ion Collider (RHIC),* Phys. Rev. C **79** (2009) 064903.

[68] ALICE Collaboration, K. Aamodt et al., *Strange particle production in proton–proton collisions at $\sqrt{s}$ = 0.9 TeV with ALICE at the LHC,* Eur. Phys. J. C **71** (2011) 1594.

[69] ALICE Collaboration, B. Abelev et al., *Production of $K^*(892)^0$ and $\phi(1020)$ in pp collisions at $\sqrt{s}$ = 7 TeV,* Eur. Phys. J. C **72** (2012) 2183.

[70] ATLAS Collaboration, G. Aad et al, *The differential production cross section of the $\phi(1020)$ meson in $\sqrt{s}$ = 7 TeV pp collisions measured with the ATLAS detector,* Eur. Phys. J. C **74** (2014) 2895.

[71] LHCb Collaboration, R. Aaij et al., *Measurement of the inclusive ϕ cross-section in pp collisions at $\sqrt{s}$ = 7 TeV,* Phys. Lett. B **703** (2011) 267.

[72] L. Bertanza et al., *Possible Resonances in the $\Xi\pi$ and KK Systems,* Phys. Rev. Lett. **9** (1962) 180.

[73] A. Marcinek, *ϕ meson production in proton-proton collisions in the NA61/SHINE experiment at CERN SPS,* PhD thesis, Jagiellonian U., Kraków, 2016.

[74] L. de Nooij, *The $\phi(1020)$-meson production cross section measured with the ATLAS detector at $\sqrt{s}$=7 TeV,* PhD thesis, University of Amsterdam, Amsterdam, 2014.

[75] T. Sjöstrand, S. Mrenna, and P. Skands, *A brief introduction to PYTHIA 8.1,* Comput. Phys. Commun. **178** (2009) 852.

[76] T. Sjöstrand et al., *An Introduction to PYTHIA 8.2,* Comput. Phys. Commun. **191** (2015) 159.

[77] K. Werner, *The hadronic interaction model EPOS,* Nucl. Phys. B - Proc. Sup. **175-176** (2008) 81.

[78] A. Buckley et al., *General-purpose event generators for LHC physics,* Phys. Rept. **504** (2011) 145.

[79] T. Sjöstrand, *Status and developments of event generators,* PoS LHCP2016 (2016) 007.

[80] T. Sjöstrand and M. van Zijl, *A multiple-interaction model for the event structure in hadron collisions,* Phys. Rev. D **36** (1987) 2019.

[81] T. Sjöstrand, *The Development of MPI Modeling in Pythia,* in Multiple Parton Interactions at the LHC, ed. P. Bartalini and J. R. Gaunt, World Scientific, 2018.

[82] T. Pierog et al., *EPOS LHC: Test of collective hadronization with data measured at the CERN Large Hadron Collider,* Phys. Rev. C **92** (2015) 034906.

[83] ATLAS Collaboration, *Further ATLAS tunes of PYTHIA6 and Pythia 8,* ATL-PHYS-PUB-2011-014, https://cds.cern.ch/record/1400677/.

[84] ATLAS Collaboration, *The Pythia 8 A3 tune description of ATLAS minimum bias and inelastic measurements incorporating the Donnachie-Landshoff diffractive model,* ATL-PHYS-PUB-2016-017, https://cds.cern.ch/record/2206965/

[85] A. Cătălin et al., *Study of Monte Carlo event generators for proton-proton collisions at LHC energies in the forward region,* Chinese Phys. C **43** (2019) 083001.

[86] S. Porteboeuf, T. Pierog, and K. Werner, *Producing hard processes regarding the complete event: the EPOS event generator,* in *Proceedings, 45th Rencontres de Moriond on QCD and High Energy Interactions: La Thuile, Italy, March 13-20, 2010.* arXiv:1006.2967 [hep-ph]

[87] T. Pierog and K. Werner, *EPOS Model and Ultra High Energy Cosmic Ray,* Nucl. Phys. B - Proc. Sup. **196** (2009) 102.

[88] K. Werner et al., *Evidence for hydrodynamic evolution in proton-proton scattering at 900 GeV,* Phys. Rev. C **83** (2011) 044915.

[89] H. J. Drescher et al., *Parton based Gribov-Regge theory,* Phys. Rept. **350** (2001) 93.

[90] Ł. Fulek, *Charged particle production in diffractive proton-proton scattering at the RHIC and LHC energies,* PhD thesis, AGH University of Science and Technology, Kraków, 2020.

[91] K. Werner et al., *Event-by-event simulation of the three-dimensional hydrodynamic evolution from flux tube initial conditions in ultrarelativistic heavy ion collisions,* Phys. Rev. C **82** (2010) 044904.

[92] C. Blume and C. Markert, *Strange hadron production in heavy ion collisions from SPS to RHIC,* Prog. Part. Nucl. Phys. **66** (2011) 834.

[93] R. Pasechnik and M. Šumbera, *Phenomenological Review on Quark–Gluon Plasma: Concepts vs. Observations,* Universe **3** (2017) 7.

[94] J. Rafelski, *Discovery of Quark-Gluon Plasma: Strangeness Diaries,* Eur. Phys. J. Spec. Top. **229** (2020) 1.

[95] P. Koch, B. Müller, and J. Rafelski, *Strangeness in relativistic heavy ion collisions,* Phys. Rept. **142** (1986) 167.

[96] L. McLerran, *Strangeness in the central region,* Nucl. Phys. A **461** (1987) 245.

[97] N. K. Behera, R. Sahoo and B. K. Nandi, *Constituent Quark Scaling of Strangeness Enhancement in Heavy-Ion Collisions,* Adv. High Energy Phys. **2013** (2013) 273248.

[98] STAR Collaboration, J. Adams et al., *Experimental and theoretical challenges in the search for the quark-gluon plasma: the star collaboration's critical assessment of the evidence from RHIC collisions,* Nucl. Phys. A **757** (2005) 102.

[99] PHENIX Collaboration, K. Adcox et al., *Formation of dense partonic matter in relativistic nucleus-nucleus collisions at RHIC: experimental evaluation by the PHENIX Collaboration,* Nucl. Phys. A **757** (2005) 184.

[100] J. Rafelski and B. Müller, *Strangeness production in the quark-gluon plasma,* Phys. Rev. Lett. **48** (1982) 1066.

[101] J. Rafelski and B. Müller, *Strangeness production in the Quark-Gluon plasma,* Phys. Rev. Lett. **56** (1986) 2334.

[102] R. Sahoo, T. K. Nayak, *Possible early universe signals in proton collisions at the Large Hadron Collider,* Current Science **121** (2021) 1403.

[103] ALICE Collaboration, J. Adam et al., *Enhanced production of multi-strange hadrons in high-multiplicity proton–proton collisions,* Nature Phys **13** (2017) 535.

[104] A. Cisek and A. Szczurek, *Two-gluon production of ϕ and η' mesons in proton-proton collisions at high energies,* Phys. Rev. D **103** (2021) 114008.

[105] Ch. Bierlich, G. Gustafson, L. Lönnblad and A. Tarasov, *Effects of overlapping strings in pp collisions,* J. High Energ. Phys. **2015** (2015) 148.

[106] S. Zhang et al., *Multiplicity Dependence of Charged Particle, ϕ Meson and Multi-strange Particle Productions in $p+p$ Collisions at $\sqrt{s}$ = 200 GeV with PYTHIA Simulation,* NUCL SCI TECH **29** (2018) 136.

[107] A. Shor, *ϕ-Meson Production as a Probe of the Quark-Gluon Plasma,* Phys. Rev. Lett. **54** (1985) 1122.

[108] NA49 Collaboration, C. Alt et al., *Energy dependence of ϕ meson production in central Pb+Pb collisions at $\sqrt{s_{NN}}$ = 6 to 17 GeV,* Phys. Rev. C **78** (2008) 044907.

[109] L. Evans and P. Bryant, *LHC Machine,* JINST **3** (2008) S08001.

[110] O. Brüning, H. Burkhardt and S. Myers, *The Large Hadron Collider,* Prog. Part. Nucl. Phys. **67** (2012) 705.

[111] *Overall view of the LHC*, https://cds.cern.ch/record/1708847/.

[112] ATLAS Collaboration, G. Aad et al., *The ATLAS Experiment at the CERN Large Hadron Collider*, JINST **3** (2008) S08003.

[113] CMS Collaboration, S. Chatrchyan et al., *The CMS Experiment at the CERN LHC,* JINST **3** (2008) S08004.

[114] LHCb Collaboration, A. A. Alves, Jr. et al., *The LHCb Detector at the LHC,* JINST **3** (2008) S08005.

[115] ALICE Collaboration, K. Aamodt et al., *The ALICE experiment at the CERN LHC,* JINST **3** (2008) S08002.

[116] K. Schindl, LEP performance, *LEP performance. Proceedings, 9th Workshop, Chamonix, France, January 26-29, 1999: The injector chain for the LHC. 1999. CERN-PS-99-018-DI,* https://cds.cern.ch/record/384396/.

[117] B. Roderik et al., *Proceedings, 57th ICFA Advanced Beam Dynamics Workshop on High-Intensity and High-Brightness Hadron Beams (HB2016) : Malmö, Sweden, July 3-8, 2016: LHC Run 2: Results and challenges. 2016. CERN-ACC-2016-0103,* http://cds.cern.ch/record/2201447/.

[118] K. Potamianos, *The upgraded Pixel detector and the commissioning of the Inner Detector tracking of the ATLAS experiment for Run-2 at the Large Hadron Collider,* PoS EPS-HEP2015 (2015) 261, arXiv:1608.07850 [physics.ins-det].

[119] ATLAS Collaboration, *ATLAS Inner Detector: Technical Design Report, 1,* CERN-LHCC-97-16, ATLAS-TDR-4 (1997), https://cds.cern.ch/record/331063/; *ATLAS Inner Detector: Technical Design Report, 2,* CERN-LHCC-97-017, ATLAS-TDR-5 (1997), https://cds.cern.ch/record/331064/.

[120] ATLAS Collaboration, *ATLAS pixel detector: Technical Design Report,* CERN-LHCC-98-013, ATLAS-TDR-11 (1998), https://cds.cern.ch/record/381263/.

[121] ATLAS Collaboration, G. Aad et al., *ATLAS pixel detector electronics and sensors,* JINST **3** (2008) P07007.

[122] ATLAS Collaboration, M. Capeans et al., *ATLAS Insertable B-Layer Technical Design Report,* ATLAS-TDR-19 (2010), https://cds.cern.ch/record/1291633/.

[123] E. Stanecka, *ATLAS Inner Tracker Performance at the Beginning of the LHC Run 2,* Acta Phys. Pol. B **47** (2016) 1739.

[124] ATLAS Collaboration, G. Aad et al., *Operation and performance of the ATLAS semiconductor tracker,* JINST **9** (2014) P08009.

[125] ATLAS TRT Collaboration, E. Abat et al., *The ATLAS Transition Radiation Tracker (TRT) proportional drift tube: design and performance,* JINST **3** (2008) P02013.

[126] F. Huegging, *The ATLAS Pixel Detector,* IEEE Trans. Nucl. Sci. **53** (2006) 1732.

[127] C. Troncon, *Detailed Studies of the ATLAS Pixel Detectors,* IEEE Trans. Nucl. Sci. **47** (2000) 737.

[128] M. Keil, *Operational Experience with the ATLAS Pixel Detector at the LHC,* Phys. Procedia **37** (2012) 907.

[129] A. Abdesselam et al., *The barrel modules of the ATLAS semiconductor tracker,* Nucl. Instrum. Meth. A **568** (2006) 642.

[130] A. Abdesselam et al., *The ATLAS semiconductor tracker end-cap module,* Nucl. Instr. Methods A **575** (2007) 353.

[131] ATLAS TRT Collaboration, E. Abat et al., *The ATLAS TRT barrel detector,* JINST **3** (2008) P02014.

[132] ATLAS TRT Collaboration, E. Abat et al., *The ATLAS TRT end-cap detectors,* JINST **3** (2008) P10003.

[133] E. Hines, *Performance of Particle Identification with the ATLAS Transition Radiation Tracker,* in *Proceedings, The Meeting of the Division of Particles and Fields of the American Physical Society (DPF), 2011*, arXiv:1109.5925 [physics.ins-det].

[134] A. Sidoti, *Minimum Bias Trigger Scintillators in ATLAS Run II,* JINST **9** (2014) C10020.

[135] ATLAS Collaboration, M. Aaboud et al., *Measurement of the Inelastic Proton-Proton Cross Section at $\sqrt{s}$ = 13 TeV with the ATLAS Detector at the LHC,* Phys. Rev. Lett. **117** (2016) 182002.

[136] ATLAS Collaboration, *ATLAS liquid-argon calorimeter: Technical Design Report,* CERN-LHCC-96-041, ATLAS-TDR-2 (1996), https://cds.cern.ch/record/331061/.

[137] ATLAS Collaboration, *ATLAS tile calorimeter: Technical design report,* CERN-LHCC-96-42 (1996), https://cds.cern.ch/record/331062/.

[138] ATLAS Collaboration, *ATLAS muon spectrometer: Technical Design Report,* CERN-LHCC-97-022, ATLAS-TDR-10 (1997) https://cds.cern.ch/record/331068/.

[139] A. Artamonov et al., *The ATLAS Forward Calorimeter,* JINST **3** (2008) P02010.

[140] P. Jenni et al., *ATLAS Forward Detectors for Measurement of Elastic Scattering and Luminosity,* ATLAS-TDR-18 (2008), http://cds.cern.ch/record/1095847/.

[141] S. Abdel Khalek et al., *The ALFA Roman Pot Detectors of ATLAS,* JINST **11** (2016) P11013.

[142] L. Adamczyk et al., *Technical Design Report for the ATLAS Forward Proton Detector,* ATLAS-TDR-024 (2015), https://cds.cern.ch/record/2017378/.

[143] ATLAS Collaboration, G. Aad et al., *Measurement of the total cross section from elastic scattering in pp collisions at $\sqrt{s}$ = 7 TeV with the ATLAS detector,* Nucl. Phys. B **889** (2014) 486.

[144] J. Chwastowski et al., *Feasibility studies of the diffractive bremsstrahlung measurement at the LHC,* Eur. Phys. J. C **76** (2016) 354.

[145] ATLAS Collaboration, G. Aad et al., *The ATLAS Simulation Infrastructure,* Eur. Phys. J. C **70** (2010) 823.

[146] ATLAS Collaboration, *ATLAS Computing Technical Design Report,* ATLAS-TDR-17, CERN-LHCC-2005-022 (2005), https://cds.cern.ch/record/837738/.

[147] A. R. Martínez, *The Run-2 ATLAS Trigger System,* J. Phys. Conf. Ser. **762** (2016) 012003.

[148] ATLAS Collaboration, *ATLAS high-level trigger, data acquisition and controls: Technical design report,* CERN-LHCC-2003-022, ATLAS-TRD-016 (2003), https://cds.cern.ch/record/616089/.

[149] ATLAS TDAQ Collaboration, M. Abolins et al., *The ATLAS Data Acquisition and High Level Trigger system,* JINST **11** (2016) P06008.

[150] S. Ask et al., *The ATLAS central level-1 trigger logic and TTC system,* JINST **3** (2008) P08002.

[151] B. Allongue et al., *The electronics system of the ALFA forward detector for luminosity measurements in ATLAS,* JINST **7** (2012) C02034.

[152] G. Galster, *The Central Trigger Processor of the ATLAS Experiment at the LHC and its Monitoring,* PhD thesis, University of Copenhagen, Copenhagen, 2019.

[153] N. Ellis et al., *The ATLAS Level-1 Central Trigger Processor (CTP),* ATL-DAQ-2003-036, http://cds.cern.ch/record/685567/.

[154] S. Jakobsen, *ALFA latency for Run1 and expectations for Run2, Tech. Rep.* ATL-COM-LUM-2013-018.

[155] R. Sikora, *Measurement of the diffractive central exclusive production in the STAR experiment at RHIC and the ATLAS experiment at LHC,* PhD thesis, AGH University of Science and Technology, Kraków, 2020.

[156] GEANT4 Collaboration, S. Agostinelli et al., *GEANT4: A Simulation toolkit,* Nucl. Instrum. Meth. A **506** (2003) 250.

[157] A. P. Lind, *A Study of Diffractive Scattering with the ATLAS and ALFA Experiment,* Master's thesis, University of Copenhagen, Copenhagen, 2017.

[158] P. Bussey, *FPTrack Programme,* http://www.ppe.gla.ac.uk/ bussey/FPTRACK, (2008).

[159] S. S. Mortensen, *Kinematic reconstruction of diffractive processes - with tagged protons in the ALFA detector at $\sqrt{s}$ = 8 TeV,* Master's Thesis, University of Copenhagen, Copenhagen, 2013.

[160] M. A. Medici, *Diffraction with ALFA and ATLAS at $\sqrt{s}$ = 8 TeV,* Master's Thesis, University of Copenhagen, Copenhagen, 2013.

[161] S. Carrazza, S. Forte, and J. Rojo, *Parton Distributions and Event Generators,* in *Proceedings, 43rd International Symposium on Multiparticle Dynamics (ISMD 13)*, 2013, arXiv:1311.5887 [hep-ph].

[162] ATLAS Collaboration, *Charged-particle distributions at low transverse momentum in $\sqrt{s}$ = 13 TeV pp interactions measured with the ATLAS detector at the LHC,* Eur. Phys. J. C **76** (2016) 502.

[163] ATLAS Collaboration, *Dijet production in $\sqrt{s}$ = 7 TeV pp collisions with large rapidity gaps at the ATLAS experiment,* Phys. Lett. B **754** (2016) 214.

[164] S. Czekierda, *Hadronic final states in diffractive pp scattering at $\sqrt{s}$ = 13 TeV using the ATLAS detector,* PhD thesis, The H. Niewodniczański Institute of Nuclear Physics, Polish Academy of Sciences, Kraków, 2019.

[165] ATLAS Collaboration, *dE/dx measurement in the ATLAS Pixel Detector and its use for particle identification,* ATLAS-CONF-2011-016, https://cds.cern.ch/record/1336519/.

[166] ATLAS Collaboration, *Search for metastable heavy charged particles with large ionization energy loss in pp collisions at $\sqrt{s}$ = 13 TeV using the ATLAS experiment,* Phys. Rev. D **93** (2016) 112015.

[167] H. Bethe and J. Ashkin, *Experimental Nuclear Physics.* Wiley, New York, 1953.

[168] S. Das, *A simple alternative to the Crystal Ball function,* arXiv:1603.08591 [hep-ex].

[169] I. Łakomiec, *Production of strange hadrons in proton-proton scattering using ATLAS detector,* Master's thesis, AGH University of Science and Technology,, Kraków, 2017.

[170] L. Adamczyk and I. Lakomiec, *Study of the proton reconstruction efficiency with the ALFA detector using an overlay technique of Monte Carlo signal events with zero-bias collider data,* ATL-COM-FWD-2021-016, https://cds.cern.ch/record/2779697/.

[171] ATLAS Collaboration, *Studies of the ATLAS Inner Detector material using $\sqrt{s}$ = 13 TeV pp collision data,* ATL-PHYS-PUB-2015-050, http://cdsweb.cern.ch/record/2109010/.

[172] L. Adamczyk and R. Sikora, *Central Exclusive Production in proton-proton collisions at $\sqrt{s}$ = 13 TeV with the measurement of forward protons in ALFA,* ATL-COM-PHYS-2022-194, https://cds.cern.ch/record/2804943/.

[173] ATLAS Collaboration, *Charged-particle multiplicities in pp interactions measured with the ATLAS detector at the LHC,* New J. Phys. **13** (2011) 053033.

Appendix A

Fits to the distributions of $\ln(\mathrm{d}E/\mathrm{d}x)$ in MC and data.

A.1 MC

ExpGaussExp (3.4) fits to $\ln(\mathrm{d}E/\mathrm{d}x)$ distributions for PYTHIA 8. The fits were performed in six ranges of the reconstructed momentum, corrected for the bias in the momentum reconstruction (the corrections are described in Section 3.1) momentum: 0.29 - 0.4 - 0.5 - 0.7 - 0.9 - 1.1 - 1.2 GeV - separately for negatively and positively charged pions (Figures A.1.1 - A.1.6), kaons (Figures A.1.7 - A.1.12) and protons (Figures A.1.13 - A.1.18) and for two, three and more than three PD hits. The fitting description is discussed in Section 3.2. The fit results are displayed in the plots.

Dependencies of ExpGaussExp (3.4) fit parameters (σ, k_{L} and k_{H}) on the momentum - separately for negatively and positively charged pions (Figures A.1.19 - A.1.21), kaons (Figures A.1.22 - A.1.24) and protons (Figures A.1.25 - A.1.27) and for two, three and more than three PD hits. Linear, second order polynomial or exponential functions were fitted to describe the dependencies of the fit parameters on the momentum and the results are displayed in the plots. The fitting description is presented in Section 3.2.

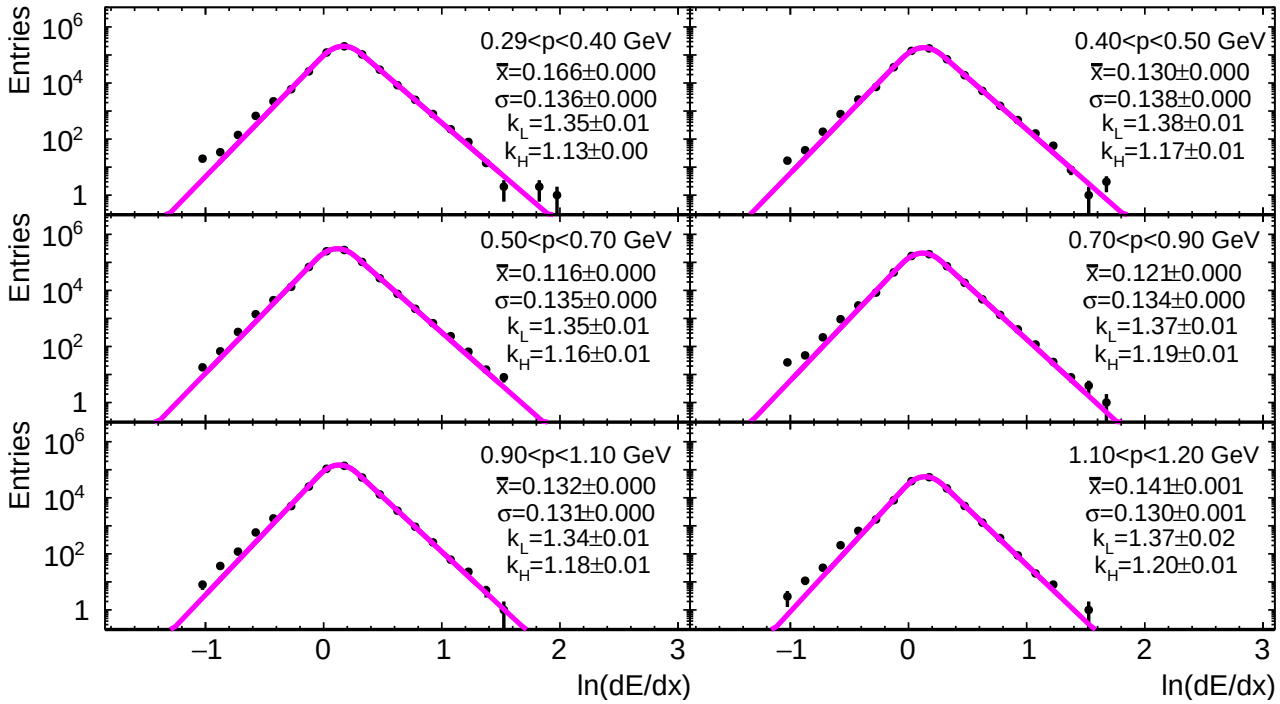

Figure A.1.1: Distributions of $\ln(\mathrm{d}E/\mathrm{d}x)$ for PYTHIA 8 in six momentum ranges for negative pions and two PD hits. The parameters of the fitted function (3.4) are displayed in the plots.

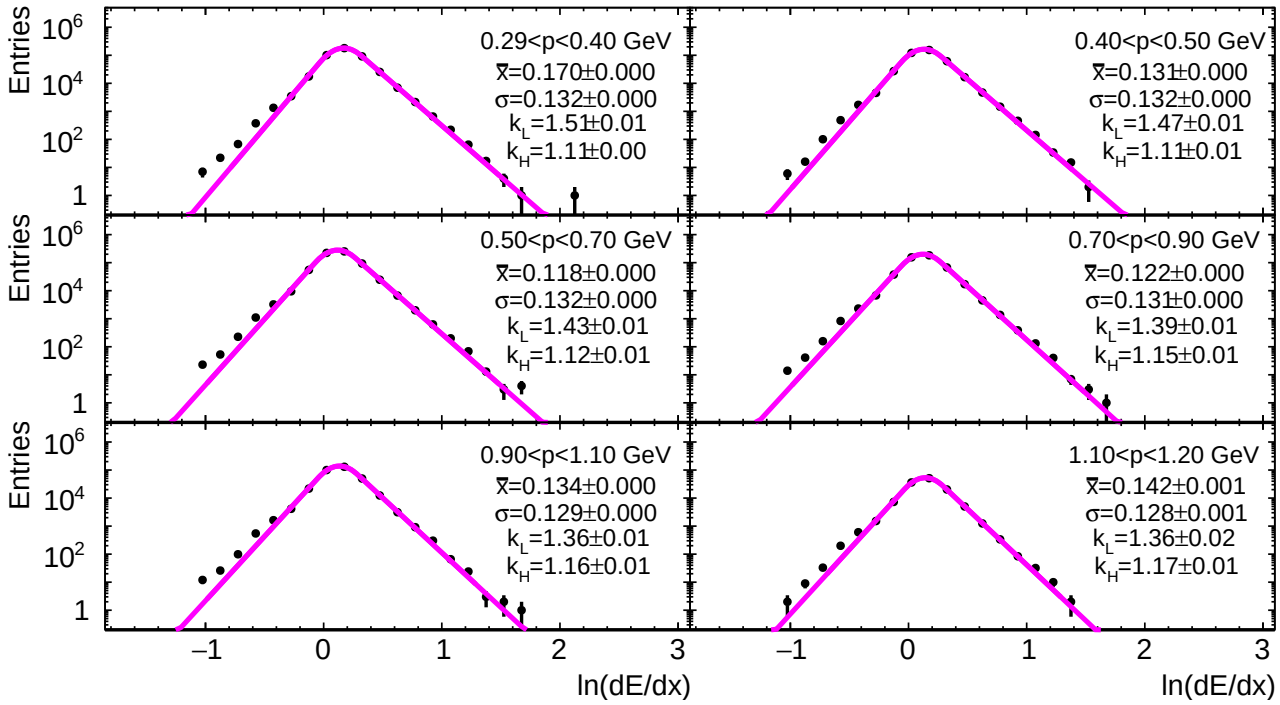

Figure A.1.2: Distributions of $\ln(\mathrm{d}E/\mathrm{d}x)$ for PYTHIA 8 in six momentum ranges for positive pions and two PD hits. The parameters of the fitted function (3.4) are displayed in the plots.

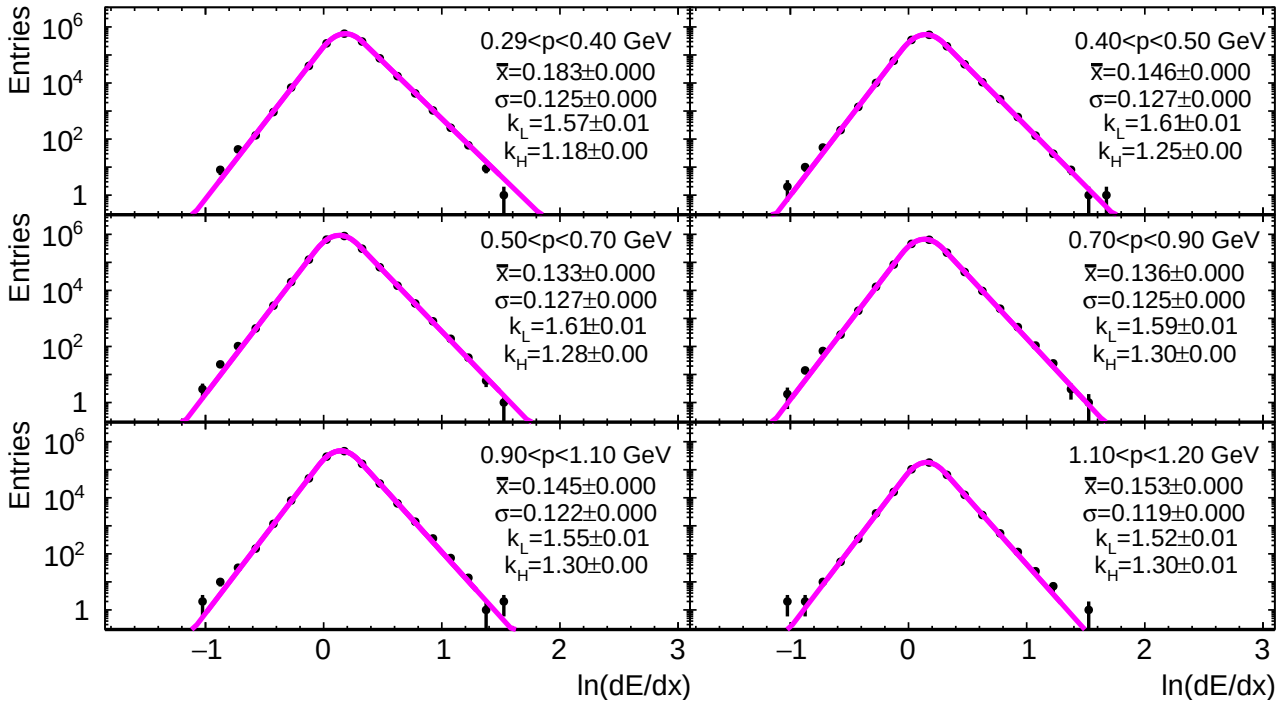

Figure A.1.3: Distributions of $\ln(\mathrm{d}E/\mathrm{d}x)$ for PYTHIA 8 in six momentum ranges for negative pions and three PD hits. The parameters of the fitted function (3.4) are displayed in the plots.

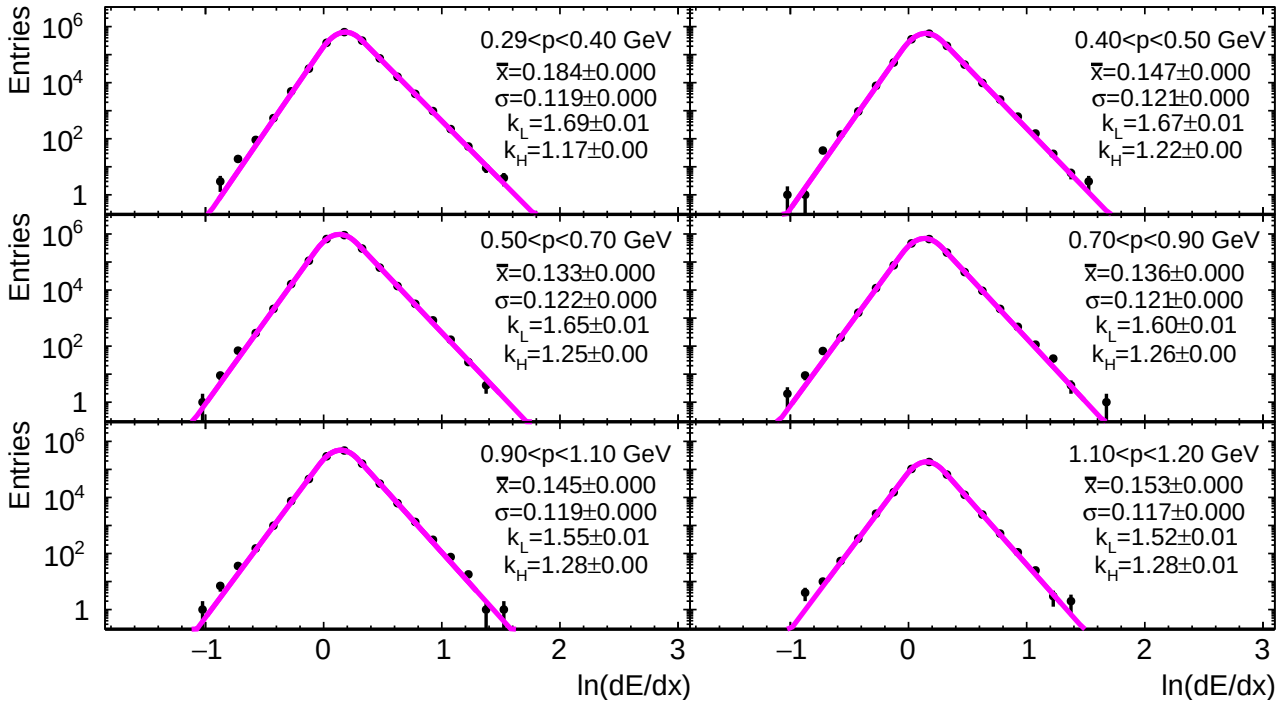

Figure A.1.4: Distributions of $\ln(\mathrm{d}E/\mathrm{d}x)$ for PYTHIA 8 in six momentum ranges for positive pions and three PD hits. The parameters of the fitted function (3.4) are displayed in the plots.

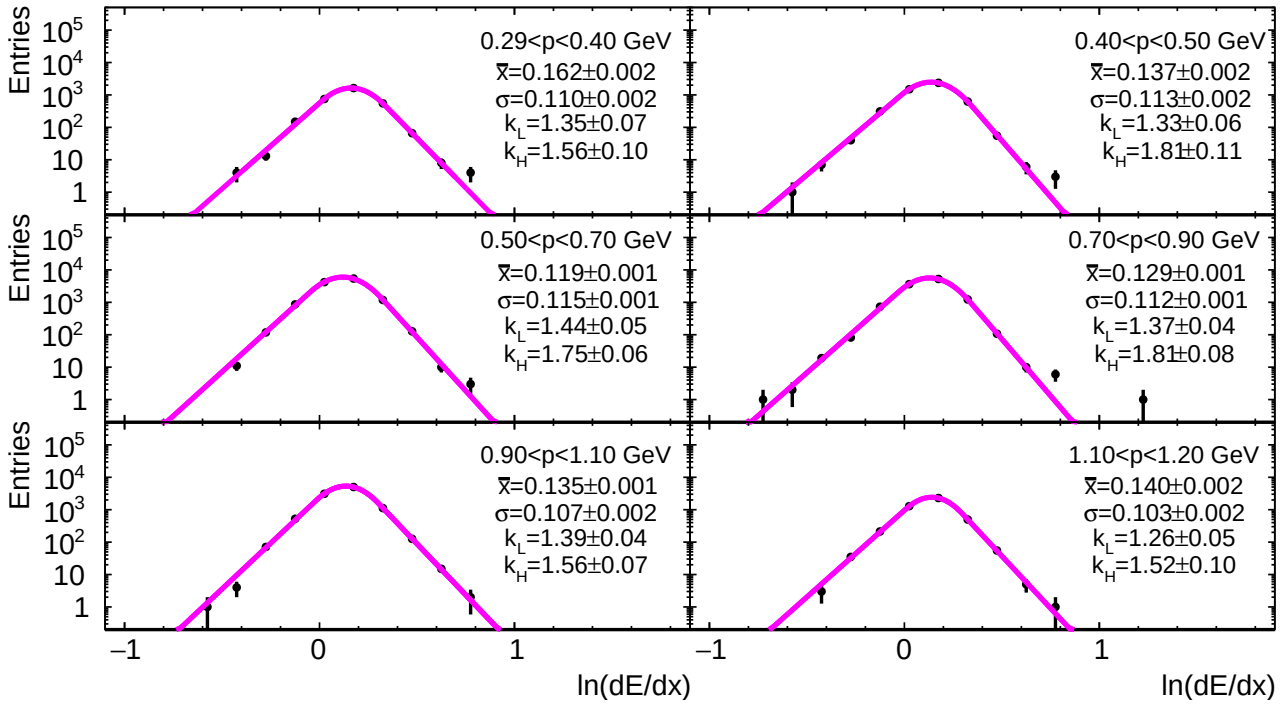

Figure A.1.5: Distributions of $\ln(\mathrm{d}E/\mathrm{d}x)$ for PYTHIA 8 in six momentum ranges for negative pions and more than three PD hits. The parameters of the fitted function (3.4) are displayed in the plots.

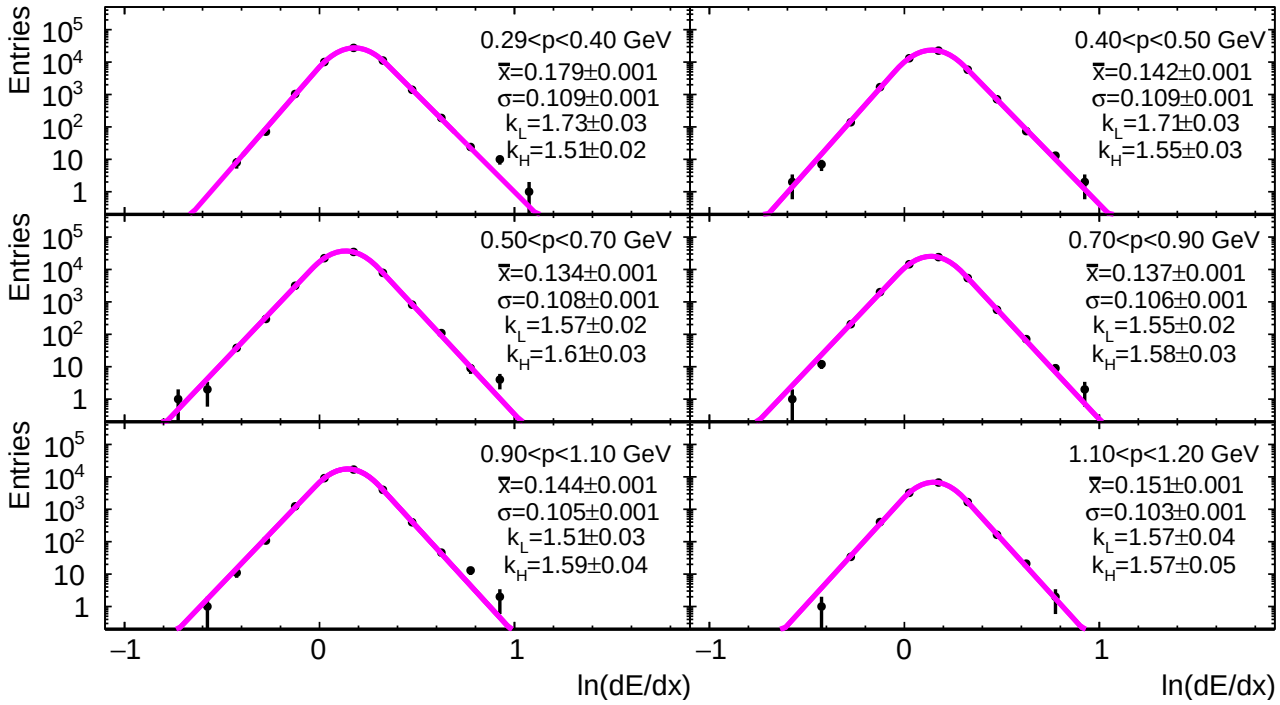

Figure A.1.6: Distributions of $\ln(\mathrm{d}E/\mathrm{d}x)$ for PYTHIA 8 in six momentum ranges for positive pions and more than three PD hits. The parameters of the fitted function (3.4) are displayed in the plots.

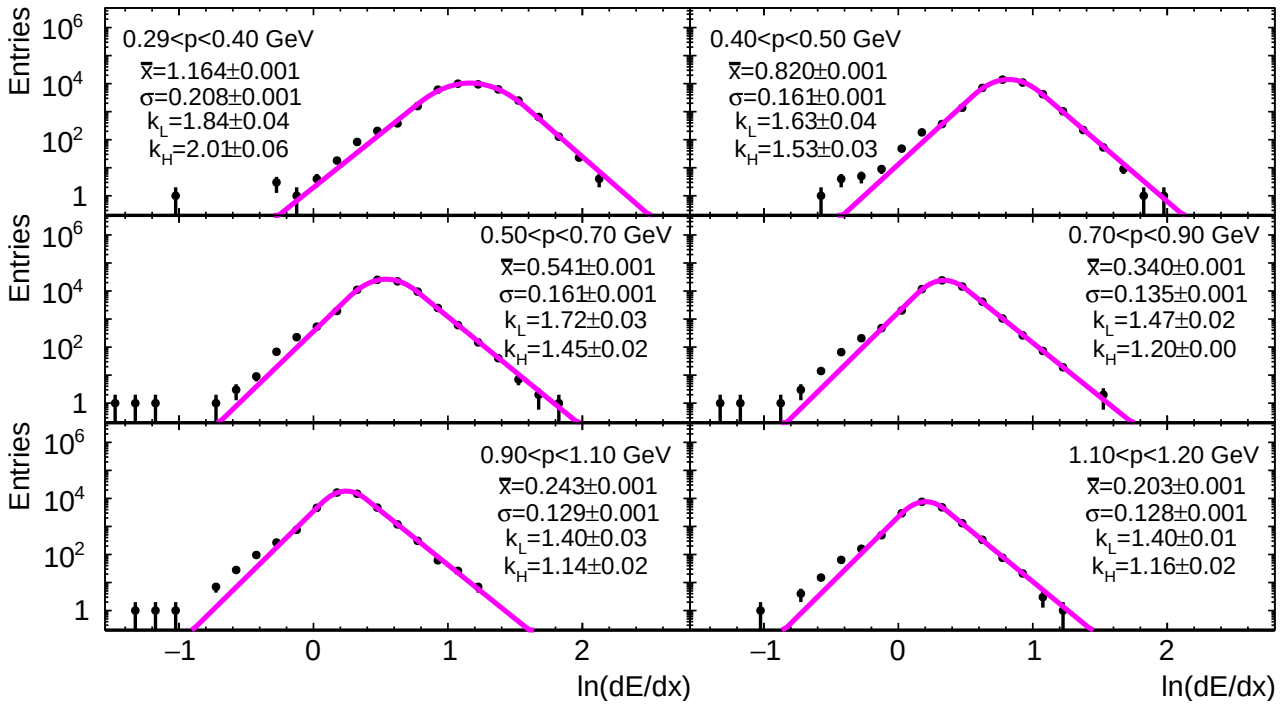

Figure A.1.7: Distributions of $\ln(\mathrm{d}E/\mathrm{d}x)$ for PYTHIA 8 in six momentum ranges for negative kaons and two PD hits. The parameters of the fitted function (3.4) are displayed in the plots.

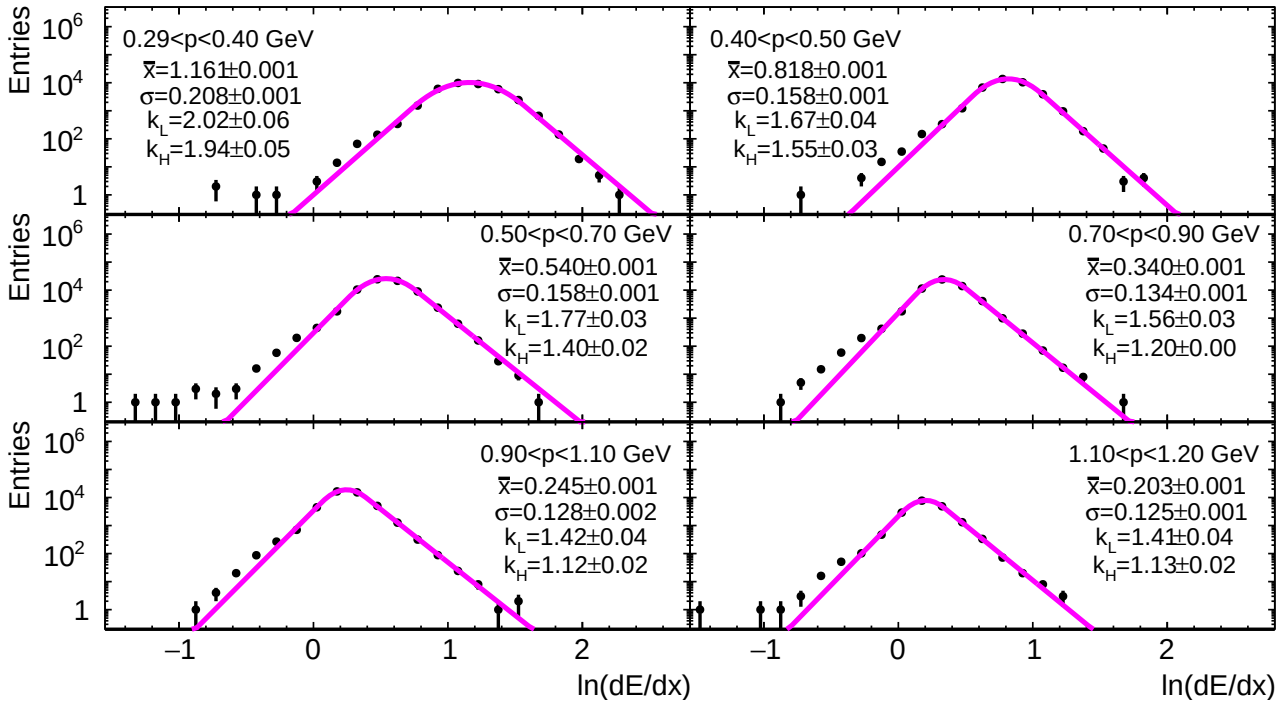

Figure A.1.8: Distributions of $\ln(\mathrm{d}E/\mathrm{d}x)$ for PYTHIA 8 in six momentum ranges for positive kaons and two PD hits. The parameters of the fitted function (3.4) are displayed in the plots.

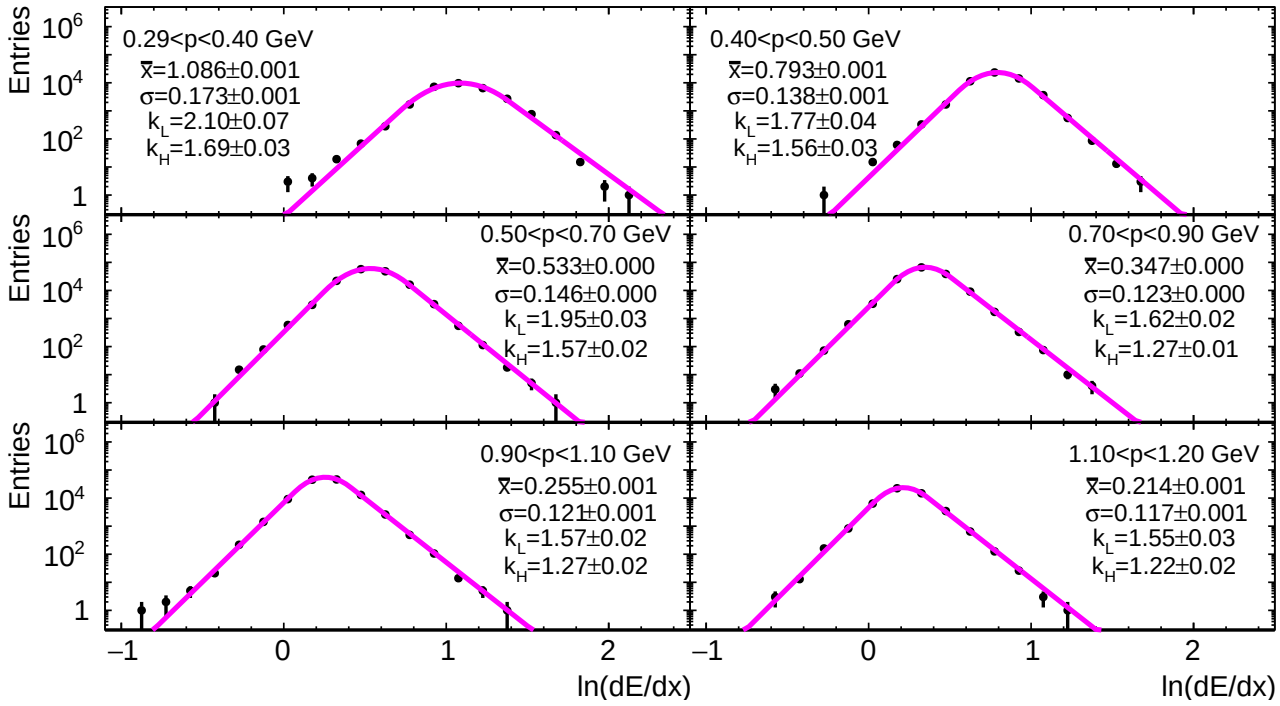

Figure A.1.9: Distributions of $\ln(\mathrm{d}E/\mathrm{d}x)$ for PYTHIA 8 in six momentum ranges for negative kaons and three PD hits. The parameters of the fitted function (3.4) are displayed in the plots.

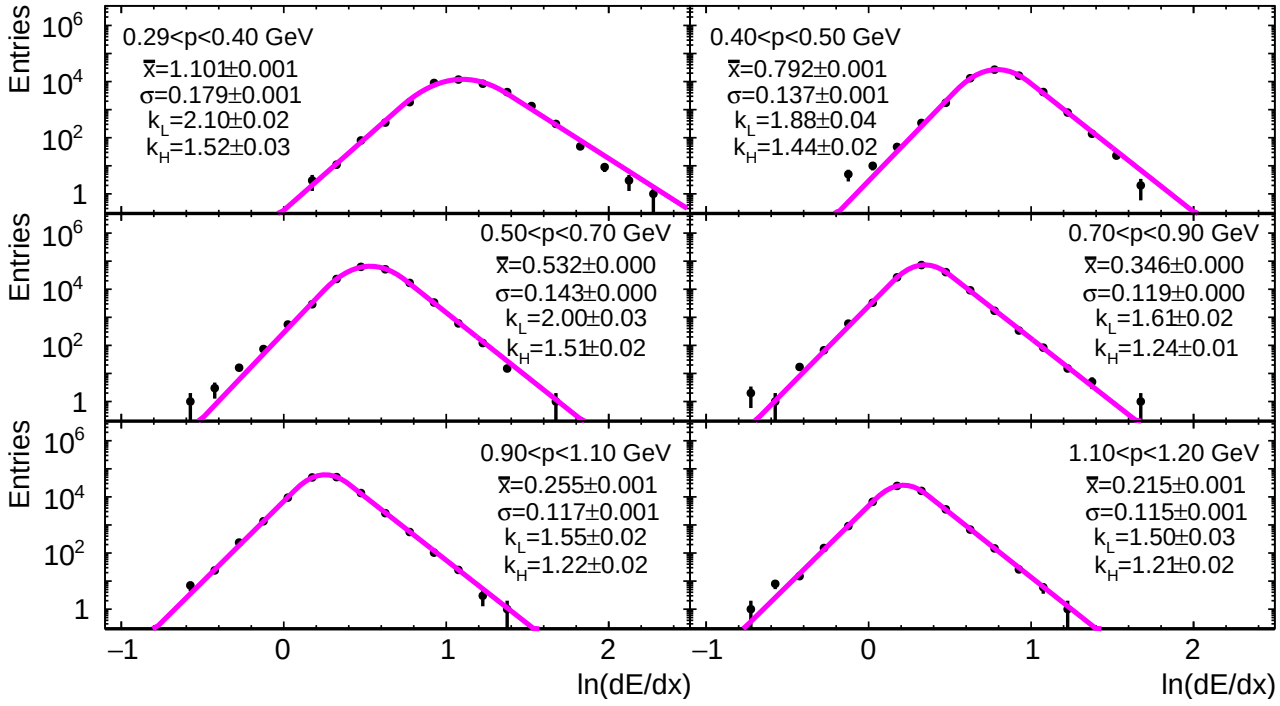

Figure A.1.10: Distributions of $\ln(\mathrm{d}E/\mathrm{d}x)$ for PYTHIA 8 in six momentum ranges for positive kaons and three PD hits. The parameters of the fitted function (3.4) are displayed in the plots.

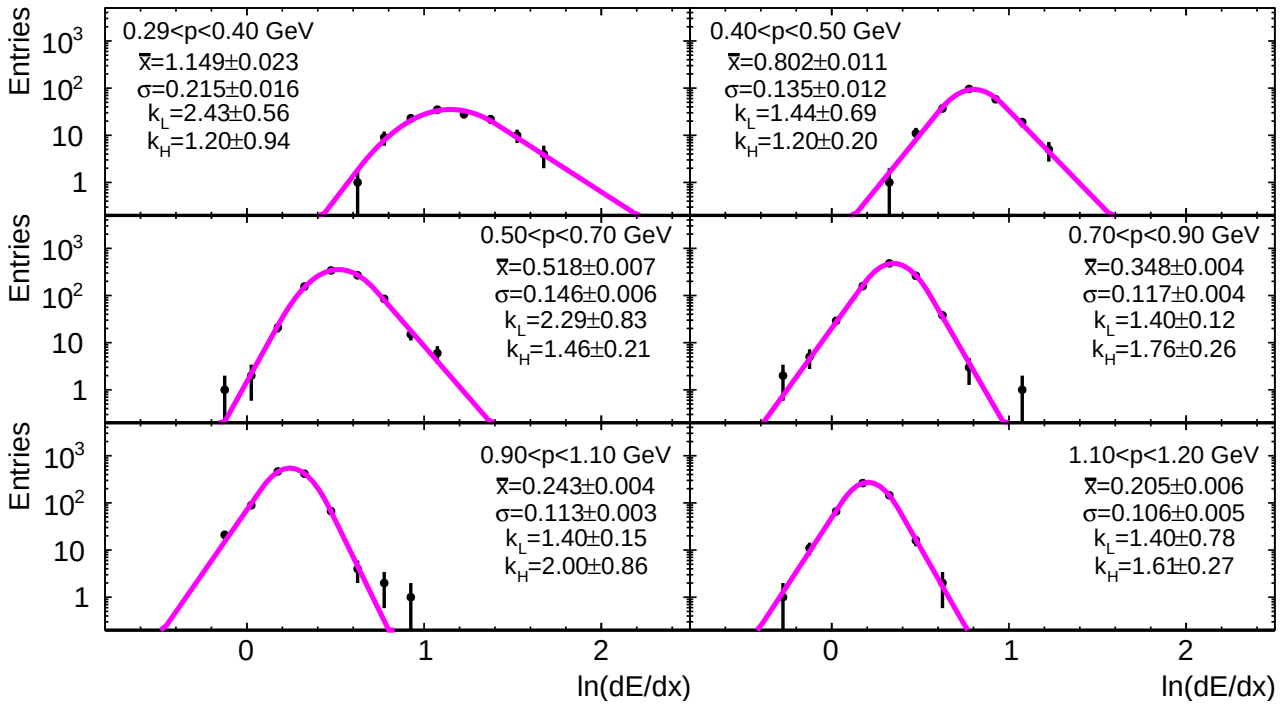

Figure A.1.11: Distributions of $\ln(\mathrm{d}E/\mathrm{d}x)$ for PYTHIA 8 in six momentum ranges for negative kaons and more than three PD hits. The parameters of the fitted function (3.4) are displayed in the plots.

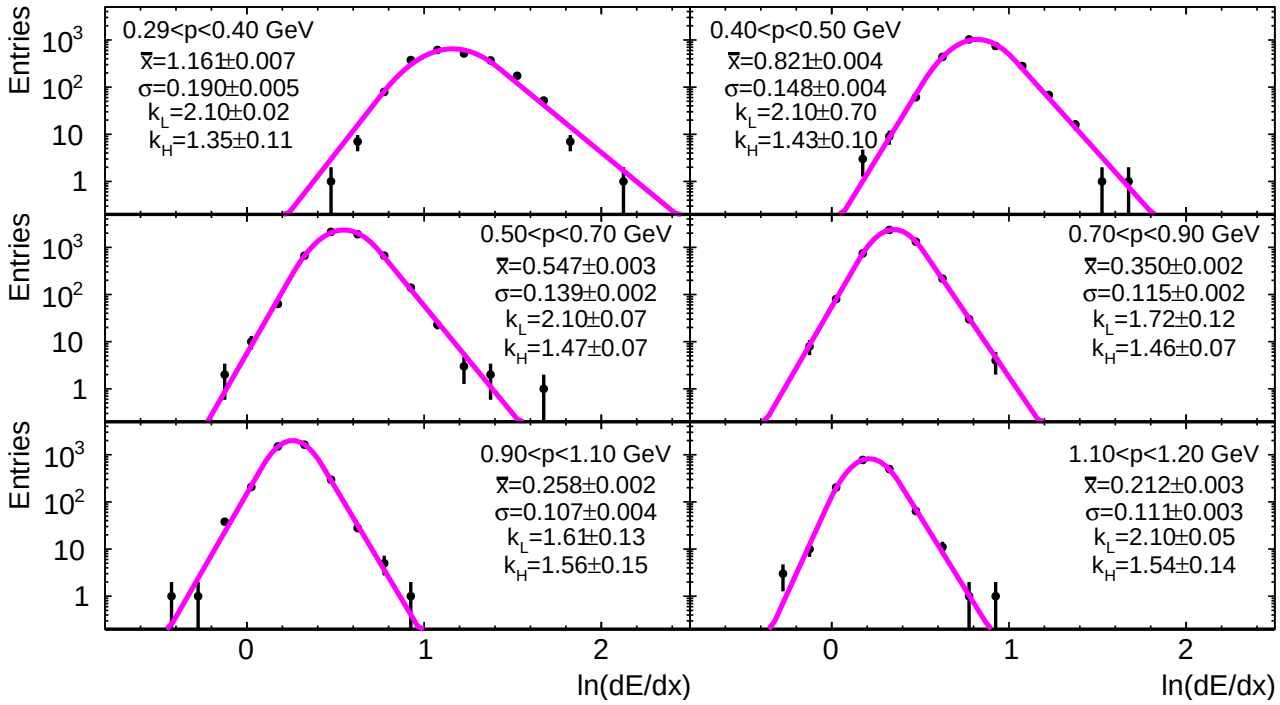

Figure A.1.12: Distributions of $\ln(\mathrm{d}E/\mathrm{d}x)$ for PYTHIA 8 in six momentum ranges for positive kaons and more than three PD hits. The parameters of the fitted function (3.4) are displayed in the plots.

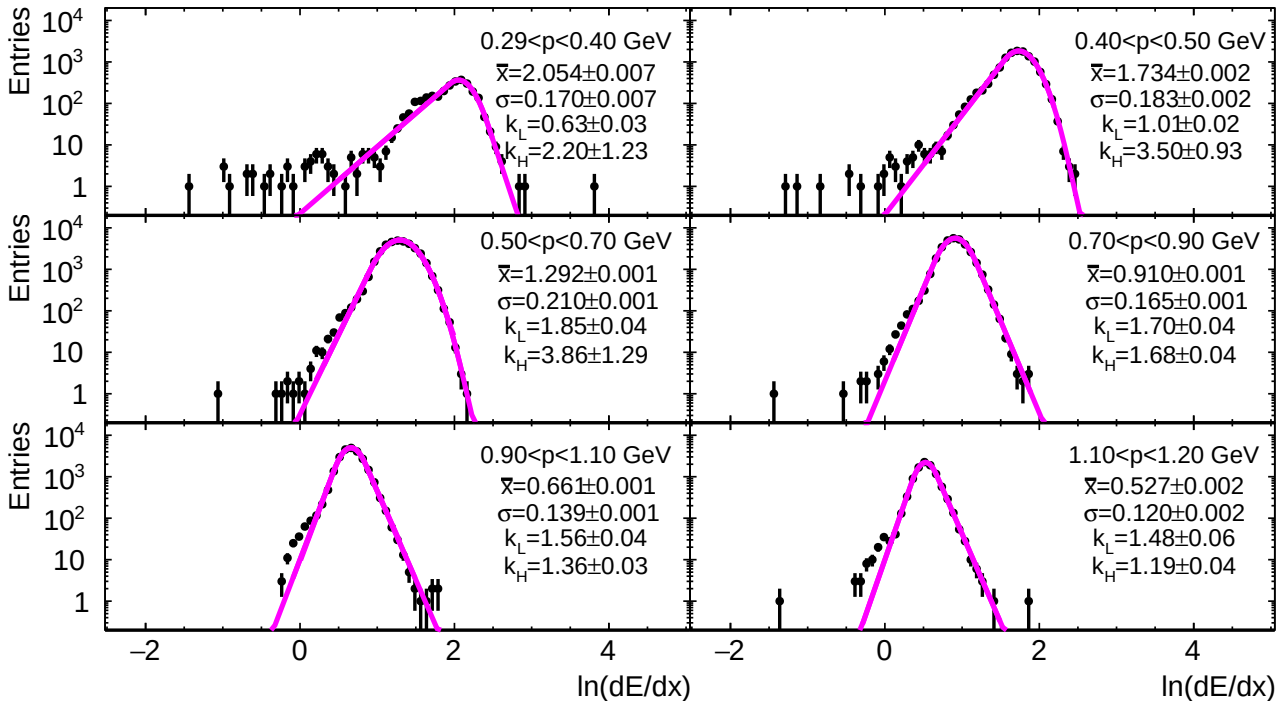

Figure A.1.13: Distributions of $\ln(\mathrm{d}E/\mathrm{d}x)$ for PYTHIA 8 in six momentum ranges for antiprotons and two PD hits. The parameters of the fitted function (3.4) are displayed in the plots.

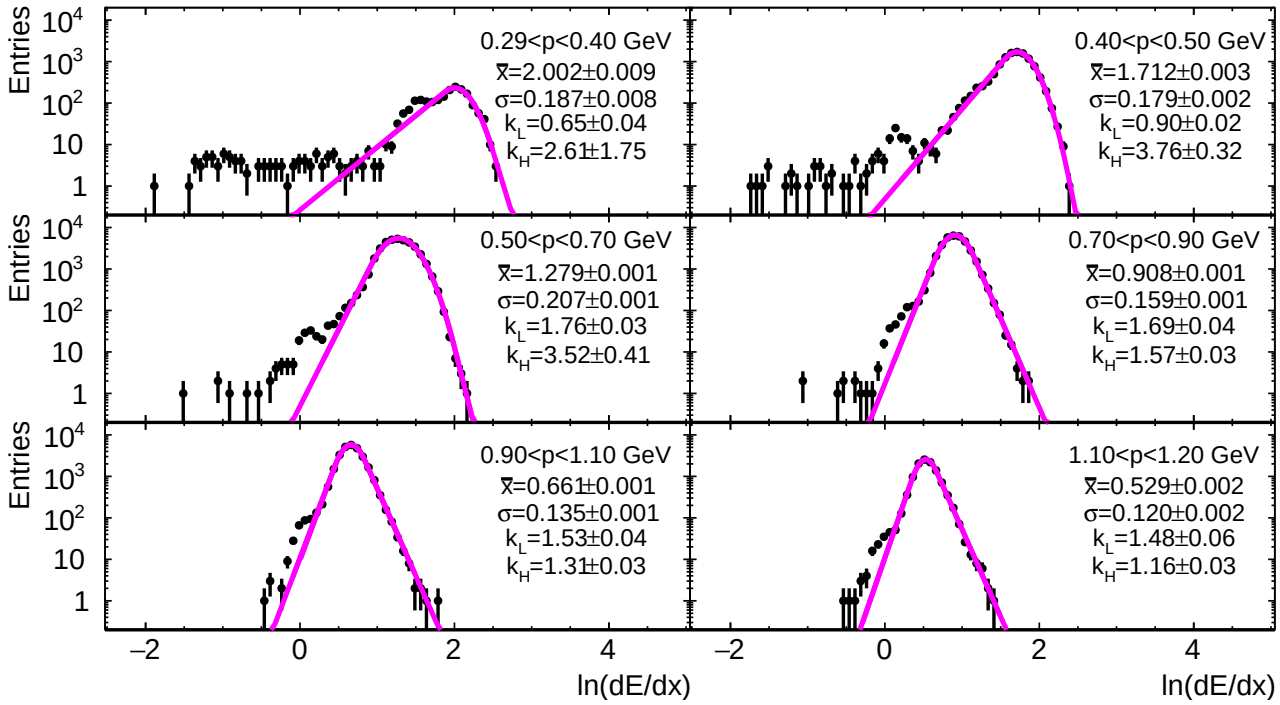

Figure A.1.14: Distributions of $\ln(\mathrm{d}E/\mathrm{d}x)$ for PYTHIA 8 in six momentum ranges for protons and two PD hits. The parameters of the fitted function (3.4) are displayed in the plots.

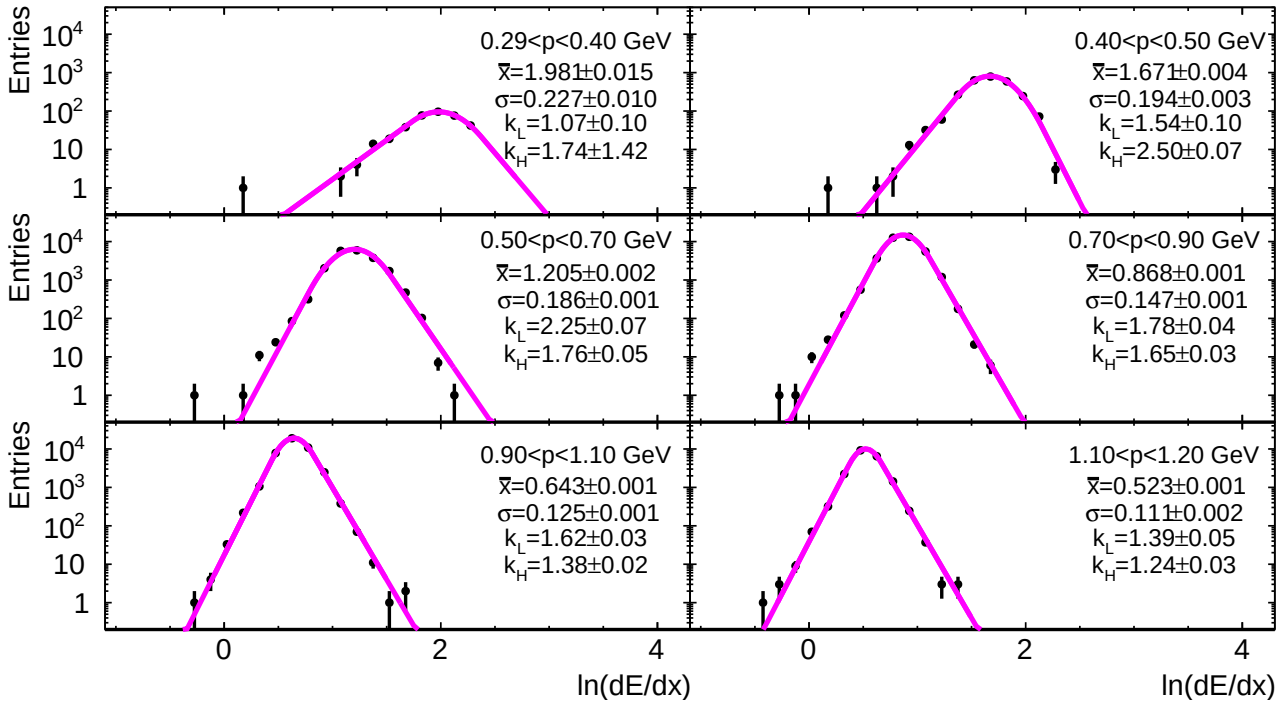

Figure A.1.15: Distributions of $\ln(\mathrm{d}E/\mathrm{d}x)$ for PYTHIA 8 in six momentum ranges for antiprotons and three PD hits. The parameters of the fitted function (3.4) are displayed in the plots.

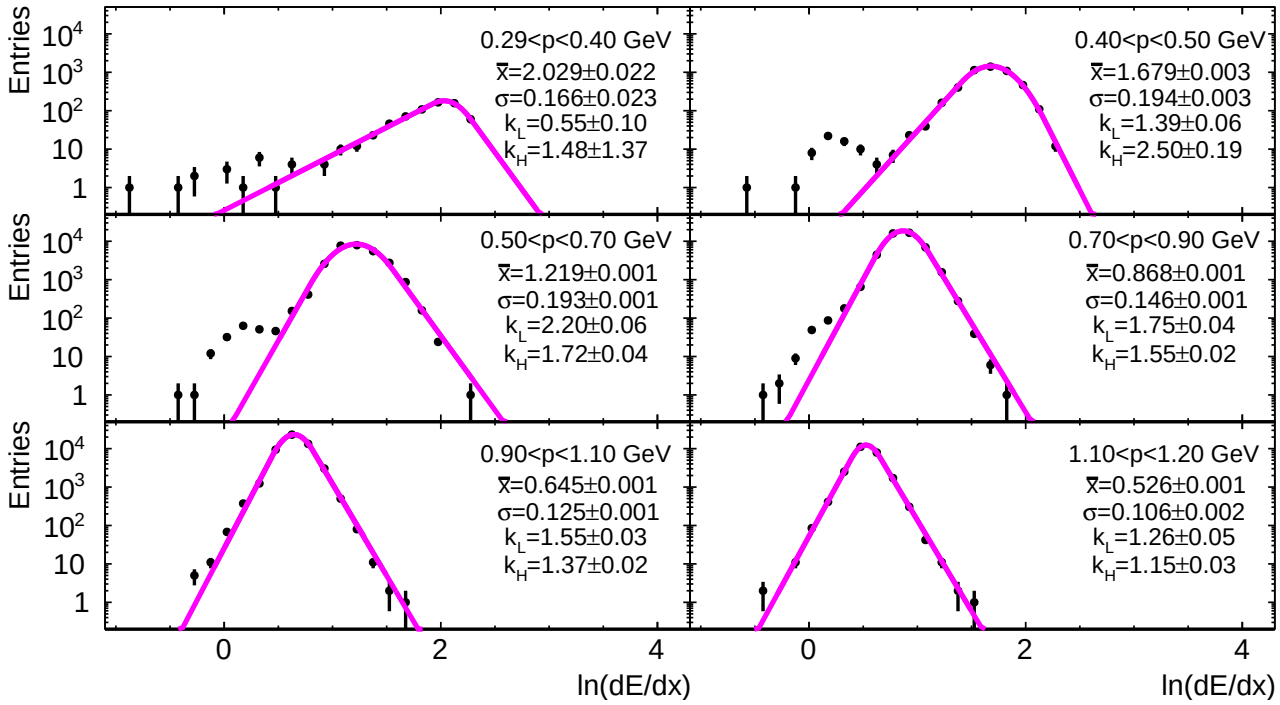

Figure A.1.16: Distributions of $\ln(\mathrm{d}E/\mathrm{d}x)$ for PYTHIA 8 in six momentum ranges for protons and three PD hits. The parameters of the fitted function (3.4) are displayed in the plots.

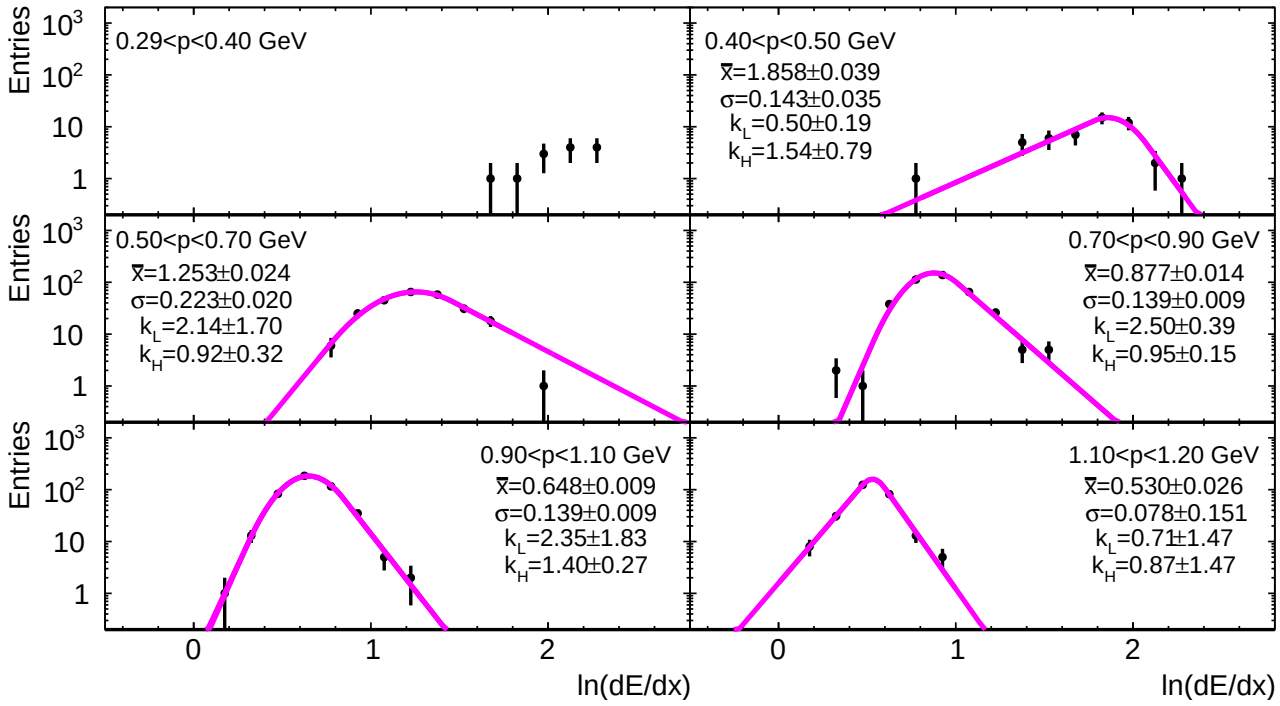

Figure A.1.17: Distributions of $\ln(\mathrm{d}E/\mathrm{d}x)$ for PYTHIA 8 in six momentum ranges for antiprotons and more than three PD hits. The parameters of the fitted function (3.4) are displayed in the plots.

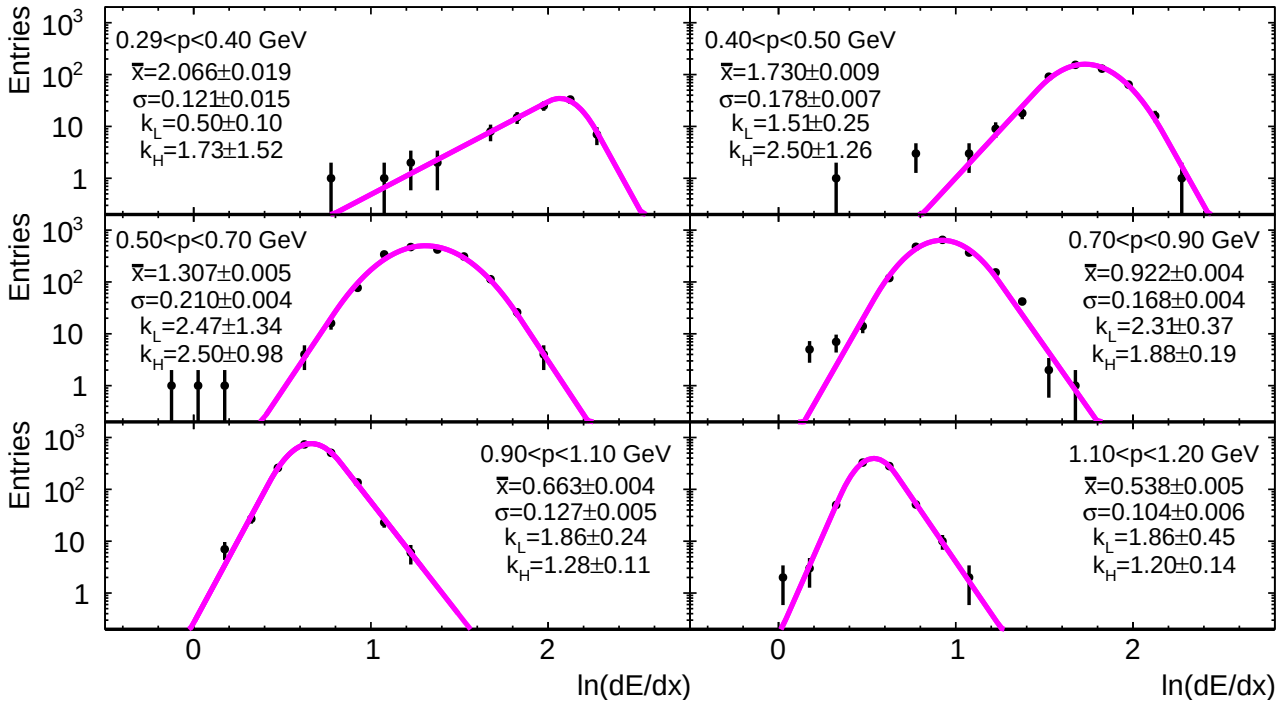

Figure A.1.18: Distributions of $\ln(\mathrm{d}E/\mathrm{d}x)$ for PYTHIA 8 in six momentum ranges for protons and more than three PD hits. The parameters of the fitted function (3.4) are displayed in the plots.

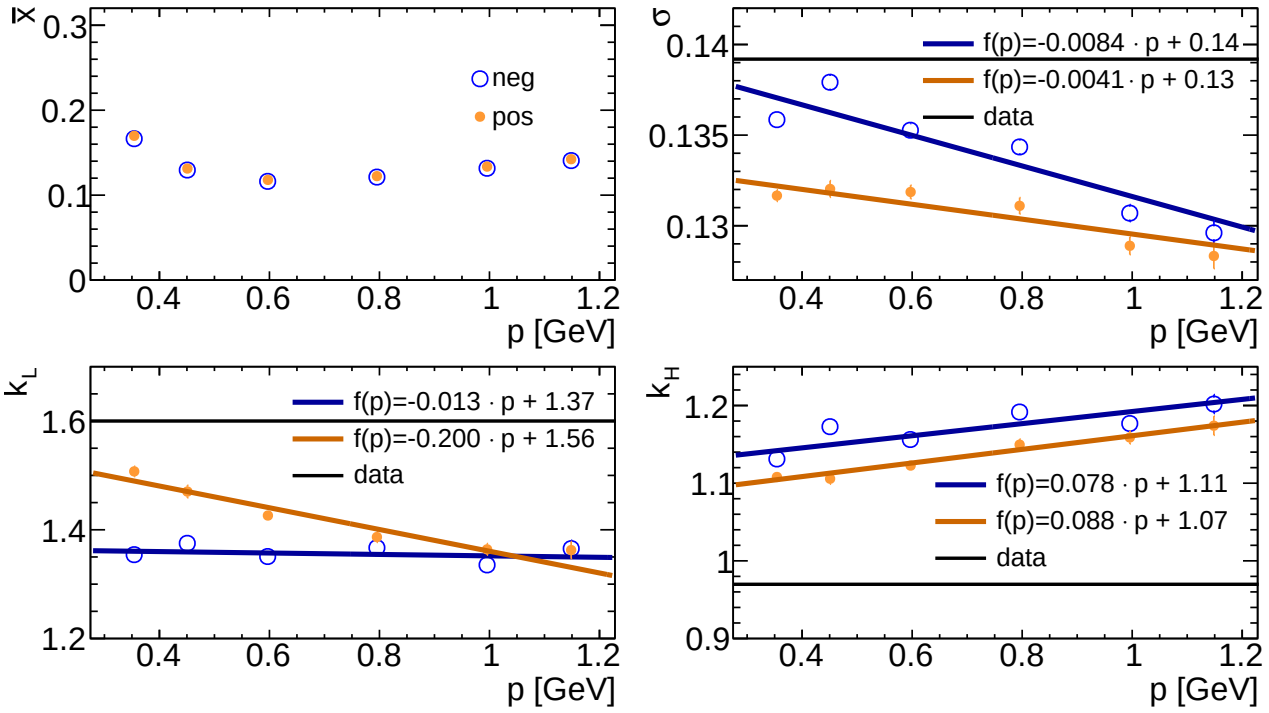

Figure A.1.19: Dependencies of fit parameters on the momentum (fits shown in Figures A.1.1 and A.1.2) for PYTHIA 8 for positive (pos) and negative (neg) pions and two PD hits.

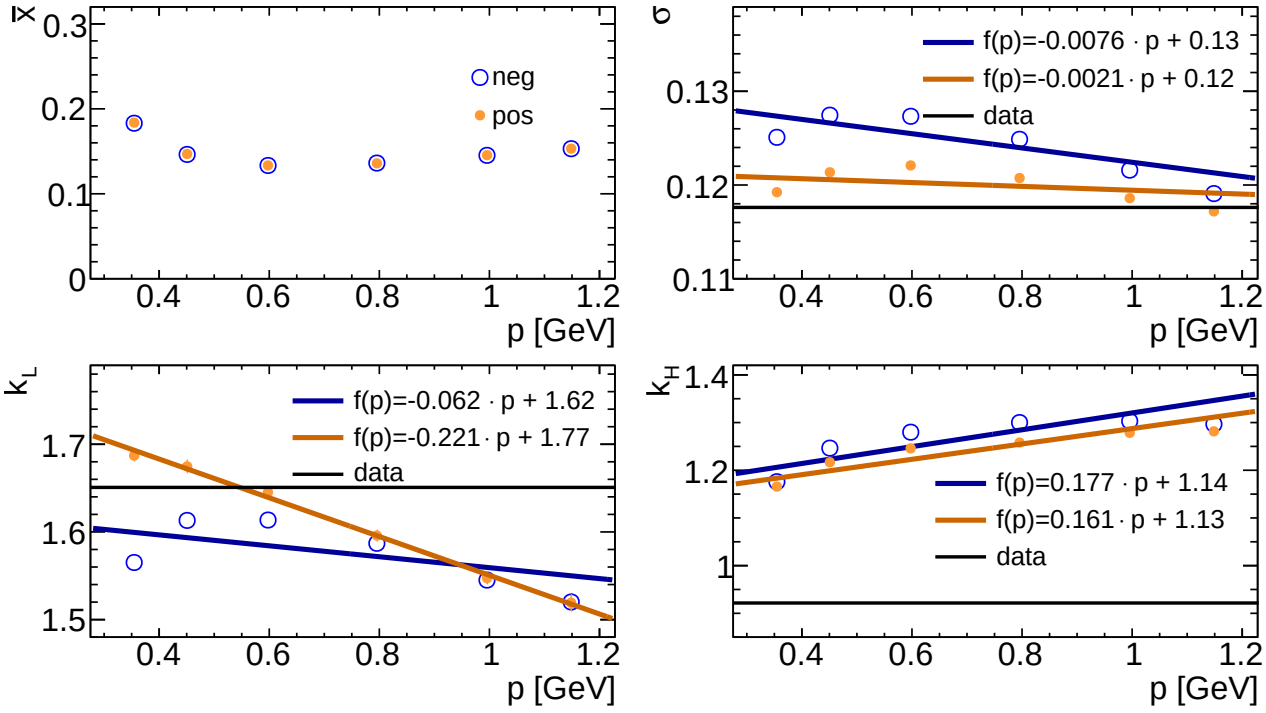

Figure A.1.20: Dependencies of fit parameters on the momentum (fits shown in Figures A.1.3 and A.1.4) for PYTHIA 8 for positive (pos) and negative (neg) pions and three PD hits.

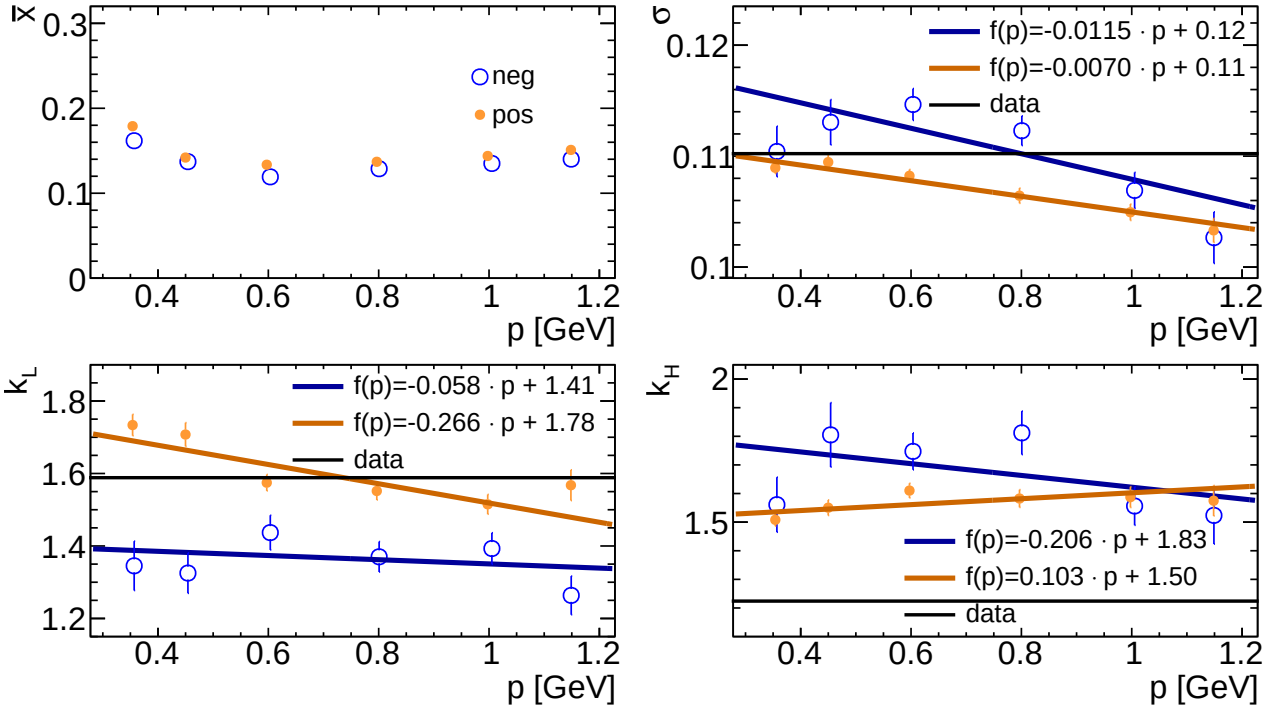

Figure A.1.21: Dependencies of fit parameters on the momentum (fits shown in Figures A.1.5 and A.1.6) for PYTHIA 8 for positive (pos) and negative (neg) pions and more than three PD hits.

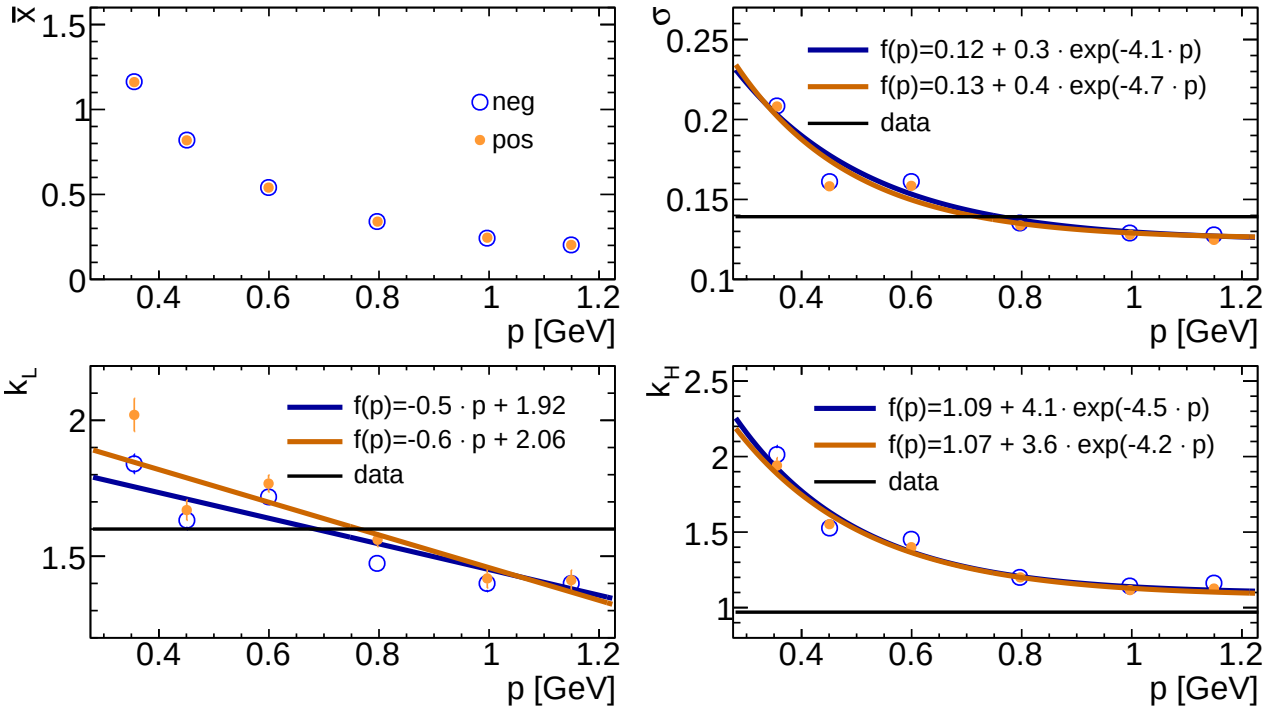

Figure A.1.22: Dependencies of fit parameters on the momentum (fits shown in Figures A.1.7 and A.1.8) for PYTHIA 8 for positive (pos) and negative (neg) kaons and two PD hits.

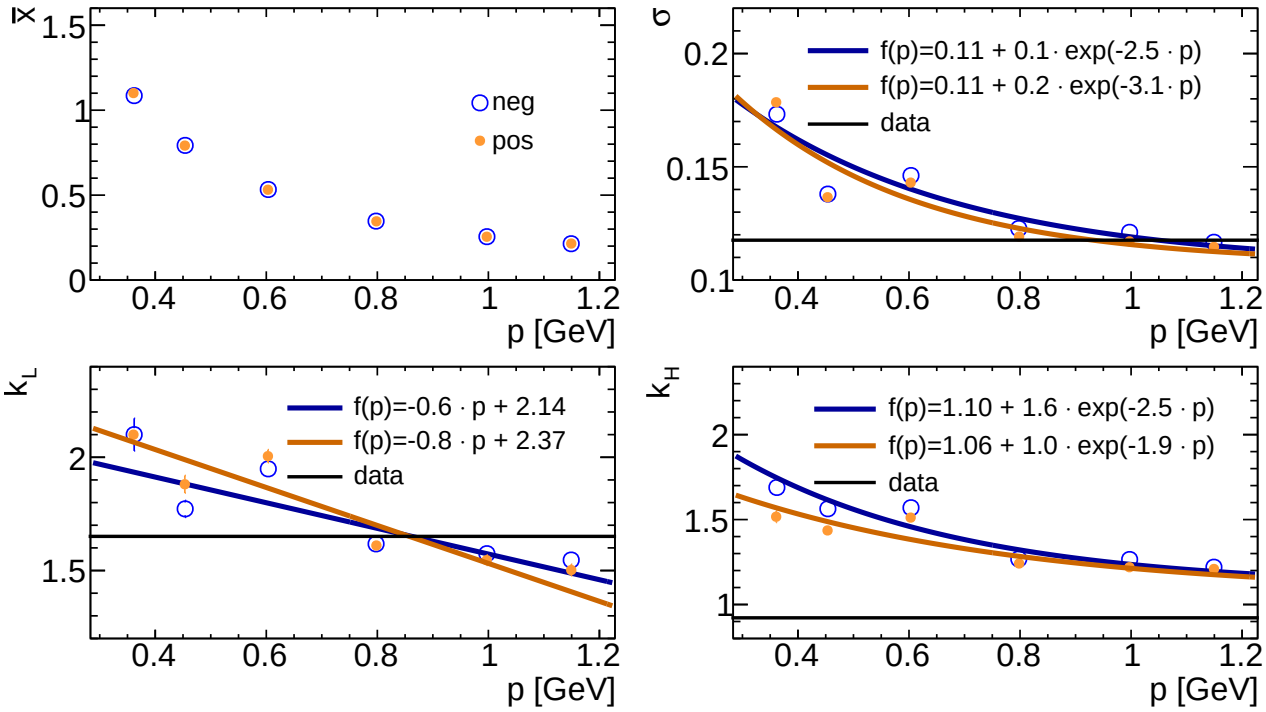

Figure A.1.23: Dependencies of fit parameters on the momentum (fits shown in Figures A.1.9 and A.1.10) for PYTHIA 8 for positive (pos) and negative (neg) kaons and three PD hits.

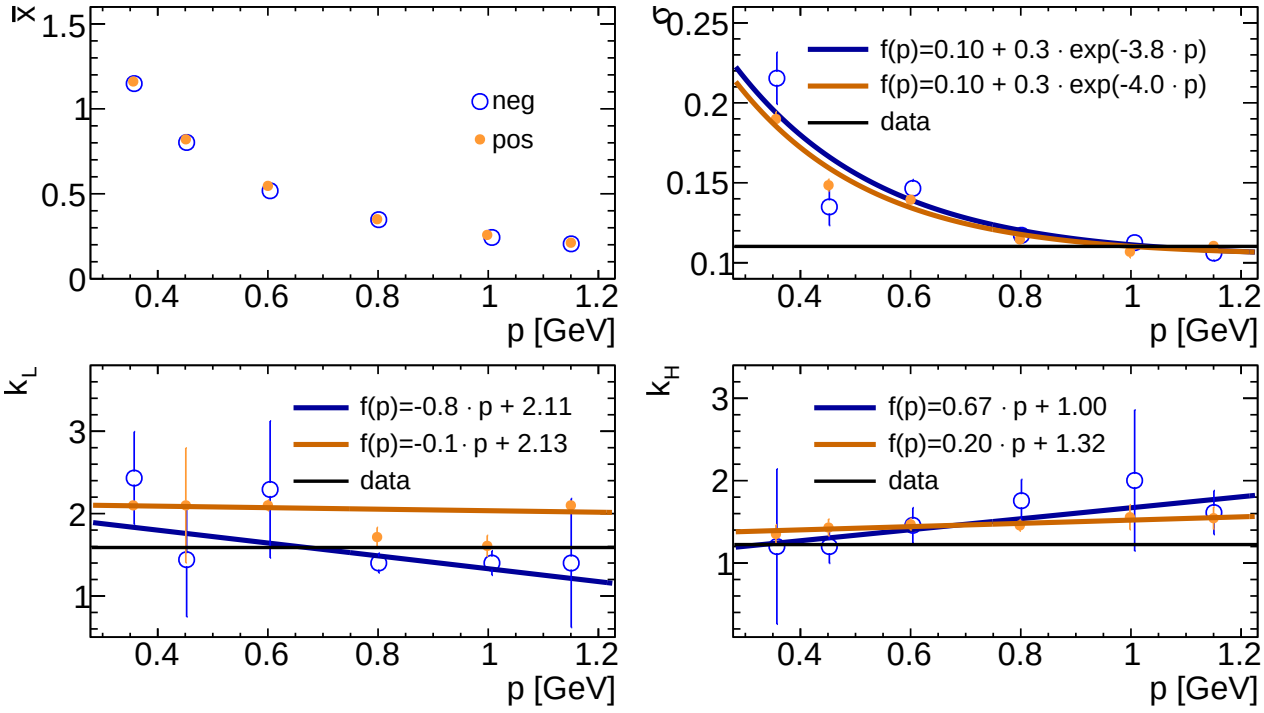

Figure A.1.24: Dependencies of fit parameters on the momentum (fits shown in Figures A.1.11 and A.1.12) for PYTHIA 8 for positive (pos) and negative (neg) kaons and more than three PD hits.

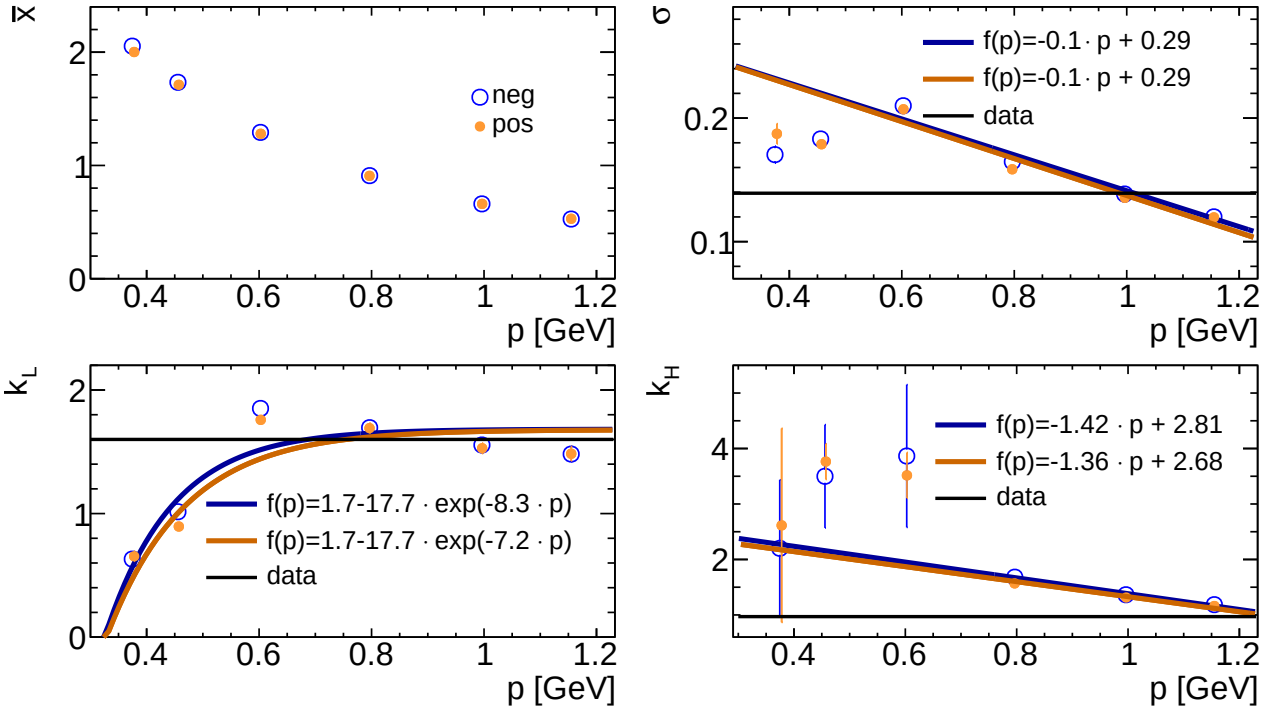

Figure A.1.25: Dependencies of fit parameters on the momentum (fits shown in Figures A.1.13 and A.1.14) for PYTHIA 8 for protons (pos) and antiprotons (neg) and two PD hits.

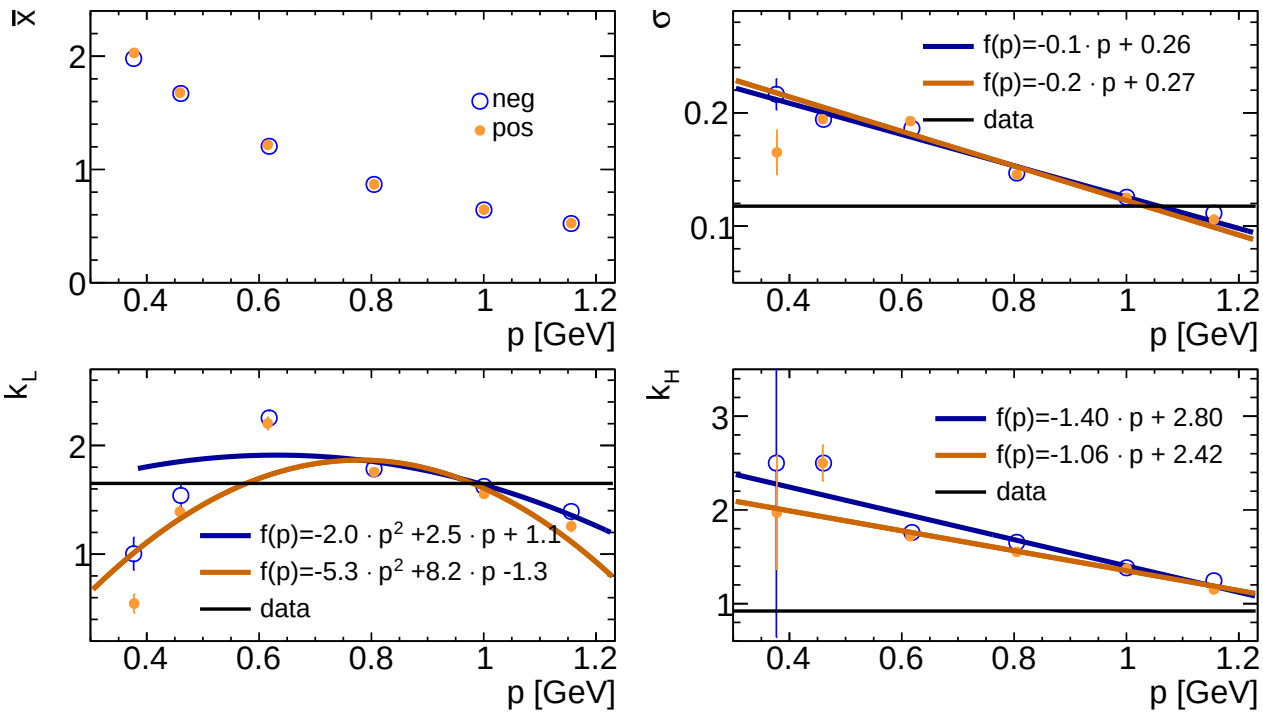

Figure A.1.26: Dependencies of fit parameters on the momentum (fits shown in Figures A.1.15 and A.1.16) for PYTHIA 8 for protons (pos) and antiprotons (neg) and three PD hits.

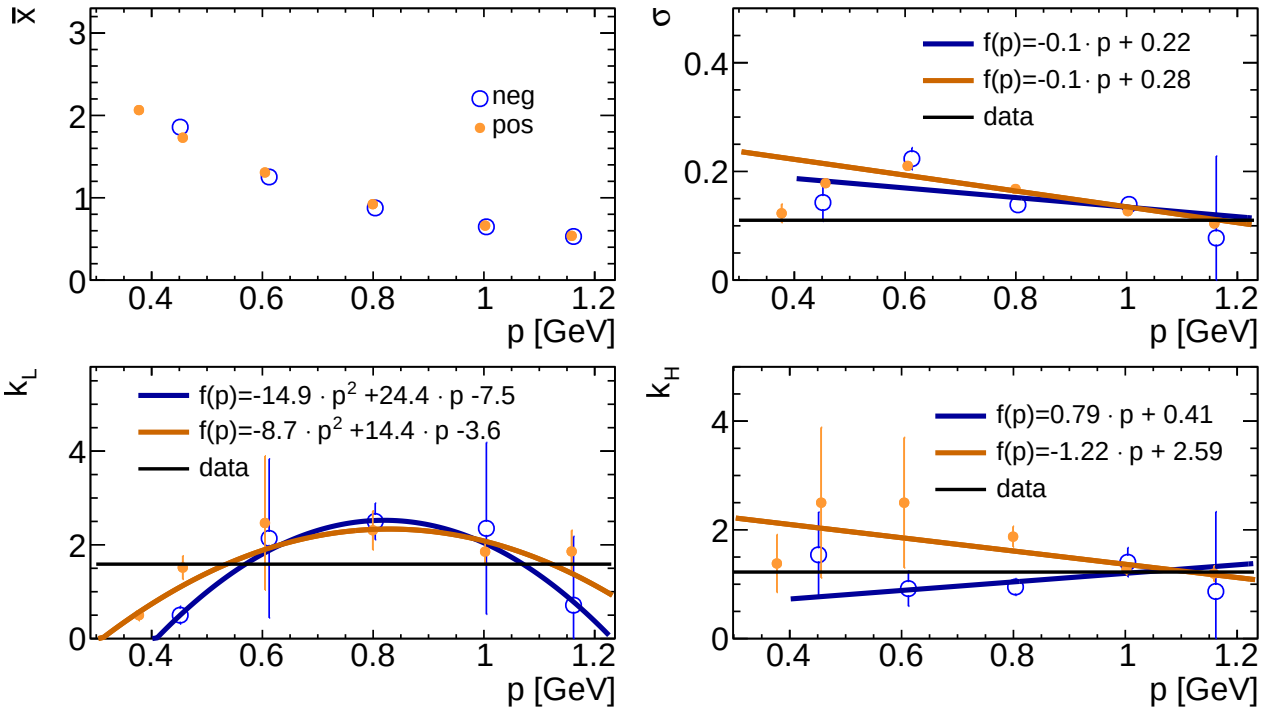

Figure A.1.27: Dependencies of fit parameters on the momentum (fits shown in Figures A.1.15 and A.1.16) for PYTHIA 8 for protons (pos) and antiprotons (neg) and more than three PD hits.

A.2 Data

ExpGaussExp (3.4) fits to $\ln(\mathrm{d}E/\mathrm{d}x)$ distributions for data. The fits with hypotheses of pion, kaon and proton masses were performed in the momentum range of 0.3 - 1.0 GeV in ten slices of equal width in $\ln(p)$ - separately for negatively and positively charged particles and for two, three and more than three PD hits. The fitting procedure is discussed in Section 3.2.

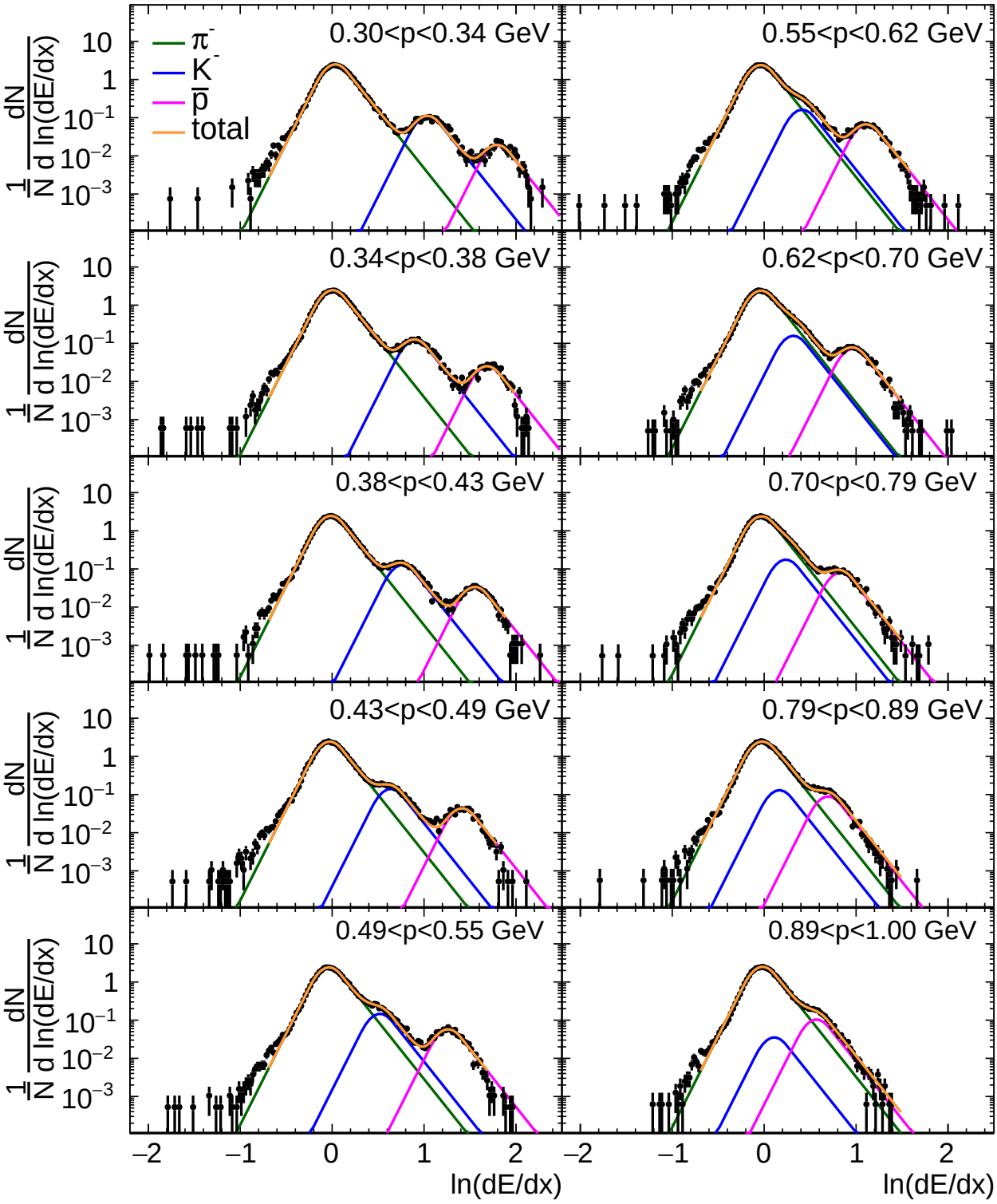

Figure A.2.1: Distributions of $\ln(\mathrm{d}E/\mathrm{d}x)$ for data in ten momentum ranges for negatively charged particles and two PD hits. The sum of three ExpGaussExp functions (3.4) with a hypothesis of π, K and p masses was fitted in each momentum slice.

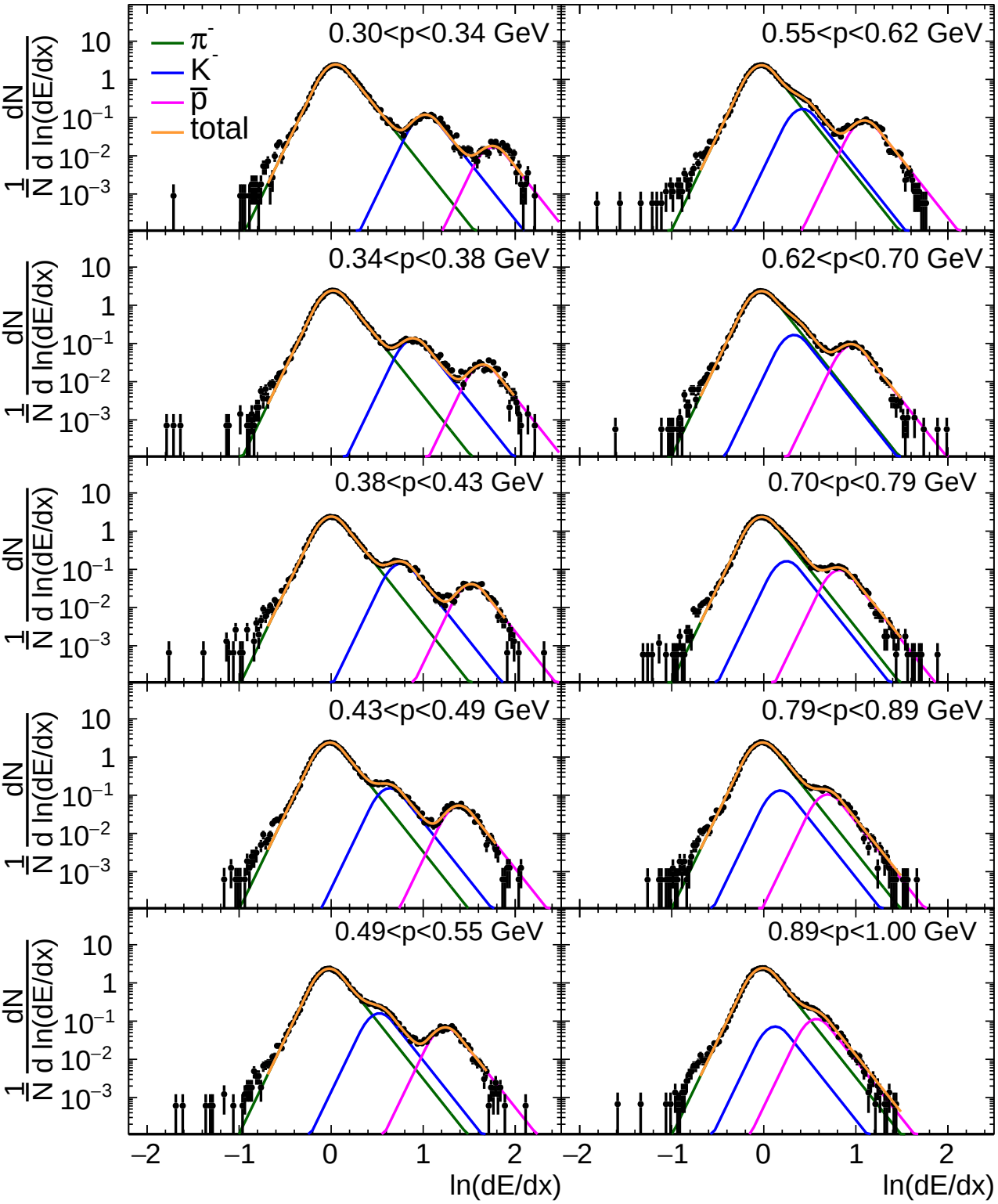

Figure A.2.2: Distributions of $\ln(\mathrm{d}E/\mathrm{d}x)$ for data in ten momentum ranges for positively charged particles and two PD hits. The sum of three ExpGaussExp functions (3.4) with a hypothesis of π, K and p masses was fitted in each momentum slice.

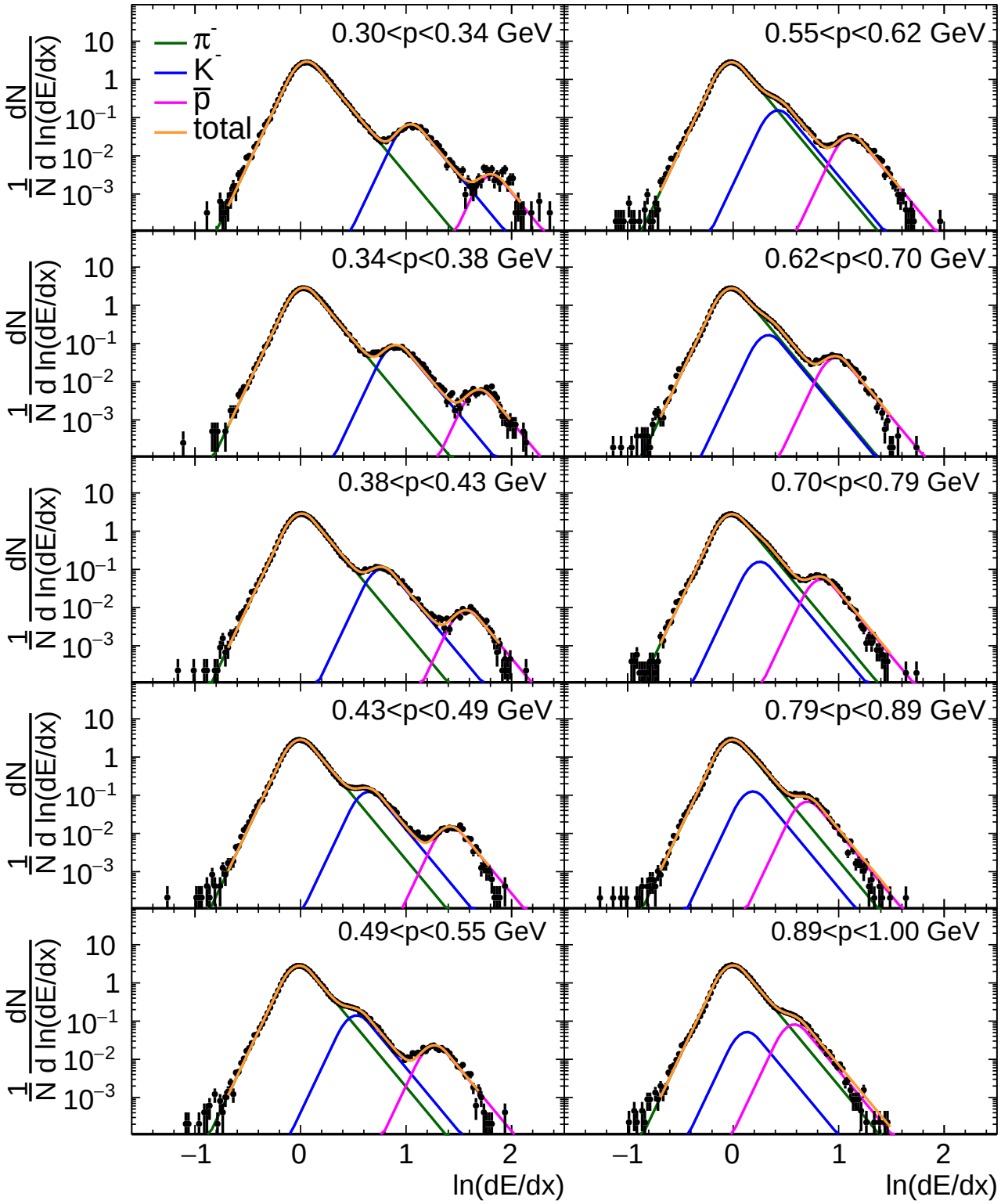

Figure A.2.3: Distributions of $\ln(\mathrm{d}E/\mathrm{d}x)$ for data in ten momentum ranges for negatively charged particles and three PD hits. The sum of three ExpGaussExp functions (3.4) with a hypothesis of π, K and p masses was fitted in each momentum slice.

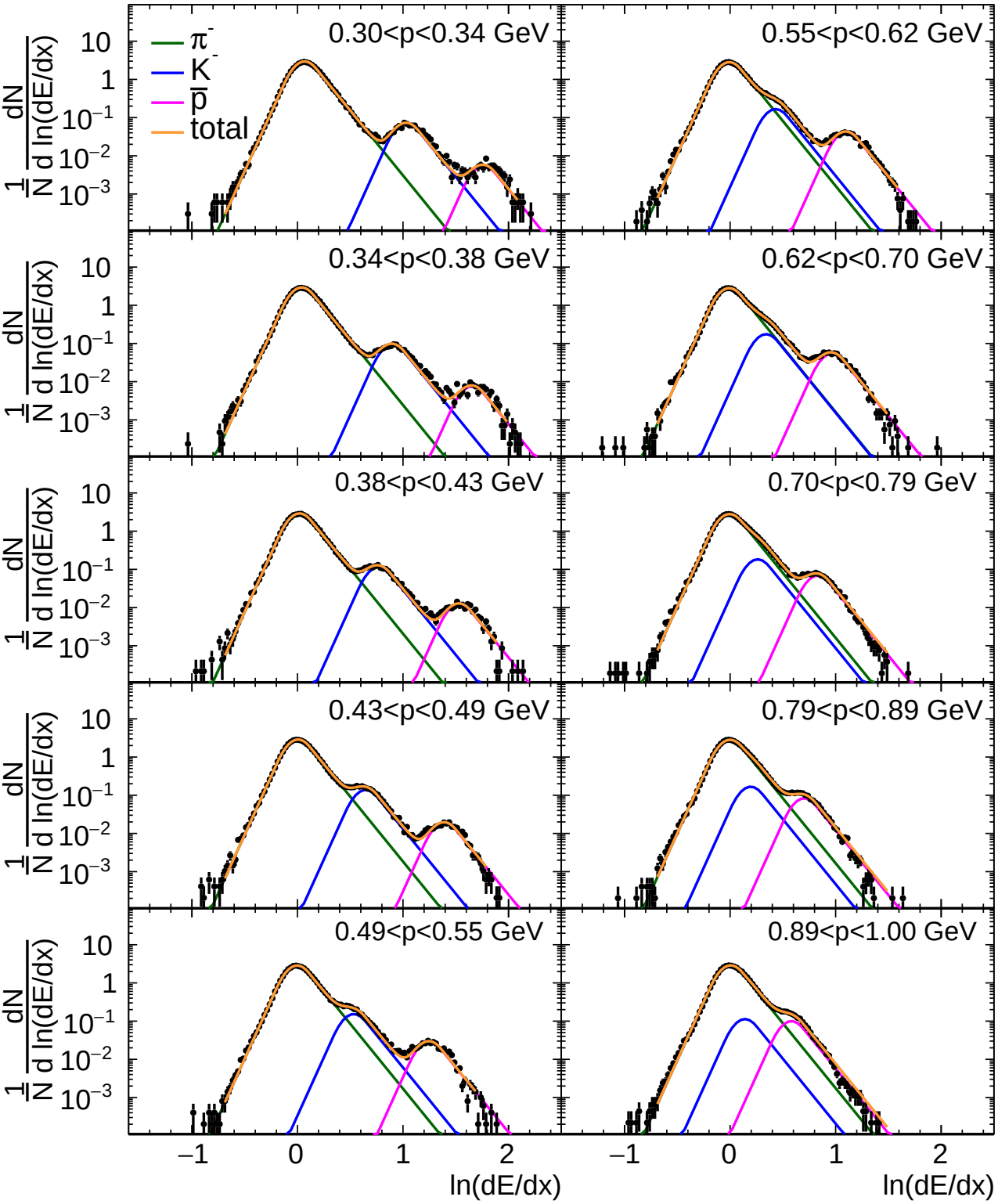

Figure A.2.4: Distributions of $\ln(\mathrm{d}E/\mathrm{d}x)$ for data in ten momentum ranges for positively charged particles and three PD hits. The sum of three ExpGaussExp functions (3.4) with a hypothesis of π, K and p masses was fitted in each momentum slice.

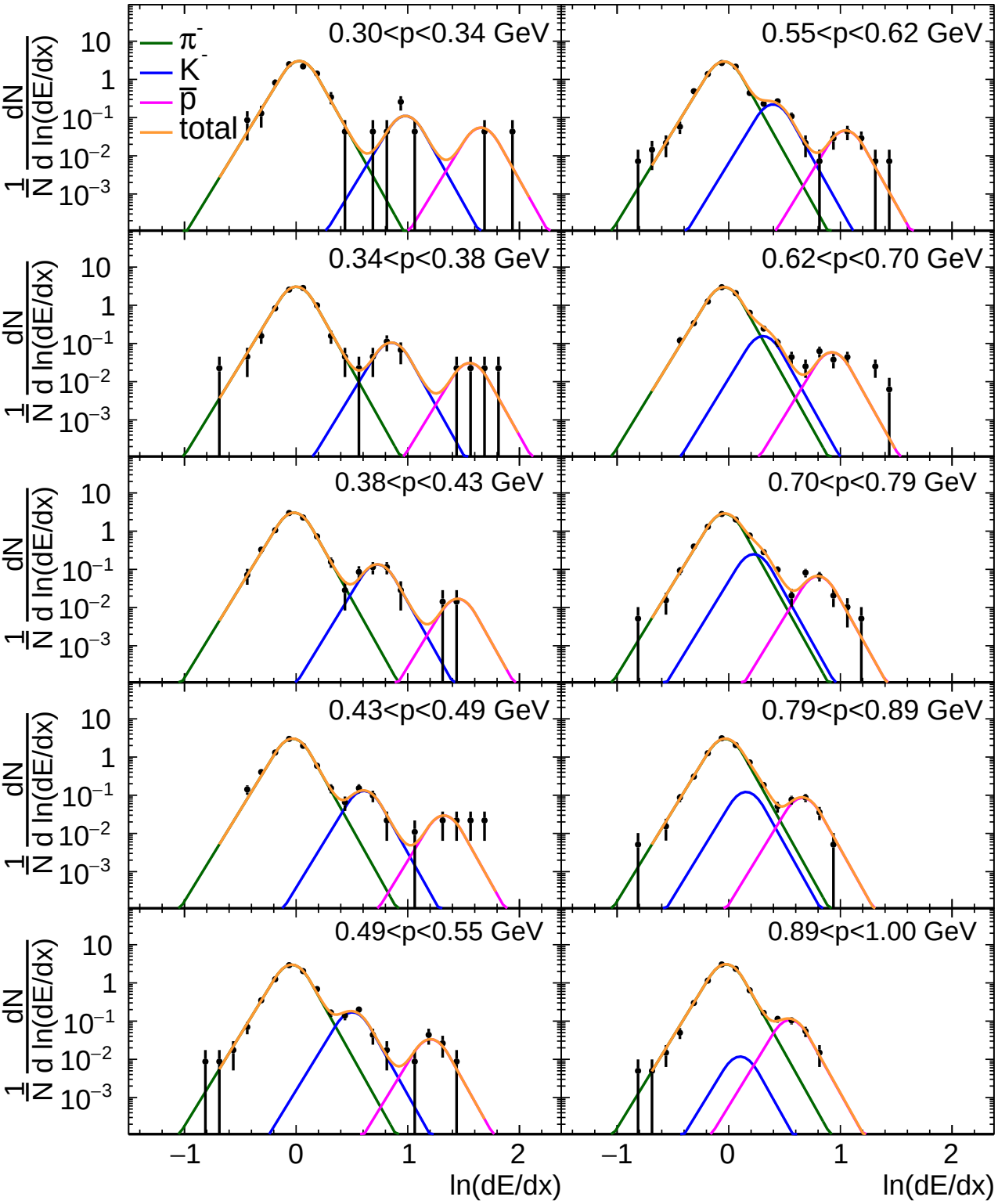

Figure A.2.5: Distributions of $\ln(\mathrm{d}E/\mathrm{d}x)$ for data in ten momentum ranges for negatively charged particles and more than three PD hits. The sum of three ExpGaussExp functions (3.4) with a hypothesis of π, K and p masses was fitted in each momentum slice.

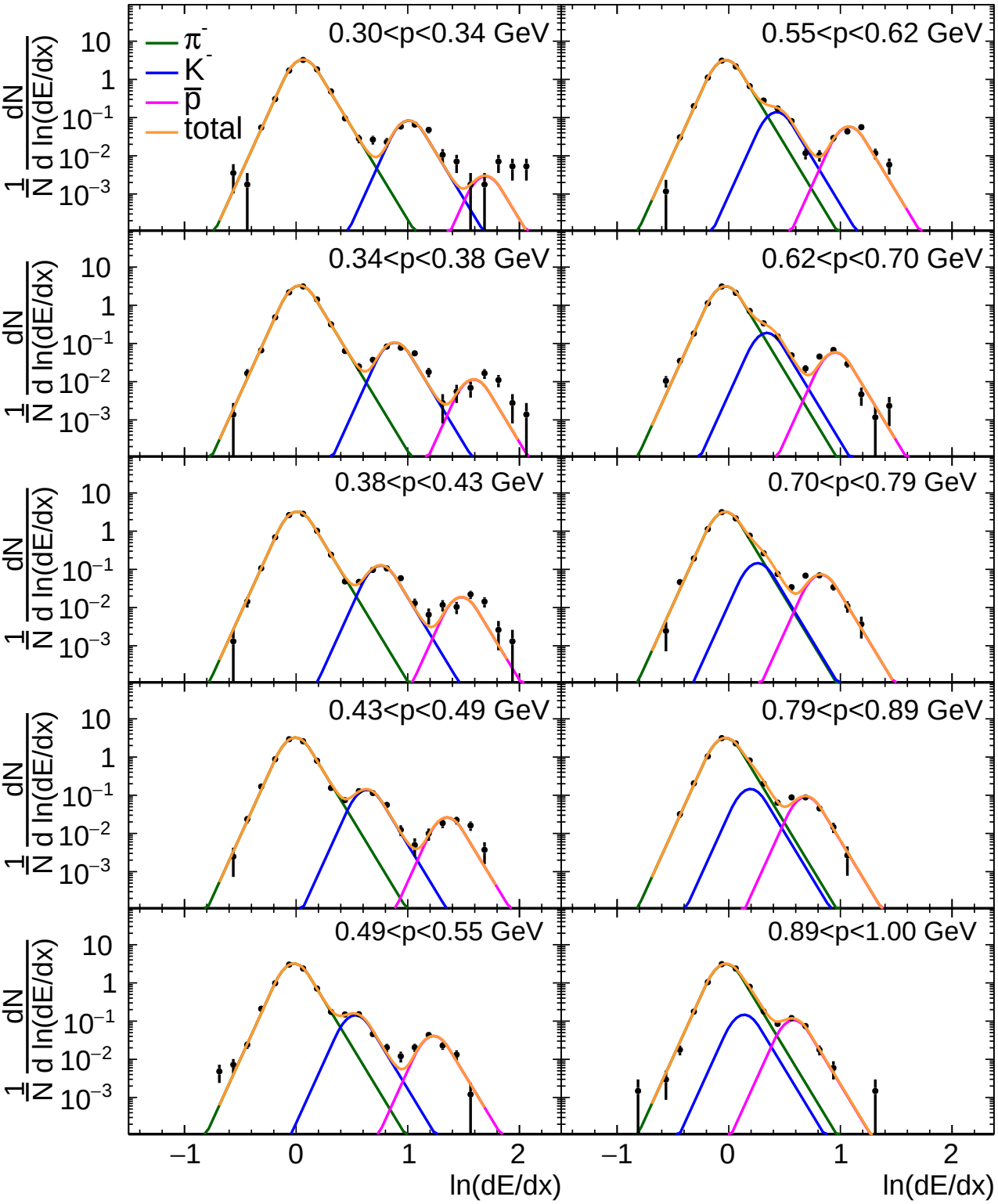

Figure A.2.6: Distributions of $\ln(\mathrm{d}E/\mathrm{d}x)$ for data in ten momentum ranges for positively charged particles and more than three PD hits. The sum of three ExpGaussExp functions (3.4) with a hypothesis of π, K and p masses was fitted in each momentum slice.

Appendix B

Fits to the invariant mass distributions of the ϕ meson candidates for SD, CD and MB data.

B.1 Single Diffraction Analysis

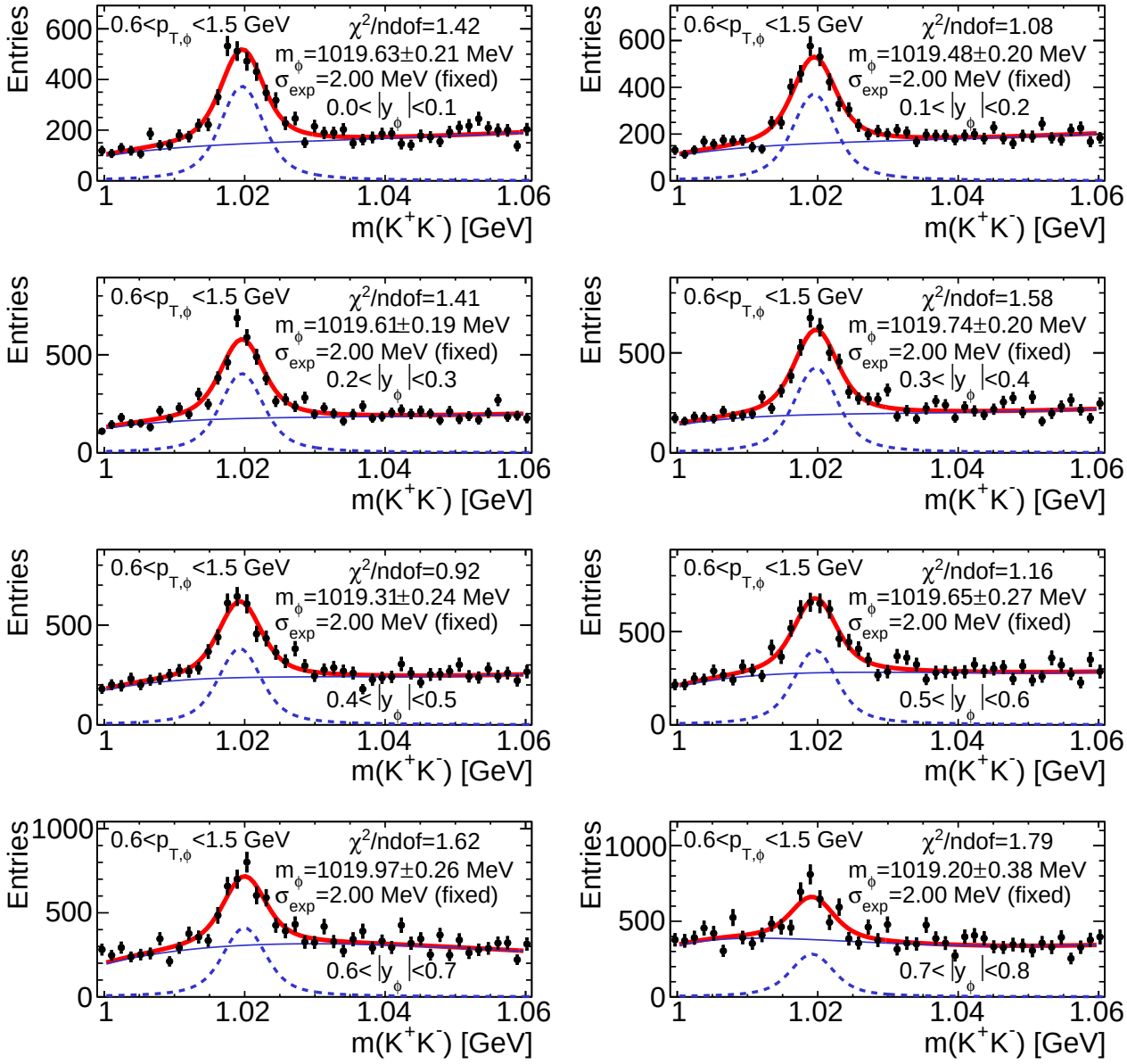

Figure B.1.1: Fits to invariant mass distributions of pairs of oppositely charged kaon candidates for SD data. Formulas (6.1), (6.2), (6.6) and corrections for the bias in the momentum reconstruction were applied. The distributions are shown in eight ranges of $|y_\phi|$. The red curves represent a convolution of the non-relativistic Breit-Wigner function with the Gaussian distribution as a signal function (5.5) plus a background fitting function (5.7). The blue solid lines represent the background shape and the dashed blue curves - the signal contribution. The extracted signal yields were used to obtain the $|y_\phi|$ spectra shown in right plots in Figure 8.2.

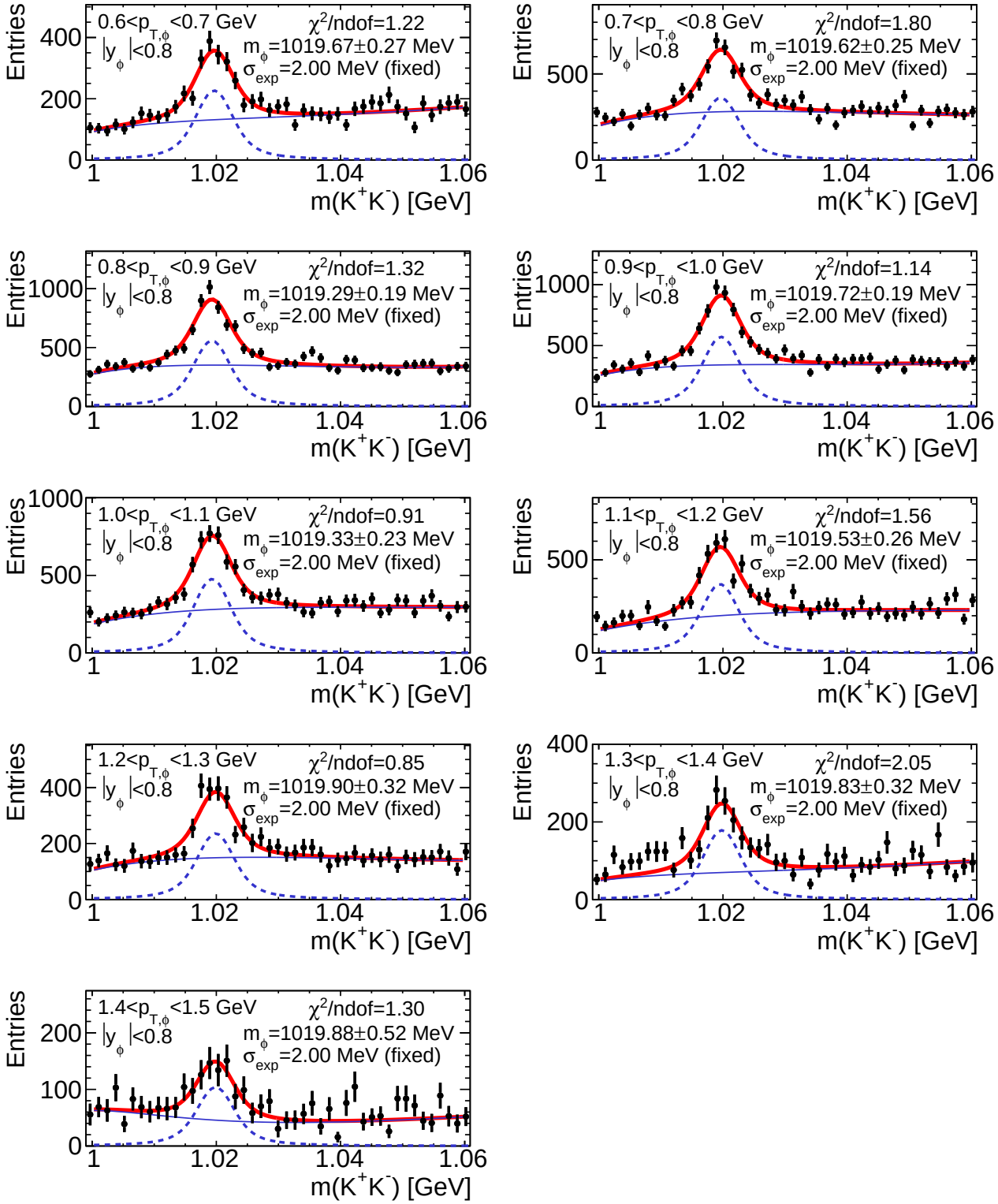

Figure B.1.2: Fits to invariant mass distributions of pairs of oppositely charged kaon candidates for SD data. Formulas (6.1), (6.2), (6.6) and corrections for the bias in the momentum reconstruction were applied. The distributions are shown in nine ranges of $p_{\mathrm{T},\phi}$. The red curves represent a convolution of the non-relativistic Breit-Wigner function with the Gaussian distribution as a signal function (5.5) plus a background fitting function (5.7). The blue solid lines represent the background shape and the dashed blue curves - the signal contribution. The extracted signal yields were used to obtain the $p_{\mathrm{T},\phi}$ spectra shown in left plots in Figure 8.2.

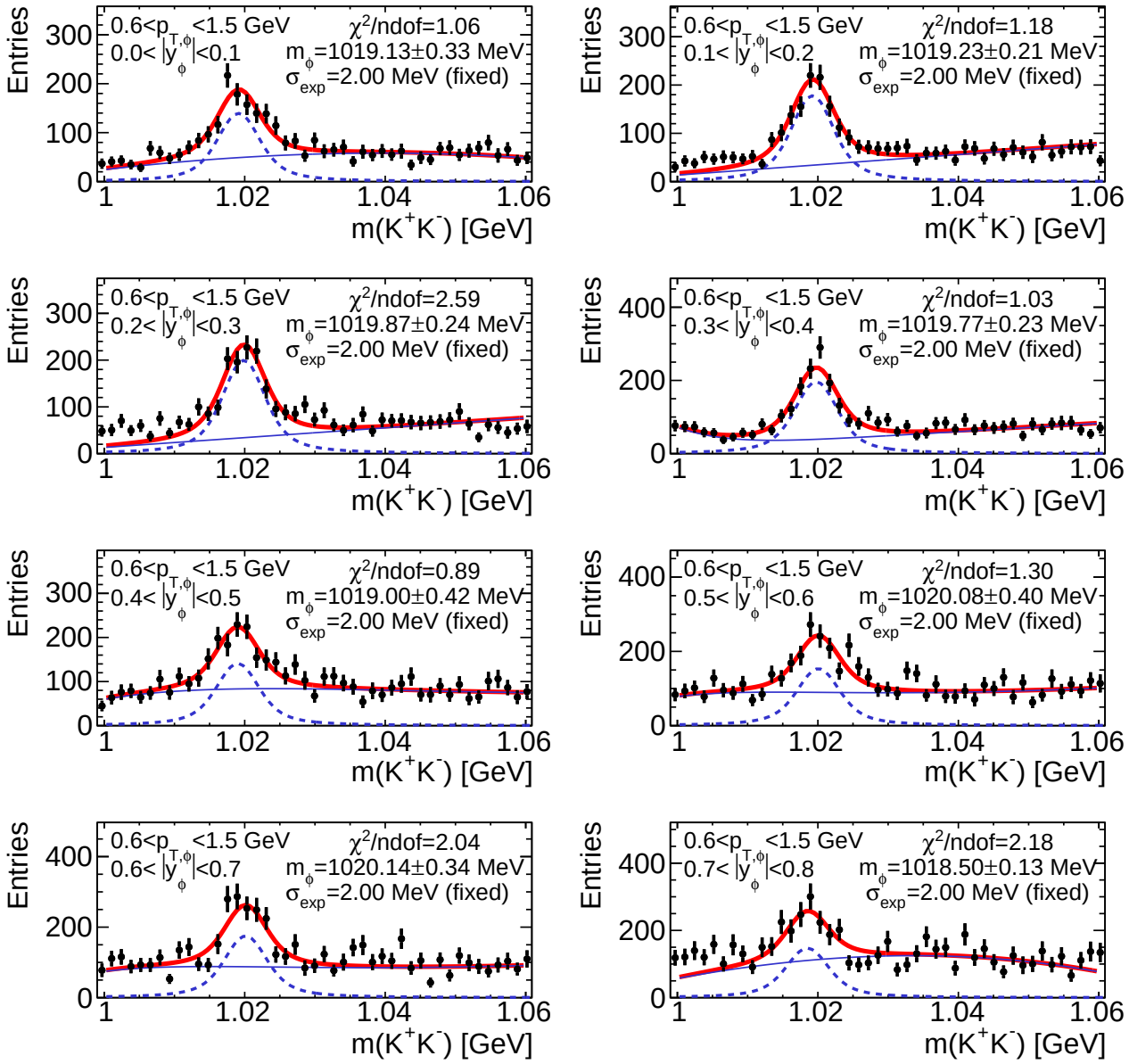

Figure B.1.3: Fits to invariant mass distributions of oppositely charged pairs of kaon candidates for SD data. Formulas (6.1), (6.2), (6.6) and corrections for the bias in the momentum reconstruction were applied. The distributions are shown in eight ranges of $|y_\phi|$. The red curves represent a convolution of the non-relativistic Breit-Wigner function with the Gaussian distribution as a signal function (5.5) plus a background fitting function (5.7). The blue solid lines represent the background shape and the dashed blue curves - the signal contribution. The extracted signal yields were used to obtain the $|y_\phi|$ spectra for $\xi < 0.035$ shown in right plots in Figure 8.3.

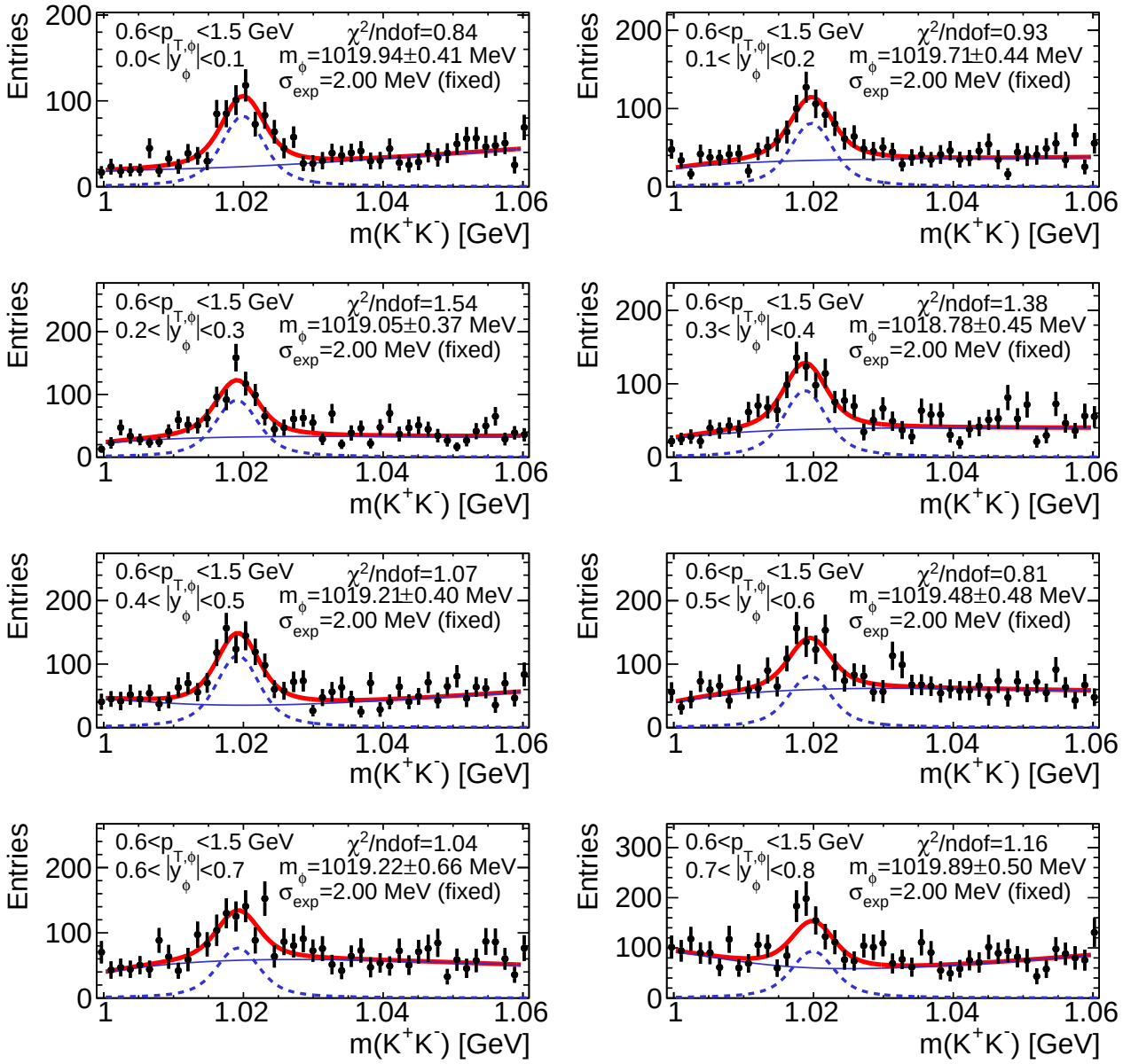

Figure B.1.4: Fits to invariant mass distributions of pairs of oppositely charged kaon candidates for SD data. (6.1), (6.2), (6.6) and corrections for the bias in the momentum reconstruction were applied. The distributions are shown in eight ranges of $|y_\phi|$. The red curves represent a convolution of the non-relativistic Breit-Wigner function with the Gaussian distribution as a signal function (5.5) plus a background fitting function (5.7). The blue solid lines represent the background shape and the dashed blue curves - the signal contribution. The extracted signal yields were used to obtain the $|y_\phi|$ spectra for $0.035 < \xi < 0.08$ shown in right plots in Figure 8.3.

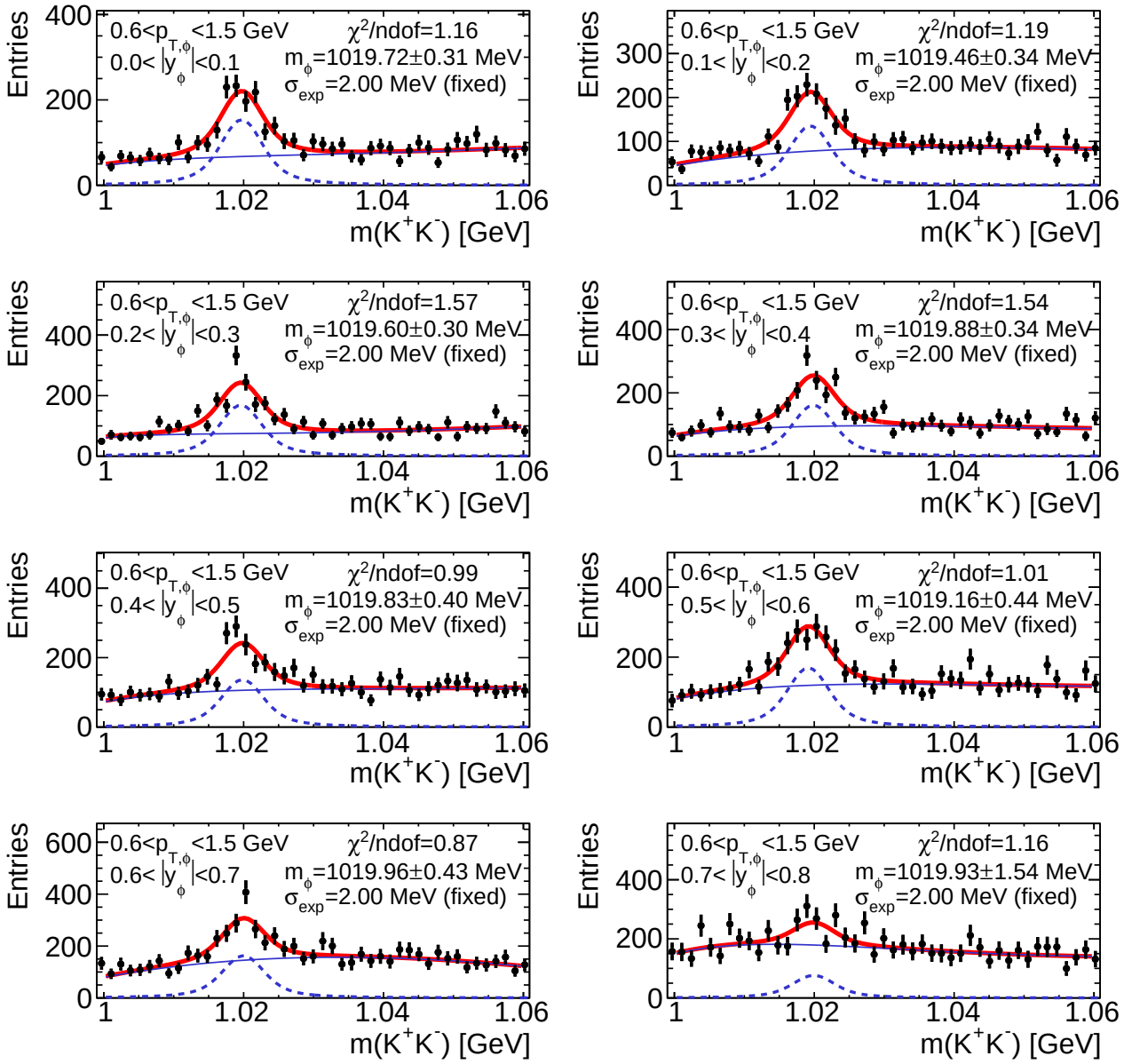

Figure B.1.5: Fits to invariant mass distributions of pairs of oppositely charged kaon candidates for SD data. Formulas (6.1), (6.2), (6.6) and corrections for the bias in the momentum reconstruction were applied. The distributions are shown in eight ranges of $|y_\phi|$. The red curves represent a convolution of the non-relativistic Breit-Wigner function with the Gaussian distribution as a signal function (5.5) plus a background fitting function (5.7). The blue solid lines represent the background shape and the dashed blue curves - the signal contribution. The extracted signal yields were used to obtain the $|y_\phi|$ spectra for $0.08 < \xi < 0.016$ shown in right plots in Figure 8.3.

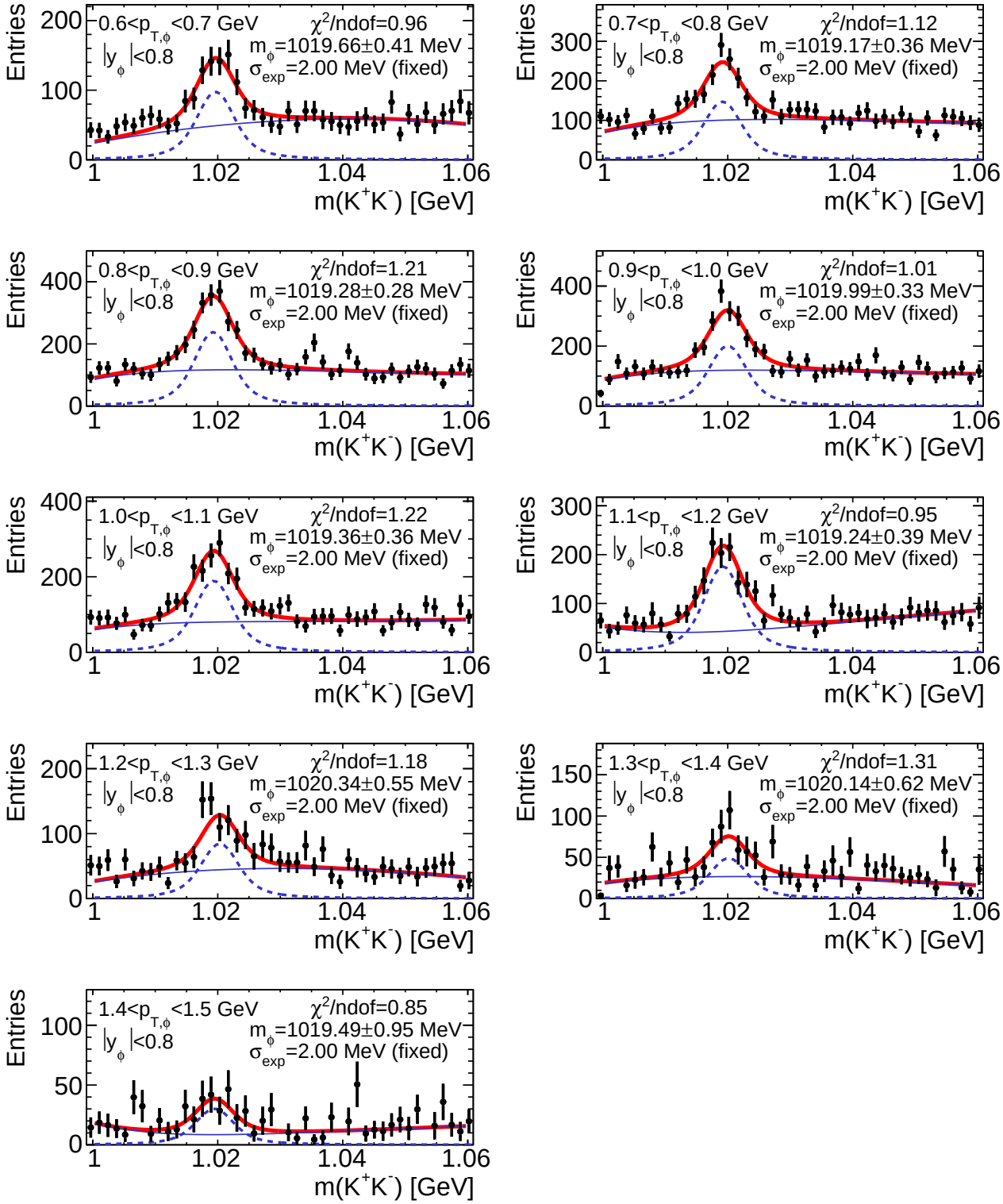

Figure B.1.6: Fits to invariant mass distributions of pairs of oppositely charged kaon candidates for SD data. (6.1), (6.2), (6.6) and corrections for the bias in the momentum reconstruction were applied. The distributions are shown in nine ranges of $p_{\mathrm{T},\phi}$. The red curves represent a convolution of the non-relativistic Breit-Wigner function with the Gaussian distribution as a signal function (5.5) plus a background fitting function (5.7). The blue solid lines represent the background shape and the dashed blue curves - the signal contribution. The extracted signal yields were used to obtain the $p_{\mathrm{T},\phi}$ spectra for $\xi < 0.035$ shown in left plots in Figures 8.3.

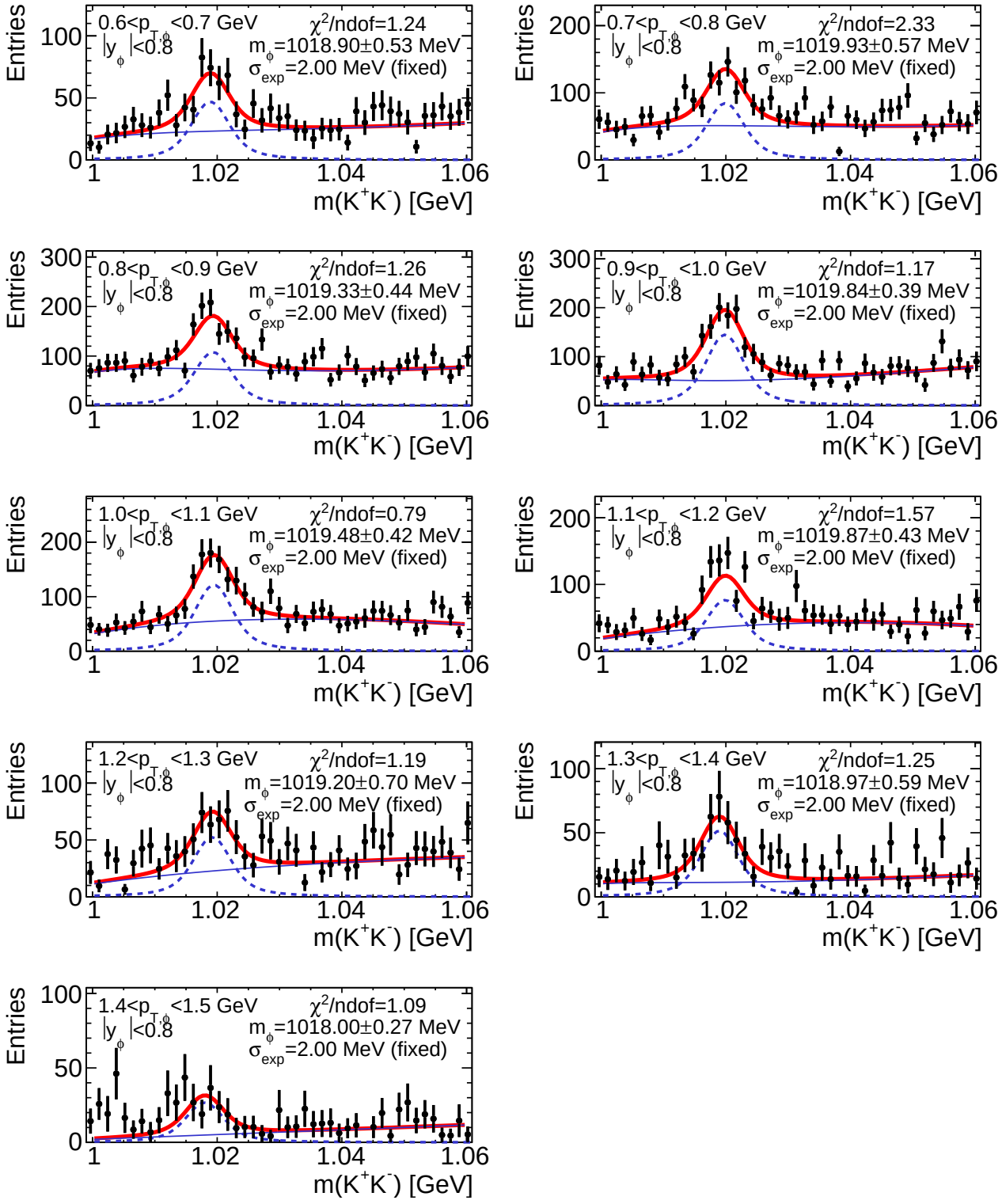

Figure B.1.7: Fits to invariant mass distributions of pairs of oppositely charged kaon candidates for SD data. Formulas (6.1), (6.2), (6.6) and corrections for the bias in the momentum reconstruction were applied. The distributions are shown in nine ranges of $p_{\mathrm{T},\phi}$. The red curves represent a convolution of the non-relativistic Breit-Wigner function with the Gaussian distribution as a signal function (5.5) plus a background fitting function (5.7). The blue solid lines represent the background shape and the dashed blue curves - the signal contribution. The extracted signal yields were used to obtain the $p_{\mathrm{T},\phi}$ spectra for $0.035 < \xi < 0.08$ shown in left plots in Figure 8.3.

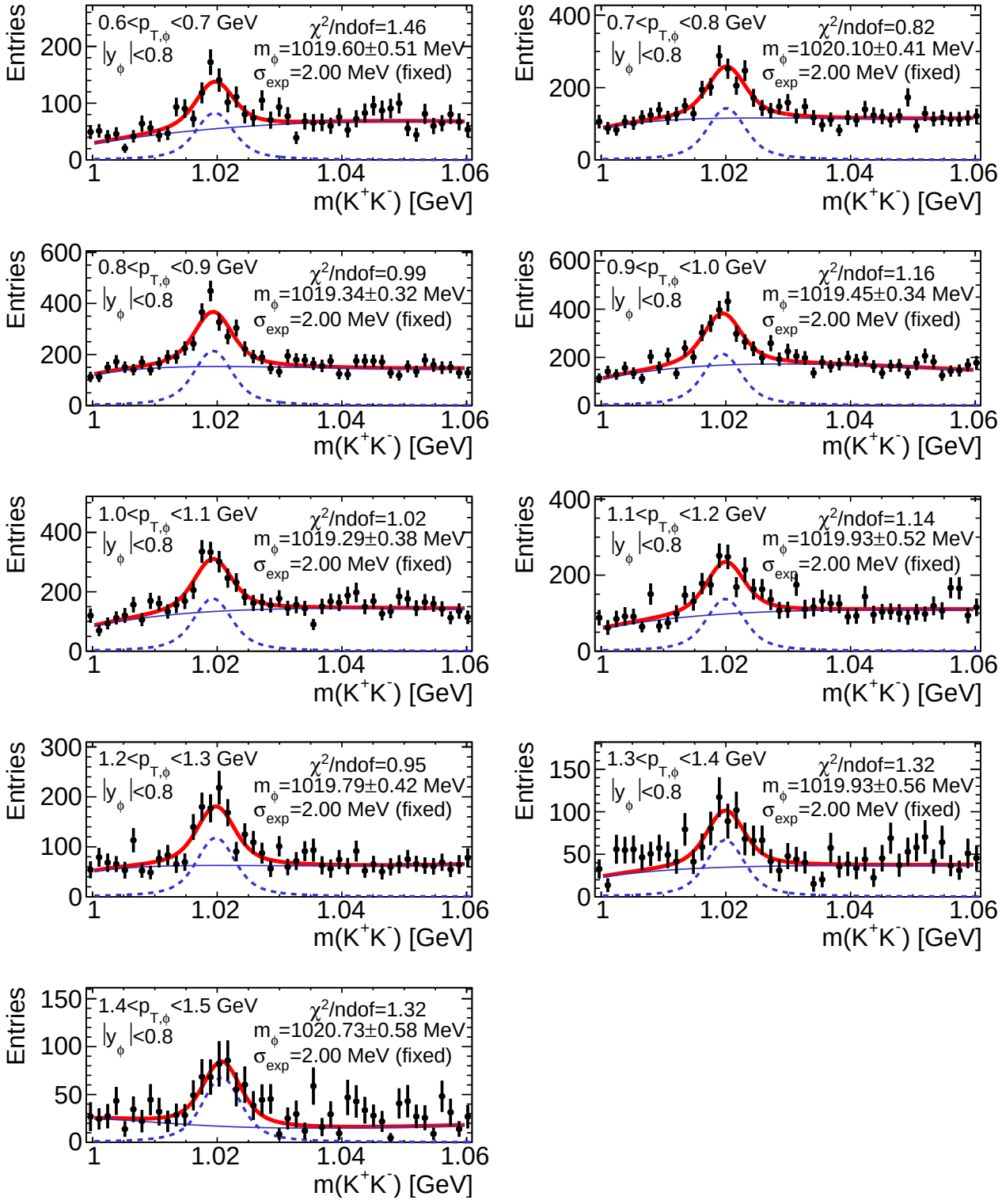

Figure B.1.8: Fits to invariant mass distributions of pairs of oppositely charged kaon candidates for SD data. Formulas (6.1), (6.2), (6.6) and corrections for the bias in the momentum reconstruction were applied. The distributions are shown in nine ranges of $p_{\mathrm{T},\phi}$. The red curves represent a convolution of the non-relativistic Breit-Wigner function with the Gaussian distribution as a signal function (5.5) plus a background fitting function (5.7). The blue solid lines represent the background shape and the dashed blue curves - the signal contribution. The extracted signal yields were used to obtain the $p_{\mathrm{T},\phi}$ spectra for $0.08 < \xi < 0.16$ shown in left plots in Figure 8.3.

B.2 Central Diffraction Analysis

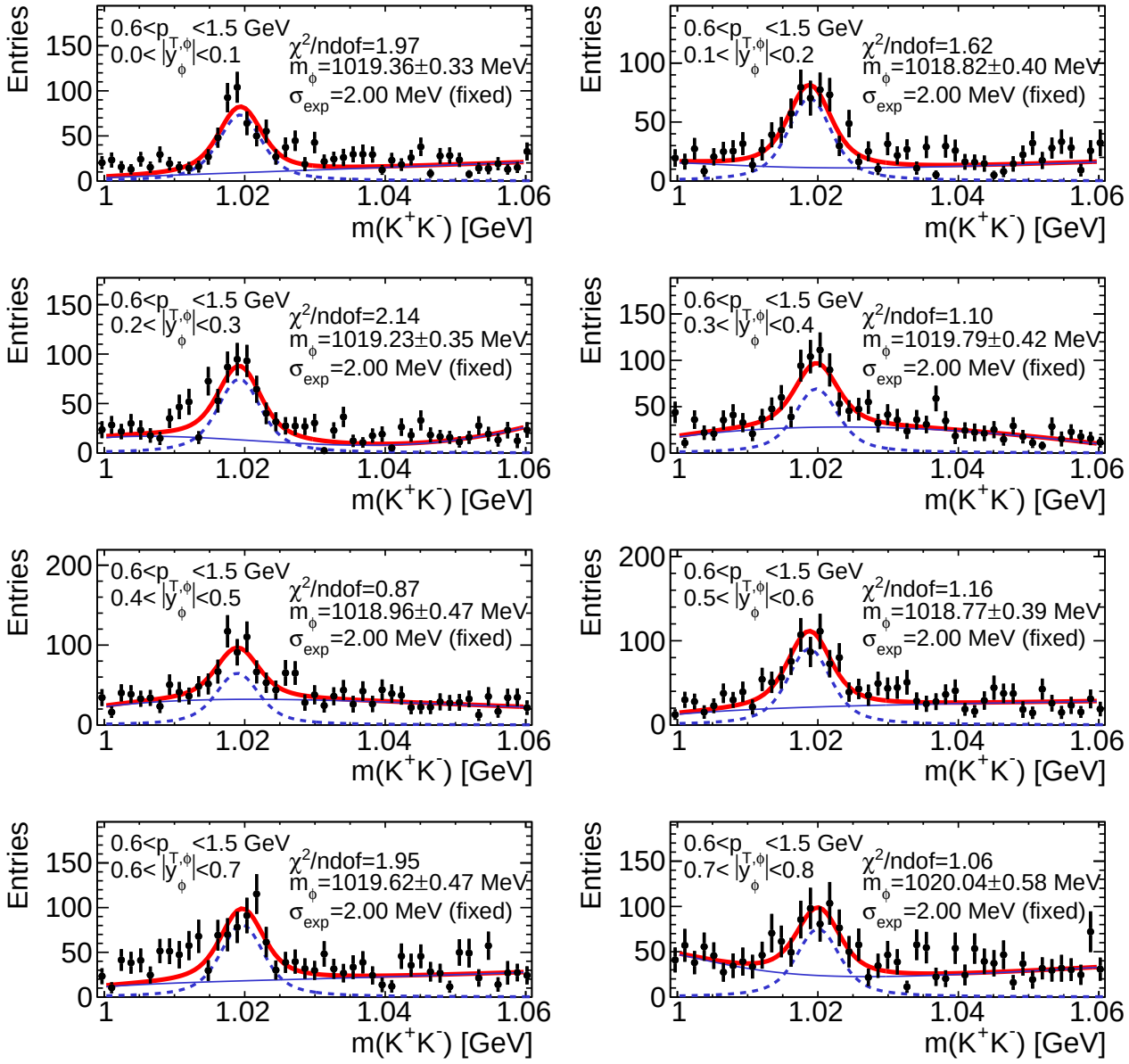

Figure B.2.1: Fits to invariant mass distributions of pairs of oppositely charged kaon candidates for CD data. Formulas (6.1), (6.2), (6.6) and corrections for the bias in the momentum reconstruction were applied. The distributions are shown in eight ranges of $|y_\phi|$. The red curves represent a convolution of the non-relativistic Breit-Wigner function with the Gaussian distribution as a signal function (5.5) plus a background fitting function (5.7). The blue solid lines represent the background shape and the dashed blue curves - the signal contribution. The extracted signal yields were used to obtain the $|y_\phi|$ spectra shown in right plots in Figure 8.9.

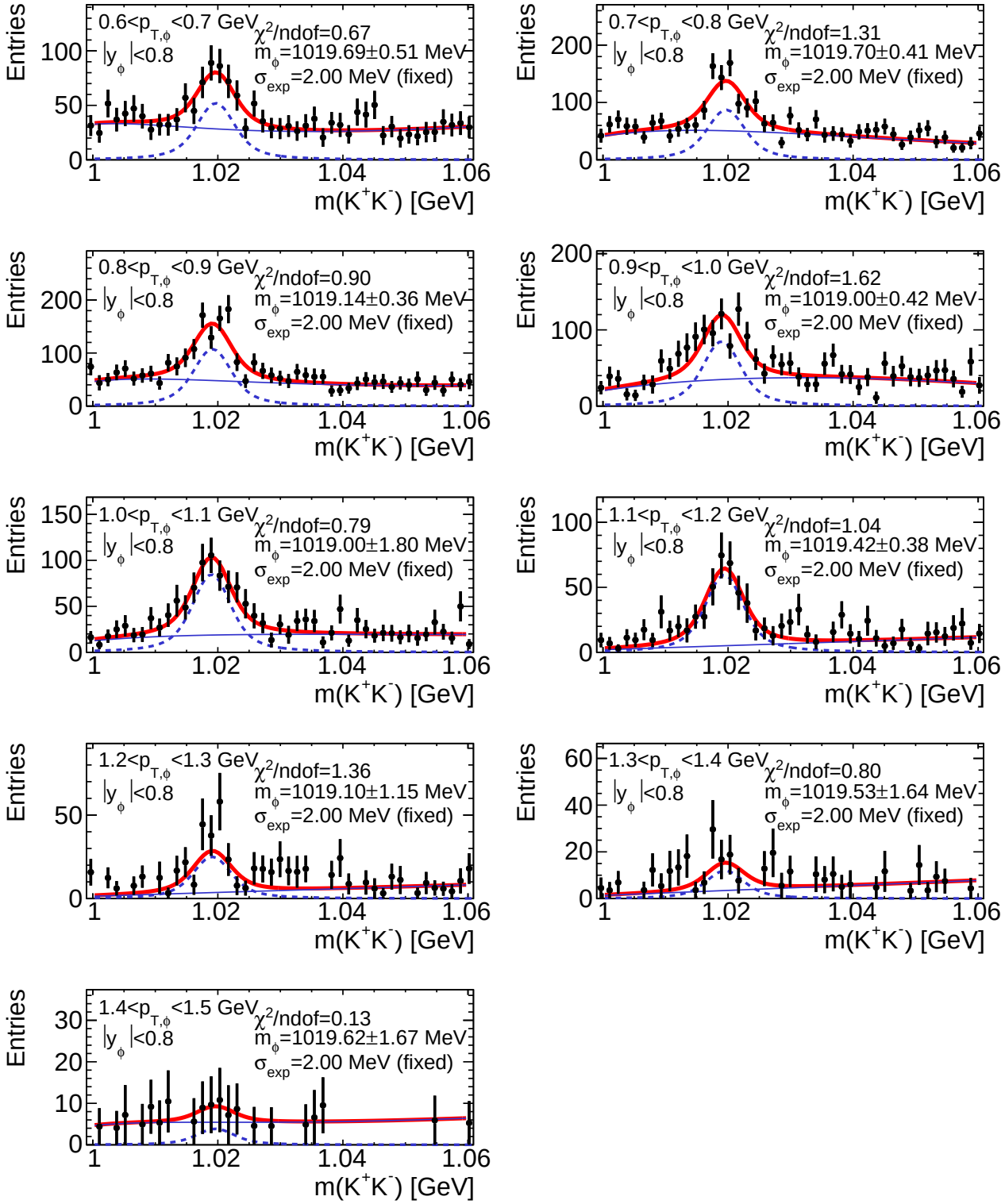

Figure B.2.2: Fits to invariant mass distributions of pairs of oppositely charged kaon candidates for CD data. Formulas (6.1), (6.2), (6.6) and corrections for the bias in the momentum reconstruction were applied. The distributions are shown in nine ranges of $p_{\mathrm{T},\phi}$. The red curves represent a convolution of the non-relativistic Breit-Wigner function with the Gaussian distribution as a signal function (5.5) plus a background fitting function (5.7). The blue solid lines represent the background shape and the dashed blue curves - the signal contribution. The extracted signal yields were used to obtain the $p_{\mathrm{T},\phi}$ spectra shown in left plots in Figure 8.9.

B.3 Minimum Bias Analysis

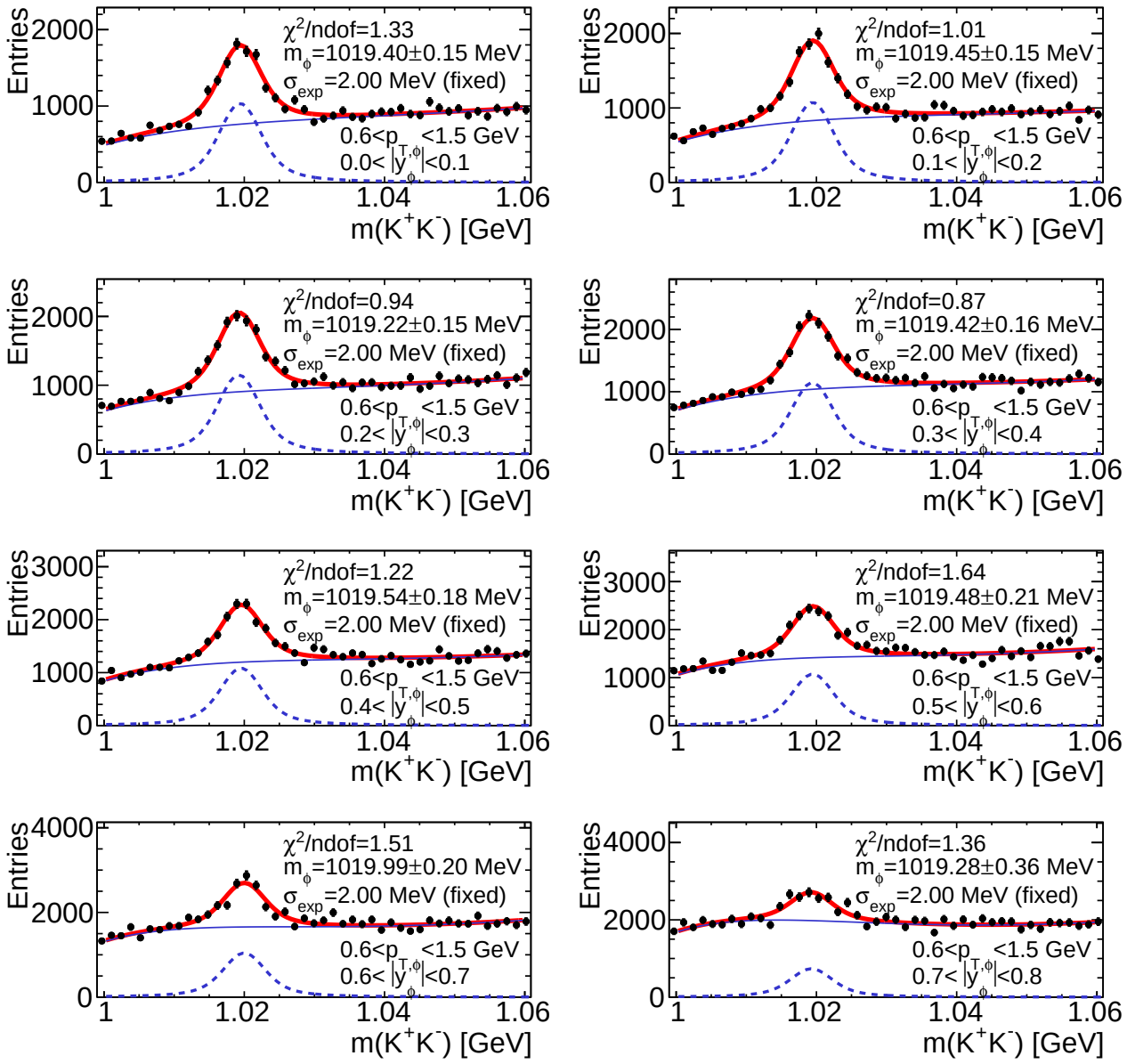

Figure B.3.1: Fits to invariant mass distributions of pairs of oppositely charged kaon candidates in MB data. Formulas (6.1), (6.2), (6.6) and corrections for the bias in the momentum reconstruction were applied. The distributions are shown in eight ranges of $|y_\phi|$. The red curves represent a convolution of the non-relativistic Breit-Wigner function with the Gaussian distribution as a signal function (5.5) plus a background fitting function (5.7). The blue solid lines represent the background shape and the dashed blue curves - the signal contribution. The extracted signal yields were used to obtain the $|y_\phi|$ spectra shown in right plots in Figure 8.10.

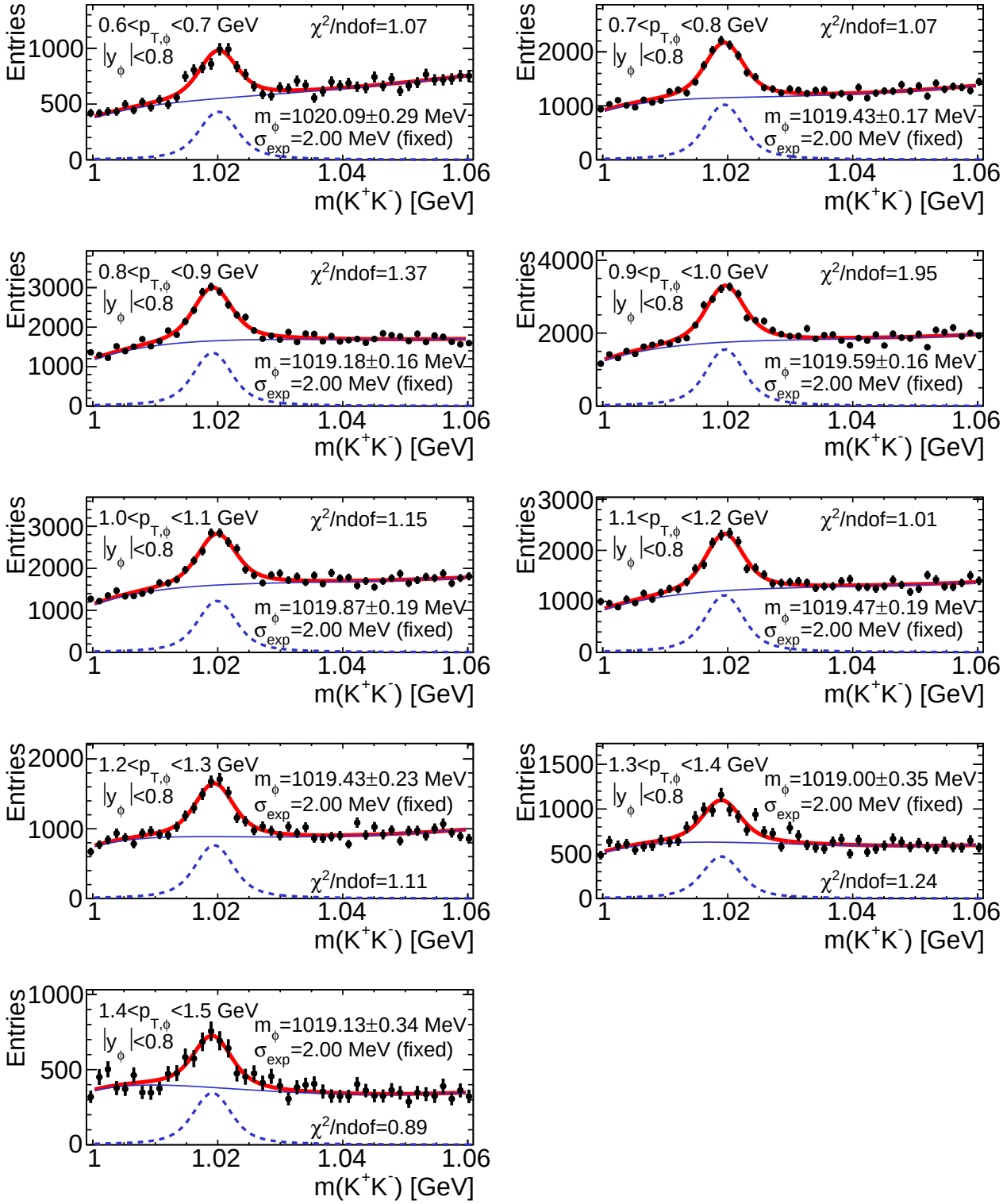

Figure B.3.2: Fits to invariant mass distributions of pairs of oppositely charged kaon candidates for MB data. Formulas (6.1), (6.2), (6.6) and corrections for the bias in the momentum reconstruction were applied. The distributions are shown in nine ranges of $p_{\mathrm{T},\phi}$. The red curves represent a convolution of the non-relativistic Breit-Wigner function with the Gaussian distribution as a signal function (5.5) plus a background fitting function (5.7). The blue solid lines represent the background shape and the dashed blue curves - the signal contribution. The extracted signal yields were used to obtain the $p_{\mathrm{T},\phi}$ spectra shown in left plots in Figure 8.10.